



TECHNISCHE UNIVERSITÄT MÜNCHEN



Fakultät für Physik

# Neutron Depolarization of Ferromagnetic Materials under Ultra-High Pressures

Marc Seifert, M. Sc.

Vollständiger Abdruck der von der Fakultät für Physik der Technischen Universität München zur Erlangung des akademischen Grades eines

**Doktors der Naturwissenschaften (Dr. rer. nat.)**

genehmigten Dissertation.

Vorsitzender: Prof. Dr. Martin Zacharias

Prüfer der Dissertation: 1. Prof. Dr. Christian Pfeiderer  
2. Prof. Dr. Peter Böni

Die Dissertation wurde am 27.08.2021 bei der Technischen Universität München eingereicht und durch die Fakultät für Physik am 02.12.2021 angenommen.



---

## Abstract

The present work reports on the investigation of the ferri-/ferromagnetic properties of magnetite,  $\text{SrRuO}_3$ ,  $\text{CePd}_{1-x}\text{Rh}_x$ , and  $\text{CePt}$  under ultra-high hydrostatic pressures. The neutron depolarization (ND) technique was used for the measurements due to its ability to probe ferromagnetism on different length scales and its compatibility with complex sample environments, such as low temperatures and high pressures. As several of the ND measurements are close to the resolution limit of the utilized ND setups, the theoretical length and time scale resolution of ND was estimated and relevant errors and artifacts are discussed.

ND measurements on natural single-domain magnetite show a reordering of the magnetic domains at the Verwey transition. The results enable further measurements under pressure motivated by the potential use of magnetite as a geobarometer. The magnetic phase diagram of the itinerant ferromagnet  $\text{SrRuO}_3$  was investigated and confirmed up to a pressure of 17.1 GPa using the ND technique. Furthermore, ND studies were performed on the ferromagnetic Kondo-lattices  $\text{CePd}_{1-x}\text{Rh}_x$  and  $\text{CePt}$ , which can both be driven toward a quantum phase transition. The ferromagnetism of  $\text{CePd}_{1-x}\text{Rh}_x$  progressively changes into a Kondo cluster glass with increasing  $x$  due to disorder introduced by doping. The magnetic phase diagram of  $\text{CePt}$  was investigated up to a pressure of 12.1 GPa showing clean ferromagnetic behavior up to the quantum phase transition.



## Kurzfassung

Die vorliegende Arbeit befasst sich mit der Untersuchung der ferri-/ferromagnetischen Eigenschaften von Magnetit,  $\text{SrRuO}_3$ ,  $\text{CePd}_{1-x}\text{Rh}_x$  und  $\text{CePt}$  unter ultra-hohen hydrostatischen Drücken. Für die Messungen wurde die Neutronen-Depolarisations (ND) Methode verwendet, da sie Ferromagnetismus auf verschiedenen Längenskalen untersuchen kann und kompatibel mit komplexen Probenumgebungen ist, wie zum Beispiel tiefe Temperaturen und hohe Drücke. Weil einige der ND-Messungen nahe am Auflösungslimit der verwendeten ND-Experimentaufbauten sind, wurden die mit ND theoretisch messbaren Längen- und Zeitskalen abgeschätzt und relevante Fehler und Artefakte diskutiert.

ND-Messungen an natürlichem eindomänigem Magnetit zeigen eine Umordnung der magnetischen Domänen am Verwey-Übergang. Die Ergebnisse ermöglichen weitere Messungen unter Druck, welche durch die mögliche Verwendung von Magnetit als Geobarometer motiviert werden. Das magnetische Phasendiagramm des itineranten Ferromagneten  $\text{SrRuO}_3$  wurde mithilfe der ND-Methode bis zu einem Druck von 17.1 GPa untersucht und bestätigt. Weiterhin wurden ND-Studien an den ferromagnetischen Kondo-Gittern  $\text{CePd}_{1-x}\text{Rh}_x$  und  $\text{CePt}$  durchgeführt, die beide in die Nähe eines Quantenphasenübergangs gebracht werden können. Der Ferromagnetismus von  $\text{CePd}_{1-x}\text{Rh}_x$  degradiert mit zunehmendem  $x$  wegen der durch Dotierung eingebrachten Unordnung und geht kontinuierlich in ein Kondo-Cluster-Glas über. Das magnetische Phasendiagramm von  $\text{CePt}$  wurde bis zu einem Druck von 12.1 GPa untersucht und zeigt rein ferromagnetisches Verhalten bis zum Quantenphasenübergang.



# Contents

<b>1. Introduction</b>	<b>1</b>
<b>2. Experimental Methods</b>	<b>7</b>
2.1. Neutron Depolarization Measurements	7
2.1.1. Theory of Neutron Depolarization Measurements	8
2.1.1.1. Neutron Depolarization by Ferromagnetic Order	9
2.1.1.2. Detectable Length and Time Scales of Ferromagnetic Order	13
2.1.2. Neutron Depolarization Setups	15
2.1.2.1. 1d Polarization Analysis Setup	16
2.1.2.2. Neutron Imaging and Imaging Detectors	18
2.1.2.3. Neutron Depolarization Imaging	23
2.1.2.4. Neutron Depolarization Measurements at High Pressures	26
2.1.3. Neutron Depolarization Data Acquisition and Evaluation Procedure	30
2.1.3.1. Error Sources in Neutron Depolarization Measurements	33
2.1.3.2. The Impact of the Scintillator Afterglow on the Polarization	41
2.1.3.3. Polarization Changes due to Relative Movement of the Pinhole of the DAC	45
2.1.3.4. On the Interpretation of Polarization Signals using the High-Pressure Neutron Depolarization Setup	46
2.2. Diamond Anvil Cells	48
2.3. Samples	52
2.3.1. Magnetite	52
2.3.2. $\text{CePd}_{1-x}\text{Rh}_x$	53
2.3.3. CePt	54
2.3.4. $\text{SrRuO}_3$	55
<b>3. Single-Domain Magnetite on Chiton Teeth</b>	<b>57</b>
3.1. State of the Art	58

3.2. Experimental Results	59
3.3. Discussion	64
3.4. Conclusions	65
<b>4. The Itinerant Ferromagnet SrRuO<sub>3</sub></b>	<b>67</b>
4.1. State of the Art	69
4.2. Experimental Results	73
4.3. Discussion	84
4.4. Conclusions	87
<b>5. Ce-based Ferromagnetic Kondo Lattices</b>	<b>89</b>
5.1. Introduction	89
5.2. Neutron Depolarization Study of CePd <sub>1-x</sub> Rh <sub>x</sub>	91
5.2.1. Introduction to CePd <sub>1-x</sub> Rh <sub>x</sub>	91
5.2.2. Experimental Results	93
5.2.3. Discussion of CePd <sub>1-x</sub> Rh <sub>x</sub>	99
5.3. Neutron Depolarization of CePt under Pressure	102
5.3.1. Introduction to CePt	102
5.3.2. Experimental Results	106
5.3.2.1. Magnetization and Susceptibility	107
5.3.2.2. Neutron Depolarization Measurements at Zero Pressure	107
5.3.2.3. High Pressure Neutron Depolarization Measurements	112
5.3.3. Discussion of CePt	124
5.3.3.1. Properties of CePt at Ambient Pressure	124
5.3.3.2. Properties of CePt at High Pressures	126
5.4. Conclusions	128
<b>6. Conclusions</b>	<b>131</b>
<b>A. Appendix</b>	<b>135</b>
A.1. Neutron Depolarization Imaging of UGe <sub>2</sub>	135
A.2. Supplementary Magnetite Data	137
A.3. Supplementary SrRuO <sub>3</sub> Data	139
A.3.1. 3 × 3 Guide Pattern Polarizations of Measurements Shown in Sec. 4.2	139
A.3.2. Inconclusive SrRuO <sub>3</sub> Measurements	143
<b>Bibliography</b>	<b>155</b>

# 1. Introduction

Ferromagnetism (FM) in condensed matter emerges from the quantum-mechanical exchange interaction between the spin and charge degrees of freedom of the electrons, forcing the resulting magnetic moments to align in parallel. Although the macroscopic manifestation of FM expressed by a finite magnetization is similar for all FM materials, the microscopic description of the moments can differ greatly. The magnetic moments are often described in two limiting cases: the local-moment and the itinerant electron picture. In local-moment FM the electrons contributing to the magnetism are assumed to be strongly localized at the atomic sites, which can, for example, explain the integral magnetic moment of magnetite ( $\text{Fe}_3\text{O}_4$ ) of  $4\mu_B$ . However, when comparing magnetite to elemental Fe, the non-integer ordered moment of Fe of  $2.2\mu_B$  is not compatible with local moments. Instead a description of the magnetic properties of Fe is given by the itinerant electron picture that is characterized by the assumption of electrons that are free to move and thus are conduction electrons. Itinerant FM, also referred to as band magnetism, is based on Landau-Fermi-liquid (FL) theory, the standard model of metals. For several decades this comparatively simple description of itinerant FM was widely accepted due to good agreement between experiment and theory. However, in recent years exceptions were found where itinerant FMs showed non-Fermi-liquid (NFL) behavior giving rise to the question if a FL is indeed the normal state of an itinerant FM [1, 2].

To investigate the electronic ground state of a FM it is beneficial to suppress the Curie temperature  $T_C$  to lowest temperatures in order to remove parasitic high-temperature effects and signatures caused by the magnetism itself. In many systems this can be done by means of a non-thermal control parameter such as hydrostatic pressure  $p$ , chemical composition  $x$ , or magnetic field  $B$ . Following, for example, the arguments by Wohlfarth [3] it is generally possible to reduce the  $T_C$  of an itinerant FM by decreasing the lattice spacing that can be accomplished via hydrostatic or chemical pressure. If  $T_C$  is suppressed to zero, the magnetic phase transition is driven by quantum fluctuations instead of thermal fluctuations, motivating the name quantum phase transition (QPT). In recent years QPTs have attracted great interest due to the appearance of exotic phases close to QPTs, such as the partial order in MnSi [4] or unconventional superconductivity (SC) in UGe<sub>2</sub> [5],

resulting in the investigation of a multitude of quantum critical FMs and the mapping of their phase diagrams.

Although the early theory of FM QPTs by Hertz [6] assumed a continuous 2nd order phase transition down to  $T_C = 0$ , an increasing number of systems was discovered, such as the itinerant FMs MnSi [7] and ZrZn<sub>2</sub> [8], featuring a tricritical point where the phase transition changes from 2nd to 1st order. In 1999 Belitz *et al.* [9] showed that the coupling of the magnetization to electronic soft modes generically results in a 1st order phase transition in itinerant FMs if the system is sufficiently clean, putatively explaining the different phase diagrams. The generic phase diagram considered by Belitz *et al.* has been observed in several compounds; however, different escape routes to quantum criticality were found as well, such as the appearance of an adjacent phase, e.g. antiferromagnetism in CeRu<sub>2</sub>Ge<sub>2</sub> [10] or spin-glass behavior in CePd<sub>1-x</sub>Rh<sub>x</sub> [11] (see Ref. [2] for a review on this topic).

In order to differentiate between the universal behavior of quantum critical FMs and the properties of particular systems, the mapping of further FM phase diagrams is required. In the case of pressure-driven QPTs two approaches can be used to investigate the phase diagram: exerting chemical pressure through substitution of one ligand with smaller atoms or applying hydrostatic pressure using pressure cells. The advantage of substitution is its simplicity compared to the technical efforts required for pressure cells. However, the substitution with different atoms can change the electronic properties locally compared to the undoped system and, moreover, introduce disorder into a formerly clean system that can alter the QPT. In contrast, the application of hydrostatic pressure is a rather clean and controlled way to drive a FM system toward a QPT. Additionally, not only the phase transition between the paramagnetic (PM) and FM phase may be pressure-dependent but also other phase transitions such as the Verwey-transition in magnetite, an electronic low-temperature transition.

For the investigation of quantum critical FMs measurements of the magnetization at high hydrostatic pressures are required. However, several experimental aspects have to be considered for such measurements. Depending on the pressure range and measurement technique different designs of pressure cells are used. The low and medium pressure range up to about 3 GPa can be accessed with clamp cells that offer sample volumes of up to several dozens of mm<sup>3</sup> and are relatively easy to use. Due to the compact and simple design this type of pressure cell is suitable for standard magnetization and susceptibility measurements. For high pressures above 3 GPa pressure cells featuring opposing anvils are used, such as Bridgman cells or diamond anvil cells (DAC). These pressure cells require more experimental experience and feature much smaller sample volumes than clamp cells

– typically less than  $0.01 \text{ mm}^3$ . The small sample volume compared to the dimensions of an opposed anvil cell results in large background signals in magnetization measurements that require a precise setup for the measurements and sophisticated evaluation routines. Although conventional magnetization measurements can successfully be performed at high pressures [12, 13], the complexity involved promotes the utilization of complementary or alternative measurement techniques for the investigation of quantum critical FMs at high pressures, such as the neutron depolarization (ND) technique.

The ND technique is highly sensitive to FM order due to the interaction of the neutron's spin with magnetic fields [14]. Moreover, the large penetration depth of neutrons enables the investigation of magnetism in bulk samples up to several cm in size and the usage of massive sample environment equipment such as cryostats, magnets, and pressure cells. From the ND of a FM sample  $T_C$  can be determined to high precision but also information can be gained about the behavior of the FM domains and about possible magnetic anisotropies [15–18]. Furthermore, the technique of neutron depolarization imaging (NDI) enables one to measure the ND with a spatial resolution which can, for example, be utilized for the determination of the metallurgical homogeneity of a sample [19, 20].

In the course of the present work the FM properties of four materials were investigated under pressure: the ferrimagnetic mineral magnetite, the itinerant FM  $\text{SrRuO}_3$ , and the FM Kondo-lattices  $\text{CePd}_{1-x}\text{Rh}_x$  and  $\text{CePt}$ . The type of FM of the materials varies widely but can be sorted with respect to the complexity of the FM. The two opposing theories of FM, the local-moment and the itinerant electron pictures, are the easiest to apply with the local-moment picture being arguably more intuitive. However, there are intermediate cases of FM partly showing aspects of both pictures resulting in a rather complex behavior. Another aspect is the type of electron orbital participating in the magnetic order. Transition metal systems tend to feature less complex behavior due to the comparatively extended d-orbitals and the therefore more direct interaction between the d-electrons. In contrast, f-electron orbitals are situated closer to the nucleus, often preventing a simple direct exchange with neighboring f-electron orbitals. Instead, in many cases an indirect interaction is established through a hybridization of the f-electrons with conduction electrons, resulting in a more complex description of the FM. Therefore, the four investigated materials can be arranged with increasing complexity as follows. Magnetite features the least complex FM order due to the local-moment description of the 3d-electrons. The transition metal oxide  $\text{SrRuO}_3$  is more complex than magnetite due to its itinerant FM and the rarity of 4d FM. The 4f systems  $\text{CePd}_{1-x}\text{Rh}_x$  and  $\text{CePt}$  show the highest amount of complexity with  $\text{CePt}$  ranking higher than  $\text{CePd}_{1-x}\text{Rh}_x$ , as the investigation of  $\text{CePt}$  requires hydrostatic pressure in

contrast to the doping series  $\text{CePd}_{1-x}\text{Rh}_x$ . In the following the structure of this thesis is described as well as a brief introduction is given for each of the four materials.

Chap. 2 describes the experimental methods utilized during the work presented here with a strong focus on the ND technique. After an introduction to the theory of ND, the detection limits of ND regarding the length scale of FM domains as well as the time scale of FM fluctuations are discussed in order to provide a basis for the interpretation of ND measurements of complex forms of FM order. Furthermore, details on the different ND setups and the measurement procedures are given. As several ND measurements feature tiny signals almost indistinguishable from noise, all relevant statistic and systematic error sources are discussed, approaches on how to minimize the noise in ND measurements are given, and a guide on how to interpret ND measurements despite the presence of significant noise is presented. Additionally, Chap. 2 covers the DACs utilized, specifically designed for ND experiments, and the investigated samples.

Chap. 3 reports on the investigation of the Verwey transition in natural magnetite. Magnetite is of interest in several fields of research due to its occurrence in animals and the human brain [21–24], its possible application in spintronics [25], its usage as an indicator for the climate on Mars [26–28], and its significance for geo- and paleomagnetism [29–31]. The pressure-dependence of the Verwey transition in magnetite could, for example, be utilized as a geobarometer for the determination of shock at meteorite impact sites [32]. However, a detailed understanding of the link between exerted stress on polycrystalline magnetite and the signature of the Verwey transition observed in the magnetic properties is still missing, calling for further investigation. Hence, magnetization and ND measurements of natural magnetite were performed and compared. While both techniques can clearly identify the Verwey transition, differences are observed in the determination of the coercivities with the ND measurements showing slightly larger values of the coercivity. However, the differences may be explained by the sensitivity of ND to the size of magnetic domains, in contrast to conventional magnetization measurements that average over the whole sample. The results motivate further experiments under hydrostatic pressure.

Chap. 4 covers the suppression of magnetic order in the itinerant FM  $\text{SrRuO}_3$ . This compound is an example for deviating behavior between hydrostatic and chemical pressure. A high-pressure susceptibility study [33] was able to trace a linear suppression of  $T_C$  from 164 K at ambient pressure to about 43 K at a pressure of 17.2 GPa that would extrapolate to a critical pressure  $p_C = 23.8$  GPa. Chemical pressure can be exerted in this system by substituting Sr with the isoelectric, but smaller, Ca. Similar to an increase of  $p$  in  $\text{SrRuO}_3$ , an increase of the Ca concentration  $x$  in  $\text{Sr}_{1-x}\text{Ca}_x\text{RuO}_3$  results in a decrease of  $T_C$ ; however, the disorder introduced by the Ca atoms additionally causes the appearance

of a Griffiths phase [34]. A substitution of Sr with the larger Ba results counter-intuitively also in a decrease of  $T_C$  due to predominant electronic effects caused by the Ba atoms [35]. Therefore, further measurements of SrRuO<sub>3</sub> using the clean control parameter  $p$  are necessary in order to expand the phase diagram to higher pressures and determine the ground state of SrRuO<sub>3</sub> close to the putative QPT. High-pressure ND measurements were performed up to a pressure of 17.1 GPa which are shown and discussed in Chap. 4. The results are in good agreement with previous high-pressure studies and an updated phase diagram is given. Furthermore, the results indicate that ND measurements of SrRuO<sub>3</sub> are possible at even higher pressures close to the putative QPT.

In Chap. 5 the separate ND studies on the FM Kondo-lattices CePd<sub>1-x</sub>Rh<sub>x</sub> and CePt are presented and compared. The FM Kondo-lattice CePd<sub>1-x</sub>Rh<sub>x</sub> is another example for the appearance of a Griffiths phase close to a QPT [11], where the FM order is governed by the competition of the RKKY interaction and the Kondo effect based on the Doniach model [36]. With increasing  $x$  the FM order is continuously suppressed due to chemical pressure, but also disorder is introduced affecting the formation of the FM on both the microscopic (interatomic) and the mesoscopic (magnetic domains/clusters) length scales [11, 20]. As a result, the phase diagram of CePd<sub>1-x</sub>Rh<sub>x</sub> shows a smeared QPT, deviating from the Doniach model. In contrast, the isostructural FM Kondo-lattice CePt seems to feature a pressure-induced QPT at  $p_C = 12.1$  GPa in good agreement with Doniach's phase diagram [37]. However, there is only one study [37] tracing  $T_C$  up to  $p_C$  using susceptibility and resistivity measurements and, therefore, a direct observation of the FM order parameter, the magnetization, is still missing at high pressures. ND measurements were performed on both materials in order to investigate the FM ground states and the magnetic phase diagrams.

The results of CePd<sub>1-x</sub>Rh<sub>x</sub> confirm the phase diagram and the Kondo cluster glass model by Westerkamp *et al.* which describes the smearing of the QPT and the formation of FM clusters surrounded by paramagnetic regions close to the QPT due to increasing disorder [11]. Furthermore, the strong magnetic anisotropy of CePd<sub>1-x</sub>Rh<sub>x</sub> and its influence on ND measurements were investigated.

High-pressure ND measurements of CePt were performed up to a pressure of 12.2 GPa confirming the phase diagram determined by susceptibility and resistivity measurements [37]. The insights gained from the study of the anisotropy of CePd<sub>1-x</sub>Rh<sub>x</sub> were used for a better interpretation of the high-pressure ND results of CePt that features a similar anisotropy. The results of both systems are compared with a focus on the different routes towards quantum criticality. Although both systems feature the same crystal structure and are both FM Kondo-lattices with very similar microscopic interactions, the introduction

of disorder can severely affect the quantum critical behavior as can be seen from the investigated phase diagrams.

Finally, the main results and conclusions of this thesis are summarized in Chap. 6.

## 2. Experimental Methods

This chapter describes the experimental methods that were utilized in the framework of this thesis. Magnetization measurements were performed using a standard Physical Property Measurement System (PPMS) by Quantum Design. However, most of the results were acquired with the ND technique which is described in Sec. 2.1. Details on the pressure cells used for the application of up to 17.1 GPa are given in Sec. 2.2. Finally, the investigated samples are described in Sec. 2.3.

### 2.1. Neutron Depolarization Measurements

The ND technique dates back to the first theoretical description of the passage of neutrons through a FM by Halpern and Holstein [14] in 1941. First ND measurements were performed in 1950 by Burgy *et al.* [38], who investigated worked steel sheets made with different fabrication techniques by determining the average domain size from the depolarization data. With the advent of high-flux neutron sources and dedicated polarization devices in the 1960s, polarized neutrons became accessible to a larger user base which lead to an increase of ND studies. These early studies already made apparent the potential of the ND technique to investigate FM phase transitions [15, 39–44]. Notably, the first measurements that can be interpreted as NDI were performed by Drabkin *et al.* in 1969 by scanning a pinhole mask over a Ni sample [43]. An extension of the ND technique developed by Rekveldt [16] in 1973 was the 3d depolarization analysis setup which enables the investigation of domain correlations, magnetic textures, and FM anisotropies [17]. Another improvement was the utilization of pulsed neutrons by Mitsuda and Endoh [45, 46] in order to measure the wavelength dependence of the depolarization. A better theoretical understanding of ND and advanced experimental setups led then to the investigation of more complex systems, such as spin-glasses [47–50], ferrofluids [51], superparamagnets [52], high temperature superconductors [53], and quantum critical FMs [54]. The development of modern neutron imaging detectors allowed the operation of polarized imaging setups [55] and, furthermore, a tomographic reconstruction of ND data [19]. More detailed reviews about the history of ND are given in Refs. [18, 56, 57].

Next to the semiclassical ND theory formulated by Halpern and Holstein a quantum mechanical description of ND was developed by Maleev, Ruban, and Toperverg [58, 59] in the 1970s. The latter theory describes ND via neutron scattering due to correlations between magnetic domains along different neutron trajectories. Later it was shown that both theories give essentially the same results [60–62]. As the theory by Halpern and Holstein is sufficient for the interpretation of the results of this work, the theory by Maleev, Ruban, and Toperverg is not discussed below. Sec. 2.1.1 gives an introduction to the theory of ND measurements. In Sec. 2.1.2 the ND setups that are utilized in the present work are described and in Sec. 2.1.3 an explanation of the data evaluation process is given.

### 2.1.1. Theory of Neutron Depolarization Measurements

In the following the spin of a neutron  $\vec{S}$  is described as a classical vector with a length of  $|\vec{S}| = 1$ . The polarization of a neutron beam is then defined as the average over a large number of neutrons

$$\vec{P} = \langle \vec{S} \rangle \quad (2.1)$$

where the brackets  $\langle \dots \rangle$  denote the average over the beam. As the ND methods presented here analyze the polarization in the y-direction, only the y-component  $P_y$  of  $\vec{P} = (P_x, P_y, P_z)$  is measured. The polarization is therefore reduced to a scalar value in the interval  $(-1, 1)$  and defined as  $P := P_y$  from here. If a neutron beam is completely polarized in the positive y-direction, all neutron spins point in the same direction and thus  $P = 1$ . If the beam is unpolarized, the neutron spins point in arbitrary directions and the averaging of Eq. 2.1 results in  $P = 0$ .

The time evolution of a neutron spin in an external field  $\vec{B}(t)$  is given by the Larmor equation

$$\frac{d}{dt} \vec{S}(t) = \gamma \vec{S}(t) \times \vec{B}(t) \quad (2.2)$$

where  $\gamma = 183 \text{ MHz/T}$  is the gyromagnetic ratio of the neutron. The solution of the differential equation 2.2 for a constant field describes a precession of the neutron spin  $\vec{S}$  around  $\vec{B}$  with the Larmor frequency  $\vec{\omega}_L = -\gamma \vec{B}$ . Therefore, after passing a magnetic field, a neutron spin collects a Larmor phase  $\varphi_L$  which is proportional to the field integral along the neutron's flight path.

When considering fields that are not constant over time and space, a calculation in the inertial frame of the neutron is advantageous as it converts spatial variations to temporal

variations. Describing the temporal variation of a magnetic field by  $\omega_B = 2\pi B^{-1}dB/dt$  the adiabaticity is then given by

$$k = \frac{\omega_L}{\omega_B}. \quad (2.3)$$

The dimensionless adiabaticity  $k$  is a measure for a field change as seen by a neutron. If the adiabaticity is large, i.e.  $\omega_L \gg \omega_B$ , the field change is slow compared to the Larmor frequency and it is called adiabatic. In this case the neutron spin follows the orientation of the external field. This can be used, for example, to guide the polarization through an experimental setup by installing sufficiently strong permanent fields along the neutron beam. In the non-adiabatic case, i.e.  $\omega_L \ll \omega_B$ , the field change is too abrupt for the neutron spin to follow the field. Instead, the spin starts to precess around the new field direction. A detailed calculation of the spin state for any field change can be found in Ref. [63].

The behavior of a neutron in a magnetic field summarized above is applied to the case of a FM sample in a polarized neutron beam in the following Sec. 2.1.1.1. The presented theoretical considerations predict a depolarization of the beam due to FM order and additionally give information on the magnitude of this depolarization. In the subsequent Sec. 2.1.1.2 the order of magnitude on which ND caused by FM order can be observed and measured is discussed.

### 2.1.1.1. Neutron Depolarization by Ferromagnetic Order

In order to discuss the effect of a FM sample on a polarized neutron beam, a simple model of FM is considered and four assumptions are made [14, 16]. (i) The orientation of the net magnetizations of the magnetic domains are distributed randomly. (ii) The dimensions of the domains are all in the same order of magnitude and can be described by an average domain size  $\delta$ . (iii) The magnitude of the magnetic field in each domain  $B_0 = \mu_0 M_0$  is constant and given by the saturation magnetization  $M_0$  and the vacuum permeability  $\mu_0$ . (iv) The transition from one domain to an adjacent domain is non-adiabatic, i.e. the domain walls are sufficiently thin.

A sketch of a FM sample with length  $d$  is shown in Fig. 2.1. A neutron beam passes through the sample from the left side which is indicated by the horizontal blue arrows. The red arrows depict the orientation of single neutron spins. As the neutron beam is considered to be completely polarized ( $P = 1$ ) before entering the sample, all neutron spins point in the same direction. When non-adiabatically entering a FM domain a neutron spin precesses around the field  $B_0$  in the domain. When leaving the sample after passing

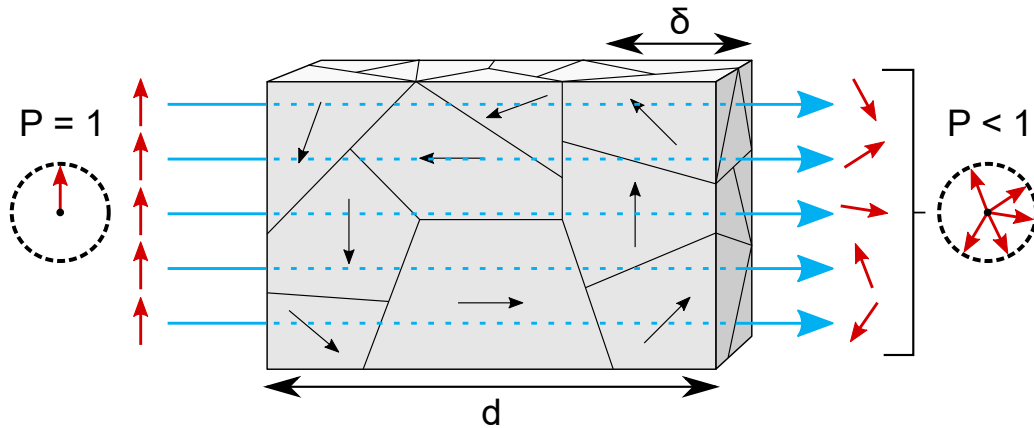


**Figure 2.1.:** Neutron depolarization due to FM. The figure shows a FM bulk sample with thickness  $d$  and randomly distributed domains with an average domain size  $\delta$ . A completely polarized neutron beam is considered passing through the sample from the left side. An individual neutron spin, indicated by a red arrow, sees a certain domain configuration and, therefore, acquires a certain Larmor phase on its trajectory through the sample (dashed blue arrow). Neutrons with slightly different trajectories acquire different Larmor phases due to a finite beam divergence and the random constellation of domains. Averaging over an ensemble of neutrons, e.g. in a detector pixel, results in an overall decrease of the beam polarization. Figure adapted from Ref. [64].

several domains, a neutron spin collects a certain Larmor phase depending on the neutron's flight path through the sample and on the constellation of domains. A neutron with a slightly different flight path collects a different Larmor phase due to the random domain orientations. Therefore, after passing through the sample, the neutron spins point in different directions. After averaging over a set of neutrons in a detector pixel, the measured polarization is thus  $P < 1$ , i.e. the neutron beam is depolarized by the FM. When crossing from the PM into the FM phase by changing an external control parameter such as the temperature, a decrease of the polarization at the phase transition is expected.

It is important to note that the depolarization is caused by the finite magnetizations  $M_0$  and not by the single magnetic moments of the FM. A neutron wave-package averages the magnetic moments of a crystal over the neutron's coherence volume [56] which can include several thousand magnetic moments in the case of a cold collimated neutron beam [65]. Therefore, paramagnetic, diamagnetic, and antiferromagnetic systems do not depolarize a neutron beam as the magnetic moments average out on the scale of the coherence volume of the neutron.

In the following a mathematical description of ND due to FM is given based on the theory developed by Halpern and Holstein [14] and extended by Rekveldt [16]. The

polarization of a neutron beam after passing  $N = d/\delta$  FM domains is given by

$$P = P_0 \left[ \left\langle \frac{B_{\parallel}^2}{B_0^2} \right\rangle + \left\langle \frac{B_{\perp}^2}{B_0^2} \right\rangle \left\langle \cos \left( \gamma B_0 \frac{\delta}{v} \right) \right\rangle \right]^N \quad (2.4)$$

where assumptions (ii) to (iv) were applied.  $B_{\parallel}$  and  $B_{\perp}$  are the parallel and perpendicular component of  $B_0$  in one domain as seen from the neutron spin, respectively. The angular brackets  $\langle \dots \rangle$  describe an average over a large number of domains and  $v$  is the neutron velocity which can be calculated from the neutron wavelength  $\lambda = h/m_n v$  with Planck's constant  $h$  and the neutron mass  $m_n$ .  $P_0$  is a normalization factor containing the finite efficiencies of the polarization analysis setup and equals to the polarization that is measured without any depolarizing effects. From assumption (i), the random distribution of domain orientations, follows

$$\begin{aligned} \left\langle \frac{B_{\parallel}^2}{B_0^2} \right\rangle &= \frac{1}{3} \\ \left\langle \frac{B_{\perp}^2}{B_0^2} \right\rangle &= \frac{2}{3}. \end{aligned} \quad (2.5)$$

When considering the argument of the cosine function in Eq. 2.4 it is evident that the argument is the same as the Larmor phase

$$\varphi_L = \gamma B_0 \frac{\delta}{v} = \omega_L t. \quad (2.6)$$

In the case of small spin rotations per domain,  $\varphi_L \ll 2\pi$ , Eq. 2.4 can then be approximated by

$$P = P_0 \exp \left( -\frac{1}{3} \gamma^2 \frac{d}{v^2} B_0^2 \delta \right). \quad (2.7)$$

As  $d$  and  $v$  are usually constant during an experiment, this equation mainly depends on the field in a domain  $B_0$  and the average domain size  $\delta$ . The product  $B_0^2 \delta$  describes the FM of the sample and determines the depolarization. Larger values of  $B_0^2 \delta$  are ascribed to a stronger FM and result in larger depolarization while the opposite holds true for smaller values of  $B_0^2 \delta$ . A temperature dependence of the magnetization (and thus also for  $B_0$ ) is

given by a Ginzburg-Landau approach

$$M^2(T) = M_0^2 \left( \frac{T - T_C}{T_C} \right)^{1/\beta} \quad (2.8)$$

with the magnetization at zero temperature  $M_0$  and the exponent  $1/\beta$  which can assume different values depending on the particular theory describing the type of FM.

As  $M(T > T_C) = 0$ , the polarization  $P(T > T_C) = P_0$  is constant in the PM phase. When decreasing the temperature below  $T_C$ ,  $B_0(T) = \mu_0 M(T)$  assumes a finite value larger than zero and the exponential function of Eq. 2.7 decreases. Therefore, the polarization decreases when the sample becomes FM which agrees with the considerations above.

In the case of  $\varphi_L > 2\pi$ , which is associated with a strong FM, Eq. 2.4 is approximated by

$$P = P_0 \left( \frac{1}{3} \right)^N. \quad (2.9)$$

This expression is constant and depends only on the number of passed domains  $N$  or the average domain size  $\delta = d/N$ . As the equation is only valid in the FM regime, the temperature dependence is a step function which equals  $P_0$  above  $T_C$  and the right side of Eq. 2.9 below  $T_C$ .

In real samples the observed  $T_C$  can vary spatially within the sample due to internal stresses, temperature gradients, crystal defects, and variations of the sample composition. In order to reflect this in Eqs. 2.7 and 2.9 both functions are convoluted with a normalized gaussian distribution centered at  $T_C$ . The FWHM of the gaussian distribution  $\Delta T_C$  is a measure for the spread of transition temperatures along the flight path of the neutrons. The convolution effectively smears out the sharp features of the Eqs. 2.7 and 2.9 observed at  $T_C$ .

The main results of this section, Eqs. 2.7 and 2.9, provide a basis for the interpretation and evaluation of ND data. However, they are not applicable to every data set due to several constraints. (i) The equations do not cover the intermediate regime  $0 < \varphi_L < 2\pi$ . It is expected that the exponential decay of Eq. 2.7 continuously transforms into the step function of Eq. 2.9. However, a general solution for the average of the cosine function in Eq. 2.4 cannot be calculated. Therefore, a quantitative evaluation of ND data in this regime of the Larmor angle per domain is not possible. (ii) The assumptions on which the calculations above are based describe a very simple form of FM. Effects resulting from magnetic anisotropies, sample shape effects, finite domain walls, domain correlations, and the case of a small number  $N$  of traversed domains are not included. (iii) A requirement for

the quantitative interpretation of ND data is that all detected neutrons must have passed through the sample. The ND setup used for high-pressure studies described below in Sec. 2.1.2.4 does not fulfill this requirement due to the utilized focusing optics and small sample sizes. (iv) 1d ND setups, as used here for all measurements, lack the ability to distinguish between a depolarization of the neutron beam and a rotation of the polarization vector. However, the latter case may be recognized as such by careful setup checks, comparison of different parameter scans, and the experimenter's experience. To sum up, in some cases it is not possible to extract all quantitative parameters from the shape of a depolarization curve such as  $B_0$  and  $\delta$  from Eq. 2.7. Nevertheless, the identification of the FM transition temperature  $T_C$  is usually possible and similar data sets can be compared in order to identify trends.

A mathematical framework for the interpretation of ND measurements was presented. In the introduction it was stated that ND is a highly sensitive technique for the detection of FM order in bulk samples. The following Sec. 2.1.1.2 tries to put the word "highly" into numbers, i.e. deriving estimates on the length and time scales ND is able to detect.

### 2.1.1.2. Detectable Length and Time Scales of Ferromagnetic Order

When suppressing the FM of a sample, as for example by driving it close to a QPT, the strength of the FM decreases and, therefore, also the depolarization signal. At some point the depolarization may fall below the detection threshold of the ND technique and be indistinguishable from noise. In that case, although the sample might still show some traces of FM order, the polarization signal would indicate a non-magnetic sample state. Furthermore, ND is able to sense fluctuating forms of FM order, such as superparamagnetism and the critical fluctuations close to a FM phase transition, as up to a certain time scale these fluctuations look static from the viewpoint of a neutron. In the course of this section, estimates will be derived on the length and time scales that ND is able to detect.

As stated in Sec. 2.1.1.1, the main parameters describing the strength of the FM order are the average domain size  $\delta$  and the magnetic field in a domain  $B_0$ . If one of these parameters or both decrease, the depolarization decreases as well. Depending on the value of  $B_0$ , below a certain length scale  $\delta$  the depolarization cannot be resolved anymore. A lower limit for  $\delta$  can be estimated by considering Eq. 2.7 which describes a weak type of FM. For the estimation it is useful to set  $P_0 = 1$ , which translates to a normalized polarization signal, and to replace the polarization  $P$  with the depolarization  $D = 1 - P$ . Solving Eq. 2.7 for  $\delta$  then yields

$$\delta = -3 \log(1 - D) \frac{v^2}{\gamma^2 B_0^2 d}. \quad (2.10)$$

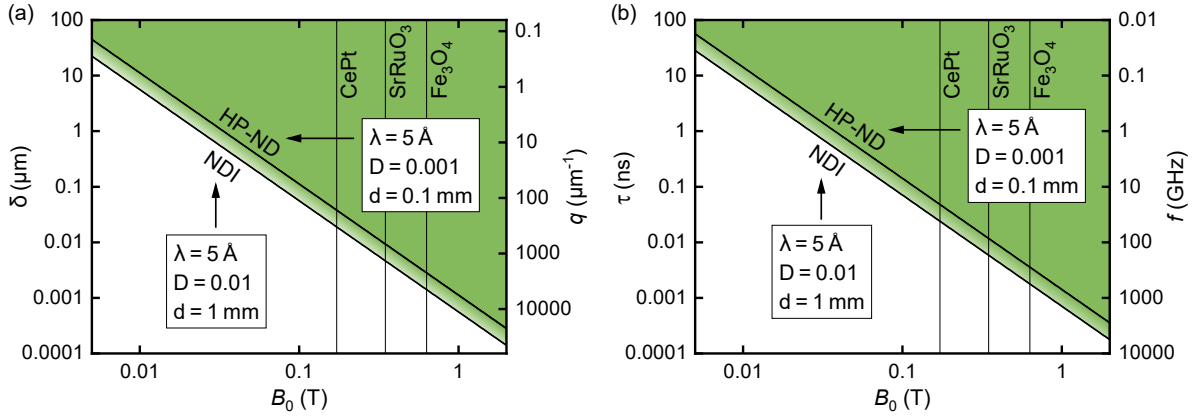


**Figure 2.2.:** Theoretical length and time scale resolutions for the high-pressure ND (HP-ND) setup and the NDI setup. (a) Length scale resolution  $\delta$  as a function of the magnetic flux per domain  $B_0$  calculated using Eq. 2.10 for the two setups. A sample with a  $\delta$ - $B_0$  combination lying in the green area above a threshold line depolarizes the neutron beam to a measurable level depending on the setup. For the two setups different sample thicknesses  $d$  and maximum detectable polarization changes  $D$  were assumed which leads to a lower threshold for the NDI setup. The length scale is converted to a scattering vector on the right y-scale using  $q = 2\pi/\delta$ . The values for  $B_0$  of CePt, SrRuO<sub>3</sub>, and Fe<sub>3</sub>O<sub>4</sub> at low temperatures and ambient pressure were calculated from magnetic moments and crystal structures and are indicated with vertical lines. (b) Time scale resolution of the two setups. The threshold lines show the same data as in (a) converted to a time scale via  $\tau = \delta/v$  where  $v$  is the velocity of a neutron with  $\lambda = 5 \text{ \AA}$ . The time scale is also converted to a frequency on the right y-axis using  $f = \tau^{-1}$ .

If a minimum detection threshold for the depolarization is inserted into Eq. 2.10 as  $D$  and typical values for  $v$  and  $d$  are assumed, the length scale ND is able to resolve can be evaluated as a function of  $B_0$  which is shown in Fig. 2.2(a). The black lines show for which values of  $\delta$  and  $B_0$  Eq. 2.10 holds true and mark therefore the detection threshold of the ND technique. If a pair of  $\delta$ - $B_0$ -values lies above the corresponding line (green colored area), the neutron beam is sufficiently depolarized and the polarization change can be detected by the setup. A point below the line results in depolarization that cannot be resolved by the utilized ND setup. Eq. 2.10 is evaluated in Fig. 2.2 for the high-pressure ND (HP-ND) setup and the NDI setup separately which are both described in Sec. 2.1.2. Both setups use a neutron wavelength of  $\lambda = 5 \text{ \AA}$  but different sample thicknesses  $d$  and depolarization resolutions  $D$ . The NDI setup is designed for large samples and an intermediate depolarization resolution described by  $d = 1 \text{ mm}$  and  $D = 0.01$ , respectively. In contrast, the HP-ND setup is used to investigate thin samples with a high depolarization resolution. Therefore, the values  $d = 0.1 \text{ mm}$  and  $D = 0.001$  were used for the calculation of the HP-ND setup. In comparison, the NDI setup can detect lower values of  $B_0^2\delta$  due to the much larger sample thickness. Additionally, the  $B_0$ -values of CePt, SrRuO<sub>3</sub>, and Fe<sub>3</sub>O<sub>4</sub>

were derived from the crystal structures and the magnetic moments at ambient pressure [66–70]. Vertical lines mark the positions of  $B_0(\text{CePt})= 172 \text{ mT}$ ,  $B_0(\text{SrRuO}_3)= 347 \text{ mT}$ , and  $B_0(\text{Fe}_3\text{O}_4)= 630 \text{ mT}$ . In order to more readily compare ND with scattering techniques,  $\delta$  is converted to a scattering vector via  $q = 2\pi/\delta$  on the right y-axis.

The resulting values for  $\delta$  in the relevant  $B_0$ -region from 0.1 T to 1 T are in the range from 1 nm to 100 nm and are in good agreement with estimates from the literature [50, 61, 71, 72]. This means that FM ordered clusters of a few spins can be detected using the ND technique as for example shown in a ND study of the Kondo cluster glass  $\text{CePd}_{1-x}\text{Rh}_x$  [20, 73] (c. Sec. 5.2).

A neutron beam can also be depolarized by fluctuating forms of FM [40, 43, 45, 46, 52, 58, 60] as already mentioned above. From the viewpoint of a neutron there is no difference if the neutron passes a static constellation of domains on a length scale  $\delta$  with random magnetization directions, or if the magnetization changes the direction randomly on a time scale  $\tau$ . The argument is therefore analogous to the one above, and the length scale in Eq. 2.10 can be replaced by a time scale  $\tau = \delta/v$ . Fig. 2.2(b) shows the time scale  $\tau$  as a function of  $B_0$  evaluated for the same sets of parameters as in Fig. 2.2(a). On the right y-scale  $\tau$  is converted to a frequency  $f = \tau^{-1}$ . In the case of a strong FM the time scale resolution ranges down to pico-seconds. These results predict a better time scale resolution than previous studies which range from 10 to 100 ps [18, 52, 74, 75]. However, the difference can be explained by the better polarization resolutions of the setups used here. It is important to note that the considerations regarding the time scale implicitly assume large FM domains. If  $\delta$  approaches values close to the detection threshold, the resolvable time scale  $\tau$  increases.

### 2.1.2. Neutron Depolarization Setups

All ND measurements were performed at the neutron imaging beam line ANTARES at the research neutron source Heinz Maier-Leibnitz (FRM II) in Garching, Germany. Details on the specifications of the beam line can be found elsewhere [76]. Two different ND setups were used for the measurements presented in this thesis: the NDI setup and the high-pressure ND (HP-ND) setup. In principle, both setups are 1d neutron polarization setups as introduced in Sec. 2.1.2.1 below. In order to clarify several technical aspects of neutron imaging, a corresponding introduction describing neutron imaging and the relevant detector technique is given in Sec. 2.1.2.2. Sec. 2.1.2.3 then describes NDI, essentially a combination of neutron polarization analysis and neutron imaging. Finally, the dedicated HP-ND setup is described in Sec. 2.1.2.4.

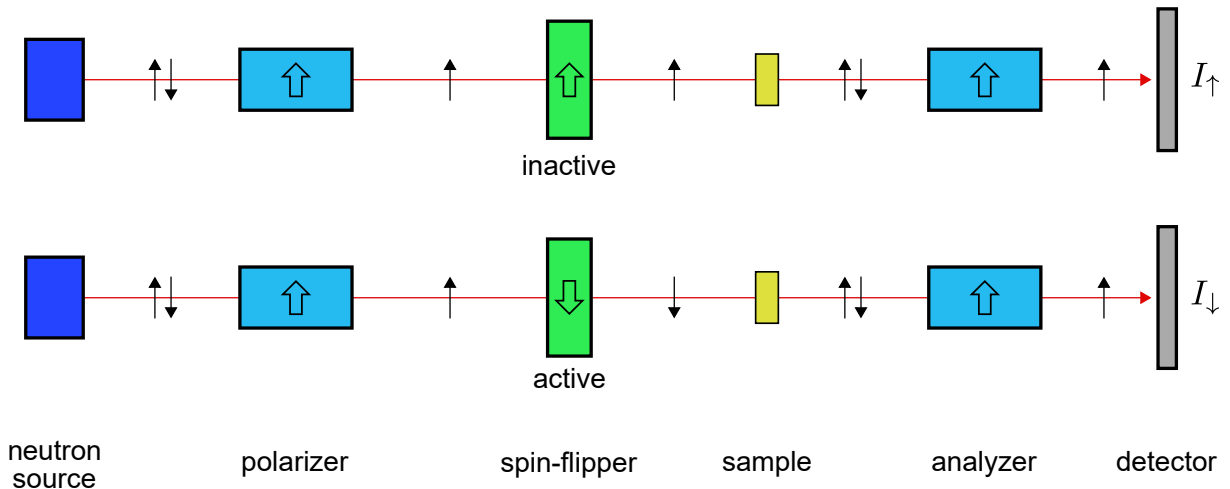
If not stated otherwise, the right-handed ANTARES coordinate system is used in the following explanations.  $z$  points along the horizontal neutron flight path from neutron source to the detector and  $y$  points upwards (against the direction of gravity).  $x$  points perpendicular to the neutron beam in the horizontal direction.

### 2.1.2.1. 1d Polarization Analysis Setup

The polarization of a 1d polarization analysis setup is usually determined by measuring the neutron intensities  $I_{\uparrow}$  and  $I_{\downarrow}$  with the initial polarization pointing in the positive and the negative direction, respectively. The beam polarization  $P$  is then given by

$$P = P_0 \frac{I_{\uparrow} - I_{\downarrow}}{I_{\uparrow} + I_{\downarrow}} \quad (2.11)$$

where  $P_0$  is a normalization factor which includes finite efficiencies of polarizer, analyzer, and spin-flipper – devices which are explained further below. Due to the denominator in Eq. 2.11 acting as a normalization to the beam intensity the polarization is independent of absorption effects caused by the sample or other components in the beam.



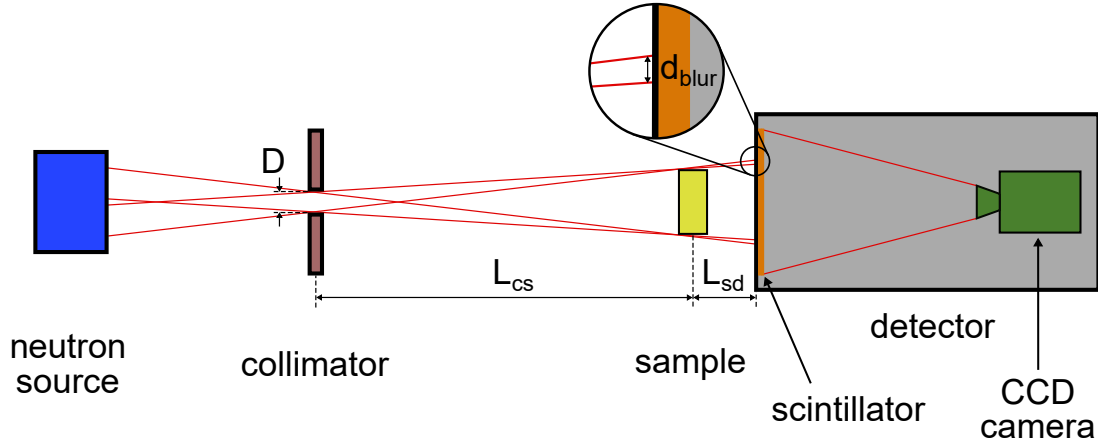
**Figure 2.3.:** Sketch of a 1d neutron polarization analysis setup. The neutron source emits neutrons with random spin states up ( $\uparrow$ ) and down ( $\downarrow$ ), which are indicated by black arrows. A subsequent polarizer absorbs neutrons with spin state down while neutrons with spin state up can pass the polarizer. The spin-flipper can change the spin direction depending on the state of the spin-flipper: "inactive" leaves the neutron spin unaffected while "active" flips the spin from up to down. The sample can change the neutron spin depending on the sample's magnetic properties. An analyzer selects the neutrons with spin state up (like the polarizer) which then are counted in a neutron detector.

Fig. 2.3 shows the principle of a 1d neutron polarization setup. The horizontal red arrows indicate the flight path of a neutron and the vertical black arrows indicate the possible spin directions of a neutron at the respective position in the setup. A neutron source generally emits a completely unpolarized beam, i.e. 50 % of the neutrons are in the spin-up state ( $\uparrow$ ) and 50 % are in the spin-down state ( $\downarrow$ ). In order to achieve a beam polarization  $P \neq 0$  a polarizer is installed at the beginning of the polarization setup. A polarizer generally uses the spin-dependence of a neutron absorption or scattering process in order to remove one spin direction – in this example the down-neutrons – from the neutron beam. Due to the quantum-mechanical nature of these processes the beam polarization after the polarizer can only reach a value closely below 1 but never equal 1. However, for the understanding of a 1d polarization analysis setup it is sufficient to assume  $P = 1$  as effects resulting from a polarization lower than 1 can be corrected by a simple normalization.

In order to change the polarization direction for the determination of  $I_{\uparrow}$  and  $I_{\downarrow}$ , a spin-flipper is installed after the polarizer. A spin-flipper is a device that can change the polarization direction from up to down ( $\pi$ -flip). One method to flip the polarization by  $\pi$  is the installation of a solenoid in the beam which creates a magnetic field perpendicular to the beam polarization. The resulting Larmor precession of the polarization is then set to  $\pi$  by adjusting the amplitude of the magnetic field using a regulated power supply. If the spin-flipper is inactive, i.e. the perpendicular field is zero, the polarization remains unaffected while in the active state the polarization is flipped from up to down. This allows to select a neutron beam with one or the other polarization direction to be imparted on the sample.

The sample can depolarize the neutron beam depending on its microscopic magnetic properties as described in Sec. 2.1.1.1. Therefore, all spin directions are possible after the sample. An analyzer is placed downstream of the sample which blocks the down-neutrons from passing, exactly as the polarizer does. The neutron intensities measured with the detector are then labeled  $I_{\uparrow}$  and  $I_{\downarrow}$  for the spin-flipper states "inactive" and "active", respectively.

As the neutron spin is very susceptible to small magnetic fields, Earth's magnetic field or stray fields from electrical components can depolarize the neutron beam. In order to remedy these effects, guide fields with a strength of 0.5 to 5 mT are installed between the components of the polarization setup (not shown in the figure).



**Figure 2.4.:** Basic neutron imaging setup based on the principle of a pinhole camera. The highly-divergent neutron beam emerging from the neutron source is collimated by a pinhole with diameter  $D$  (collimator). The sample is placed in the collimated beam in front of a 2d neutron detector where the collimator-sample distance  $L_{cs}$  is chosen much smaller than the sample-detector distance  $L_{sd}$  in order to decrease blurring of the sample on the detector. The red lines show the construction of the geometrical blur  $d_{\text{blur}}$  which is determined by the parameters  $D$ ,  $L_{cs}$ , and  $L_{sd}$ . Inside the detector a scintillator screen converts the neutrons to visible light which is then detected by a CCD camera.

### 2.1.2.2. Neutron Imaging and Imaging Detectors

Fig. 2.4 shows the basic principle of a neutron imaging setup. Neutrons are emitted isotropically by the finite-sized neutron source which leads to a highly-divergent neutron beam. As a divergent neutron beam blurs the absorption image of the sample on the detector, a neutron-absorbing aperture (collimator) with diameter  $D$  is placed in the beam. The resulting collimation at a distance  $L$  downstream from the collimator is then given by the ration  $L/D$ , where on the one hand larger  $L$  and smaller  $D$  lead to a better collimation, but on the other hand to a reduced neutron flux. Typical values of  $L/D$  for neutron imaging are in the range from 400 to 1600 and can be achieved in the case of ANTARES by placing differently sized collimators in the neutron beam.

The geometrical blur of a sharp feature of the sample (e.g. an edge) on the detector is indicated in Fig. 2.4 by red lines and can be calculated with

$$d_{\text{blur}} = \frac{L_{sd}}{L_{cs}} D \quad (2.12)$$

where  $L_{sd}$  is the distance sample-detector and  $L_{cs}$  is the distance collimator-sample. For a sharp image at a given collimation  $L/D$ ,  $L_{sd}$  should be minimized, i.e. the sample should be placed as close to the detector as possible. In the case of a ND setup  $L_{sd}$  is usually limited by the length of the analyzer which has to be placed between sample and detector.

In order to detect the neutron intensity with a good spatial resolution, a scintillator screen is used to convert the neutrons to visible light. A low-noise CCD camera is focused with an objective on the backside of the scintillator and detects the light. As the light output of the scintillator is directly proportional to the absorbed neutron flux, the resulting image captured by the camera represents the incoming neutron flux accurately. Both components, scintillator and camera, are enclosed in a light-tight box in order to minimize stray light from reaching the camera.

The camera used for all measurements shown in this work is an Andor iKon-L 936 CCD [77] with  $2048 \times 2048$  pixels. The objective is set to a magnification of 1:3.7 which results in a pixel size of  $75 \mu\text{m}$ .

In order to take one image, the neutron beam and the internal camera shutter are opened for a defined exposure time  $t_{\text{exp}}$ . The CCD integrates the light flux over  $t_{\text{exp}}$  in every pixel and returns a 16-bit gray level image. The gray level of each pixel is proportional to the neutron flux at the respective pixel position. Furthermore, the instrument control software saves all instrument parameters and settings, such as sample temperature and magnetic field, in the header of the image file.

The CCD pixel readout values feature a constant positive offset even if no light reaches the CCD chip. This so called dark current has to be determined and subtracted from the data images for each pixel. Therefore, a series of images is taken before measurements are performed with the same exposure time as the data images and a closed neutron beam. In order to increase statistics and suppress artifacts, a median filter is applied to the image stack returning the median of the gray values for each pixel coordinate. The result is called dark image (DI).

Furthermore, in neutron imaging the data images have to be normalized to an image without a sample to cancel effects from scintillator inhomogeneities and from neutron flux variations across the neutron beam. Therefore, an open beam image (OB) is taken without a sample in the beam and with the same exposure time as the data images. The normalized intensity image  $I(x,y)$  is calculated by

$$I(x,y) = \frac{\text{DATA}(x,y) - \text{DI}(x,y)}{\text{OB}(x,y) - \text{DI}(x,y)} \quad (2.13)$$

where  $x$  and  $y$  are the pixel coordinates and DATA is the untreated image from the corresponding measurement.

A common artifact in images from neutron detectors using a CCD camera are gamma spots. They appear when gamma radiation hits the CCD chip and causes a massive charge increase in one or more surrounding pixels. In the images the gamma spots are seen as

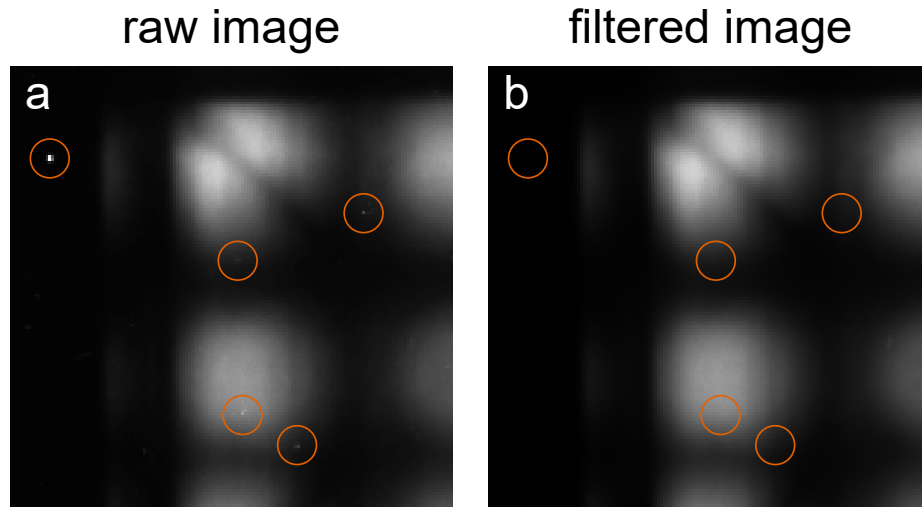


**Figure 2.5.:** Comparison of a raw data image versus a filtered image. (a) Untreated neutron imaging data from a neutron depolarization measurement. The orange circles mark artifacts (gamma spots) caused by gamma radiation hitting the CCD chip of the detector. (b) Processed data from (a) after applying an image filter as described in Sec. 2.1.3. The orange circles are in the same positions as in (a) and reveal the effective elimination of the gamma spots.

small bright spots with an intensity which is often about one order of magnitude larger than the actual signal from the scintillator. In Fig. 2.5(a) a  $150 \times 150$  pixels region of an unprocessed neutron image from a ND measurement is shown. The orange circles mark gamma spots with the gamma spot in the top left corner being the most distinct spot. A typical image using the ND setups as described below features up to several hundred gamma spots with varying intensities.

In order to remedy this effect and correct the data, several images per measurement point are taken. As the appearance of the gamma spots is randomly distributed, it is unlikely that a gamma spot will appear at the same pixel position several times in a row. The application of a pixelwise median filter to a stack of images at the same measurement point is therefore a robust way to remove gamma spots from the data. Fig. 2.5(b) shows the filtered output of a stack of five images including the data from panel (a). The orange circles are at the same positions as in panel (a). The gamma spots were all detected by the filtering algorithm and were removed from the image. Furthermore, the processed image shows a smoother intensity distribution due to the increased statistics. The filtered image is then used in Eq. 2.13 as  $\text{DATA}(x,y)$  for the calculation of the normalized image  $I(x,y)$ .

A detailed description of the data processing and an advanced filtering algorithm is given in more detail in Sec. 2.1.3.

Another artifact in neutron imaging is the slowly decaying light yield of the scintillator, also referred to as afterglow. This effect was recently investigated in more detail [78] and can cause an imprint of an image on the subsequently taken images, alter the measured neutron intensities and, thus, change the measured polarization significantly. Therefore, in the following a brief introduction on neutron scintillators and the current state of research of the afterglow effect are given. The measurements by Neuwirth *et al.* presented below are published in Ref. [78]. The impact of the afterglow effect on the measured polarization is discussed in Sec. 2.1.3.2.

Neutron scintillator screens are usually a composite material of a neutron absorber, a light emitter, and a binding agent. When a neutron is captured by the absorber, secondary radiation from the absorber can activate the light emitter into an excited state. The light emitter is chosen to feature a short-lived state which emits a photon in the visible range almost instantly. In our ND measurements a scintillator manufactured by RC Tritec [79] with a thickness<sup>1</sup> of 200  $\mu\text{m}$  and a composition of  $^6\text{LiF}$  (absorber) and  $\text{ZnS:Cu}$  (light emitter) was used.

Although the life-time of the excited state of the light emitter is in the order of milliseconds and therefore much smaller than the typical time scale on which neutron data is acquired, recent measurements revealed an afterglow of the scintillator in the order of seconds to minutes [78]. This can be observed when the scintillator is first illuminated by a neutron beam and then the beam is shut off. When taking images after closing the beam, still a slowly decaying light output from the scintillator is measured. Vice versa, the effect is also seen when opening the neutron beam. Due to the delayed emission of photons, the detected intensity takes several minutes until it reaches saturation. When taking a series of images, the afterglow can hence lead to an imprint of an image on the subsequent images.

Fig. 2.6 shows the afterglow of a  $\text{LiF/ZnS:Cu}$  scintillator, similar to the screen used in the ND measurements, but with a thickness of 100  $\mu\text{m}$  instead of 200  $\mu\text{m}$ . The scintillator was illuminated with a white neutron beam for several minutes until the intensity was no longer increasing. Then, at  $t = 0$ , the instrument shutter was closed and a continuous series of images was taken with an exposure time of  $t_{\text{exp}} = 10\text{ s}$  each. The intensity of each image is integrated over the whole scintillator and normalized to the last image taken before closing the shutter. No data was acquired in the first 20 s after closing the shutter due to limitations by the instrument control software. The intensity shows a quick drop to

---

<sup>1</sup> The thickness of a scintillator is a good estimate for the intrinsic spatial resolution of the scintillator.

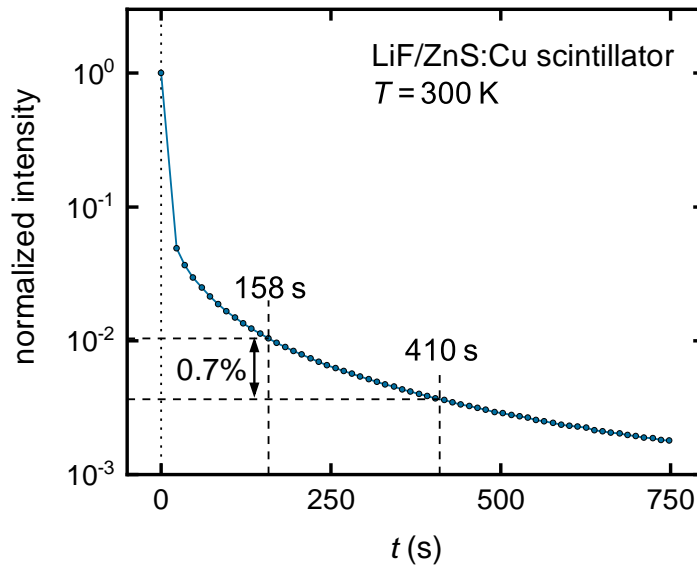


**Figure 2.6.:** Afterglow of a LiF/ZnS:Cu neutron scintillator. After illuminating the scintillator for several minutes the neutron beam was closed at  $t = 0$ . The figure shows the integrated intensity of the whole scintillator screen normalized to the full beam intensity as a function of time  $t$ . The marked times and intensities at 158 s and 410 s are typical values for the ND setup as described in Sec. 2.1.2.4. Data from Ref. [78].

5% within 20 s and then a slower decay down to 0.2% at  $t = 750$  s. The data cannot be described by an exponential decay law (note the logarithmic intensity scale). Typical time scales observed in ND measurements are marked at 158 s and 410 s which are later used in Sec. 2.1.3.1.

If the beam is opened and closed repeatedly in constant time intervals, e.g. opening the beam for 1 min, then keeping it closed for 2 min, the afterglow can be driven into a steady state. During the 1 min open-state the increase over time is still visible, however the mean value of the intensity of the 1 min intervals reaches a constant value. This makes the intensity mean values comparable, as only a constant background has to be subtracted. ND measurements often feature a similar time structure during a temperature or magnetic field scan. The data acquisition for one data point takes about 10 min. After that the neutron beam is closed and the scan parameter (such as  $B$  or  $T$ ) is changed. If this change of the scan parameter always takes the same time and the average intensity variation between the data points is small, the afterglow affects all data points equally.

Further investigations have shown that the afterglow is not quantitatively reproducible when the scintillator was used for other experiments in between the afterglow measurements. Scintillators that were older and exposed to more neutrons typically featured a more

pronounced afterglow than newer scintillators. In another test the temperature dependence of the afterglow effect was studied. Heating the scintillator to 80 °C drastically reduces the afterglow intensity by one order of magnitude and shifts it to smaller decay times compared to room temperature measurements.

The effects of aging and temperature on the afterglow suggest crystal defects in the scintillator material induced by neutron radiation as a possible source for the afterglow. The crystal defects could change the local band structure at the luminescence sites of ZnS:Cu and modify the lifetime of the photo-emission. In combination with a multi-level decay this could also explain the shape of the afterglow curve shown in Fig. 2.6. However, the exact processes that are involved are still subject to current investigations. A description of how the afterglow effect was taken into account in the data evaluation is given in Sec. 2.1.3.

### 2.1.2.3. Neutron Depolarization Imaging

The installation of a polarization setup at a neutron imaging beam line allows for the spatial resolution of magnetic sample properties when using, for example, the ND technique as described in Sec. 2.1.1. A sketch of the NDI setup used at ANTARES is given in Fig. 2.7.

The beam port of ANTARES points at the cold source of the FRM II and features a wide spectrum ranging from thermal to cold wavelengths. However, the components of the polarization setup require a narrow wavelength band in the cold wavelength regime for an

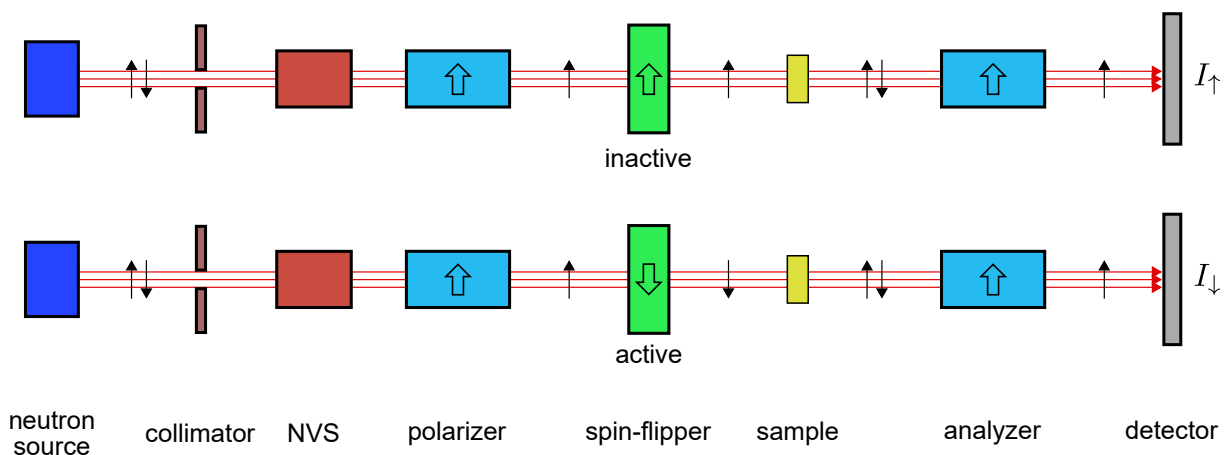


**Figure 2.7.:** Sketch of the neutron depolarization imaging (NDI) setup at the beam line ANTARES. A polarization setup (c. Fig. 2.3) consisting of polarizer, spin-flipper, and analyzer is installed at a neutron imaging beam line. A collimator provides a collimated neutron beam (indicated by three parallel red arrows) which can be used for imaging. A neutron velocity selector (NVS) is placed before the polarization setup in order to produce a monochromatic neutron beam.

efficient operation. Therefore, a neutron velocity selector (NVS) is placed right after the collimator. The NVS is designed to select a given wavelength with a wavelength spread of  $\Delta\lambda/\lambda = 10\%$ . Additionally, reducing the spectrum to a single wavelength simplifies the quantitative data evaluation as the depolarization directly depends on the neutron wavelength (c. Eq. 2.7).

The polarizer used at ANTARES is a five-mirror V-cavity made by SwissNeutronics [80, 81], mounted on rotational and translational motor stages for a precise adjustment. The magnetic supermirrors of the V-cavity reflect the neutrons with spin down into an absorbing layer while spin up neutrons can pass through the device. As the supermirrors have to be aligned at a shallow angle with respect to the neutron beam, a single supermirror only covers a small cross-section of the beam. In order to increase the cross-section coverage, five supermirrors in a V-configuration are placed next to each other. However, the small parts of the cross-section where the supermirrors touch are not polarized. This has to be taken into account when imaging samples that are larger than the width of one supermirror-V.

A Mezei-type spin-flipper [82] was used to flip the polarization from up to down. This device consists of two flat coils wound on top of each other but with a perpendicular orientation of the windings. The outer coil produces a vertical field that is adjusted to cancel the guide fields within the coil. The inner coil produces a horizontal field perpendicular to the neutron polarization and is adjusted to flip the polarization by  $\pi$ .

A conventional electro-magnet is placed at the sample stage which can apply fields up to 300 mT in both the positive and negative vertical direction [83]. A field in the magnet in the opposite direction of the guide fields would, without further measures, cause a zero-field crossing and therefore a depolarization of the beam. This can be prevented by installing horizontal guide fields, which ensure an adiabatic field transition between the components before and after the magnet. Thus, complete field loops in positive and negative directions can be measured. A detailed description of the guide field arrangement is given in Ref. [84].

The analyzer is a three-mirror V-cavity by SwissNeutronics which is mounted on a five-axis motor stage for precise alignment.

Fig. 2.8 shows photographs of the NDI setup in the first measurement chamber of ANTARES. The setup is shown in two separate images as the narrow bunker of the beam line prevents a total view of the whole setup. The first part of the setup is shown in Fig. 2.8(a) where the neutrons enter the chamber on the left side of the image. An aperture (which should not be confused with the collimator) consisting of adjustable white  $B_4C$ -plates confines the beam cross-section to the entrance window of the polarizer in order to prevent unnecessary neutron exposure. Behind the aperture the polarizer and

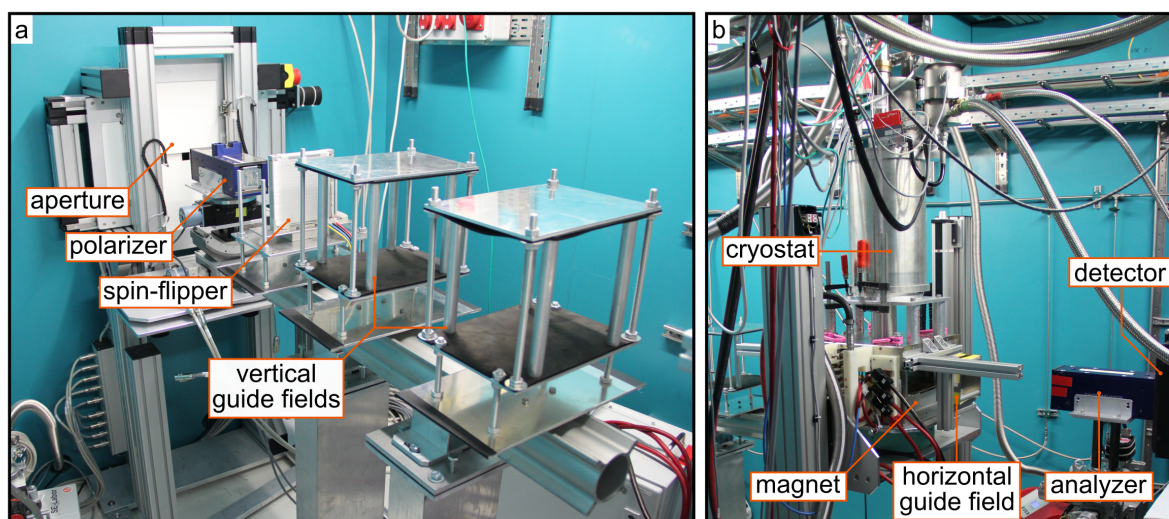


**Figure 2.8.:** Photographies of the NDI setup at the imaging beam line ANTARES. (a) First part of the setup showing the polarizer, the spin-flipper, and vertical guide fields. An aperture is used to reduce the beam cross-section to the window size of the polarizer. (b) Second part of the setup showing the sample stage, the analyzer, and a part of the detector box. The image is mirrored horizontally in order to be consistent with the neutron flight direction of (a).

subsequently the spin-flipper are placed. Two vertical guide fields are installed between spin-flipper and sample stage in order to prevent a depolarization of the neutron beam. Fig. 2.8(b) shows the second part of the setup with the neutron beam coming from the left side. This image was mirrored horizontally to be consistent with Fig. 2.8(a). The sample stage consists of the magnet and the cryostat. Horizontal guide fields are installed before (hidden by the magnet) and after the sample stage for an adiabatic coupling of the guide fields to the field of the magnet. A V-cavity analyzer is placed right in front of the detector box which is only partly visible on the right side of the image.

The best spatial resolution for this NDI setup is constrained by the requirement to place an analyzer between sample and detector. This increases the sample-detector distance to  $L_{sd} \approx 50$  cm. With a standard collimation of  $L/D = 500$  for this setup the spatial resolution is 1 mm. It is possible to increase the collimation to higher values resulting in a finer resolution. However, doubling the collimation to  $L/D = 1000$  reduces the neutron flux by a factor of 4<sup>1</sup> and results in longer exposure times. Therefore, usually a collimation of  $L/D = 500$  is used. Nevertheless, a more sophisticated NDI setup featuring a Wolter optic was recently able to improve the spatial resolution to 0.1 mm with similar neutron statistics as the conventional NDI setup [85].

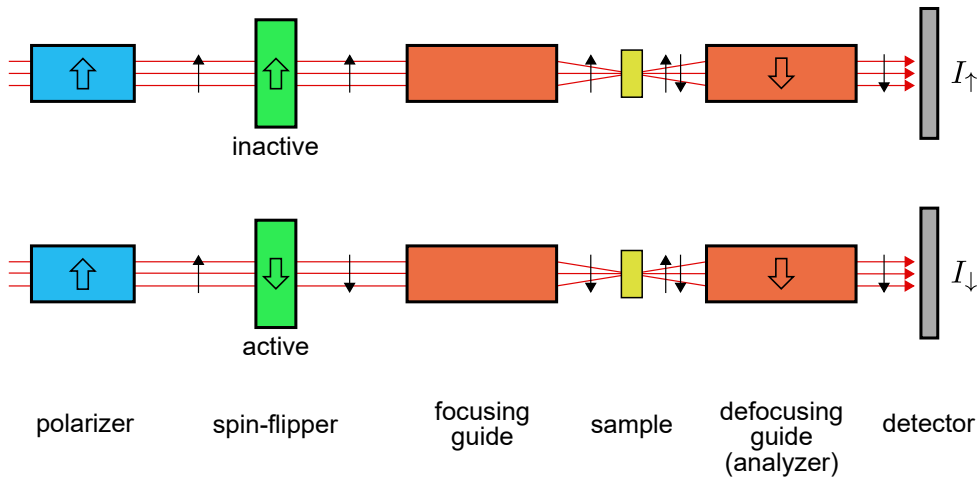
<sup>1</sup> The collimation is proportional to  $1/D$  while the neutron flux is proportional to  $D^2$ .

As most of the magnetic transitions are observed at low temperatures, the sample is mounted in a cryostat. The magnet was designed to be compatible with the standard cryostats at the MLZ. For the measurements either a closed-cycle (CC) cryostat or a  $^3\text{He}$ -cryostat were utilized, which can reach base temperatures of 2.8 K and 500 mK, respectively.

The advantage of the NDI setup compared to a conventional polarization setup is the possibility to investigate the magnetic properties of a sample with spatial resolution. As the magnetic properties are often dependent on the chemical composition or residual stresses within a sample, the NDI technique can give information on the sample homogeneity. Such a sample characterization was performed for a  $\text{UGe}_2$  single crystal and is given in appendix A.1 as an example for a typical NDI measurement.

#### 2.1.2.4. Neutron Depolarization Measurements at High Pressures

One of the main aspects of the present work is the investigation of FM at high pressures using the ND technique. Due to the general decrease of sample size with increasing pressure, the NDI setup had to be adapted as the polarization accuracy scales with the sample area. For this reason a ND setup with focusing neutron guides that is optimized for high-pressure studies was designed by Jorba in the framework of his PhD thesis [86]. A summary of the setup is given below, whereas a detailed description of the design and optimization is given elsewhere [64, 86].



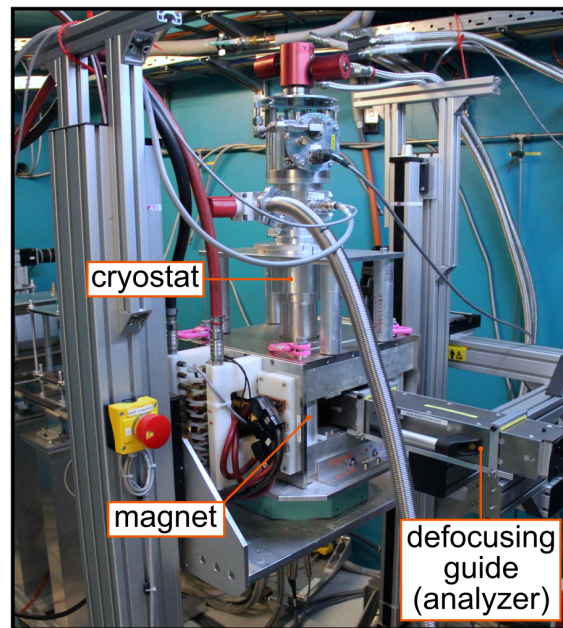
**Figure 2.9.:** Schematic drawing of the high-pressure ND setup using focusing neutron guides. In order to increase the neutron statistics when measuring small samples, a focusing neutron guide was added before the sample to the polarization setup described in Fig. 2.3. A defocusing guide with polarized supermirror surfaces is placed after the sample and replaces the V-cavity analyzer.

Fig. 2.9 shows a schematic drawing of the modified polarization setup using a pair of focusing neutron guides. The first guide focuses the beam to a spot with a diameter (FWHM) of 0.5 mm at the sample position. The second guide between sample and detector defocuses the beam and also works as the analyzer, as it is coated with a magnetic neutron supermirror. As the defocusing guide is a reflection polarizer, in contrast to the V-cavity polarizer, but the guide fields of both devices point in the same direction, the defocusing guide analyzes the polarization in the opposite direction. This leads to a negative polarization when calculating the polarization with Eq. 2.11. Therefore, ND measurements using the high-pressure setup have to be multiplied with a factor of  $-1$ .

The focusing guide has a rectangular cross-section with a  $20\text{ mm} \times 20\text{ mm}$  entrance window. The parabolically shaped mirrors are 500 mm long and are covered with an  $m = 6$  Ni/Ti coating. The length between the exit window of the guide and the focal spot of the parabola is 80 mm. The defocusing guide features the same parabolic curvature as the focusing guide; however, the mirrors are shorter by 40 mm which is compensated by a 40 mm longer distance between focal spot and guide entrance. The top and bottom mirrors are also covered with an  $m = 6$  Ni/Ti coating, while the left and right mirrors are covered with an  $m = 5$  Fe/Si coating. If the latter coating is polarized by a magnetic field larger than 30 mT, the supermirror reflects only one neutron spin direction and functions therefore as an analyzer. As only the left and right supermirrors are polarizing, only the three spots on the left and the three spots on the right of the  $3 \times 3$  intensity pattern are polarized and can be used for polarization analysis. In order to ensure a constant polarization, the guide is placed in a magnetic casing which produces a constant, homogeneous field in the vertical direction with a value of 42 mT.

Fig. 2.10 shows the assembled high-pressure ND setup at ANTARES. The image is taken from a similar perspective as Fig. 2.8(b) and is also mirrored horizontally for consistency. The focusing guides are mounted on a kinematic holder with a horizontal rail system which enables the simultaneous movement of both guides in x-direction relative to the sample. As the vertical motor stage (y-direction) of the sample table is decoupled from the mounting of the guides, this stage ensures the vertical movement of the guides relative to the sample. The guides have to be aligned relative to each other every time the setup is assembled. For the alignment the guides are held in the magnetic cages by adjusting screws close to the guide entrance and exit in both vertical and horizontal directions.

The alignment process is realized in several steps which are depicted in Fig. 2.11. First, setup 1 is realized by only installing the focusing guide (FG) and a neutron image is taken. The reflections of the neutrons from the supermirror surfaces in the guide form a pattern with nine intensity spots arranged in a  $3 \times 3$  pattern (panel 1). The orientation of the



**Figure 2.10.:** Photography of the HP-ND setup at the imaging beam line ANTARES. The image is mirrored horizontally in order to be consistent with Fig. 2.8. While the focusing guide is hidden behind the sample stage consisting of magnet and cryostat, the defocusing guide is visible on the right side of the image.

focusing guide is tuned using the adjusting screws until the pattern is symmetric. Then an optical lamp with a highly collimated beam is mounted in front of the focusing guide. As the supermirror surfaces of the guide also reflect light, the  $3 \times 3$  pattern can be reproduced with the lamp at the detector position if the lamp is mounted in the right orientation (panel 2). Thus, the neutron beam is effectively replaced by the lamp. After that setup 2 is realized by mounting the defocusing guide (DFG) on its holder and the entrance window of the DFG is aligned with the light beam (panel 3). The holders are designed such that the focal spots of both guides coincide at the sample position. Therefore, the focused light from the first guide can be defocused by the second guide. The  $3 \times 3$  pattern is reflected in the defocusing guide which results in a smaller  $3 \times 3$  pattern at the detector position. The adjusting screws of the defocusing guide are then tuned until the pattern is symmetric again (panel 4). After removing the lamp the alignment is verified by taking a neutron image (panel 5). At that point, the guides are adjusted relative to each other and can be used for ND measurements. Since the mounting plates for the guides feature precise milled slots which fit to spikes on the bottom of guides, the orientation and position of the guides is reproducible after removing the guides without further adjustment. After mounting the pressure cell at the sample position the x- and y-positions of the guides

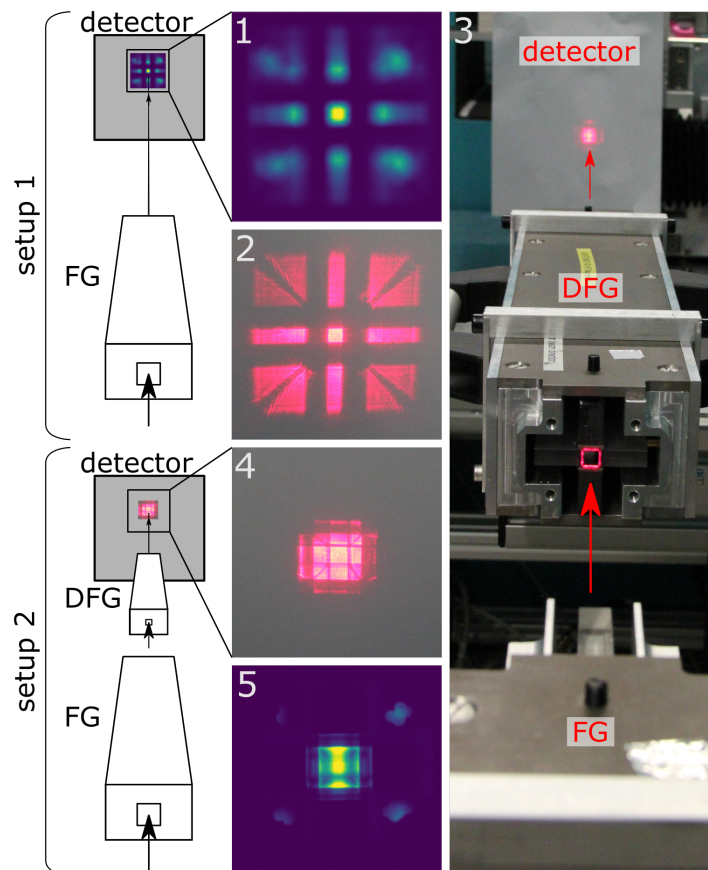


**Figure 2.11.:** Alignment procedure of the focusing guides. Setup 1 uses only the focusing guide (FG) which is first aligned with neutrons until the reflection pattern on the detector is symmetric (panel 1). (2) An optical lamp is installed before the FG and adjusted to reproduce the reflection pattern on the detector. (3) The defocusing guide (DFG) is mounted and the entrance window of the DFG is aligned with respect to the light from the lamp. (4) The alignment of the DFG is adjusted until the reflection pattern of the light on the detector is symmetric. (5) The lamp is removed from the setup and the alignment is checked with the neutron beam. Figure adapted from Ref. [64].

are moved relative to the sample in order to focus the neutron beam on the sample. This alignment is performed to an accuracy of  $50\ \mu\text{m}$ .

A problem that can appear with this setup when scanning large temperature ranges is an unwanted vertical movement of the sample due to thermal expansion of the cold head in the cryostat. Experience shows that a temperature change from 5 to 200 K can move the sample vertically by up to  $200\ \mu\text{m}$ . This offset is sufficient to produce vertical asymmetries in the  $3 \times 3$  pattern which result in polarization changes. A detailed discussion of this effect is given further below in Sec. 2.1.3.3.

### 2.1.3. Neutron Depolarization Data Acquisition and Evaluation Procedure

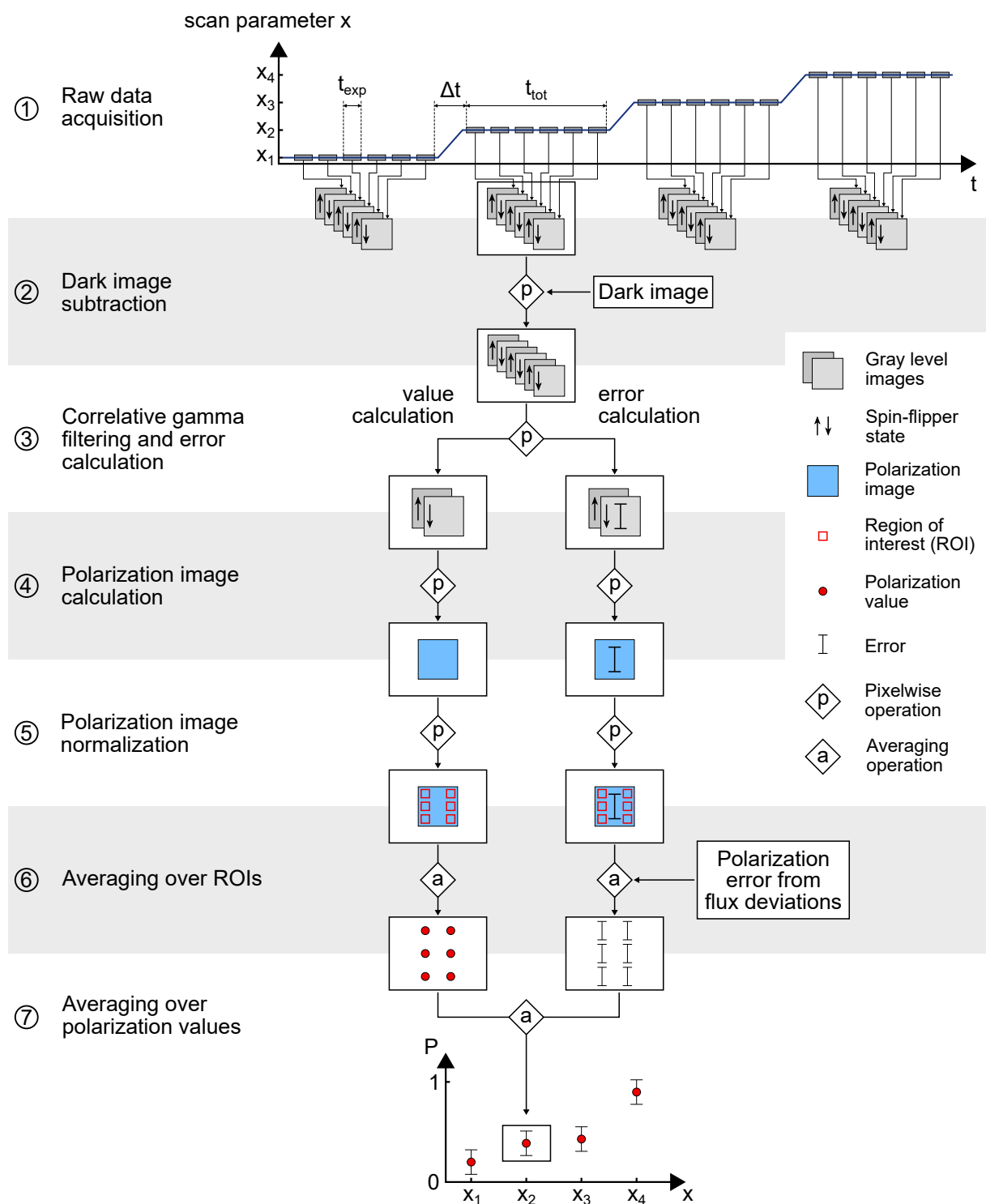
This section explains in detail how the ND raw data is acquired and how the polarization is calculated from the raw data. In general, the data acquisition for a system under investigation using the ND technique takes several days to weeks. As the access to neutrons at the FRM II is regulated by a proposal system and the instruments are usually overbooked, the data acquisition is split into several measurement campaigns consisting of 5 to 12 days, commonly referred to as beam times. The beam times are often separated by several weeks due to the cyclic operation of the reactor and therefore require a new installation and adjustment of the utilized setup. Hence, the data sets acquired at different beam times may differ, for example, in resolution due to a slightly different alignment of the polarization devices.

Fig. 2.12 shows the basic evaluation process as a flow chart with a symbol legend on the right hand side. The evaluation process consists of seven steps which are marked in the chart by circled numbers.

In a ND scan, the polarization  $P$  is measured as a function of a scan parameter  $x$ , most often the temperature  $T$  or the applied magnetic field  $B$ . The graph at the top of Fig. 2.12 shows the scan parameter  $x$  as a function of time  $t$  depicted by a blue line.  $x$  is held constant during the data acquisition for a discrete scan parameter value ( $x_1, x_2, \dots$ ). The required time  $\Delta t$  to change the value of  $x$  from one value to the next is not instantaneous and may take from several seconds up to 10 min depending on the parameter that is scanned.

**(1) Raw data acquisition:** The data acquisition (1) is depicted by gray rectangles on the blue line where the width of the rectangles indicates the exposure time  $t_{\text{exp}}$  of a single image, which was set to 30 s for most scans. At least one image pair with spin-flipper states "inactive" ( $\uparrow$ ) and "active" ( $\downarrow$ ), respectively, has to be taken to calculate the polarization. For each scan parameter value usually several image pairs are taken in order to increase the neutron statistics. The number of images per scan parameter value and  $t_{\text{exp}}$  are constant throughout a scan and add up to the total acquisition time for one data point  $t_{\text{tot}}$ . For each scan parameter value a stack of images with alternating  $\uparrow$  and  $\downarrow$  images is acquired which is indicated in Fig. 2.12 below the graph by a series of gray squares with the respective arrows. In this example three  $\uparrow$  and three  $\downarrow$  images are considered and the further process of the polarization calculation is shown for one (arbitrary) scan parameter value  $x_2$ .

**(2) Dark image subtraction:** Every raw image from the detector features an offset, that may differ for every pixel, as explained above in Sec. 2.1.2.2. Therefore, a dark image has to be subtracted from every data image which is done in step (2). The rhombus symbol



**Figure 2.12.:** Flow chart of the ND data evaluation process. The top graph shows a scan parameter  $x$ , such as the temperature or the magnetic field, as a function of time  $t$ . (1) For a constant value of  $x = x_2$  several neutron images with an exposure time of  $t_{exp}$  are acquired. (2) The dark image is subtracted from the raw data. (3) The average for a stack of images with a constant  $x$  is calculated separately for the up and down images. An error is calculated using the standard deviation of the gray values. (4) The polarization image is calculated from the up and down images. (5) The polarization image is normalized to 1. (6) The polarization image is averaged over given ROIs. (7) The values resulting from the previous step are again averaged. This yields the final polarization value and error for the evaluated scan parameter value  $x_2$ .

indicates that the data is processed and the label "p" refers to a pixelwise operation. This means that the calculation is performed for each pixel independently and the result is again an image. In this case the value of the dark image  $DI(x,y)$  at the pixel coordinates  $(x,y)$  is subtracted from the value of the data image  $DATA(x,y)$  at the same pixel coordinates.

**(3) Correlative gamma filtering and error calculation:** In step (3) the stacks of  $\uparrow$  and  $\downarrow$  images are reduced to one  $\uparrow$  and one  $\downarrow$  image in order to increase neutron statistics. As the raw images feature gamma spots, a simple pixelwise average filter is not an appropriate option. Therefore, an implementation of the correlative gamma filter developed by Gustschin [87] is used here. The filter first calculates a pixelwise median image of the image stack. The median image usually features no gamma spots since they are randomly distributed over the image and rarely appear more than once on the same pixel. The median image is then subtracted from every image in the stack. As the gray level values of the gamma spots deviate strongly from the median, the gamma spots appear as strong deviations from 0 in the generated difference images. The difference images are then compared against an empirical threshold value of 20 gray levels. If the absolute of a pixel gray level in the difference image is larger than the threshold, the pixel is marked as a gamma spot in a binary mask for each image. Finally, the pixelwise average of the image stack is calculated, with the constraint, that only non-masked values are considered. Therefore, the pixels featuring gamma spots are excluded from the averaging process. This results in one  $\uparrow$  and one  $\downarrow$  image without gamma spots and with low gray level noise. Additionally, one  $\uparrow$  and one  $\downarrow$  "error image" is generated by calculating the pixelwise standard deviation of the non-masked pixels. This is indicated in the figure below the label "error calculation" with an error bar in the gray level images. The further processing of the errors is described below in Sec. 2.1.3.1.

**(4) Polarization image calculation and (5) normalization:** In step (4) the polarization image is calculated by applying Eq. 2.11 pixelwise to the resulting  $\uparrow$  and  $\downarrow$  images from the previous step. As the polarization image still contains the instrument polarization  $P_0$ , the polarization image has to be normalized which is done in step (5). In the case of a temperature scan the normalization image  $P_0(x,y)$  is calculated as the pixelwise average of the polarization images above  $T_C$ . In the case of a field scan usually a normalization image from a temperature scan of the same sample is used. For the normalization the polarization image from step (4) is divided by  $P_0(x,y)$ .

**(6) Averaging over ROIs:** The normalized polarization image usually covers a larger beam cross-section than the sample for NDI measurements or more than the  $3 \times 3$  pattern of the focusing guide setup. In order to only evaluate polarization values from the sample, predefined regions of interest (ROI) are used to mask the polarization image. In the case

of NDI measurements a ROI is chosen that only covers the sample and in the case of the focusing guide setup six ROIs are chosen, that cover the six polarized intensity spots of the  $3 \times 3$  pattern. The latter ROIs are indicated in the figure by red rectangles.

In step (6) the polarization of the area masked by a ROI is then averaged. As the operation is not pixelwise, an "a" is used as a label in the rhombus symbol. The averaging operation uses the weighted average for a given ROI

$$\bar{P}_{\text{ROI}} = \frac{\sum_{x,y \in \text{ROI}} w(x,y) \cdot P(x,y)}{\sum_{x,y \in \text{ROI}} w(x,y)} \quad (2.14)$$

where the weights  $w(x,y)$  are defined by the polarization errors  $P_{\text{err}}(x,y)$ :

$$w(x,y) = \frac{1}{P_{\text{err}}(x,y)^2}. \quad (2.15)$$

The resulting average polarization  $\bar{P}_{\text{ROI}}$  of a ROI is therefore a single value which is shown in the figure as a red circle marker. As each ROI yields one polarization value, when more than one ROI is evaluated, it is necessary to average over the polarization values which is done in step (7).

**(7) Averaging over polarization values:** Again the weighted average is used. The final result is a polarization value with an associated error for the scan parameter value  $x = x_2$ . This evaluation is performed for every  $x$  of a scan and yields therefore the polarization  $P$  as a function of  $x$ . In a subsequent step, which is not shown in the figure, the polarization data can be fitted using a model function in order to extract, for example, the FM transition temperature  $T_C$ .

The algorithm described above was implemented in a Python 2.7 [88] script which utilizes parallel processing for independent calculations to speed up the evaluation. Depending on the amount of raw data the evaluation of a typical ND scan takes 1 to 4 min on a 24-core cluster.

### 2.1.3.1. Error Sources in Neutron Depolarization Measurements

A typical ND measurement is shown in Fig. 2.13 where the polarization of a CePt sample at a pressure of  $p = 0.8$  GPa is shown as a function of temperature  $T$ . The Curie temperature of CePt at the given pressure is  $T_C = 7.5$  K resulting in a constant polarization for  $T > T_C$  and a decrease of the polarization to lower temperatures. However, as in all real measurements, the data is subject to a certain level of statistical noise indicated by the

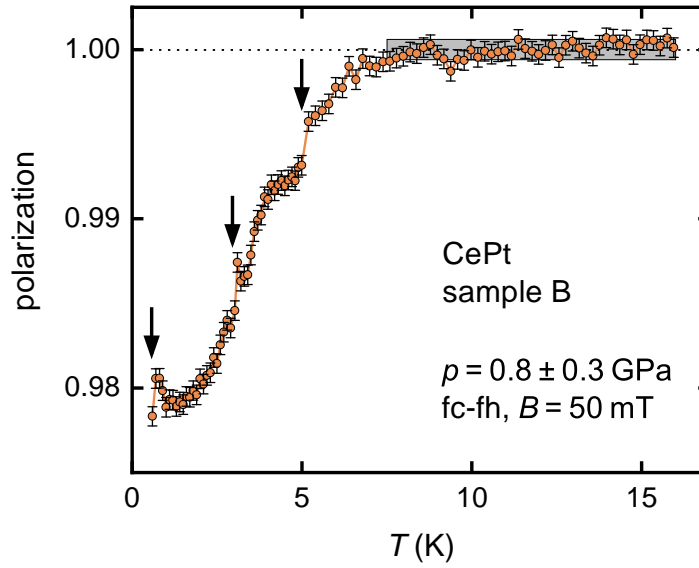


**Figure 2.13.:** ND data of a CePt sample featuring noise and artifacts. The polarization as a function of temperature  $T$  shows statistical noise in the order of the error bars. Additionally, a gray rectangle in the region of constant polarization above  $T_C = 7.5$  K indicates the  $1\sigma$  error interval around a polarization of 1. Black arrows mark jumps in the polarization caused by the afterglow effect.

error bars. In this example the statistical noise is much smaller than the depolarization caused by the FM of the sample. In other measurements, where the FM is weak due to its proximity to a QPT, much smaller depolarization signals are observed. In order to distinguish between noise and depolarization a quantitative error estimation is necessary. Therefore, all possible sources for statistical deviations of the polarization signal were evaluated and are presented in this section.

Additionally, in some measurements discontinuities can be seen in the polarization, marked in Fig. 2.13 with black arrows. These jumps can be traced back to the afterglow effect and are therefore results of a systematic error. A discussion of the impact of the afterglow effect on the polarization and an algorithm for the detection and correction of the resulting jumps are given in Sec. 2.1.3.2 below. In order to avoid confusion in the following discussion, relative errors are given in percent while absolute polarization values are always given in numbers.

For every polarization value an associated error is calculated. Numerous error sources were considered and are listed in table 2.1. The list is an attempt to compile all error sources that can vary the polarization signal and estimate the impact of the errors on the measured polarization. The errors are only estimated for the relevant time scales: The

**Table 2.1.:** List of all considered error sources and the corresponding estimates for the polarization errors. The derivations of the error estimates can be found in Sec. 2.1.3.1. In two cases the error is given as 0 because the error is too small for a quantitative estimation. The afterglow effect may be considered a special case and is discussed in Sec. 2.1.3.2 separately.

Error source	Polarization error	Remarks
CCD camera noise	$4 \cdot 10^{-3}$	per pixel
Neutron flux variation due to reactor control	$2 \cdot 10^{-3}$	
Atmospheric pressure variation	$1 \cdot 10^{-4}$	for the region of Munich
Wavelength stability of the NVS		
• Depolarization by the sample	$3 \cdot 10^{-4}$	
• Spin-flipper	$3 \cdot 10^{-5}$	
• Polarizer and analyzer	0	too small for estimation
Spin-flipper current stability	$2 \cdot 10^{-5}$	
Magnetic background	0	too small for estimation
Afterglow effect	$3 \cdot 10^{-4}$	can appear randomly

exposure time  $t_{\text{exp}} \sim 30$  s and the time between scan parameter values  $\Delta t$  which is in the order of 10 to 20 min. As the polarization is calculated from the intensities  $I_{\uparrow}$  and  $I_{\downarrow}$ , any effect that can change the intensities over time, or the ratio of the intensities, has to be considered.

The absolute noise of the polarization signal measured with the focusing guide setup is on the order of  $1 \cdot 10^{-3}$  to  $2 \cdot 10^{-3}$ . Therefore, errors estimated to be much smaller than  $1 \cdot 10^{-3}$  were considered as negligible and are not included in the calculation of the polarization error.

The most obvious error results from the CCD camera of the detector. Thermal noise leads to an uncertainty of a few gray levels per pixel. Furthermore, the dark current of the camera can vary over time by 2 gray levels. These two effects can be directly measured when taking several images under the same conditions. The error for one pixel intensity is then calculated from the standard deviation of the pixel intensities in the image stack. For typical values, such as a noise of 5 gray levels, a collimation of  $L/D = 500$ , an exposure time of  $t_{\text{exp}} = 30$  s and a beam polarization of  $P_0 = 0.8$ , the polarization error results in  $4 \cdot 10^{-3}$  for one pixel. If the polarization is averaged over a large number of pixels the error can be greatly reduced. Another error caused by the camera is the precision of the

exposure time. The exposure time is controlled by a mechanical shutter in the camera. However, the timing accuracy of the shutter is estimated to be in the order of 1 ms, which is much smaller than the typical exposure time of 30 s. Therefore, this error is negligible. Nevertheless, it is still captured in the error estimate using the standard deviation of several images.

As the depolarization due to FM order depends on the neutron wavelength, the stability of the rotational speed of the neutron velocity selector has to be considered. When set to 5 Å the NVS rotates at 12 400 rpm with a stability of 2 rpm (determined by a NVS sensor) on a time scale of 30 s. Due to the linear dependency between rotational speed of the NVS and the wavelength, the relative wavelength stability is 0.016 %. Applying this value to Eq. 2.7 yields a change in polarization of  $3 \cdot 10^{-4}$  due to the depolarization of the sample. This error is an upper boundary and may be much smaller as the accuracy of the rotational frequency sensor is unknown, and therefore cannot be subtracted from the error estimate. No significant error is expected from the polarization devices due to a change of the wavelength, as the devices are operated well below the critical angle of the polarizing supermirrors.

The spin-flipper uses a solenoid in order to flip the polarization by  $\pi$ . A variation in the driving current of the solenoid therefore changes  $I_{\downarrow}$  as the Larmor rotation of the polarization is affected. A TDK-Lambda Genesys<sup>TM</sup> 40-19 power supply with a current accuracy of 0.01 % is used to control the current. As the field is directly proportional to the current of the solenoid and the Larmor angle is directly proportional to the field, the relative uncertainty of the Larmor angle is also 0.01 %, or 0.3 mrad for a  $\pi$ -flip. For a beam polarization of 0.8 this results in a polarization error of  $2 \cdot 10^{-5}$  and is therefore negligible. The effect of the wavelength stability given by the NVS on the Larmor angle of the spin-flipper is very similar, as the wavelength dependency of the Larmor angle is also linear. A relative wavelength stability of 0.016 % results therefore in a polarization error of  $3 \cdot 10^{-5}$  for a beam polarization of 0.8.

The guide fields are larger than 0.5 mT throughout the setup and are therefore much larger than Earth's magnetic field. Additional magnetic background can be caused by electronic devices or current-carrying cables close to the polarized beam. The cables of the electro-magnet are at their closest position, which is the connection to the electro-magnet, at a distance of 40 cm from the beam. At a maximum current of 200 A this would result in a field of 32  $\mu$ T at the beam position. However, this stray field is always overruled by the magnetic field of the electro-magnet and the guide fields. The only other cables close to the polarized beam are the cables for the motor stages and for the spin-flipper. Both may conduct up to 2 A of current and are both about 20 cm away from the beam. This results

in a field of  $0.6 \mu\text{T}$  at the beam axis which is much smaller than the guide field. To cause a change in polarization the stray fields would have to create a non-adiabatic field transition which can be eliminated due to the small amplitude of the stray fields. Therefore, the effect of the magnetic background on the polarization is considered negligible.

Although it is often stated that the polarization is independent of the neutron flux, this is only true if the neutron flux is constant over time. If the flux changes during the measurements of  $I_{\uparrow}$  and  $I_{\downarrow}$  the polarization also changes. Assuming a statistical error of the measured neutron intensities

$$\Delta I = \Delta I_{\uparrow}/I_{\uparrow} = \Delta I_{\downarrow}/I_{\downarrow} \quad (2.16)$$

an upper boundary for the polarization can be derived. According to the laws of propagation of error the polarization error can be calculated as

$$\Delta P = \sqrt{\left(\frac{\partial P}{\partial I_{\uparrow}} \Delta I_{\uparrow}\right)^2 + \left(\frac{\partial P}{\partial I_{\downarrow}} \Delta I_{\downarrow}\right)^2}. \quad (2.17)$$

Inserting the partial derivatives of Eq. 2.11 with  $P_0 = 1$  for simplicity, Eq. 2.17 can be rewritten as

$$\Delta P = \frac{2}{(I_{\uparrow} + I_{\downarrow})^2} \sqrt{(I_{\downarrow} \Delta I_{\uparrow})^2 + (I_{\uparrow} \Delta I_{\downarrow})^2}. \quad (2.18)$$

Including Eq. 2.16 into Eq. 2.18 results in

$$\Delta P = \sqrt{8} \Delta I \underbrace{\frac{I_{\uparrow} I_{\downarrow}}{(I_{\uparrow} + I_{\downarrow})^2}}_{=Q} \quad (2.19)$$

where the last term labeled  $Q$  can be further analyzed. Defining  $r = I_{\uparrow}/I_{\downarrow}$  and expressing the polarization in terms of  $r$  as

$$P = \frac{r - 1}{r + 1} \quad (2.20)$$

gives

$$Q = \frac{I_{\uparrow} I_{\downarrow}}{(I_{\uparrow} + I_{\downarrow})^2} = \frac{r}{(r + 1)^2} = \frac{1 - P^2}{4}. \quad (2.21)$$

From the last step it is obvious that  $Q < 1/4$  as the polarization can only take values in the range  $0 < P < 1$ . This finally results in an upper boundary for the polarization error of

$$\Delta P < \frac{\Delta I}{\sqrt{2}}. \quad (2.22)$$

For a conservative assumption of  $P > 0.6$  the upper boundary of the polarization error shrinks to

$$\Delta P < 0.45 \Delta I. \quad (2.23)$$

Two effects were considered that can change the neutron beam intensity over time: the atmospheric air pressure and the neutron flux variation due to reactor control. As neutrons are absorbed and scattered by air and humidity, the neutron flux decreases depending on the amount of air it passed. The atmospheric pressure determines the air density and a variation in air pressure can therefore affect the neutron flux at the detector position. In order to estimate the order of magnitude of this effect, a simple Beer-Lambert law of the form  $I(z) = I_0 \exp(-\mu_{\text{air}}z)$  is assumed.  $I_0$  is the incoming neutron flux from the source,  $I(z)$  is the neutron flux after passing a distance  $z$  through air and  $\mu_{\text{air}}$  is the attenuation coefficient of air including scattering and absorption processes. The attenuation coefficient for air at 24 °C, 1 bar, and a humidity of 50 % is  $\mu_{\text{air}} = 0.064 \text{ m}^{-1}$  [89] and is directly proportional to the atmospheric pressure. An inquiry to Germany's National Meteorological Service (DWD) gave the information that the atmospheric pressure usually varies in the region of Munich with a rate of 1 mbar/h and in extreme weather conditions with up to 4 mbar/h. A normal change of 0.17 mbar within 10 min at an atmospheric pressure of 1 bar results therefore in a change of 0.017 % of the attenuation coefficient. For a flight path of  $z = 10 \text{ m}$  through air the relative neutron flux changes therefore by  $\Delta I = 0.02 \%$ . Using Eq. 2.23 this gives a maximum polarization error of  $\Delta P = 1 \cdot 10^{-4}$  which is considered too small to be noticeable in the polarization data. In the case of an extreme change with a pressure change rate of 4 mbar/h the polarization error is  $\Delta P = 4 \cdot 10^{-4}$  which is an error that may be accounted for. However, no extreme weather situations were present during the acquisition of the ND data.

Another error source for  $\Delta I$  is the neutron flux variation due to reactor control. Unfortunately, no direct measurements of the neutron flux of the cold source as a function of time are available. However, the data of a neutron monitor positioned at the entrance of the beam line SANS-1 was evaluated. SANS-1 is located at the end of a cold neutron guide

and therefore the data of the neutron monitor should be proportional to the flux of the cold source. After subtracting the error caused by counting statistics of the neutron monitor, the flux from the cold source features a relative standard deviation of  $\Delta I = 0.45\%$  on a time scale of 10 min. Therefore, the maximum polarization error according to Eq. 2.23 is  $\Delta P = 2 \cdot 10^{-3}$  which is the largest statistical error of the polarization and was therefore implemented in the data evaluation which is explained below.

The data evaluation visualized in Fig. 2.12 also shows the error calculation parallel to the calculation of the polarization value. As mentioned before a pixelwise error is calculated in step (3) from the standard deviation of the image stacks' gray levels. This error includes noise from the CCD chip as well as variations of the beam intensity on a time scale of  $t_{\text{tot}}$ . In step (4), the polarization image calculation, the errors are converted pixelwise to polarization errors using Eq. 2.18. In step (5) the errors are normalized to the same value as the polarization images. As already mentioned, in step (6) the polarization values are averaged using the weighted average defined in Eq. 2.14 and the weights  $w(x,y)$  defined in Eq. 2.15. The error of the polarization value  $\Delta \bar{P}_{\text{ROI}}$  is then calculated by

$$\Delta \bar{P}_{\text{ROI}} = \sqrt{\frac{1}{\sum_{x,y \in \text{ROI}} w(x,y)}}. \quad (2.24)$$

However, at closer inspection this error calculation is biased and yields errors which are too small due to incorrectly treating two different kinds of errors in an equivalent manner. On the one hand, the pixel errors determined in step (3) contain uncertainties due to pixel noise which are independent from each other. On the other hand, the pixel errors also contain uncertainties due to variations of the beam intensity which show a strong correlation between the pixels. The latter uncertainty is falsely leveled out in the error calculation performed in Eq. 2.24. As both uncertainties cannot be measured independently,  $\Delta \bar{P}_{\text{ROI}}$  is corrected by quadratically adding the error estimate derived in Eq. 2.23 with  $\Delta I = 0.45\%$ . Finally, in step (7) when averaging over the polarization values the largest error is chosen as a worst-case error estimate.

In some cases the described procedure fails to deliver reasonable error bars. As an example the polarization data of a temperature scan of a CePt sample under pressure is shown in Fig. 2.14. As the HP-ND setup was used for the measurement, the six polarized spots of the  $3 \times 3$  guide pattern are evaluated independently resulting in the six differently colored polarization curves. The insert shows a detector image of the guide pattern where the six evaluated spots are marked in the same colors as the corresponding polarization curves. The naming of the legend refers to the position of the spots in the guide pattern

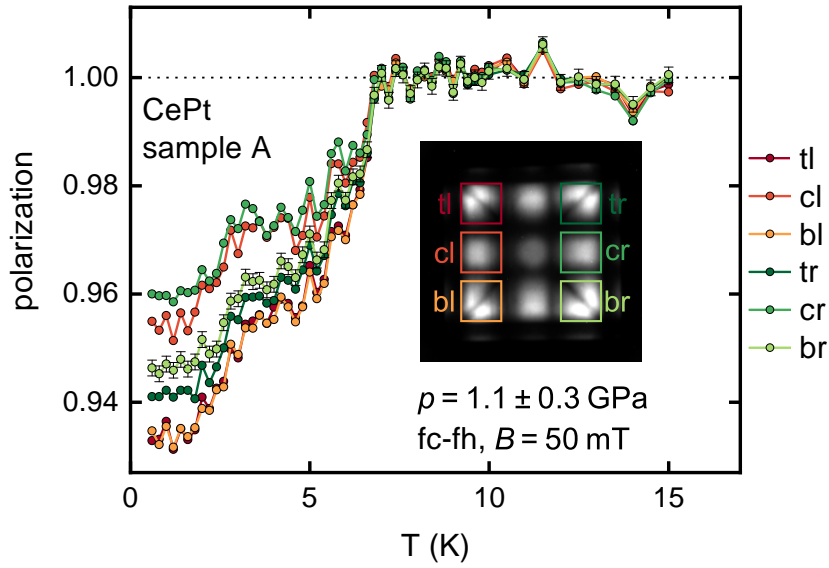


**Figure 2.14.:** Example for an underestimation of the polarization errors. The plot shows the polarization as a function of temperature of a CePt sample under pressure, evaluated for the six polarized ROIs of the  $3 \times 3$  guide pattern. The insert shows the guide pattern and marks the ROIs with rectangles of the corresponding color. For a better readability only the error bars for the br ROI are displayed. The error bars clearly underestimate the overall noise of the polarization data.

with the abbreviations **top**, **center**, **bottom**, **left**, and **right**. The error bars calculated using the described procedure are shown for the light green br polarization curve and are on the order of  $1.5 \cdot 10^{-3}$ . The errors of the other polarization curves are in the same order of magnitude and are not shown for better readability.

In this example, the calculated errors are clearly too small to explain the overall noise of the polarization signals. Especially in the region above  $T_C = 7.0$  K, a constant polarization is expected. The standard deviation of the polarization values above  $T_C$  is  $2.4 \cdot 10^{-3}$  which is significantly larger than the calculated errors. The appearance of an increased noise level compared to the calculations seems to depend on the beam time. Either all polarization scans of a beam time feature an increased noise level or none. Upon closer inspection the putative noise of the polarization signal shows strong correlation between the six polarization curves. This can be seen particularly for temperatures  $T > T_C$ , where all polarization curves follow the same noise pattern. Therefore, the error source can be limited to an effect that affects the whole beam intensity on a time scale of 10 min. The sample itself cannot be excluded as a cause, but this is unlikely as this increase of noise was observed in a number of different systems. Possible explanations include an increase of neutron flux fluctuations due to reactor control, or the afterglow effect which is described

in the following section. In cases where the error calculation delivered unreasonable results, the standard deviation of the polarization values above  $T_C$  was used for all data points as an error estimate.

### 2.1.3.2. The Impact of the Scintillator Afterglow on the Polarization

One error source not discussed so far is the scintillator screen, and connected with that the afterglow effect which is described in Sec. 2.1.2.2. Effectively, the afterglow adds a positive background signal  $I_{ag}$  to the measured intensities  $I_{\uparrow}$  and  $I_{\downarrow}$ .  $I_{ag}$  depends on the previous neutron beam exposure, the time difference to the previous image, the scintillator temperature, and the usage of the scintillator; however, further unknown dependencies may exist. If all dependencies were known and calibration measurements available, the afterglow offset could be subtracted from the raw images similar to the subtraction of the dark image. As this is not the case, the afterglow has to be treated as a systematic error.

In order to evaluate the effects of the afterglow on the measured polarization, a constant  $I_{ag}$  is added to the intensities  $I_{\uparrow}$  and  $I_{\downarrow}$ . Therefore, Eq. 2.11 changes to

$$P = P_0 \frac{(I_{\uparrow} + I_{ag}) - (I_{\downarrow} + I_{ag})}{(I_{\uparrow} + I_{ag}) + (I_{\downarrow} + I_{ag})} = P_0 \frac{I_{\uparrow} - I_{\downarrow}}{I_{\uparrow} + I_{\downarrow} + 2I_{ag}}. \quad (2.25)$$

If  $I_{ag} \ll I_{\uparrow}$  and  $I_{ag} \ll I_{\downarrow}$ , a Taylor expansion of Eq. 2.25 at  $I_{ag} = 0$  yields

$$P \approx P_0 \frac{I_{\uparrow} - I_{\downarrow}}{I_{\uparrow} + I_{\downarrow}} - P_0 \frac{2I_{ag}(I_{\uparrow} - I_{\downarrow})}{(I_{\uparrow} + I_{\downarrow})^2}. \quad (2.26)$$

Introducing the relative intensity of the afterglow  $I_{ag}^{rel} = I_{ag}/(I_{\uparrow} + I_{\downarrow})$  Eq. 2.26 finally results in

$$P = P_0 \frac{I_{\uparrow} - I_{\downarrow}}{I_{\uparrow} + I_{\downarrow}} (1 - 2I_{ag}^{rel}). \quad (2.27)$$

Therefore, a small intensity offset caused by the afterglow results in a small polarization offset with an inverted sign.

As stated in Sec. 2.1.2.2, the afterglow can be driven into a steady state by keeping the time structure of the image acquisition constant. Two time scales of the time structure have to be discussed under the assumption of small depolarization signals: the time between the images of one scan parameter value  $x_i$  and the time  $\Delta t$  between two scan parameter values  $x_i$  and  $x_{i+1}$ . The first is in the order of 3 s (depending mainly on detector settings) and is constant for a scan. The afterglow intensities within an image stack of one scan

parameter value can vary due to the buildup of the afterglow. However, the afterglow intensities from image  $i$  imprinted on image  $i + 1$  are the same for the whole scan. After averaging over the  $\uparrow$  and  $\downarrow$  images of the stack, the criterion of a constant  $I_{\text{ag}}$  is fulfilled. Therefore, the afterglow appearing within the image acquisition of one data point results in a constant polarization offset. This offset is usually in the order of 0.01 (c. Fig. 2.6) and masked by the normalization in the evaluation process. Thus, the polarization values are affected only quantitatively but not qualitatively.

As the afterglow decays slower on longer time scales, the collective afterglow of images acquired for one data point  $x_i$  and subsequently imprinted on the next data point  $x_{i+1}$  has to be considered as well. The magnitude of this afterglow is mainly determined by the time between the data points  $\Delta t$ . If  $\Delta t$  is constant throughout a parameter scan, as for example in a field scan, the same argument as discussed above is valid and all polarization values feature a constant (but small) offset. In contrast, a temperature scan may feature certain temperature values where the temperature controller took longer or shorter to stabilize due to instabilities of the PID controller. This change in time between the data points leads to a different afterglow background  $I_{\text{ag}}$  as shown in Fig. 2.6. Thus, the polarization of this data point will also feature a significant offset which may be misinterpreted as statistical noise or sample signal if not identified properly.

As an example of how artifacts due to the afterglow are identified and in a later stage corrected, ND data from a temperature scan of a CePt sample at 0.8 GPa is shown in Fig. 2.15(a). The uncorrected orange data set is the polarization data as calculated using the algorithm described above. Data points above 5 K are hidden behind the corrected pink data points as both data sets coincide in that region. The error bars for the uncorrected data set are the same as for the corrected data set and are not displayed for better readability. The data shows a decrease in polarization for temperatures below 7.5 K due to depolarization by the FM sample. Additionally, several jumps larger than the average noise can be observed in the uncorrected data notably at 0.7, 3.1, and 5.1 K.

Fig. 2.15(b) shows the time between two subsequent data points  $\Delta t(T)$  of the ND data from (a). The temperature of each data point is now labeled as  $T_i$  where  $i$  is an index describing the order of the measured temperatures.  $\Delta t(T_i)$  is measured from the end of the last image acquisition of the previous data point  $i - 1$  to the beginning of the first image acquisition of the data point  $i$  under consideration. At temperatures  $T \leq 5$  K the polarization data was acquired in temperature steps of 0.1 K, whereas at  $T > 5$  K the size of the temperature steps was increased to 0.2 K. As the temperature controller takes longer for larger temperature differences, a pronounced step in  $\Delta t$  is visible at  $T = 5$  K. Due to the increase of  $\Delta t$  the afterglow background at 5.1 K is smaller than at 5 K. The

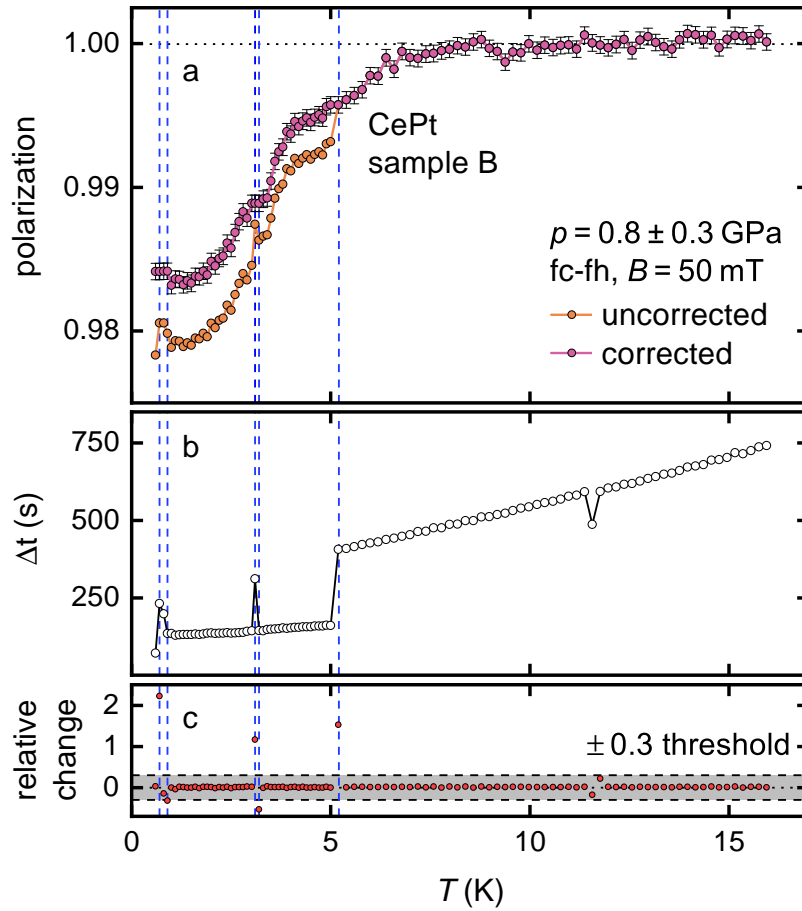


**Figure 2.15.:** Example of the afterglow detection and correction. (a) Neutron depolarization data featuring jumps caused by the afterglow effect. The uncorrected data (orange) taken from a temperature scan of a CePt sample at a pressure of 0.8 GPa shows discontinuities at the temperatures marked with blue dashed lines. The discontinuities are not caused by the sample or noise but can be ascribed to the afterglow effect. A description of how the corrected data (pink) is generated is given in the text. (b) Time between the data points  $\Delta t$  of the ND data shown in panel (a). The time is measured from the end of the previous data point to the beginning of the data point. (c) Relative change of  $\Delta t(T_i)$  compared to  $\Delta t(T_{i-1})$ . Values outside of the marked interval  $(-0.3, +0.3)$  are used as a reference for the blue dashed lines.

corresponding  $\Delta t$  of 410 and 158 s are marked in Fig. 2.6 as a reference. However, due to the aging effect on the afterglow, only a qualitative comparison of Fig. 2.6 and Fig. 2.15 is possible. As the afterglow background decreases from 5.0 to 5.1 K, Eq. 2.27 predicts a jump to a larger polarization which is also observed in the ND data.

In order to drive the afterglow into a steady state, five to eight data points were measured, but not evaluated, prior to all scans. Therefore, the first data point at 0.6 K is larger than zero. At the first temperature change from 0.6 K to 0.7 K a large amount of condensed  $^3\text{He}$  evaporates. More heating is required to increase the temperature which

leads to a relatively large  $\Delta t$  at 0.7 K. Two further instabilities of the temperature controller are seen at 3.1 K and 11.6 K. As the heat capacity of sample holder, pressure cell, and cold head increases and the heat conductivity decreases with increasing temperature, the temperature change requires more heating and the temperature control becomes slower. This explains the monotonic increase of  $\Delta t$  which is not caused by instabilities of the temperature controller.

The jumps in the uncorrected ND data always occur at the same temperatures where  $\Delta t$  changes strongly. In order to quantify these changes, the relative change  $(\Delta t(T_i) - \Delta t(T_{i-1}))/\Delta t(T_{i-1})$  is calculated and shown in Fig. 2.15(c). An empiric threshold of  $\pm 0.3$  is marked with horizontal dashed lines and a gray background. If a value of the relative change lies outside of the threshold interval, the resulting afterglow strongly affects the polarization data. The vertical blue lines are all derived from the position of the outliers. Furthermore, Eq. 2.27 consistently predicts the signs of the discontinuities in the polarization data, which strongly suggests the afterglow effect as the likely cause.

After identifying artifacts in the polarization data resulting from the afterglow effect by evaluating  $\Delta t(T)$ , the polarization data can then be corrected using a simple algorithm. At a jump caused by the afterglow at  $T = T_i$  the polarization difference  $\Delta P_i = P(T_i) - P(T_{i-1})$  is calculated. As the afterglow generates a linear offset,  $\Delta P_i$  is then subtracted from all data points with  $T < T_i$ . This procedure is applied to all afterglow artifacts, starting at the artifact with the highest temperature and subsequently moving to lower temperatures. As the polarization is usually normalized to the high-temperature region, the resulting data does not have to be normalized again. The pink data set in Fig. 2.15(a) shows the ND data after applying the described correction algorithm. Also the error bars calculated according to the procedure described in Sec. 2.1.3.1 are displayed.

The downside of the correction algorithm is that the two subsequent polarization values at the artifact are equal, as exactly the difference of the polarization values is subtracted. However, the artifacts are usually larger than the error bars and larger than a typical polarization change caused by the sample. Therefore, the corrected version of the polarization data is expected to give a better representation of the sample behavior than the uncorrected version. Furthermore, not all polarization scans featuring artifacts resulting from the afterglow can be treated with this correction algorithm, as for example when several discontinuities in  $\Delta t(T)$  appear subsequently. In addition, the increased noise level shown in Fig. 2.14 may result from the afterglow effect. However, no discontinuities were found when evaluating  $\Delta t(T)$ . Additional unknown dependencies of the afterglow changing randomly could possibly explain the noise.

### 2.1.3.3. Polarization Changes due to Relative Movement of the Pinhole of the DAC

As already stated in Sec. 2.1.2.4, when scanning large temperature ranges, as for example in the case of SrRuO<sub>3</sub> (c. Sec. 4.2), the thermal expansion of the cold head of the cryostat results in a vertical movement of the sample of up to 200 μm with changing temperature. In the case of the NDI setup this effect would barely be visible as it is smaller than the spatial resolution of the detector. However, in the case of the high-pressure ND setup the neutron beam is focused through the pinhole of the DAC which is adjusted to a precision of 50 μm relative to the neutron beam. Therefore, when using the high-pressure ND setup and scanning large temperature intervals the setup continuously moves out of alignment. As a result the relative intensities of the spots of the 3 × 3 guide pattern change, thus inducing a change of the polarizations of the spots.

This behavior is linked to the direction of the relative movement of the DAC's pinhole. For a vertical movement the 3 × 3 guide pattern remains symmetric along a vertical mirror axis, however, asymmetries are seen along a horizontal mirror axis. In other words, the polarizations of the spots aligned in a row (left and right) show similar behavior while the polarizations of the spots aligned in a column (top, center, and bottom) show deviating behavior. In a similar fashion the horizontal movement of the neutron beam relative to the pinhole induces asymmetries between the polarizations of the right-side spots and the left-side spots. A horizontal relative movement can for example be seen when the magnetic field is scanned and the clamps of the focusing guides feature a small amount of clearance. As the magnetic housings of the guides extend into the magnet, the interaction between them can overcome gravity at a sufficiently large applied field. As the clamps are pressing the guides on the kinetic mounts from the top, but feature clearance to the left and right side, the guides are then pushed in the horizontal direction. The effects of the movement of the neutron beam relative to the pinhole of the DAC were verified by artificially scanning the position of the DAC in the horizontal and the vertical direction using the available linear motor stages resulting in the described behavior.

In order to illustrate the effect of a vertical movement of the DAC on the polarizations of the 3 × 3 guide pattern an exemplary temperature scan of a SrRuO<sub>3</sub> sample under pressure is shown in Fig. 2.16. The letters of the legend refer to the position of the corresponding spot in the guide pattern: **top**, **center**, **bottom**, **left**, and **right**. While the polarizations of both top (tl and tr), both center (cl and cr), and both bottom (bl and br) polarizations correlate, respectively, a negative correlation is observed when comparing, for example, the top polarizations with the bottom polarizations. In this case (which is the scan featuring the most prominent effect) the vertical movement of the DAC induces variations of the

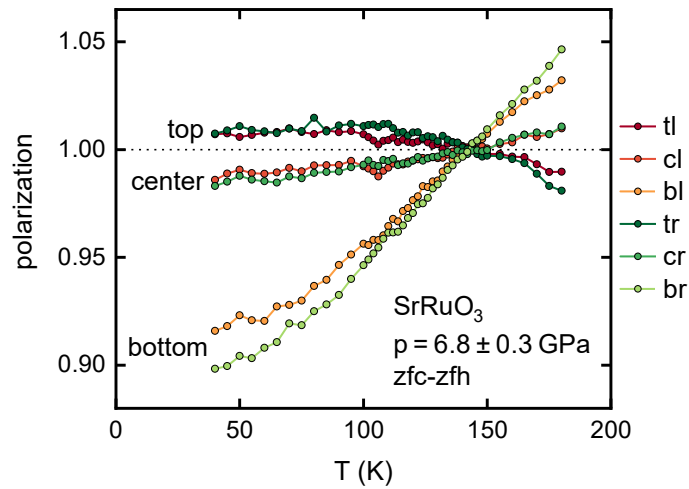


**Figure 2.16.:** Example for the polarization change induced by vertical movement of the pressure cell. The polarization of the six polarized spots of the  $3 \times 3$  guide pattern is shown as a function of temperature  $T$  where the legend refers to the positions of the spots in the pattern: **top**, **center**, **bottom**, **left**, and **right**. Clearly, the polarization curves of both top, center, and bottom spots show very similar behavior, respectively, while the polarizations of the left and the right spots show opposing behavior.

polarization masking any effects caused by the sample. In order to counteract this effect in subsequent temperature scans, the linear motor axis controlling the vertical position of the sample was used to compensate the movement caused by the thermal expansion of the cold head. The best compensation was achieved by adjusting the pinhole position at 4 to 5 different temperatures and noting down the respective position before the temperature scan. Then during the temperature scan at every temperature point that was measured, the vertical position of the DAC was adjusted using a linear interpolation of the noted values. In most cases this compensation was not able to completely remove the effect, however, the changes of the polarization were significantly reduced.

On a side note, the intersection of all polarization curves in Fig. 2.16 at 140 K features no special meaning as it results from the symmetry of the curves. The data set is normalized to the average polarization above 118 K, however, a different normalization would shift the intersection along the temperature axis.

#### 2.1.3.4. On the Interpretation of Polarization Signals using the High-Pressure Neutron Depolarization Setup

In the previous sections different errors affecting ND measurements were identified, qualitatively discussed and, if possible, estimated. Most of the statistical errors discussed in

Sec. 2.1.3.1 are not significant except for the polarization error caused by variations of the neutron flux due to reactor control, eventually limiting the resolution of the ND setups to about 0.1 to 0.2%. The systematic errors resulting from the afterglow effect (c. Sec. 2.1.3.2) and the relative movement of the DAC's pinhole to the neutron beam (c. Sec. 2.1.3.3) can be reduced by following certain measurement protocols, however, a complete compensation could rarely be achieved. Hence, not only the FM of the sample but also several errors can affect the polarization signal simultaneously. The question arises how a change of polarization in a ND measurement should be interpreted in general and how the different effects can be identified. In order to answer these questions the key features of the different effects are summarized in the following focusing on their differences. As NDI measurements are rarely affected by systematic errors and feature a good signal-to-noise ratio this section only discusses polarization signals measured with the high-pressure ND setup. The analysis of correlated behavior of the six polarization signals from the  $3 \times 3$  guide pattern can then be used as an indicator which effect most likely causes a variation of the polarization.

**Effect of the sample.** As the sample is usually situated at the focal spot between the focusing guides and the size of the spot is larger than the sample, it can be assumed that all six polarization signals are affected similarly, therefore, showing correlated behavior. Furthermore, the investigated samples are typically well characterized with techniques such as susceptibility and magnetometry. The results from the characterization are used in the ND measurements to determine the resolution of the scanned parameter, i.e. the temperature or the magnetic field, such that for example the phase transition at  $T_C$  can be resolved in detail. Hence, the polarization changes only slowly with a changing scan parameter. If all six polarizations of the  $3 \times 3$  guide pattern feature positively correlated behavior and change slowly during a scan, the variation of the polarization is caused by the sample.

**Statistical noise.** Two types of statistical noise have to be differentiated: statistical noise affecting the whole neutron beam intensity such as intensity variations due to reactor control, and statistical noise affecting the six polarizations individually, such as noise from the CCD camera. If the whole beam intensity is subject to noise the six polarizations are changed equally, therefore, resulting in correlated behavior of the polarizations in the order of 0.2% but changing randomly from data point to data point. In contrast, if the statistical noise affects the spots of the  $3 \times 3$  guide pattern individually, the six polarizations do not correlate with each other and randomly scatter on a scale of about 0.2% from data point to data point. Statistical noise is therefore usually characterized by

its small amplitude and high frequency but can feature behavior ranging from positive correlation to no correlation at all.

**Afterglow effect.** As the afterglow effect is caused by the scintillator used in the detector, it affects the spots of the  $3 \times 3$  guide pattern equally, resulting therefore in correlated behavior of the six polarizations. Although the impact of the afterglow effect on the polarization can usually be minimized by reaching a steady state, small interruptions during a scan (caused for example by an instability of the temperature controller at a certain temperature) can result in sudden jumps in the polarization data. Hence, when the polarization is affected by the afterglow effect, the behavior of the six polarizations is similar to the case of statistical noise acting on the whole neutron beam: the six polarizations are positively correlated and the polarization changes with a high frequency, however, the amplitude is typically larger for the afterglow effect and the jumps are isolated events.

**Relative movement of the DAC's pinhole.** In contrast to the other effects, the movement of the pinhole of the DAC relative to the neutron beam results in a negative correlation of some of the six polarizations of the  $3 \times 3$  guide pattern. The changes of the polarizations are usually slow in the case of a temperature scan due to the small but steady thermal expansion. In the case of a field scan the polarizations can change much more rapidly when the magnetic field overcomes the weight of the neutron guides. However, in both cases some of the six polarizations show negatively correlated behavior, which is a clear indicator for a relative movement of the DAC's pinhole.

As already stated in Sec. 2.1.3, in some cases it was not possible to calculate error bars for a data set which can satisfactorily explain the statistical and systematic errors. However, by applying the considerations presented above the contributions to the depolarization of the listed effects can be separated and the actual effect of the sample can be isolated on a qualitative level. This procedure was especially utilized for the interpretation of the ND results of  $\text{SrRuO}_3$  shown in Sec. 4.2 due to the simultaneous appearance of all mentioned effects.

## 2.2. Diamond Anvil Cells

In order to apply hydrostatic pressure onto a sample, it is usually placed into a pressure cell. The basic principle of all pressure cells is the same: The sample is located in a confined sample space that is filled with a pressure transmitting medium (PTM). One or more anvils with a cross-section  $A$  apply a force  $F$  on the PTM resulting in a hydrostatic pressure  $p = F/A$  on the sample. From this principle a large variety of pressure cell designs have been developed [90–92] in order to provide suitable and tailored designs for each specific

kind of experiment. The main parameters affecting the design of a pressure cell are the pressure range and the measurement technique being utilized [91, 92].

A pressure cell for the investigation of the systems introduced in Sec. 1 with the ND technique has to fulfill several requirements. (i) Pressures of up to 20 GPa must be achievable with the pressure cell, limiting the selection to diamond anvil cells (DAC). (ii) The pressure cell must be compatible with a ND setup. (iii) The dimensions of the pressure cell have to fit into the constraints of the sample environment (cryostat and electro-magnet). (iv) The pressure cell has to operate at low temperatures and must be non-magnetic in order to not distort the ND measurements. A DAC fulfilling all of these requirements was developed by Jorba [86] and was also used for all measurements presented in this thesis.

The basic principle of a DAC is shown in Fig. 2.17. Two opposed diamond anvils exert a force  $\vec{F}$  on a sample space which is enclosed by a gasket. The pressure  $p = F/A$  within the sample space can be determined from  $\vec{F}$  and the area of the culet  $A = d_c^2\pi/4$  with the culet diameter  $d_c$ . A larger force and a smaller culet diameter result in a larger pressure. When designing a pressure cell usually the sample space is maximized by maximizing the size of the culets. However, an upper limit is given by both the desired pressure range and a maximum force  $\vec{F}$  determined by the fact that diamonds break when exceeding a certain load. A rule of thumb for the maximum achievable pressure with a DAC is given in Ref. [92] (Eq. 1). The DAC used in this thesis is designed for pressures up to 12 GPa

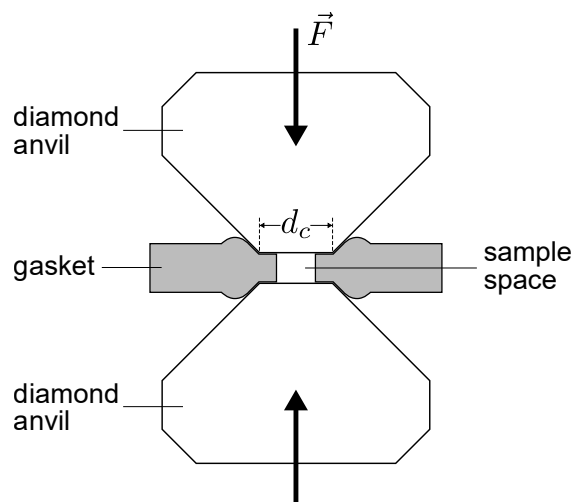


**Figure 2.17.:** Basic principle of a diamond anvil cell (DAC). Two opposed diamond anvils exert a force  $\vec{F}$  on a sample space which is enclosed by a gasket. The sample space is filled with a PTM for hydrostatic pressure conditions.

when using a culet diameter of  $d_c = 800 \mu\text{m}$  and pressures up to 20 GPa when using a culet diameter of  $d_c = 500 \mu\text{m}$ .

Fig. 2.18 shows a drawing (A) and a photo (B) of the loaded DAC. This particular design is the third iteration of a series of DACs and was named "guide pin (GP) DAC" as it features guide pins in order to fix the relative alignment of the anvils to each other. The cell bodies (1) and (2) are made from copper-beryllium (Cu:Be) as it is non-magnetic and features a good thermal conductivity at low temperatures. The load is applied by four titanium screws (3). The diamond anvils (4) are mounted on tungsten-carbide (WC) backing plates (5) in order to spread the load evenly on the cell bodies. Although diamonds can withstand very high compressive forces, they can break much easier under shear stress. Therefore, the culets of the anvils have to be aligned precisely in parallel. The lower backing plate can be moved and fixed in the horizontal plane in order to align the positions of the culets with respect to each other. The upper backing plate is mounted on a hemispherical rocker (6) which can be adjusted with three screws (7) for a parallel alignment of the culets. Three guide pins (8) fix the alignment of the anvils to each other and allow a reproducible opening and closing of the cell. Along the vertical axis are conical holes (9) through cell bodies and backing plates for optical access to the sample space.

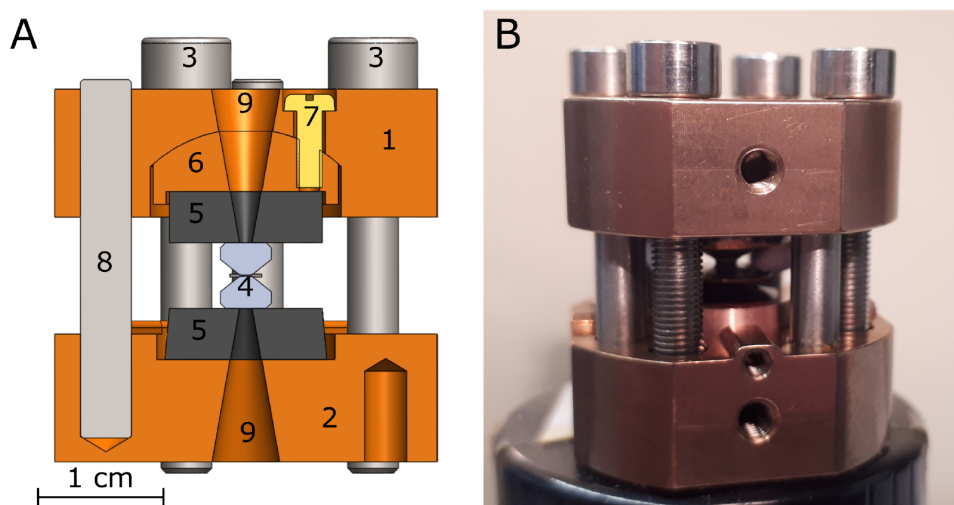


**Figure 2.18.:** Guide pin diamond anvil cell (GP-DAC). (A) Schematic of the GP-DAC. The cell bodies (1) and (2) are made from Cu:Be and provide the structural basis of the pressure cell. Four titanium screws (3) are used to adjust the load on the diamond anvils (4). The anvils are mounted on WC backing plates (5) where the alignment of the upper backing plate can be adjusted with a rocker (6) and the corresponding screws (7). The alignment of the cell bodies to each other is fixed with three guide pins (8). Conical holes (9) through cell bodies, rocker, and backing plates give optical access to the sample space. (B) Photo of a loaded GP-DAC. Figures taken from Ref. [86].

Furthermore, the holes have good utility for the neutron transmission experiments. A more detailed description of the pressure cell can be found in Ref. [86].

For early measurements moissanite anvils were used since moissanites are cheaper than diamonds. However, due to the lower hardness of moissanites (9.5 on the Mohs scale) compared to diamonds, the pressure range is limited to less than 10 GPa. After several failures of moissanite cells, diamond anvils were installed which improved the pressure range and reliability of the pressure cells significantly. The chosen gasket material depends on the pressure and temperature range of the intended experiment. For pressures up to 12 GPa and low-temperature experiments Cu:Be gaskets were used as Cu:Be is easy to handle and non-magnetic at all temperatures. At higher pressures Re gaskets were used due to the higher hardness of Re compared to Cu:Be. However, Re becomes superconductive below 2 K making it unfeasible for low-temperature ND measurements as the field repulsion of the superconductivity can change the polarization [53]. In the beginning Daphne oil was used as a PTM due to its easy handling. At a later stage the PTM was switched to a 4:1 mixture of methanol-ethanol as this PTM features better hydrostatic conditions at low temperatures. The temperature of the sample was measured by attaching a Cernox thermometer to the cell body.

The sample space of a DAC loaded with a CePt sample is shown in Fig. 2.19. The image was taken with a microscope viewing along the conical hole through one of the diamond anvils. The gasket hole measures  $d_c = 400 \mu\text{m}$  in diameter and is not completely filled by sample material in order to ensure hydrostatic pressure conditions. For the pressure determination a small ruby crystal is placed next to the sample. Ruby features

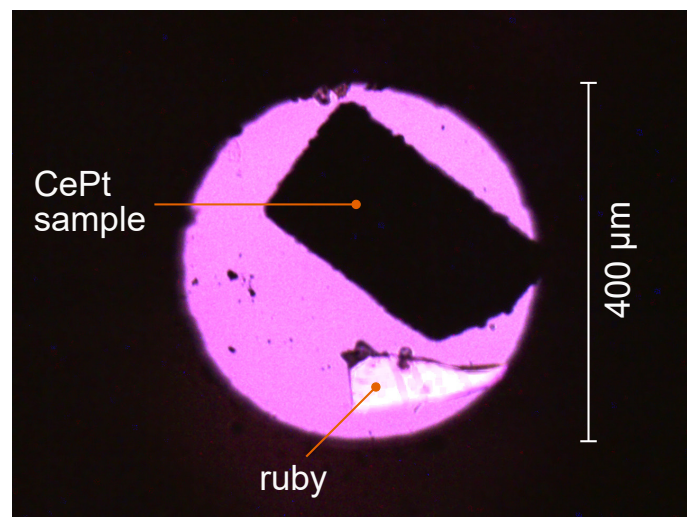


**Figure 2.19.:** Microscopy image of the sample space of a DAC. The cell is loaded with a CePt sample and a ruby crystal for the pressure determination.

two red luminescence lines, R1 and R2, which shift linearly to higher wavelengths with increasing pressure. This wavelength shift is well understood and is widely used as a pressure gauge in high-pressure experiments [93]. Usually the R1 line is utilized for the pressure determination due to its higher intensity. The proportionality between the pressure change  $\Delta p$  and the wavelength shift  $\Delta\lambda$  is given by [93, 94]

$$\frac{\Delta p}{\Delta\lambda} = (2.746 \pm 0.014) \text{ GPa/nm}. \quad (2.28)$$

A fluorescence setup was developed by Regnat in the framework of his PhD thesis [95] for the measurement of the ruby luminescence lines and was also utilized here for the pressure determination. The setup consists of a solid state excitation laser and a compact spectrometer. An integrated CCD camera and objective are used to precisely focus the laser on the ruby in the pressure cell. The positions and FWHM of R1 and R2 are then determined by fitting the sum of two Pseudo-Voigt functions to the measured spectra. After a temperature correction [93] the pressure can be calculated from the R1 wavelength and Eq. 2.28. Although the wavelength shift is mapped within a relative error of 4%, the error of the calculated pressure is usually in the order of 20% due to noise of the spectrometer, a broadening of the luminescence lines caused by the measurement at room temperature, and an uncertainty of the ruby temperature of 1 K. The temperature uncertainty is caused by the fact that the temperature of the ruby is determined by measuring the temperature of the cell body at room temperature.

## 2.3. Samples

This section summarizes the relevant properties of all samples investigated in the course of this thesis. The magnetite samples are described in Sec. 2.3.1, the CePd<sub>1-x</sub>Rh<sub>x</sub> samples in Sec. 2.3.2, the CePt samples in Sec. 2.3.3, and the SrRuO<sub>3</sub> samples in Sec. 2.3.4.

### 2.3.1. Magnetite

In the context of paleomagnetism single-domain (SD) magnetite plays an important role as it carries the major part of the remanence in magnetic rocks. In this particular type of magnetite the crystal grains are so small that they contain only one magnetic domain, resulting in the particular magnetic behavior which is further described in Sec. 3. One of the few sources of natural SD magnetite are the teeth of chitons [96], a class of marine molluscs. These animals developed a thin layer of SD magnetite on their teeth as the magnetite is harder than the underlying tooth itself and the microstructure of the magnetite further

increases the durability [97]. The teeth are located on the radula, which is similar to a tongue, and are arrayed in two rows along the radula.

For the measurements presented in Sec. 3 radulas were extracted from freshly deceased specimens of *Acanthochitona fascicularis*. Fig. 2.20(a) shows the anterior part of a chiton radula which was investigated using the NDI setup. The magnetite-covered teeth are visible as two black rows along the radula. Fig. 2.20(b) shows an image of a single chiton tooth extracted from a different radula. For the ND measurements the whole radula was measured as the biological material does not contribute to the depolarization and it fixes the teeth against movement. This magnetite sample is in the following referred to as the NDI sample. Two more radulas were investigated using a VSM which were consequently named VSM sample 1 and VSM sample 2.

### 2.3.2. $\text{CePd}_{1-x}\text{Rh}_x$

Four samples of the  $\text{CePd}_{1-x}\text{Rh}_x$  doping series were investigated using the NDI setup with Rh concentrations of  $x = 0.40, 0.60, 0.65,$  and  $0.70$ , respectively. The samples are well characterized by resistivity, ac susceptibility, magnetization, and specific heat measurements [99–101]. Details on the sample preparation and characterization are given in Refs. [84, 99–101]. All samples are polycrystals with the exception of the sample with Rh content  $x = 0.40$  which is a single crystal. The polycrystalline samples were cut into slabs with a thickness of 1 mm for the NDI measurements (c. Fig. 5.3).

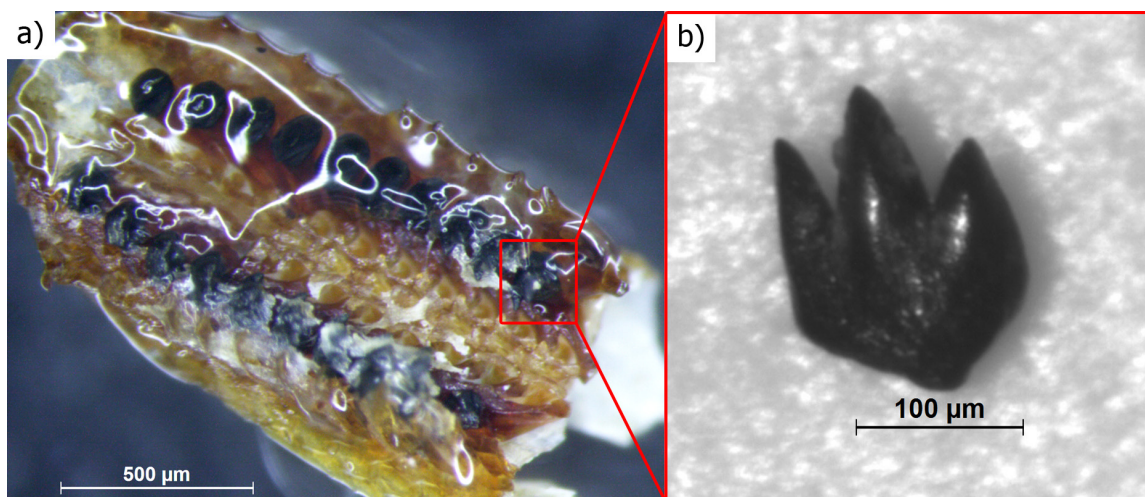


**Figure 2.20.:** Microscopy images of (a) the anterior part of a chiton radula and (b) a tooth extracted from the radula. The teeth have a size of  $200\ \mu\text{m}$  and are covered in a layer of SD magnetite resulting in the black color. About 20 teeth are arrayed in a double-row on the radula. Taken from Ref. [98].

### 2.3.3. CePt

A polycrystalline CePt sample was prepared by melting together stoichiometric amounts of Ce and Pt with purenesses of 99.995 % and 99.99 %, respectively. The sample was slowly cooled to room temperature over several hours and has the shape of a oblate spheroid with dimension of  $4.5 \times 4.5 \times 3 \text{ mm}^3$ . In the following, this sample is referred to as sample L. It was characterized by conventional magnetization and susceptibility measurements which are presented in Sec. 5.3.2.1. Furthermore, the polycrystal was characterized using the NDI setup (FRM II proposal number p14260) which is shown in Sec. 5.3.2.2. Summarized, the results of the characterization indicate a homogeneous sample with magnetic parameters close to values from the literature.

For the high-pressure ND measurements a thin slab was cut from the center of the polycrystal. The slab was then polished to a thickness of  $70 \mu\text{m}$  and cut to rectangular pieces with dimensions of several  $100 \mu\text{m}$  in order to produce samples suitable for the utilized DACs.

The high-pressure data shown in Sec. 5.3.2.3 was acquired over three separate beam times with the FRM II proposal numbers p13937, p13941, and p14766, in the following referred to as beam times A, B, and C, respectively. For each beam time a DAC was loaded with a new piece of the CePt polycrystal, therefore, the labeling also applies to the samples. The pressures measured at the beam times and their order were: (A)  $1.1 \text{ GPa} \rightarrow 5.7 \text{ GPa} \rightarrow 10.5 \text{ GPa} \rightarrow 9.3 \text{ GPa}$ , (B)  $0.8 \text{ GPa} \rightarrow 1.1 \text{ GPa} \rightarrow 1.5 \text{ GPa} \rightarrow 12.2 \text{ GPa}$ , and (C)  $4.1 \text{ GPa}$ . Tab. 2.2 summarizes the CePt samples, their dimensions, and the applied pressures.

**Table 2.2.:** Summary of all investigated CePt samples, their dimensions, and the applied pressures. Each sample was measured using the ND technique in a separate beam time indicated by the FRM II proposal numbers. The small samples A, B, and C were cut from the large sample L and measured at various pressures.

Sample label	Beam time	Dimensions	Pressure history
L	p14260	$4.5 \times 4.5 \times 3 \text{ mm}^3$	Ambient pressure
A	p13937	$400 \times 300 \times 70 \mu\text{m}^3$	$1.1 \rightarrow 5.7 \rightarrow 10.5 \rightarrow 9.3 \text{ GPa}$
B	p13941	$400 \times 250 \times 70 \mu\text{m}^3$	$0.8 \rightarrow 1.1 \rightarrow 1.5 \rightarrow 12.2 \text{ GPa}$
C	p14766	$350 \times 300 \times 70 \mu\text{m}^3$	$4.1 \text{ GPa}$

### 2.3.4. SrRuO<sub>3</sub>

The SrRuO<sub>3</sub> single crystals investigated in the framework of this thesis were synthesized and cut by the group of Braden at the University of Cologne. Details on the crystal growth are given in Ref. [102]. Transport measurements under pressure on samples from the same batch were performed by Tong indicating a good sample quality [103].

Four SrRuO<sub>3</sub> samples were investigated in three separate beam times using the HP-ND setup. In order to preclude confusion with the CePt samples, the SrRuO<sub>3</sub> samples are labeled alphabetically from D to G. For sample D a moissanite anvil cell with a culet size of 800  $\mu\text{m}$  and a Cu:Be gasket was used. ND measurements were performed at a pressure of 4.7 GPa during beam time p14766, however, the moissanite anvils failed during a subsequent pressure increase. As the backup cell containing another SrRuO<sub>3</sub> sample (not labeled) failed as well, CePt sample C was measured instead. Meanwhile a new pressure cell containing SrRuO<sub>3</sub> sample E was assembled, utilizing moissanite anvils with a culet size of 500  $\mu\text{m}$  and a Cu:Be gasket. A pressure of 6.8 GPa was reached, however, no meaningful ND data could be acquired for SrRuO<sub>3</sub> sample E due to field irregularities along the neutron flight path which could not be resolved until the end of the beam time.

Sample F was installed in a DAC with a culet size of 500  $\mu\text{m}$  and a Rh gasket. It was measured during beam time p15385 at pressures of 9.0, 11.4, 14.2, and 17.1 GPa. For beam time p15386 sample G was installed in the same DAC that was used for sample F and ND measurements were performed at pressures of 13.4 and 10.9 GPa. The SrRuO<sub>3</sub> samples and their pressure histories are listed in Tab. 2.3. Due to the irregular shapes of the samples the cross-section in beam direction is given instead of the sample dimensions.

**Table 2.3.:** Summary of all investigated SrRuO<sub>3</sub> samples, their cross-sections covering the neutron beam, and the applied pressures.

Sample label	Beam time	Cross-section $A_{\text{sample}}$	Pressure history
D	p14766	0.079 mm <sup>2</sup>	4.7 GPa
E	p14766	0.035 mm <sup>2</sup>	6.8 GPa
F	p15385	0.040 mm <sup>2</sup>	9.0 $\rightarrow$ 11.4 $\rightarrow$ 14.2 $\rightarrow$ 17.1 GPa
G	p15386	0.012 mm <sup>2</sup>	13.4 $\rightarrow$ 10.9 GPa



### 3. Single-Domain Magnetite on Chiton Teeth

Magnetite constitutes one of the most abundant magnetic minerals in the Earth's crust and preserves its magnetization over geological time scales [104]. As the magnetization orients itself preferably along Earth's magnetic field during the formation of a magnetic mineral, the magnetic properties of magnetite are a valuable probe for the investigation of the history of Earth's magnetic field. Magnetization measurements of sea sediments can, for example, verify the periodic reversal of Earth's magnetic field [105].

Next to its paramagnetic-to-ferrimagnetic transition at  $T_C = 851$  K magnetite undergoes the Verwey transition at  $T_V \approx 125$  K – a structural transition which also affects the electrical and magnetic properties [106–109]. When cooling through the Verwey transition the electrical resistivity as well as the magnetic anisotropy energy increase by two orders of magnitude leading to a rearrangement of the magnetic domains [110–113]. It was shown that  $T_V$ , after decompression to ambient conditions, changes with the previously applied pressure  $p$  with rates between  $-2$  and  $-5$  K/GPa [114–119]. Due to this pressure dependence magnetite could be utilized as a geobarometer in the GPa-range for the determination of shock created in meteorite impacts [32, 120]. However, further research is necessary as  $T_V$  depends not only on the exerted stress but also on other parameters such as the level of oxidation, the doping on Fe-sites, and the size of the crystal grains [121–128].

The latter plays an important role when comparing it to the magnetic domain size as both length scales can approach similar values in natural samples. If the grain size is smaller than  $\sim 100$  nm in the case of magnetite (but larger than the super-PM limit), the grain contains only one domain [129]. These single-domain (SD) grains are crucial for paleomagnetic properties as they carry the majority of the magnetic remanence in rocks [129]. However, the interplay between the magnetic properties of SD grains and the features in the thermodynamic parameters appearing at the Verwey transition is still not completely resolved. As the ND technique can probe the magnetism on the microscopic and the domain-size scale, a ND study was performed in order to investigate the re-arrangement

of the domains at the Verwey transition and the remanence in natural SD magnetite. The results are then compared to conventional magnetization measurements. Parts of this study are published and can be found in Ref. [98].

The rest of this chapter is structured as follows: In Sec. 3.1 the state of the art of magnetite is briefly summarized. In Sec. 3.2 the results of ND and magnetization measurements are shown which are subsequently discussed in Sec. 3.3. A conclusion of this chapter is given in Sec. 3.4.

### 3.1. State of the Art

Magnetite has the formula  $\text{Fe}_3\text{O}_4$  and crystallizes in the inverse spinel structure [29]. Therefore, the tetrahedral sites of the spinel structure are occupied by  $\text{Fe}^{3+}$  ions while the octahedral sites are occupied with an equal mixture of  $\text{Fe}^{3+}$  and  $\text{Fe}^{2+}$  ions [130]. Due to a double exchange interaction between the mixed ions on the octahedral sites the magnetic moments on these sites order ferromagnetically. Furthermore, the moments on the tetrahedral sites couple only to the  $\text{Fe}^{3+}$  ions on the octahedral sites via an antiferromagnetic superexchange interaction. Therefore, the magnetic moments of the  $\text{Fe}^{3+}$  ions cancel each other, leaving only the ferromagnetically aligned moments of the  $\text{Fe}^{2+}$  ions resulting in the observed ferrimagnetism [130]. The measured magnetic moment per formula unit of magnetite is very close to the theoretical  $4\mu_{\text{B}}$  of a  $\text{Fe}^{2+}$  ion [131].

As already mentioned above, magnetite undergoes the Verwey transition at  $T_{\text{V}} \approx 125$  K where the crystal structure transfers from cubic to monoclinic [132]. At  $T_{\text{V}}$  the extended electrons at the octahedral sites freeze which explains the sharp drop in the resistivity [32, 106]. Furthermore, the magnetic easy axis changes direction at the phase transition from cubic  $\langle 111 \rangle$  above  $T_{\text{V}}$  to uniaxial  $[001]$  below  $T_{\text{V}}$  [110, 133].

Due to the structural nature of the Verwey transition a pressure dependence of  $T_{\text{V}}$  is expected. Calculations by Coe *et al.* are in good agreement with a decrease of  $T_{\text{V}}$  under hydrostatic pressure with a rate of  $-3.7$  K/GPa; however, in the case of uniaxial pressure a positive rate of  $23.3$  K/GPa is calculated [134]. The trends of a decrease of  $T_{\text{V}}$  under hydrostatic pressure and an increase under uniaxial pressure are also confirmed experimentally [115, 119, 135–138]. These studies consider the effects of an applied pressure, however, studies by the group of Gilder found a change of  $T_{\text{V}}$  after decompression: when pressure-cycling a magnetite sample to a certain pressure, the Verwey temperature measured at ambient conditions increases with a rate between  $1$  and  $3$  K/GPa [32, 120]. A driving factor of these studies is the potential application of magnetite as a geobarometer since the simple determination of  $T_{\text{V}}$  could reveal the peak pressure a sample was exposed to.

## 3.2. Experimental Results

Three SD magnetite samples from chiton teeth were investigated which are further described in Sec. 2.3.1. Magnetic field loops of VSM sample 1 and VSM sample 2 at different temperatures were measured using a conventional VSM. The results of VSM sample 1 are shown in Fig. 3.1 while the results of VSM sample 2 are shown in Fig. A.2 in the appendix A.2 as the results of both are very similar. Field loops of VSM sample 1 were acquired at (a) 80 K, (b) 140 K, and (c) 300 K between  $-0.5$  and  $0.5$  T. The curves show normal ferrimagnetic behavior with a visible hysteresis and saturation towards larger fields. The values of the coercivities  $B_{c1}$  and  $B_{c2}$  were determined from linear fits close to  $M = 0$ , which are shown as green lines and are listed in Tab. 3.1. For both samples the coercivity decreases with increasing temperature.

For the ND measurements the NDI sample was attached to an aluminum sample holder using aluminum tape. Due to the small sample size, measurements utilizing the HP-ND setup would have been preferable, however, at the time of the measurements the development of the setup was not completed. Therefore, the NDI setup as described in Sec. 2.1.2.3 was used. In order to consistently find the sample a neutron-absorbing Cd mask was attached on the sample holder with a 2 mm pinhole at the position of the sample. Polarization values were then calculated by averaging over the area of the pinhole. ND field loops were measured after zero-field cooling at 80, 140, and 300 K between  $-0.25$  and  $0.25$  T and are shown in Fig. 3.2. However, due to time constraints only parts of the field loop at 300 K could be measured.

The measurements show typical behavior of a ferro- or ferrimagnet: a peak in the polarization is observed at small fields and for larger fields the polarization increases again.

**Table 3.1.:** Coercivities  $B_{c1}$  and  $B_{c2}$  determined from magnetization measurements of VSM sample 1 and VSM sample 2. Two independent field loops were measured for VSM sample 2 at 300 K.

Sample	$T$ (K)	$ B_{c1} $ (mT)	$B_{c2}$ (mT)
VSM sample 1	80	25.8	26.0
	140	14.9	14.2
	300	11.6	11.1
VSM sample 2	80	27.6	27.2
	140	15.0	15.0
	300	11.6	11.1
	300	11.4	11.2

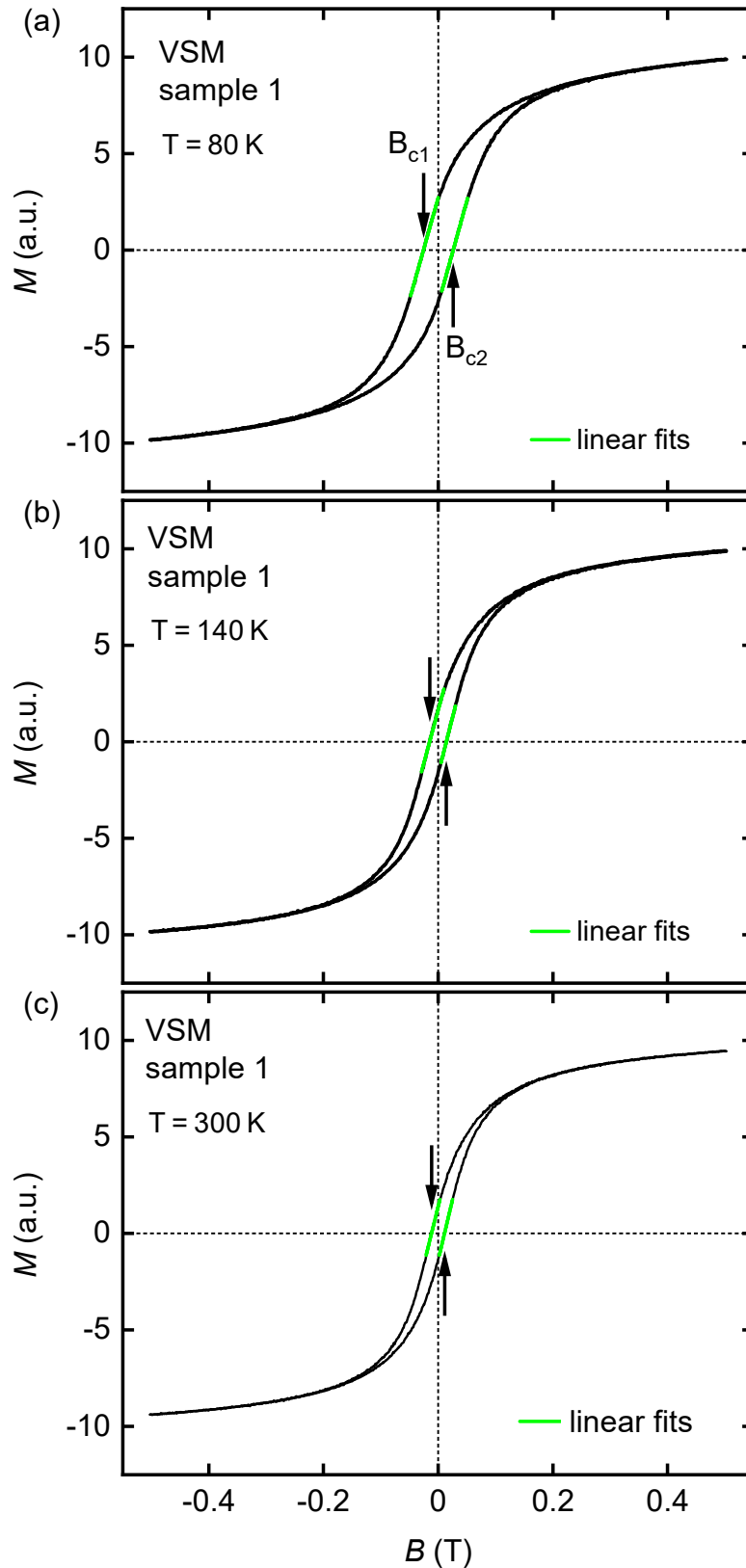


**Figure 3.1.:** Magnetization  $M$  of VSM sample 1 as a function of applied field  $B$ . Field loops were measured at temperatures of (a) 80 K, (b) 140 K, and (c) 300 K. The amount of hysteresis decreases with increasing temperature. The coercivities  $B_{c1}$  and  $B_{c2}$  were determined from linear fits (green lines) close to  $M = 0$ . Figure adapted from Ref. [98].

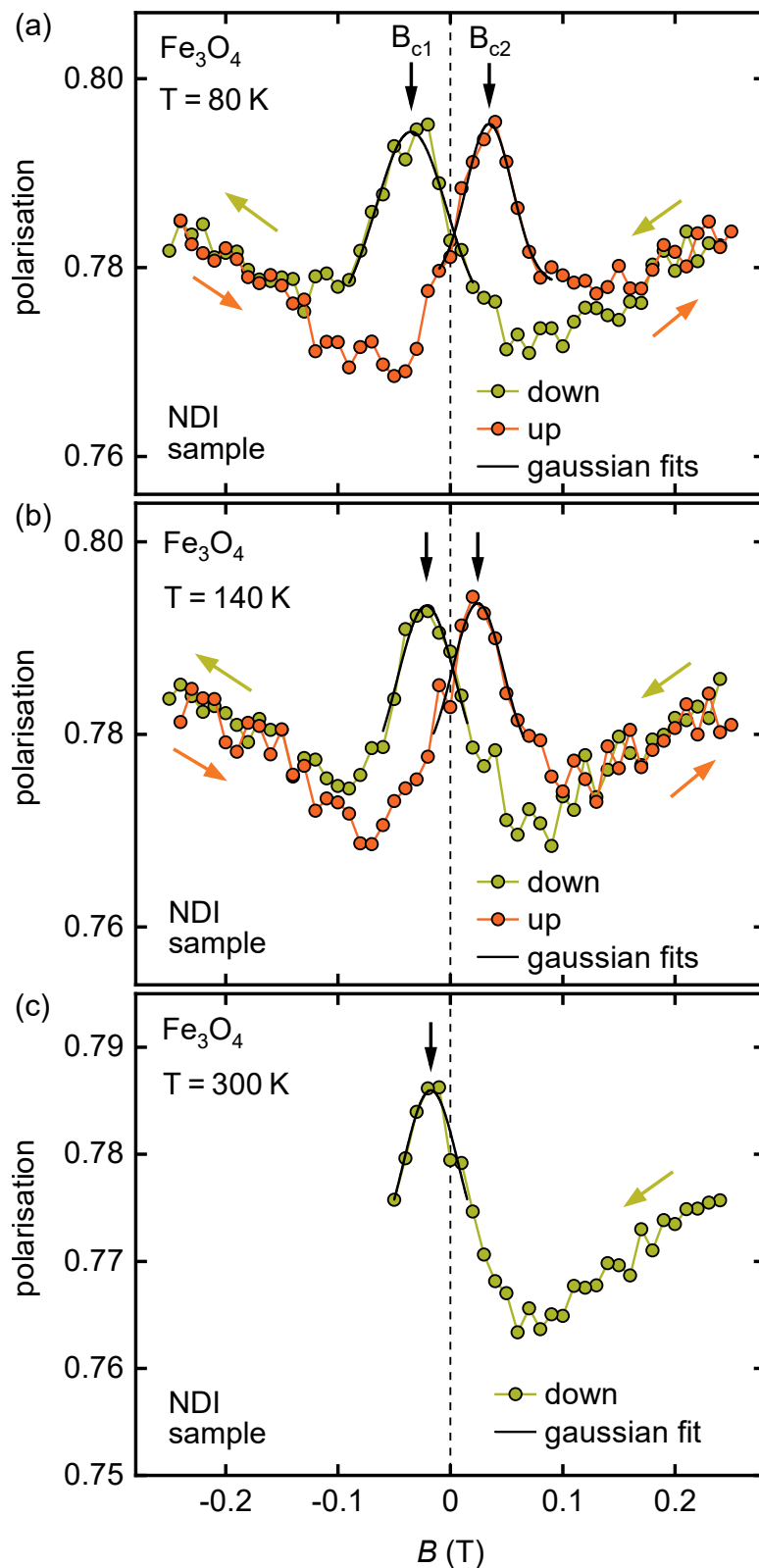


**Figure 3.2.:** Polarization of the NDI sample as a function of applied field  $B$  at temperatures of (a) 80 K, (b) 140 K, and (c) 300 K. Complete field loops were measured between  $-0.25$  and  $0.25$  T showing hysteretic behavior as expected of a ferrimagnetic sample. The coercivities  $B_{c1}$  and  $B_{c2}$  were determined by fitting a gaussian function to the peaks in the up and down scans with the fit shown as a black line. Figure adapted from Ref. [98].

The peaks feature a small offset from  $B = 0$  which is symmetric for the up and down scans. The curves can be explained by the behavior of the magnetic domains during an increase or decrease of  $B$ . At small fields the domains are relatively small and are mostly aligned along the easy axes of the crystal grains. Increasing  $B$  also increases the size of the domains pointing in the direction of  $B$  as these domains grow at the expense of domains pointing antiparallel to  $B$ . Due to the increase of the average domain size the depolarization is enhanced resulting in the rapid decrease of polarization. At larger fields the sample becomes saturated and all domains are aligned along  $B$ . In this case there is no internal field  $B_0$  perpendicular to the polarization vector. Therefore, the neutron spins do not precess around  $B_0$  and the neutron beam is not depolarized resulting in an increase of the measured polarization.

This process is reversible as can be seen from the symmetry of the up and down curves. Furthermore, a hysteresis of a few mT is observed, similar to the magnetization measurements. In order to determine the hysteresis a gaussian distribution was fitted to the peaks close to  $B = 0$  with the center of the gaussian yielding  $B_{c1}$  and  $B_{c2}$ . The choice of a gaussian distribution is empirical and was used as it is symmetrical and describes the peaks sufficiently well. The coercivities of the ND field scans are listed in Tab. 3.2. Again, the coercivity decreases with increasing temperature. Magnetization measurements of the NDI sample using a PPMS are shown in the appendix A.2.

Additionally, the Verwey transition was investigated using a VSM and the NDI setup. Fig. 3.3(a) shows a temperature scan of VSM sample 1 from 80 to 140 K performed in a VSM. After cooling the sample in zero field, a field of 1 T was applied for a few seconds. The magnetization was then acquired during heating in zero field. At 118 K the slope of  $M$  changes which can be attributed to the Verwey transition.

Furthermore, a ND temperature scan of the NDI sample is shown in Fig. 3.3(b). The sample was cooled in zero field and measured during heating in a field of 50 mT from 10 to 262 K. Although the data features a significant amount of noise the polarization clearly decreases with increasing temperature and a change of the slope can be observed at  $\sim 120$  K. In order to visualize these trends the polarization data was fitted using linear

**Table 3.2.:** Coercivities  $B_{c1}$  and  $B_{c2}$  determined from ND field loops of the NDI sample.

Sample	$T$ (K)	$ B_{c1} $ (mT)	$B_{c2}$ (mT)
NDI sample	80	34.9	34.6
	140	21.4	24.4
	300	17.5	-

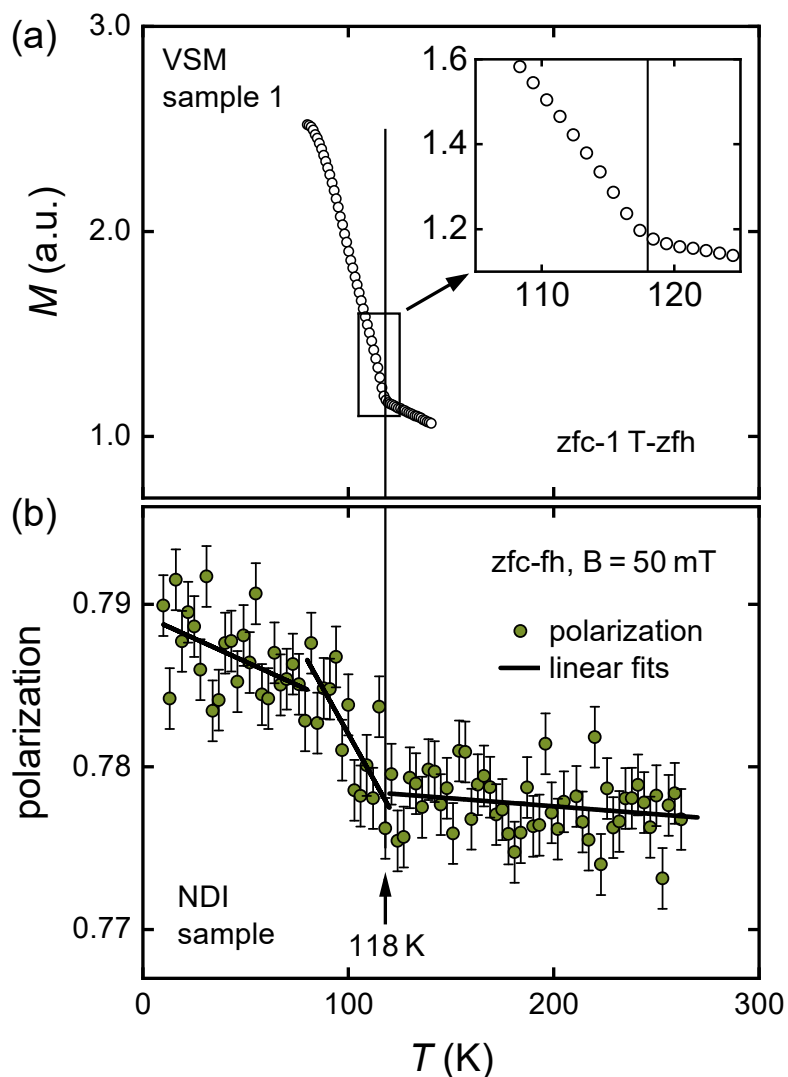


**Figure 3.3.:** Comparison of a VSM measurement and a ND measurement close to the Verwey transition of magnetite. (a) After cooling VSM sample 1 in zero field to 80 K a field of 1 T was applied for a few seconds. Then the magnetization was measured during heating in zero field up to a temperature of 140 K. A change of slope appears at the Verwey transition at 118 K which is further illustrated in the inset. (b) An ND temperature scan of the NDI sample was acquired after zero-field cooling in a field of 50 mT. The polarization decreases with increasing temperature and the slope changes around 80 and 120 K. Lines were fitted to the data in the temperature intervals (10 K, 80 K), (80 K, 120 K), and (120 K, 262 K). The latter two lines intersect at 118 K. Figure adapted from Ref. [98].

functions in the temperature intervals (10 K, 80 K), (80 K, 120 K), and (120 K, 262 K). The fits are shown in Fig. 3.3(b) as black lines. The polarization shows a similar temperature-dependency as the magnetization with a steeper decrease below 118 K and a more gradual decrease above.

### 3.3. Discussion

The coercivities obtained from the magnetic field scans using conventional magnetometers and the NDI setup are shown in Fig. 3.4 as a function of temperature. The VSM and PPMS measurements of the two VSM samples and the NDI sample are in very good agreement and show a decrease of the coercivity with increasing temperature. The decrease from 80 to 140 K is much more drastic than the decrease from 140 to 300 K which may be explained by the Verwey transition at  $T_V \approx 120$  K. As the crystal structure changes to monoclinic below  $T_V$  the sample is subject to twinning which can increase the amount of crystal defects resulting in a stronger pinning of the domain walls and, therefore, in a higher coercivity [139].

Compared to the magnetometry measurements the coercivities determined from the NDI measurements show a similar decrease, however, with a positive offset of 7 mT. Although biological samples such as the investigated chiton teeth are susceptible to natural variation, this can be discarded as an explanation for the offset since the PPMS measurements of the same sample are in very good agreement with the VSM measurements. Furthermore, an influence of the utilized electro-magnet can be ruled out as the remanence is smaller than 1 mT. Static magnetic fields at the sample position can also be excluded as this would result in a symmetrical splitting of  $B_{c1}$  and  $B_{c2}$  around their average. Therefore, the difference in the coercivities is attributed to the different measurement techniques. While conventional magnetization measurements average the fields  $B_0$  of the domains over the whole sample, ND measurements additionally probe the average domain size  $\delta$  and the constellation of the domains. The offset in the coercivities suggests that at the state where  $M = 0$  the fields  $B_0$  cancel each other out, however, the average domain size  $\delta$  has not reached a minimum yet.

The Verwey transition is clearly visible in the magnetization measurements (c. Fig. 3.3(a)) and is in good agreement with comparable data from the literature for natural magnetite samples [32, 120]. Furthermore, the reordering of the domains at the Verwey transition can also be seen in the ND measurements. This enables the possibility to investigate the Verwey transition under pressure using the HP-ND setup which would also drastically increase the statistics and precision of the ND data.

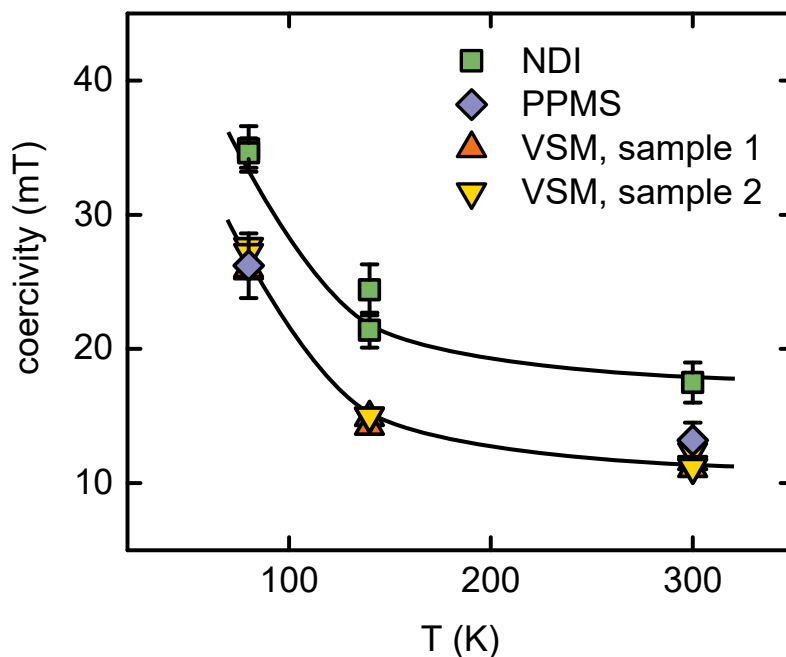


**Figure 3.4.:** Coercivities of different magnetite samples determined by the ND technique and conventional magnetometry as a function of temperature. Two different samples were investigated using a VSM while NDI and PPMS measurements were performed on the NDI sample. The magnetometry measurements show consistent behavior and a decrease of the coercivity with increasing temperature indicated by a black line (guide to the eye). However, the coercivities from the NDI measurements feature an offset of 7 mT compared to the magnetometry data. Figure taken from Ref. [98].

### 3.4. Conclusions

In conclusion, magnetization and ND measurements of natural SD magnetite were performed and compared. Coercivities from field scans of both techniques were extracted at different temperatures and a consistent discrepancy between the two techniques was discovered. Although the coercivities of both techniques show the same decrease with temperature, the ND measurements feature an offset of 7 mT compared to the magnetometry measurements. A possible explanation is the dependency of the depolarization on the domain size  $\delta$  while the magnetization measurements average over the sample. Thus, as the measurements are carried out on different length scales, magnetometry and ND measurements may differ and yield complementary results revealing the complex behavior of the magnetic domains.

Furthermore, the Verwey transition was observed in both magnetization and ND measurements. This enables the investigation of the Verwey transition in natural magnetite under high pressure using the HP-ND setup. A better understanding of the behavior of

the domains could shine light on the shift of  $T_V$  after pressure cycling and improve the utilization of magnetite as a geobarometer.

## 4. The Itinerant Ferromagnet SrRuO<sub>3</sub>

In itinerant FMs the magnetic order emerges from a spontaneous spin-splitting of the conduction band resulting in a net magnetic moment. Therefore, the magnetic moments are not localized at a lattice site, as described by the Heisenberg picture, but are delocalized. Treating the spin-splitting of the conduction band using a mean-field approach yields the Stoner criterion

$$UN(E_F) > 1 \tag{4.1}$$

with the FM exchange interaction  $U$  and the density of states at the Fermi level  $N(E_F)$  [140]. If the Stoner criterion is fulfilled, a spin-splitting of the conduction band is energetically favorable leading to a FM ground state. This theory can explain, for example, the reduced (and generally non-integral) values of the ordered moments compared to the PM Curie-Weiss moments.

The density of states is related to the bandwidth of the conduction band  $W$  via  $N(E_F) \sim 1/W$ . Therefore, an increase of the bandwidth results in a decrease of the Stoner factor  $UN(E_F)$ , consequently weakening the FM. Furthermore, the bandwidth depends on the hybridization of the electron orbitals of the conduction electrons with a stronger hybridization leading to a larger bandwidth. Thus, stronger hybridization generally weakens itinerant FM. This can, for example, be seen when comparing the 3d to the 4d transition metals as the 4d orbitals are more extended than the 3d orbitals. Due to the larger hybridization of the 4d orbitals, FM is much more commonly found in 3d metals and only very few examples of 4d FM are known – one of them being SrRuO<sub>3</sub> which is introduced further below.

Following the arguments above, hydrostatic pressure increases the hybridization due to a decrease of the lattice spacing and, therefore, suppresses itinerant FM. Using a Ginzburg-Landau approach it was shown by Wohlfarth for the case of an itinerant FM that the decrease of  $T_C$  is linear [3]. Hence, it should be possible to tune any itinerant FM towards a quantum critical point (QCP) at a sufficiently high pressure. However, this simple model neglects several aspects, such as pressure induced structural distortions

or phase transitions, and the coupling of the magnetization to magnetic fluctuations. Theoretical studies came to the conclusion that the latter generally leads to a tricritical point accompanied by metamagnetic wings, changing the phase transition to first order if the sample is sufficiently clean [9, 141, 142]. This behavior is, for example, observed in the weak itinerant FMs MnSi [143] and ZrZn<sub>2</sub> [8]. In order to clarify the situation of quantum critical itinerant FMs more data is required making the mapping of magnetic phase diagrams a necessary endeavor. For a detailed review on this topic the reader is referred to Ref. [2].

The Curie temperature of the already mentioned 4d itinerant FM SrRuO<sub>3</sub> was shown to decrease linearly from  $T_C = 164$  K [146] under pressure with a rate of  $\partial T_C / \partial p = -6.8$  K/GPa [33]. The corresponding phase diagram compiled by Hamlin *et al.* [33] determined at high pressures from the third harmonic of the ac susceptibility is shown in Fig. 4.1, where  $T_C$  could be measured up to a pressure of 17.2 GPa. For higher pressures the signal of the FM transition was lost due to a progressively decreasing signal-to-noise ratio. Extrapolating the linear decrease of  $T_C$ , as indicated by the black line, results in a critical pressure of  $p_C = 23.8$  GPa at which  $T_C$  is supposedly suppressed to zero. However, it is unclear if  $T_C$  actually shows this linear behavior down to zero or if  $T_C$  rapidly drops to

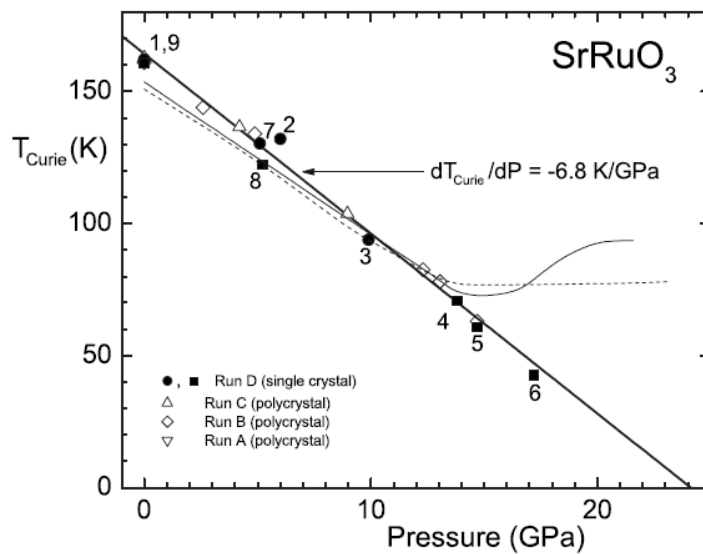


**Figure 4.1.:** Magnetic phase diagram of SrRuO<sub>3</sub> by Hamlin *et al.* [33]. The Curie temperature  $T_{\text{Curie}}$  is shown as a function of hydrostatic pressure  $p$  and was determined from ac susceptibility measurements. A linear decrease of  $T_{\text{Curie}}$  could be traced up to a pressure of 17.2 GPa. The different symbols indicate measurements using different pressure cells and samples. For comparison, measurements from Refs. [144, 145] of thin film samples are shown as dashed and lighter solid lines, deviating from the linear decrease above 15 GPa.

zero at a lower pressure after passing through a tricritical point as stated by the theory of Belitz *et al.* [141].

The incompleteness of the magnetic phase diagram caused by the technical difficulties involved when investigating FM at high pressures motivated a high-pressure ND study which is described below. In the course of this study pressures up to 17.1 GPa were achieved and the measurements largely confirm the phase diagram of Hamlin *et al.* [33]. Although the pressure range could not be extended to higher pressures in this study, we can show that it is technically feasible, justifying further ND measurements. The rest of this chapter is structured as follows: In Sec. 4.1 the state of the art of SrRuO<sub>3</sub> is summarized describing in particular the crystal structure and the associated magnetic properties. In Sec. 4.2 the results of the high-pressure ND study are presented which are subsequently discussed in Sec. 4.3. Finally, the chapter is briefly summarized in Sec. 4.4.

## 4.1. State of the Art

Similar to many systems with the general formula ABO<sub>3</sub>, SrRuO<sub>3</sub> crystallizes in a perovskite structure [146, 148, 149] which is characterized by a regular arrangement of BO<sub>6</sub> octahedra interspaced with A-cations. The overall symmetry of the perovskite structure is determined by the ionic radii of the A- and B-cations as matching ionic radii result in a cubic structure while mismatching ionic radii lead to a distorted perovskite structure with a lower symmetry. The Goldschmidt tolerance factor  $t$  is a measure for the mismatch of the ionic radii and the distortion of a perovskite lattice with  $t \approx 1$  leading to an ideal cubic structure and  $t \neq 1$  leading to a distorted structure. For SrRuO<sub>3</sub> the Goldschmidt tolerance factor is  $t = 0.908$  [147] resulting in an orthorhombic Pbnm crystal structure which is shown in Fig. 4.2. The mismatch of the ionic radii is compensated by a GdFeO<sub>3</sub> type distortion where the rigid corner-sharing RuO<sub>6</sub> octahedra are tilted from the  $c$  axis and rotated around the  $b$  axis. Therefore, the Ru-O-Ru angle  $\Phi$  is reduced from its ideal value of  $180^\circ$  to  $\Phi \approx 166^\circ$  [33]. As deviations of the Ru-O-Ru angle from  $180^\circ$  decrease the hybridization of the Ru 4d and O 2p orbitals, the distortion of the perovskite lattice plays an important role in the magnetic and electronic properties of SrRuO<sub>3</sub>. When increasing the temperature the crystal structure regains its higher symmetries in phase transitions to a tetragonal structure around 800 K and to a cubic structure at 975 K [150–152].

The octahedral environment surrounding the Ru ions causes a splitting of the 4d  $e_g$  and  $t_{2g}$  orbitals due to crystal electric fields. Therefore, the Ru ions are in a low-spin configuration implying a theoretical magnetic moment of  $\mu = 2 \mu_B$  in a localized moment picture [147, 153]. However, magnetization and neutron scattering measurements found a

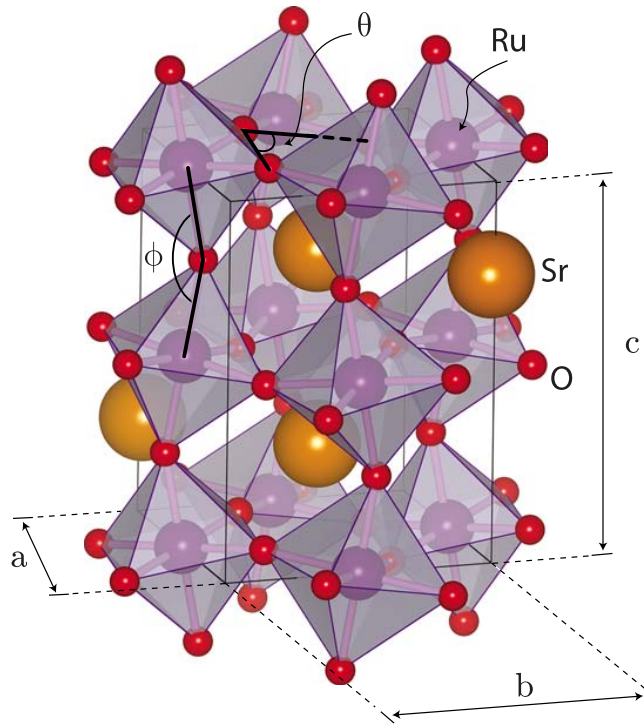


**Figure 4.2.:** Crystal structure of SrRuO<sub>3</sub> with Sr depicted as orange, Ru as violet, and O as red spheres. The mismatch of the ionic radii of Sr and Ru causes a distortion from the ideal cubic perovskite structure resulting in a tilting of the RuO<sub>6</sub> octahedra (shaded in gray). Taken from Ref. [147].

smaller ordered moment of  $\mu = 1.6 \mu_B$  indicating itinerant FM [102, 154–159] which is also supported by theoretical studies [160–162] and further experimental data [70, 149, 163] such as the absence of saturation at large magnetic fields [164]. The PM Curie-Weiss moment is about  $\mu_{\text{eff}} = 2.6 \mu_B$  which is close to the Hund’s rule value of  $2.83 \mu_B$  resulting in a classification of SrRuO<sub>3</sub> as an intermediate itinerant FM [149, 153, 155, 165–167]. A large magnetic anisotropy arises from the strong spin-orbit coupling, aligning the magnetic moments along the c-axis [102, 154, 158, 164, 168, 169]. The behavior of the magnetic domains forming in a SrRuO<sub>3</sub> thin film was investigated by Marshall *et al.* utilizing transmission electron microscopy [170]. They found that the domains arrange in a stripe pattern with a spacing of about 200 nm with the magnetization pointing along the stripes. Furthermore, pinning of the domain walls was observed at impurities of the crystal lattice and a single-domain state can be reached by applying a field of about 200 mT.

The itinerant FM is driven by an enhanced Stoner factor  $UN(E_F) > 1$  resulting from a peak in the density of states close to the Fermi level [161, 162]. Values for  $UN(E_F)$  from the literature are between 1.2 and 1.4 [161, 171]. The distortion of the RuO<sub>6</sub> octahedra

plays a crucial role in the stabilization of the itinerant FM as small distortions decrease the bandwidth  $W$  due to a decreased Ru-O hybridization, thus, increasing the Stoner factor [172]. However, a decreased Ru-O hybridization also results in a smaller FM exchange interaction  $U$  which approaches zero at a Ru-O-Ru angle of about  $136^\circ$  [172]. Therefore, at larger distortions the decrease of  $U$  outweighs the increase of  $N(E_F)$  leading to a decrease of  $UN(E_F)$  and, consequently, to a suppression of the FM. It may also be noted that a pure rotation of the  $\text{RuO}_6$  octahedra in a fixed lattice also increases the Ru-O bond length which would, as discussed by Wohlfarth, result in an increase of  $N(E_F)$  due to the decreased hybridization. However, in this case the latter effect is much smaller than the effects induced by the change of the Ru-O-Ru angle and can be neglected [172].

Such an increasing distortion is observed in the doping series  $\text{Ca}_x\text{Sr}_{1-x}\text{RuO}_3$  where Sr is replaced by the isoelectric, but smaller, Ca.  $\text{CaRuO}_3$  crystallizes in the same  $\text{GdFeO}_3$  structure as  $\text{SrRuO}_3$ , however, due to the smaller Ca ion, the cell volume of  $\text{CaRuO}_3$  is decreased and the  $\text{RuO}_6$  octahedra are rotated by about twice the value compared to  $\text{SrRuO}_3$  [151, 173–175]. Furthermore,  $\text{CaRuO}_3$  is non-magnetic down to lowest temperatures but very close to FM order, classifying this system as a Pauli-enhanced PM [176–178]. When increasing the Ca concentration  $x$  the FM is continuously suppressed on the one hand due to the increasing rotation of the  $\text{RuO}_6$  octahedra but also, on the other hand, due to a decrease of the Ru-O bond length, as chemical pressure is exerted on the crystal lattice [172, 179].  $T_C$  reaches zero at a critical Ca concentration of  $x_c \approx 0.7$ , however, disorder effects lead to a smearing of the QPT resulting in the appearance of a Griffiths phase [34, 180–182].

In 2008 Jin *et al.* were able to synthesize  $\text{BaRuO}_3$  in the cubic perovskite structure under high pressure [35] which enabled the investigation of the doping series  $\text{Ba}_y\text{Sr}_{1-y}\text{RuO}_3$ . Cubic  $\text{BaRuO}_3$  crystallizes in a non-distorted perovskite structure which is increasingly distorted with decreasing Ba concentration  $y$ . The Curie temperature of  $\text{BaRuO}_3$  is 60 K [183] which is surprisingly low as the larger lattice constants would imply a larger  $T_C$ . However, the smaller electronegativity of Ba compared to Sr pushes the electrons towards the Ru-O bond increasing the hybridization. Furthermore, the straight Ru-O-Ru angle of  $180^\circ$  also increases the hybridization. The combination of both effects outweighs the effects of a larger cell volume and leads to a reduction of  $N(E_F)$ , consequently decreasing  $T_C$  [35].

Several studies investigating the crystal structure and magnetism of  $\text{SrRuO}_3$  as a function of hydrostatic pressure were conducted and are summarized in the following. The first measurements of  $T_C$  up to a pressure of 1.1 GPa were performed using a vibrating coil magnetometer by Menyuk *et al.* in 1969, finding a linear decrease of  $\partial T_C / \partial p = -6.3 \text{ K/GPa}$  [184]. In 1994 the group of Schilling measured the resistivity and ac susceptibility of  $\text{SrRuO}_3$

up to a pressure of 6.1 GPa finding  $\partial T_C/\partial p = -5.7 \text{ K/GPa}$  [185]. In the same year Shikano *et al.* also presented resistivity and ac susceptibility measurements in the pressure range up to 1.46 GPa, however, with a larger value for the pressure-dependence of the FM transition  $\partial T_C/\partial p = -7.9 \text{ K/GPa}$  [186]. These studies were in good agreement with the theory of Wohlfarth predicting a linear decrease of  $T_C$  with increasing pressure [3].

In 2002 and 2004 the group of Triscone published resistivity and Hall effect measurements of SrRuO<sub>3</sub> thin films up to a pressure of 23.1 GPa [144, 145]. In the first run they found a linear decrease below 13 GPa with  $\partial T_C/\partial p = -5.9 \text{ K/GPa}$ ; however, for larger pressures  $T_C$  seemed to saturate and no further decrease was observed [144]. In the second run similar results were obtained at low pressures but a small increase of  $T_C$  was seen for pressures above 15 GPa. Possible explanations for the change of slope were shear stresses induced by the thin film setup or a structural transition around 15 GPa.

In 2007 the group of Schilling extended their ac susceptibility measurements to a pressure of 17.2 GPa and added x-ray diffraction measurements at pressures up to 25.3 GPa [33, 187]. The results of the ac susceptibility measurements were already discussed in the introduction to this chapter and are shown in Fig. 4.1. To recapitulate, a linear decrease with  $\partial T_C/\partial p = -6.8 \text{ K/GPa}$  was found in the complete pressure range. The structural measurements confirmed the orthorhombic structure up to 25.3 GPa and no phase transition was found. From the lattice parameters the Ru-O-Ru angle was calculated assuming a rigid rotation of the RuO<sub>6</sub> octahedra. The pressure dependence of the Ru-O-Ru angle showed interesting behavior: at low pressures a linear decrease is observed, however, after passing a minimum at 15 GPa the angle increases again for larger pressures, possibly linking it to the change of slope seen in the thin film measurements of Triscone's group. In contrast, a low-pressure neutron diffraction study by Pietosa *et al.* up to 0.55 GPa found no rotation of the RuO<sub>6</sub> octahedra [188].

In 2011 Cai *et al.* [189] and Zhong *et al.* [190] independently predicted for SrRuO<sub>3</sub> a transition to the post-perovskite structure at 40 and 32.5 GPa, respectively. This motivated two high-pressure x-ray diffraction studies, however, no transition to a post-perovskite structure was found. The first of these studies by Zhernenkov *et al.* found a structural transition to monoclinic between 10 and 21 GPa, and a transition to triclinic at 38 GPa [191]. In the second study by Kronbo *et al.* covering pressures up to 88 GPa only a phase transition to monoclinic was observed between 22.7 and 27.8 GPa [192]. In contrast to the measurements by Schilling's group, the Ru-O-Ru angle determined from the measurements of Kronbo *et al.* decreases monotonically over the complete pressure range. As the magnetism of SrRuO<sub>3</sub> is directly linked to its structure, further measurements in the

high-pressure region of both are required in order to clarify the discrepancies between the different studies.

$\text{SrRuO}_3$  is the  $n = \infty$  member of the Ruddlesden-Popper series  $\text{Sr}_{n+1}\text{Ru}_n\text{O}_{3n+1}$  where  $n$  denotes the number of perovskite layers separating the Sr layers. Due to the layered nature of the crystal structure the dimensionality evolves from 2d to 3d when increasing  $n$  from 1 to  $\infty$ . The  $n = 1$  member,  $\text{Sr}_2\text{RuO}_4$ , is well known for its unconventional superconductivity discovered by Maeno *et al.* in 1994 as it is isostructural to high- $T_C$  superconductors but does not contain Cu which has not been observed before [193, 194]. The  $n = 2$  member,  $\text{Sr}_3\text{Ru}_2\text{O}_7$ , shows a metamagnetic QCP [195] which potentially positions this system on the non-magnetic side of a QPT featuring metamagnetic wings such as proposed by Belitz *et al.* [141]. Finally, the  $n = 3$  member,  $\text{Sr}_4\text{Ru}_3\text{O}_{10}$ , features anomalous magnetism which may be placed between  $\text{Sr}_2\text{RuO}_4$  and  $\text{SrRuO}_3$  as an applied field in the ab-plane induces a metamagnetic transition while a field along the c-axis induces spontaneous FM [196]. A trend can be seen that with decreasing  $n$  FM is suppressed [197] and similarities to a QPT, such as the metamagnetism and the unconventional superconductivity, are observed as well. Since the FM of the end member  $\text{SrRuO}_3$  is also suppressed by hydrostatic pressure [33, 185, 186], one could speculate that  $\text{SrRuO}_3$  may be driven towards the lower  $n$  members with increasing pressure. This would imply a QPT at sufficiently large pressures accompanied by metamagnetic wings which would also agree with the theoretical studies by Belitz *et al.* [9, 141, 142].

Due to its chemical stability and its matching lattice parameters,  $\text{SrRuO}_3$  is often used as a conducting layer in epitaxial multilayer structures [198–202] resulting in a relatively large number of studies focusing on the properties of thin films. The recently discovered Weyl points in  $\text{SrRuO}_3$  promise further applications in spintronics and quantum computing [158, 203–206].

## 4.2. Experimental Results

ND measurements using the HP-ND setup as described in Sec. 2.1.2.4 were performed on  $\text{SrRuO}_3$  samples which are specified in Sec. 2.3.4. Pressures of up to 17.1 GPa were achieved utilizing moissanite and diamond anvil cells (c. Sec. 2.2). As the Curie temperature of  $\text{SrRuO}_3$  is 164 K at ambient pressure a standard CC cryostat was sufficient for the temperature regulation. However, the large temperature changes when scanning from base temperature to a value above  $T_C$  induce a vertical movement of the pressure cell as already discussed in Sec. 2.1.3.3. The variations of the polarization resulting from this movement are an additional error source and affect the measured polarization. In order to

separate the various effects that can change the polarization, the data presented below is interpreted as described in Sec. 2.1.3.4. The calculated error bars (c. Sec. 2.1.3) are shown as a reference for the statistical errors although they underestimate the actual noise in most cases.

A total number of 37 magnetic field and temperature scans were measured separated over 3 beam times and 4 samples. However, not all measurements are shown in this section as several of the scans were either affected by a suspected misalignment of the instrument or the signal of the sample was too weak to draw meaningful conclusions. The polarization data of these measurements can be found in the appendix A.3.2.

Fig. 4.3 shows the polarization as a function of the magnetic field  $B$  of sample D at  $T = 5.1$  K and a pressure of 4.7 GPa. When increasing the magnetic field the polarization continuously decreases and flattens out at around 80 mT. This is caused by an increase of the average domain size with increasing field. When decreasing the field again the polarization stays constant down to 25 mT and then increases but with a smaller slope than the previous decrease. The hysteresis observed in this field scan results from the pinning of domain walls resisting a decrease of the average domain size. Therefore, the hysteresis clearly indicates FM behavior.

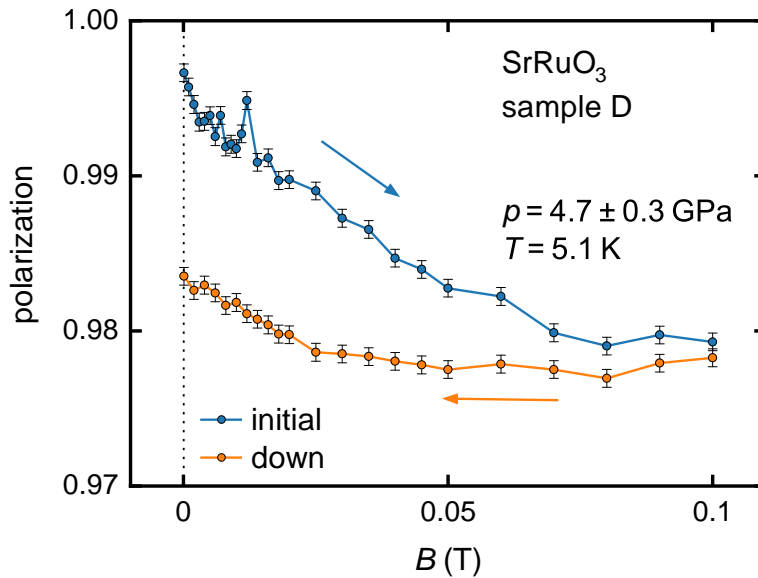


**Figure 4.3.:** Magnetic field scan at 5.1 K of SrRuO<sub>3</sub> sample D at a pressure of 4.7 GPa. After cooling the sample in zero field, the field was first increased to 0.1 T (blue markers) and then again decreased to zero (orange markers). The observed hysteresis indicates the presence of FM order.

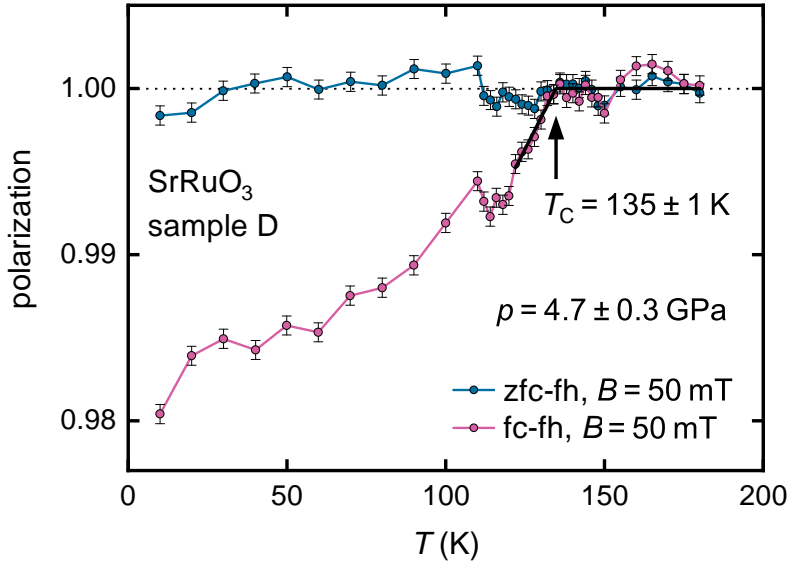


**Figure 4.4.:** ND temperature scans of SrRuO<sub>3</sub> sample D at a pressure of 4.7 GPa. During both measurements a field of 50 mT was applied, however, in the first scan the sample was cooled in zf (blue circles) while in the second scan the sample was cooled in a field of 50 mT (pink circles). The polarization of the fc-fh scan decreases below  $T_C = 135$  K indicating the onset of FM order.

At the same pressure two temperature scans were measured from 10 to 180 K which are shown in Fig. 4.4. Both scans were performed in a field of 50 mT, however, one was measured after zero-field cooling (zfc-fh) and the other after field cooling (fc-fh). While the polarization of the zfc-fh scan stays almost constant around 1, the polarization of the fc-fh scan decreases below 135 K. As  $T_C$  was expected to lie between 130 and 140 K at this pressure, the density of the data points was increased between 110 and 150 K in order to determine  $T_C$  with a better precision. However, the change of  $\Delta t$  between the data points due to temperature regulation results in jumps in the polarization at 110 and 150 K caused by the afterglow effect.

In order to better identify the different effects acting on the polarization, the polarizations of the  $3 \times 3$  guide pattern of the temperature scans are shown in Fig. 4.5 with the zfc-fh scan in (a) and the fc-fh scan in (b). The jumps at 110 and 150 K can be assigned to the afterglow effect as they appear in all six polarizations on a short scale in both scans which also agrees with the changes in  $\Delta t$ . Furthermore, clear differences can be seen between the polarizations of the top, center, and bottom spots of the  $3 \times 3$  guide pattern. While the tl and tr polarizations of the zfc-fh scan show an overall decrease with increasing temperature the bl and br polarizations increase indicating a vertical movement

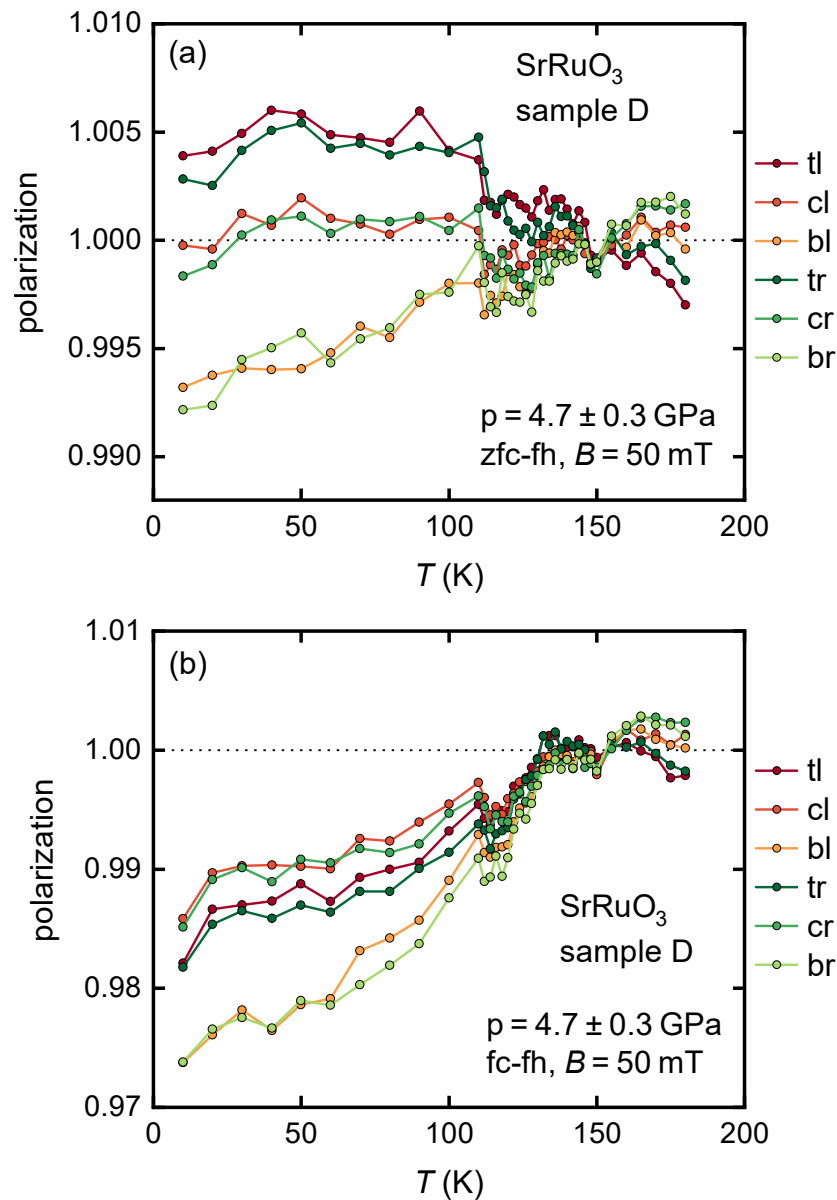


**Figure 4.5.:** Polarizations of the  $3 \times 3$  guide pattern for the temperature scans of SrRuO<sub>3</sub> sample D at 4.7 GPa (c. Fig. 4.4). (a) The zfc-fh scan with an applied field of  $B = 50$  mT shows no polarization but a negative correlation of the top, center, and bottom polarizations, respectively. Additionally, jumps caused by the afterglow effect are visible at 110 and 150 K. (b) Analogue effects can be seen in the fc-fh scan, however, with a superimposed depolarization, setting in at  $T_C = 135$  K.

of the pressure cell. As these tendencies are close to symmetric around a polarization of 1, the differences between the polarizations mostly average out when calculating the final polarization as shown in Fig. 4.4. Furthermore, the small parts that do not average out explain the deviations of the zfc-fh scan from 1.

The fc-fh scan in Fig. 4.5(b) shows similar behavior with a splitting of about 0.01 between the top and bottom polarizations at base temperature, however, superimposed with a continuous decrease of all polarizations below 135 K. As this decrease appears on a slow temperature scale, acts on all six polarizations similarly and sets in close to the expected  $T_C$ , it can be ascribed to depolarization caused by FM order. The Curie temperature  $T_C = 135$  K at this pressure was determined by a linear fit to the averaged polarization which is shown in Fig. 4.4 as a black line. The lack of depolarization in the zfc-fh measurement may result from a smaller domain size due to the cooling in zero field.

For the data sets shown below similar arguments derived from the polarizations of the  $3 \times 3$  guide pattern are required to distinguish features in the averaged polarization caused by different effects. However, in order to maintain readability and compactness, only the averaged polarizations are displayed in this section and the corresponding polarizations of the  $3 \times 3$  guide patterns are shown in the appendix A.3.1.

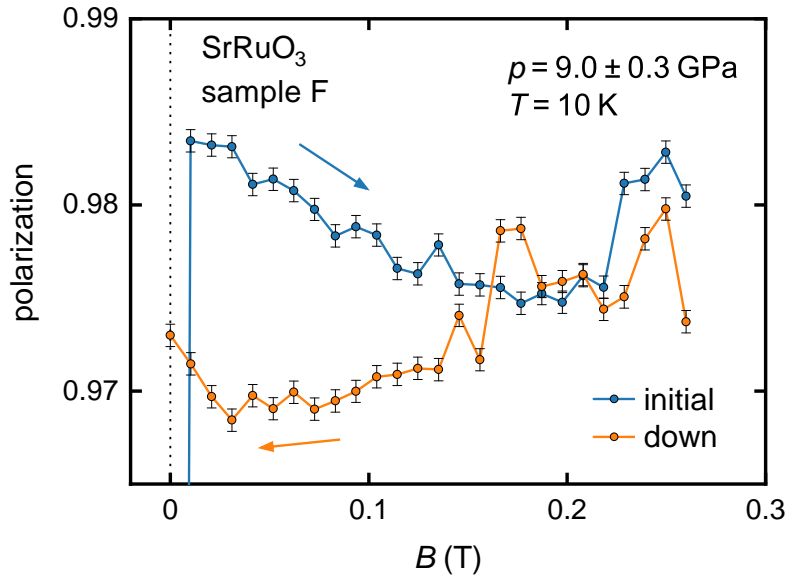


**Figure 4.6.:** Magnetic field scan at 10 K of SrRuO<sub>3</sub> sample F at a pressure of 9.0 GPa. After cooling the sample in zero field, the field was first increased to 0.26 T (blue symbols) and then again decreased to zero (orange symbols). Although the data features artifacts caused by the afterglow effect and a movement of the focusing guides, hysteresis can be observed.

A magnetic field scan of sample F at 9.0 GPa and 10 K is presented in Fig. 4.6. After cooling the sample in zero field the polarization was measured while first increasing the magnetic field to 260 mT and then decreasing it again to zero. The first data point at  $B = 0$  of the increasing-field curve is severely affected by the afterglow effect and lies several percent below the rest of the curve. When increasing the field the polarization continuously decreases up to about 200 mT, however, a jump to a higher polarization appears at 225 mT. A comparison with the polarizations of the  $3 \times 3$  guide pattern of this scan (c. Fig. A.5 in appendix A.3.1) identify this jump as a horizontal movement of the focusing guides. When decreasing the field the polarizations again show inconsistent behavior at higher fields. The difference of the polarizations at 260 mT can be explained by the afterglow effect. Furthermore, a jump of the same magnitude as the jump at 225 mT is present at 160 mT which can also be attributed to a horizontal movement of the focusing guides. At smaller fields the depolarization decreases until 30 mT where it starts to increase again.

As the two jumps in the polarization are similar in amplitude and direction, the movement of the focusing guides seems to be completely reversible. Therefore, the polarization data at fields below 150 mT is unaffected by the movement and the observed hysteresis is genuine indicating a FM ground state of the sample.

Four temperature scans of sample F were measured at 9.0 GPa which are shown in Fig. 4.7(a). ND data was acquired for different field histories in applied fields of 40 and 100 mT. Furthermore, a procedure for the compensation of the vertical movement of the pressure cell was developed during the acquisition of the data sets which was adjusted and improved between the measurements. The same curves of panel (a) are also shown in (b) but with a vertical offset of 0.01 between the curves for a better comparison. The arrangement of the curves from top to bottom corresponds to the chronological order of the acquisition with the first measurement (fc-fh, 100 mT) shown as the topmost.

For the first measurement the sample was cooled in a field of 100 mT and then measured in the same field without a compensation of the vertical movement of the pressure cell. The polarization features several jumps and peaks which are much larger than the expected statistical error. The drop of the polarization at 40 K can clearly be attributed to a movement of the pressure cell as can be seen from the polarizations of the  $3 \times 3$  guide pattern which are shown in Fig. A.6 in appendix A.3.1. The peaks at 60, 120 and 170 K are presumably related to the afterglow effect due to their appearance on a short scale. Although a decrease of the polarization can be seen below 100 K the artifacts in this measurement impede a meaningful interpretation and a determination of  $T_C$ .

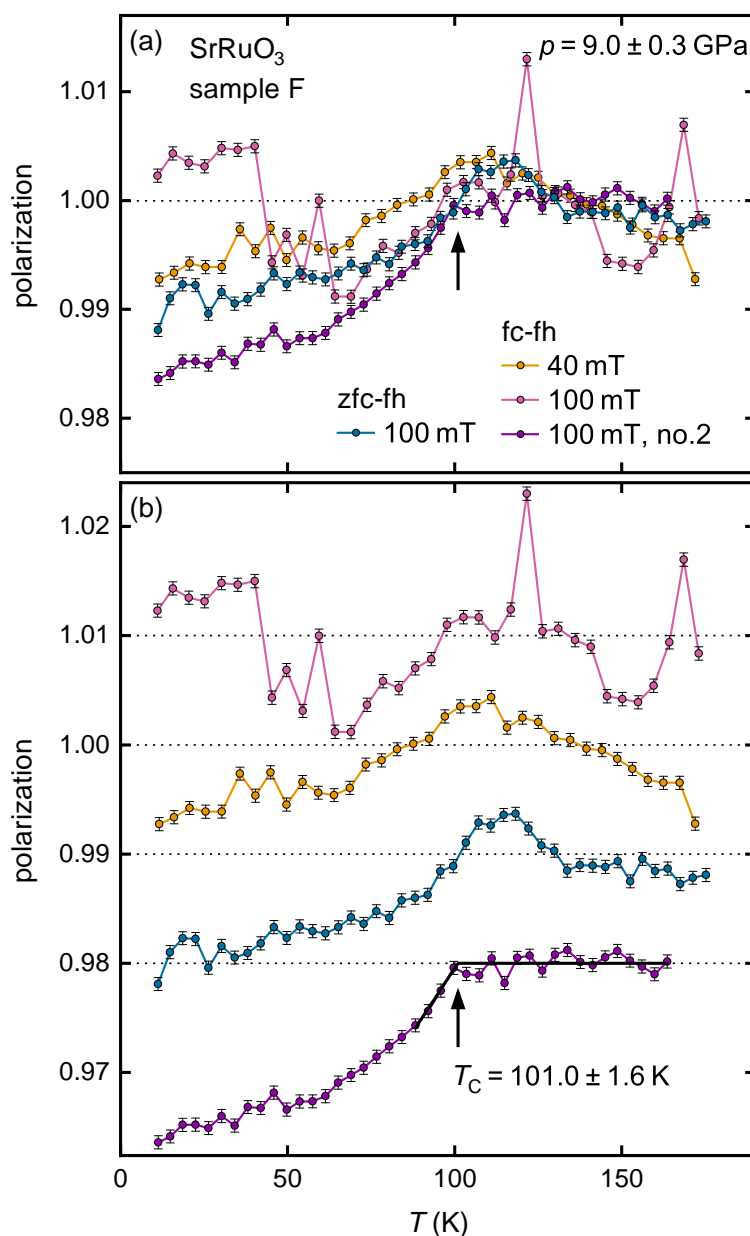


**Figure 4.7.:** ND temperature scans of SrRuO<sub>3</sub> sample F at a pressure of 9.0 GPa. The polarization was measured after zero-field cooling at 100 mT and after field cooling at 40 and 100 mT with the latter being measured twice. The data in panel (b) is the same data as in (a) but with an artificial offset of 0.01 between the scans. Furthermore, the data is arranged in a chronological order from top to bottom in (b). The first scan (fc-fh,  $B = 100$  mT) shows several artifacts caused by the afterglow effect and a movement of the focusing guides. A progressively improving measurement script was able to suppress the artifacts such that the Curie temperature  $T_C = 101$  K could be derived from the last scan (fc-fh,  $B = 100$  mT, no.2).

In order to reduce the effects of the vertical movement of the pressure cell, the pressure cell was centered separately at 10 and 180 K. These values were then used for a linear interpolation of the vertical position of the pressure cell at every temperature. For the next measurement, a fc-fh scan in a field of 40 mT, the vertical position of the sample was adjusted at every temperature using a motorized stage and the values from the interpolation. The corresponding measurement shown in Fig. 4.7 features less artifacts than the previous measurement, however, a decrease above 110 K is observed which can be traced back to a vertical movement of the pressure cell (c. Fig. A.6 in appendix A.3.1). As the vertical movement is related to the thermal expansion which is not linear in this temperature range, more positions at intermediate temperatures were required for a better interpolation.

For the zfc-fh scan with an applied field of 100 mT one additional vertical position of the pressure cell at about 90 K was added to the linear interpolation, however, still a decrease of the polarization above 120 K can be seen. Finally, a fc-fh scan with an applied field of 100 mT was measured with additional vertical positions determined at temperatures of about 60 and 120 K. This curve was labeled "no.2" in order to avoid confusion with the first temperature scan acquired at this pressure. The polarization of this final scan features a constant polarization above 100 K and a continuous decrease below. Furthermore, no artifacts resulting from the afterglow effect or the movement of the pressure cell are visible. The Curie temperature  $T_C = 101.0$  K at this pressure was determined using a linear fit shown as a black line in Fig. 4.7(b).

Fig. 4.8 shows magnetic field scans of SrRuO<sub>3</sub> sample F at a pressure of 11.4 GPa. After cooling the sample in zero field polarization measurements were performed up to 260 mT at temperatures of (a) 12 K and (b) 130 K. From the phase diagram of Hamlin *et al.* [33] and ND temperature scans (shown below) a  $T_C$  of about 90 K was expected which places one of the magnetic field scans below and one above  $T_C$ . When increasing the field at  $T = 12$  K a decrease of the polarization is observed up to 150 mT. At larger fields, however, the polarization increases again with a peak at 220 mT. When decreasing the magnetic field the polarization decreases almost linearly. The polarizations of the  $3 \times 3$  guide pattern shown in Fig. A.7 in appendix A.3.1 suggest a movement of the focusing guides relative to the pressure cell which would explain the peak at 220 mT. As no other effects could be identified at lower fields the observed hysteresis seems to be genuine indicating FM order. This is confirmed by the measurement at 130 K where the hysteresis is greatly reduced. In both data sets the calculated error underestimates the fluctuation of the data points. Therefore, the remaining hysteresis seen in the field scan at 130 K may be within the actual error and, thus, not significant.

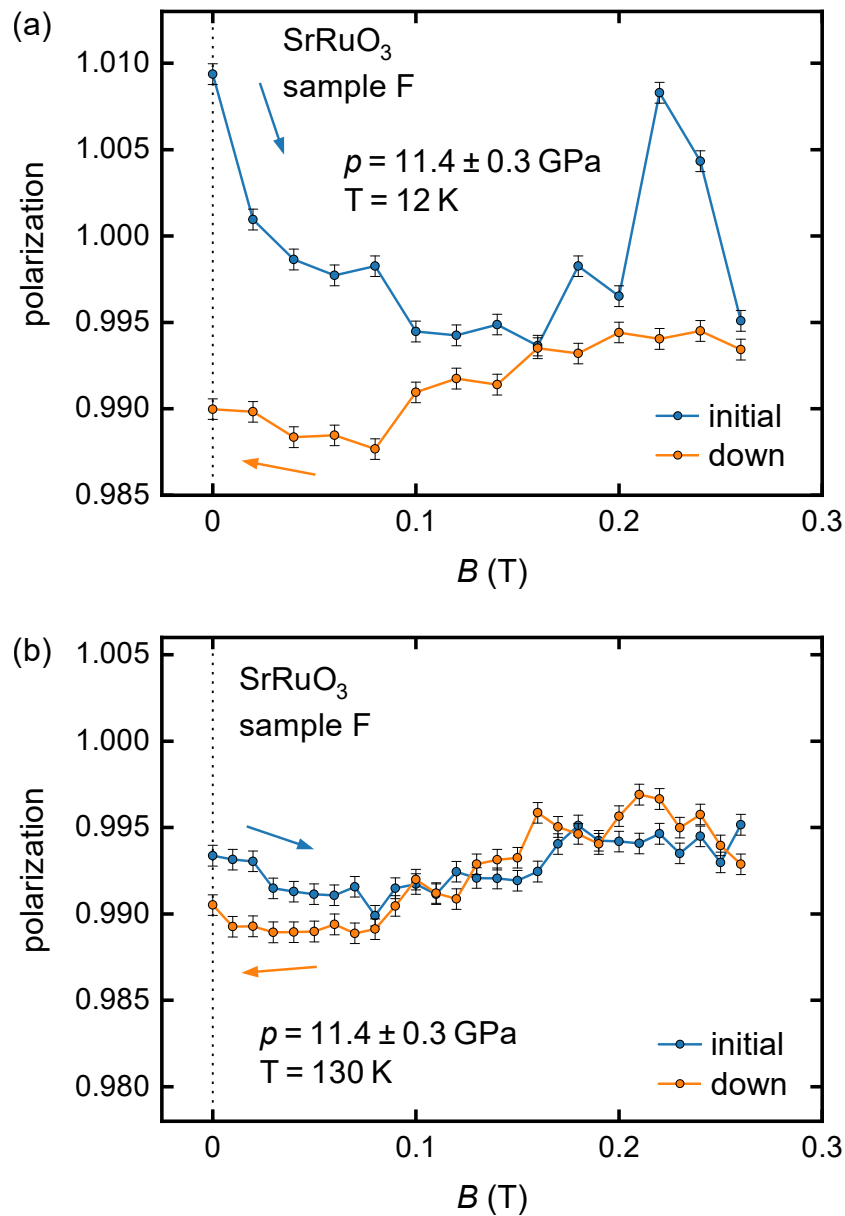


**Figure 4.8.:** Magnetic field scan at (a) 12 K and (b) 130 K of SrRuO<sub>3</sub> sample F at a pressure of 11.4 GPa. After cooling the sample in zero field to the respective temperature, the field was first increased to 0.26 T (blue symbols) and then again decreased to zero (orange symbols). (a) At 12 K hysteresis is observed below  $\sim 150$  mT and a pronounced peak appears at large fields which may be attributed to a movement of the focusing neutron guides. (b) When increasing the temperature above the expected  $T_C \approx 85$  K [33], the hysteresis almost completely vanishes.

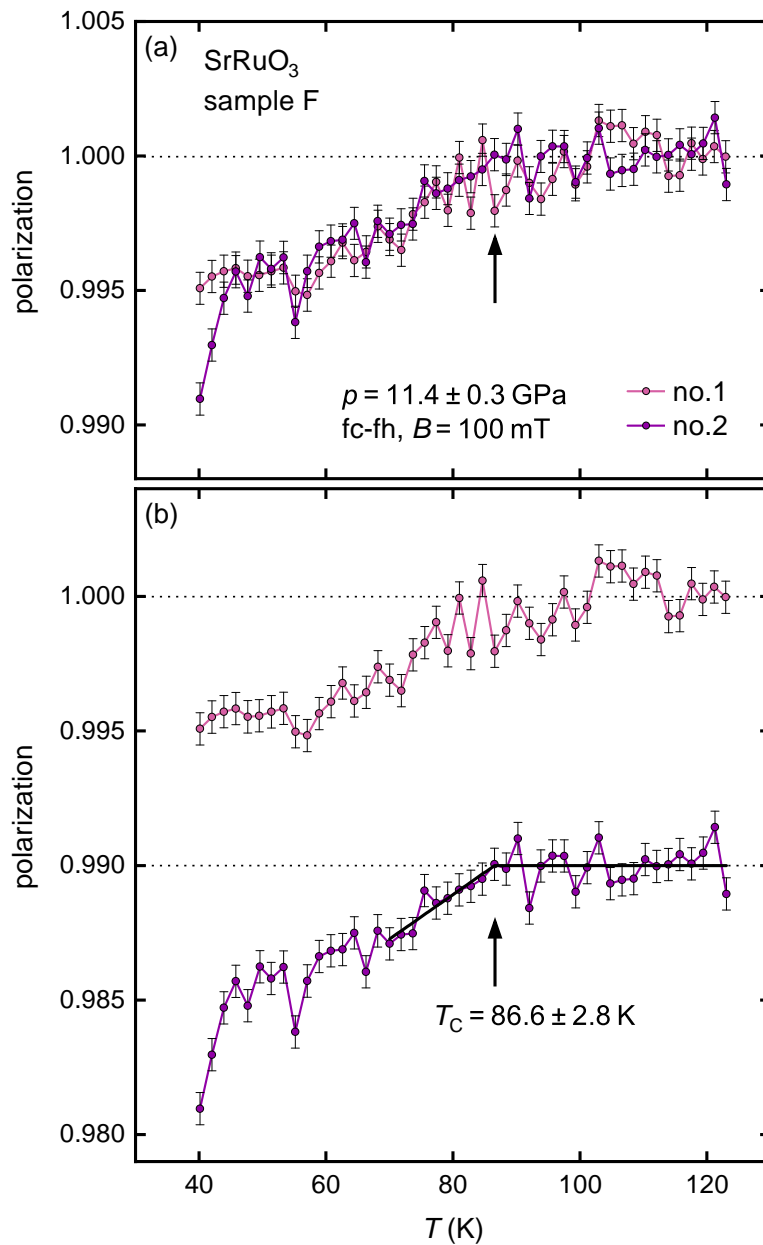


**Figure 4.9.:** ND temperature scans of SrRuO<sub>3</sub> sample F at a pressure of 11.4 GPa. The polarization was measured after field cooling at 100 mT and was repeated due to noise close to the onset of depolarization. The data in panel (b) is the same data as in (a) but with an artificial offset of 0.01 between the scans. From the second scan a Curie temperature of  $T_C = 86.6$  K could be determined by using a linear fit (black line).

Additionally, two temperature scans of sample F were measured at a pressure of 11.4 GPa which are shown in Fig. 4.9(a) on the same scale and (b) with a vertical offset of 0.01. Both scans were cooled in a field of 100 mT and measured during heating in the same field. The polarization of the first scan, labeled no.1, features a depolarization of 0.005 at base temperature and continuously increases towards 1. However, due to noise at temperatures above 80 K a determination of  $T_C$  was unfeasible. Therefore, the scan was repeated with the same set of parameters resulting in the curve labeled no.2. This second data set shows, apart from a sharp increase at 40 K due to the afterglow effect, less noise and a defined onset of depolarization. The Curie temperature  $T_C = 86.6$  K was determined using a linear fit which is shown as a black line in Fig. 4.9(b).

After increasing the pressure of sample F to 17.1 GPa a magnetic field scan was measured at 11 K which is shown in Fig. 4.10. When increasing the applied field the polarization decreases up to 150 mT where it starts to increase again. When decreasing the field the polarization decreases down to a field of 30 mT with a subsequent sharp increase towards zero field. No artifacts caused by the afterglow effect or the movement of the pressure cell were identified and the overall noise level is low. Thus, the error bars calculated from the statistical errors adequately describe the noise. The observed hysteresis is therefore significant indicating a FM ground state at 17.1 GPa.

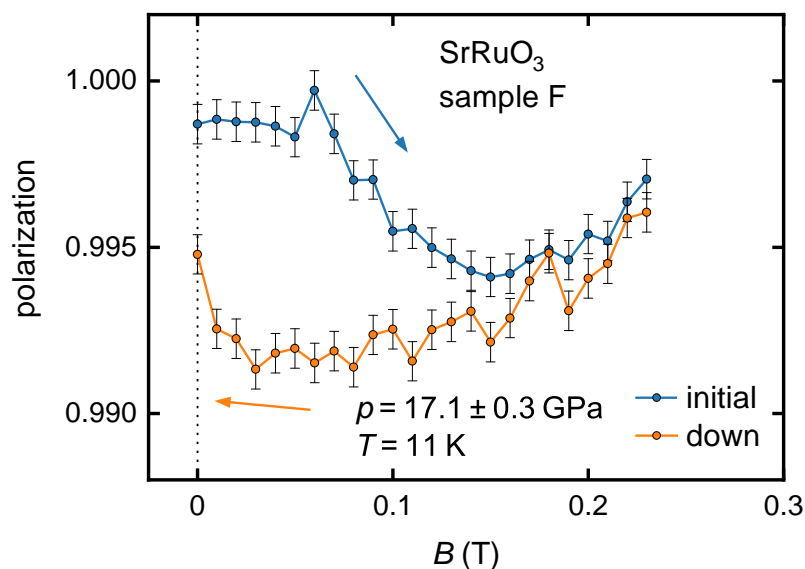


**Figure 4.10.:** Magnetic field scan at 11 K of SrRuO<sub>3</sub> sample F at a pressure of 17.1 GPa. After cooling the sample in zero field, the field was first increased to 0.23 T (blue symbols) and then again decreased to zero (orange symbols). Hysteresis is observed indicating FM behavior at this pressure.

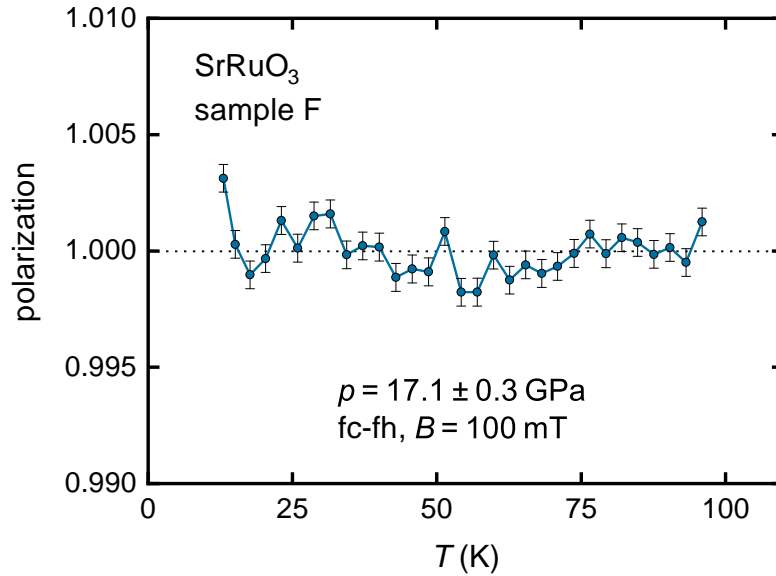


**Figure 4.11.:** ND temperature scan of SrRuO<sub>3</sub> sample F at a pressure of 17.1 GPa in an applied field of 100 mT. As no significant depolarization is observed  $T_C$  could not be determined.

Furthermore, a temperature scan of sample F at 17.1 GPa was measured from 13 to 96 K in a field of 100 mT after field-cooling. The temperature scan is shown in Fig. 4.11, however, no depolarization was observed. In a third beam time investigating sample G at pressures of 10.9 and 13.4 GPa several temperature and field scans were performed, however, no meaningful results could be obtained. The data of sample G is shown in appendix A.3.2.

### 4.3. Discussion

The results of the ND measurements on SrRuO<sub>3</sub> are summarized in the phase diagram shown in Fig. 4.12 which displays the Curie temperature  $T_C$  as a function of hydrostatic pressure  $p$ . The Curie temperatures derived from the ND temperature scans at 4.7, 9.0, and 11.4 K are depicted as red circles which are larger than the corresponding pressure and temperature errors. Additionally, the results of Hamlin *et al.* derived from susceptibility measurements [33] are shown as black circles. The values for  $T_C$  of both studies are in very good agreement confirming the linear decrease with a slope of  $\partial T_C / \partial p = -6.8$  K/GPa (black line) to at least 11.4 GPa.

Furthermore, diamond symbols indicate the pressures and temperatures at which magnetic field scans were performed using the HP-ND setup. A blue filling of the symbol

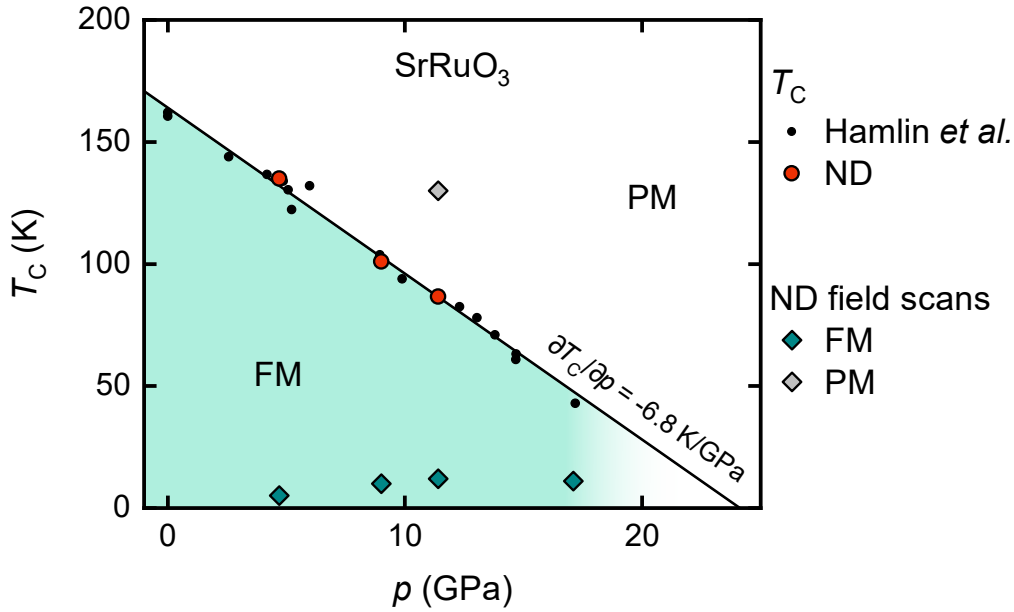


**Figure 4.12.:** Magnetic phase diagram of  $\text{SrRuO}_3$  as a function of pressure. The Curie temperature  $T_C$  obtained from ND temperature scans is depicted by red circles indicating the phase transition from the PM to the FM phase. Comparing the ND data to values of  $T_C$  from susceptibility measurements by Hamlin *et al.* [33] (black circles), who found a linear decrease of  $T_C$  with a slope of  $\partial T_C / \partial p = -6.8 \text{ K/GPa}$  (black line), results in a perfect agreement. Furthermore, diamond symbols indicate if a magnetic field scan at the respective temperature implied FM (blue filling) or PM (gray filling) behavior. The colored area below the black line refers to the FM phase, fading to white for pressures  $> 17.1 \text{ GPa}$  due to the unknown ground state in this pressure region.

depicts the observation of hysteresis in the polarization measurements implying the existence of FM, whereas a gray filling depicts a lack of hysteresis implying PM. Although no  $T_C$  could be found in the temperature scan at  $17.1 \text{ GPa}$ , the field sweep at this pressure indicates a FM ground state. The FM ground state is indicated by the green area below the black line which fades to white above  $17.1 \text{ GPa}$  symbolizing the so far unexplored region of the phase diagram.

The contradictory behavior of the temperature and field scans at  $17.1 \text{ GPa}$  – the temperature scan showing no FM transition and the field scan featuring hysteresis – can be explained by considering general differences between the two types of scans in combination with the polarization resolution of the instrument. In general, when using the HP-ND setup a field scan always features less noise compared to a temperature scan. This is a result of two facts: (1) The regulation of the power supply of the magnet is much more uniform and consistent compared to the temperature regulation. Therefore, the time between data points is almost constant in the case of a magnetic field scan leading

to a minimal afterglow effect. (2) A magnetic field scan is not affected by the vertical movement of the pressure cell as the temperature remains constant. Although there are cases where the focusing guides slightly moved out of alignment due to the applied field from the magnet, this change is much more abrupt compared to the gradual movement of a temperature scan and can therefore better be identified. As effects from the afterglow effect and from the temperature-induced vertical movement of the pressure cell are much smaller compared to a temperature scan under the same conditions, less noise is expected in the field sweeps. Furthermore, a depolarization smaller than 0.5%, as seen in the high-pressure measurements, is close to the maximum resolution of the HP-ND setup. Therefore, the increased level of noise in the temperature scan could be sufficient to mask any depolarization caused by the onset of FM order.

The lack of depolarization in the ND measurements of sample G (c. appendix A.3.2) can also be explained by limitations due to the resolution of the setup combined with a relatively small sample size. As the sample in the pressure cell is smaller than the cross-section  $A_{\text{beam}}$  of the neutron beam at the focal spot, the neutron beam cannot be completely depolarized. No direct measurements of  $A_{\text{beam}}$  are available, however, simulations of the setup by Jorba yield a diameter of the focal spot of 0.7 mm with a comparatively homogeneous intensity distribution [64]. As only the part of the neutron beam passing through the sample is depolarized, Eq. 2.7 can be written as

$$P = \left(1 - \frac{A_{\text{sample}}}{A_{\text{beam}}}\right) + \frac{A_{\text{sample}}}{A_{\text{beam}}} \exp\left(-\frac{1}{3}\gamma^2 \frac{d}{v^2} B_0^2 \delta\right) \quad (4.2)$$

with the cross-section of the sample  $A_{\text{sample}}$  and  $P_0 = 1$  for normalized measurements. When comparing the cross-sections of the investigated samples one notices that sample G is 3.3 times smaller than sample F. Thus, according to Eq. 4.2 the depolarization of sample G is expected to be about 3.3 times smaller as well. In the case of sample F at 11.4 GPa, which is similar to the pressures of sample G (10.9 and 13.4 GPa), a depolarization of 0.005 was measured. A reduction of this depolarization by a factor of 3.3 is too small to be resolved by the HP-ND setup explaining the ND measurements of sample G.

The cross-sections of the samples can be used to estimate the average domain size of SrRuO<sub>3</sub> samples under pressure which will be discussed in the following. Assuming a linear decrease of the magnetic moment with increasing pressure [161, 180, 188, 207] and using values of the unit cell volume from Ref. [187],  $B_0$  can be calculated as a function of pressure. Using the polarization values at base temperature from the temperature scans shown in Sec. 4.2 and solving Eq. 4.2 for  $\delta$  gives estimates of the average domain sizes. This results in values for  $\delta$  of 1.1, 3.2 and 1.1  $\mu\text{m}$  at pressures of 4.7, 9.0, and 11.4 GPa,

respectively. It is important to note that these values are only coarse estimates as, for example, the assumption of a random orientation of the domains is not fulfilled for SrRuO<sub>3</sub> [170] and only an estimate for the thickness of the sample of  $d = 70 \mu\text{m}$  can be given.

A study by Marshall *et al.* on SrRuO<sub>3</sub> thin films found a stripe-like pattern of the domains where the domain walls are oriented along the easy axis with a spacing of about 200 nm. The difference to the  $\mu\text{m}$ -sized domains found by the ND measurements may be explained by several factors: (1) If the easy axis is not perpendicular to the neutron beam the neutrons travel a longer distance in the domains resulting in a larger  $\delta$ . However, this can only explain a part of the increased  $\delta$  as a domain size in the order of  $\mu\text{m}$  would require an angle of  $11^\circ$  or smaller between the easy axis and the neutron beam. Although the orientation of the sample during the measurements cannot be recovered it seems unlikely that such an orientation was achieved in three consecutive measurements. (2) The shape anisotropy of the thin films can have a strong impact on the formation of the domains which, therefore, may differ from the domains of a bulk sample. (3) The assumptions leading to the derivation of Eq. 2.7 (c. Sec. 2.1.1.1) may be violated too strongly resulting in invalid estimates of  $\delta$ . A determination of the magnetic domain size in a SrRuO<sub>3</sub> bulk sample using, for example, the technique of small-angle neutron scattering could resolve this discrepancy.

## 4.4. Conclusions

In conclusion, the magnetic phase diagram of SrRuO<sub>3</sub> was investigated up to a hydrostatic pressure of 17.1 GPa using the ND technique. The FM ground state could be confirmed up to the highest pressure reached and the Curie temperature was traced up to 11.4 GPa. A linear decrease of  $T_C$  was observed which is in very good agreement with previous susceptibility measurements [33] and the considerations by Wohlfarth [3]. This suggests that the decrease of the Ru-O bond length with increasing pressure is the driving force behind the reduction of  $T_C$  as a change of  $T_C$  induced by a variation of the Ru-O-Ru angle would imply a cosine-like decrease of  $T_C$  [172].

Although the high-pressure region above 20 GPa could not be reached in this study it should, in principle, still be viable by using the existing HP-ND setup. For such an experiment the size of the sample in the pressure cell should be maximized in order to cover a large area of the focal spot of the neutron beam for a sufficiently large sample signal. Furthermore, instead of temperature scans, magnetic field scans should be measured at several different temperatures as the latter is generally more precise. This could answer the questions if the magnetism in SrRuO<sub>3</sub> can be suppressed to zero and if the phase

diagram features a continuous decrease of  $T_C$  or if a tricritical point exists as proposed by Belitz *et al.* [141]. In addition to the ND measurements further high-pressure studies on SrRuO<sub>3</sub> are prepared in our group including transport measurements as well as the novel technique of NV center magnetometry.

# 5. Ce-based Ferromagnetic Kondo Lattices

## 5.1. Introduction

Ce-based compounds often feature magnetically ordered ground states due to the electron configuration of the Ce atoms. As the difference of the 4f and 5d energy levels is relatively small, it can be energetically favorable to raise one electron from a localized 4f orbital into the 5d conduction band resulting in an unpaired 4f electron and, therefore, a net magnetic moment. These localized magnetic moments can interact with the 5d conduction electrons leading to long-range magnetic order mediated by the RKKY interaction. As the sign of the RKKY interaction oscillates with the Ce-Ce distance, both FM and AFM are possible ground states.

Another magnetic interaction in Ce resulting from the hybridization of 4f moments and conduction electrons is the Kondo effect. At low temperatures the conduction electrons couple antiferromagnetically to the magnetic moments and effectively shield them. This mechanism was proposed by Kondo in 1964 in order to describe the anomalous resistivity minimum at low temperatures measured in dilute magnetic alloys [208]. Below the Kondo temperature  $T_K$  the screening of the magnetic moments gradually sets in and develops at low temperatures into a singlet state consisting of a 4f and a 5d electron. The singlet can be described in Landau FL theory as a fermionic quasiparticle similar to an electron but with a drastically enhanced effective mass (100 to 1000 electron masses) [209]. The resulting heavy fermion (HF) behavior often gives rise to exotic phases such as unconventional superconductivity [210–212].

In Ce-based compounds usually both magnetic effects, the inter-site RKKY interaction and the on-site Kondo effect, exist [213]. While the RKKY interaction favors magnetic order, the Kondo effect tends to quench the magnetic moments resulting in a non-magnetic ground state. The interplay of both interactions can be described by the Kondo lattice (KL) model developed by Doniach in 1977 [36]. As both effects arise from the interaction of the magnetic moments with the conduction electrons, they mainly scale with the product

$|\Gamma n(E_F)|$  where  $\Gamma$  is the coupling constant between the 4f and the conduction electrons, and  $n(E_F)$  is the density of states at the Fermi level. Furthermore, the coupling constant is given by

$$\Gamma = \frac{2|V|^2}{E_{4f} - E_F} \quad (5.1)$$

where  $V$  is the hybridization integral between the 4f and the conduction electrons [214].  $E_{4f}$  and  $E_F$  are the energy level of the 4f electrons and the Fermi energy, respectively. As  $V$  depends primarily on the inter-atomic distances it follows that hydrostatic and chemical pressure are suitable tools to tune  $|\Gamma n(E_F)|$  [215].

The relevant temperature scales in the KL model are the RKKY temperature  $T_{\text{RKKY}} \propto |\Gamma n(E_F)|^2$  and the Kondo temperature  $T_{\text{K}} \propto \exp(-1/|\Gamma n(E_F)|)$  which are both plotted in Fig. 5.1 as a function of  $|\Gamma n(E_F)|$ . At small  $|\Gamma n(E_F)|$  the RKKY interaction outweighs the Kondo effect while at larger  $|\Gamma n(E_F)|$  the Kondo effect predominates. This results in a characteristic dome-shaped phase of magnetic order defined by  $T_{\text{MO}}$ , terminating in a second order QCP at a critical  $|\Gamma n(E_F)|$ . Beyond the QCP the Kondo singlet formation causes HF behavior which manifests itself in Fermi liquid (FL) behavior up to a coherence

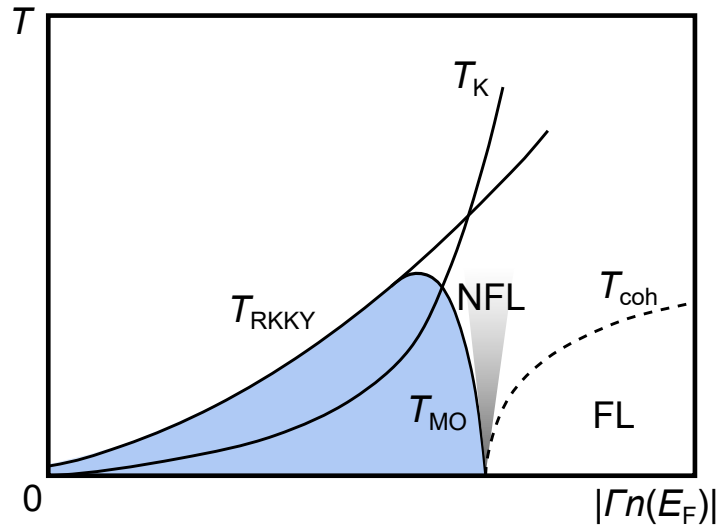


**Figure 5.1.:** Doniach's phase diagram resulting from the competition of Kondo effect and RKKY interaction [36]. The Kondo temperature  $T_{\text{K}}$  and the RKKY temperature  $T_{\text{RKKY}}$  are shown as a function of  $|\Gamma n(E_F)|$  where  $\Gamma$  is the magnetic exchange coupling between 4f and 5d electrons, and  $n(E_F)$  is the density of states at the Fermi level. If  $T_{\text{RKKY}} > T_{\text{K}}$  a phase of long range magnetic order exists below a magnetic ordering temperature  $T_{\text{MO}}$ . In the other case, when the Kondo effect is stronger than the RKKY interaction, the Kondo effect completely suppresses any magnetic order. Instead, FL behavior is found below a coherence temperature  $T_{\text{coh}}$ .

temperature  $T_{\text{coh}}$  [216, 217]. Close to the QCP non-FL (NFL) behavior is observed over a large temperature range [210, 218].

Notable examples for FM Kondo lattices are  $\text{CeRuPO}$  [219],  $\text{CeRu}_2\text{Ge}_2$  [220],  $\text{CeSi}_{1.81}$  [12],  $\text{CeAgSb}_2$  [221],  $\text{CePd}_{1-x}\text{Rh}_x$  [11], and  $\text{CePt}$  [222]. The two last mentioned compounds can be driven across a QPT, however, using different mechanisms: alloying in the case of  $\text{CePd}_{1-x}\text{Rh}_x$  and hydrostatic pressure in the case of  $\text{CePt}$ . In  $\text{CePd}_{1-x}\text{Rh}_x$  the process of alloying exerts chemical pressure but also introduces disorder into the system which significantly changes the magnetic ground state close to the QPT. Westerkamp *et al.* proposed the Kondo cluster glass model for  $\text{CePd}_{1-x}\text{Rh}_x$  where loosely coupled, FM ordered clusters survive in a sea of Kondo-screened magnetic moments [11]. The interesting time and length scales of the FM clusters initiated a ND study of  $\text{CePd}_{1-x}\text{Rh}_x$  by Schmakat *et al.* which was continued by the author of this thesis [73].

In contrast,  $\text{CePt}$  is assumed to show a clean QPT [142]. The magnetic phase diagram of  $\text{CePt}$  is only determined by resistivity and susceptibility measurements so far [37, 223]. However, a direct measurement of the magnetization at high pressures is still lacking due to the technical difficulties involved and is required for a confirmation of the phase diagram. Therefore, a ND study of  $\text{CePt}$  under high pressures was performed in order to (i) confirm the magnetic phase diagram and (ii) compare the results with the ND study of  $\text{CePd}_{1-x}\text{Rh}_x$  with a focus on the length and time scales of the detected FM order.

The remaining chapter is structured as follows: In Sec. 5.2, after a brief introduction to the  $\text{CePd}_{1-x}\text{Rh}_x$  doping series, the ND results of  $\text{CePd}_{1-x}\text{Rh}_x$  are presented and discussed. In a similar fashion Sec. 5.3 features an introduction to  $\text{CePt}$ , the results of ND measurements on  $\text{CePt}$  and a subsequent discussion. Finally, a conclusion is given in Sec. 5.4 with a comparison of the studies on  $\text{CePd}_{1-x}\text{Rh}_x$  and  $\text{CePt}$ .

## 5.2. Neutron Depolarization Study of $\text{CePd}_{1-x}\text{Rh}_x$

### 5.2.1. Introduction to $\text{CePd}_{1-x}\text{Rh}_x$

The pseudo-binary compound  $\text{CePd}_{1-x}\text{Rh}_x$  crystallizes in the CrB structure for all Rh-concentrations  $x$  and evolves from an Ising-like FM on the CePd side to a non-magnetic intermediate-valence ground state on the CeRh side [101, 224]. The FM ordering temperature decreases continuously from  $T_C = 6.6$  K at  $x = 0$  to zero at  $x_c = 0.87$  as can be seen in Fig. 5.2.  $T_C$  was determined from susceptibility  $\chi'(T)$ , magnetization  $M(T)$ , specific heat  $C(T)$ , thermal expansion  $\beta(T)$ , and ND  $P(T)$  measurements. An interesting feature of the phase boundary is the change from a negative to a positive curvature at  $x^* = 0.6$  resulting in a FM tail region of the phase diagram. The Kondo temperature  $T_K \approx \Theta_p/2$ ,

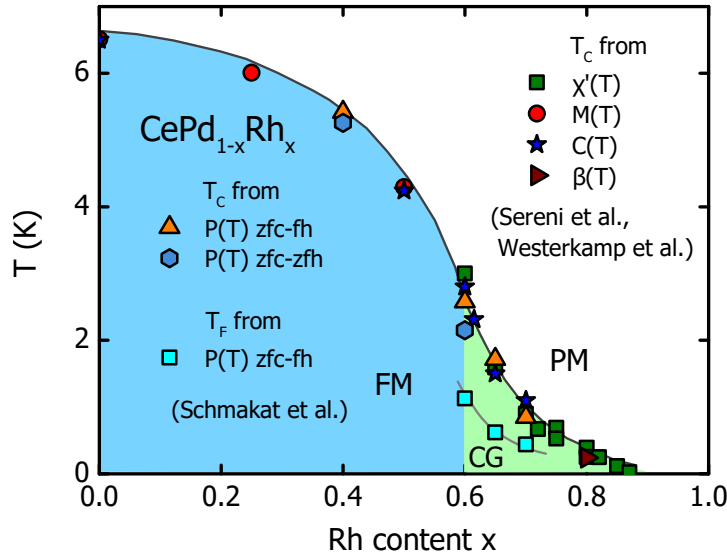


**Figure 5.2.:** Magnetic phase diagram of the FM Kondo lattice  $\text{CePd}_{1-x}\text{Rh}_x$  compiled using different techniques.  $T_C$  was determined from the measurements of the susceptibility  $\chi'(T)$ , magnetization  $M(T)$ , specific heat  $C(T)$  and thermal expansion  $\beta(T)$  [100, 101] as well as ND measurements  $P(T)$  [84].  $T_C$  decreases continuously with increasing  $x$ , however, a tail region develops for  $x > 0.6$  where the FM turns into a cluster glass state. An additional feature at temperatures labeled as  $T_F$  was observed in the tail region using the ND technique where the clusters freeze in a random constellation. Figure taken from [84].

determined from the paramagnetic Weiss temperature  $\Theta_p$ , stays almost constant until  $x^*$  and then increases rapidly for higher Rh concentrations indicating stronger Kondo interactions. The decrease of  $T_C$  in the region  $x < x^*$  can be explained in the framework of the Doniach model where  $\Gamma$  (c. Eq. 5.1) increases due to chemical pressure but also due to a shift of the Fermi level [225, 226].

The magnetic ground state in the tail region of the phase diagram is governed by disorder and can be explained by the Kondo cluster glass model by Westerkamp *et al.* [11]. Due to disorder introduced by doping, the local Kondo temperature can deviate strongly from the average. When decreasing the temperature from the PM state below the average Kondo temperature, regions of thermally fluctuating spins exist surrounded by Kondo-screened moments. Below a temperature called  $T_{\text{cluster}}$  a FM short-range interaction between the unscreened moments establishes. However, these FM clusters are still fluctuating similar to a superparamagnet. Further decreasing the temperature to  $T_C$  leads to a long-range FM interaction between the clusters. For Rh concentrations  $x > 0.70$  unusual spin glass behavior has been observed where the low temperature properties are dominated by a slow freezing transition. Therefore, the name “Kondo cluster glass” was introduced by Westerkamp *et al.* to describe this unique ground state.

The size of the FM clusters decreases continuously with increasing Rh concentration due to increasing Kondo screening. In the region  $0.8 \leq x \leq 0.87$  the clusters are estimated to consist of about 5 spins on average [11]. As the ND technique is sensitive to fluctuating forms of FM and small domain sizes (c. Sec. 2.1.1.2), which are both present in  $\text{CePd}_{1-x}\text{Rh}_x$ , Schmakat *et al.* [20, 84] and the author of this thesis performed NDI measurements on  $\text{CePd}_{1-x}\text{Rh}_x$  samples with Rh concentrations of 0.40, 0.60, 0.65, and 0.70 in order to verify the Kondo cluster glass model.

### 5.2.2. Experimental Results

The results on  $\text{CePd}_{1-x}\text{Rh}_x$  were mainly obtained at the imaging beam line ANTARES at the Maier-Leibnitz Zentrum, Garching, using the standard ND setups described in Sec. 2.1.2; however, one data set was measured at the beam line POLI at the Maier-Leibnitz Zentrum using the CryoPAD setup. A description of the latter can be found in Ref. [227]. Details on the investigated  $\text{CePd}_{1-x}\text{Rh}_x$  samples are given in Sec. 2.3.2. Parts of the data shown in this section were measured and interpreted by Schmakat in the framework of his PhD thesis [84] and are included here to illustrate the overall picture of  $\text{CePd}_{1-x}\text{Rh}_x$  derived from ND measurements.

The left column of Fig. 5.3 shows  $T_C$ -maps of the samples with Rh concentrations (a1)  $x = 0.40$ , (b1)  $x = 0.60$ , and (c1)  $x = 0.65$  with the corresponding histograms in the right column. The  $T_C$ -distributions were fitted with a gaussian distribution where the values given in the histogram plots are the center and the FWHM  $\Delta T_C$  of the gaussian. The average  $T_C$  decreases with increasing  $x$  as expected from the phase diagram. Furthermore, the width of the distribution  $\Delta T_C$  increases with increasing  $x$  which could be a signature of the increasing disorder introduced by the chemical substitution. However, no regions with significantly different  $T_C$  appear in the  $T_C$ -maps suggesting metallurgically homogeneous samples.

Fig. 5.4 shows ND data from temperature scans measured for the samples with  $x = 0.40$ ,  $x = 0.60$ , and  $x = 0.65$ . After cooling down the samples in external fields of 7.5, 15.0, and 22.5 mT the ND data was acquired during heating in the same field (field-cooled field-heated, fc-fh). Additionally, a temperature scan cooled in zero field and also measured in zero field (zfc-zfh) was performed for each sample.

The zfc-zfh measurement of the sample with  $x = 0.40$  shows a sharp drop of the polarization at  $T_C$  as expected of a FM with rather large domains in zero or weak magnetic field. The applied magnetic fields lead to a small enhancement of the depolarization. In contrast, for the sample with  $x = 0.60$  the application of small fields changes the polarization much more drastically from 0.7 in zero field to 0.2 in a field of 7.5 mT. The

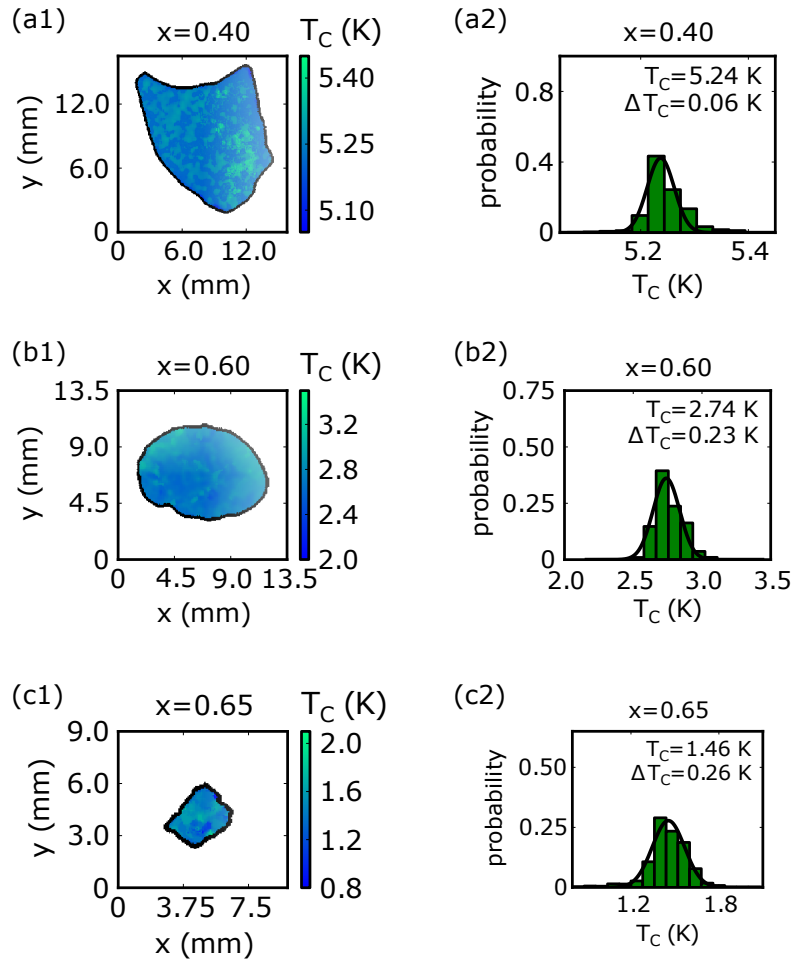


**Figure 5.3.:** NDI results of three  $\text{CePd}_{1-x}\text{Rh}_x$  samples with Rh concentrations (a)  $x = 0.40$ , (b)  $x = 0.60$ , and (c)  $x = 0.65$ . The left column shows the  $T_C$ -maps with the color bar beside each map decoding the transition temperature  $T_C$ . The histograms in the right column illustrate the corresponding distribution  $\Delta T_C$  (FWHM) of the transition temperatures. Figure adapted from Ref. [84].

shape of the curve measured without external field resembles the case where small domains and/or weak internal fields are assumed. Almost no depolarization is observed in case of the sample with  $x = 0.65$  when no field is applied. Remarkably, the application of small fields leads again to a depolarization which can be described by a weak form of FM. This infers that the external fields stabilize and amplify the FM ground state.

Furthermore, NDI measurements were performed after zero-field cooling as well as field-cooling during the controlled heating with an applied field. Fig. 5.5 shows ND data from zfc-fh and fc-fh measurements of  $\text{CePd}_{1-x}\text{Rh}_x$  samples with the Rh concentrations  $x = 0.40$ ,  $x = 0.60$ ,  $x = 0.65$ , and  $x = 0.70$ , respectively. The zfc-fh measurements show a behavior which mimics the zfc-zfh curves at lowest temperatures, drops to a lower

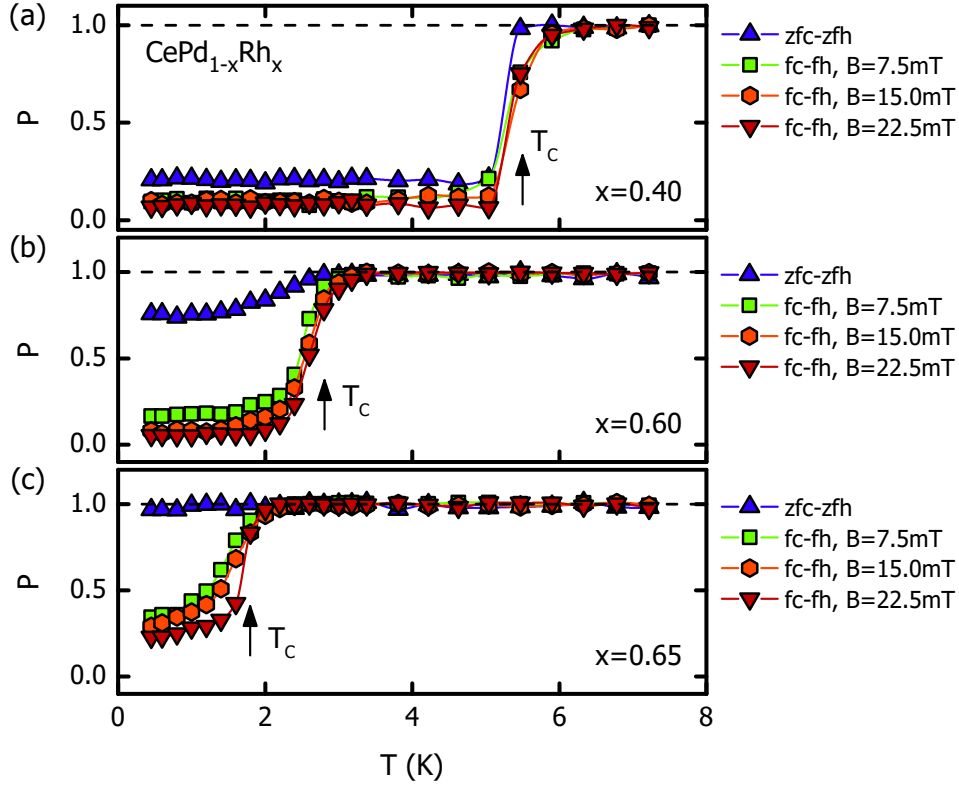


**Figure 5.4.:** Neutron polarization as a function of temperature for  $\text{CePd}_{1-x}\text{Rh}_x$  samples with Rh content (a)  $x = 0.40$ , (b)  $x = 0.60$ , and (c)  $x = 0.65$ . For each concentration  $x$  four data sets were measured in external magnetic fields of  $B = 0$ ,  $B = 7.5$  mT,  $B = 15.0$  mT and  $B = 22.5$  mT after cooling in the same field, respectively. The polarization below  $T_C$  decreases with increasing field  $B$  while the phase transition smears out.  $T_C$  for each Rh content  $x$  is determined from the zero-field measurement and is indicated by an arrow. Figure adapted from Ref. [84].

polarization at a temperature marked as  $T_F$ , and then follows the the fc-fh measurement to higher temperatures. This behavior is similar for all investigated samples and the temperature window from  $T_F$  to  $T_C$  is shifted to lower temperatures.

Due to its orthorhombic crystal structure,  $\text{CePd}_{1-x}\text{Rh}_x$  is highly anisotropic and features an easy axis for the magnetization along the  $c$  axis. If the majority of the domains in a single crystal points parallel or antiparallel along one axis, the assumption of a random constellation of domains in a ND experiment is not fulfilled. In order to explore the effects of an easy magnetization axis on ND measurements a  $\text{CePd}_{1-x}\text{Rh}_x$  single crystal with a Rh concentration of  $x = 0.40$  was investigated using two different neutron polarization analysis setups. The first setup uses the CryoPAD option of the instrument POLI at the FRM II which utilizes coupling coils (similar to a Mezei-type spin-flipper) to rotate the polarization vector in any direction with respect to the sample orientation. The second setup was the NDI setup at ANTARES as described in Sec. 2.1.2.3.

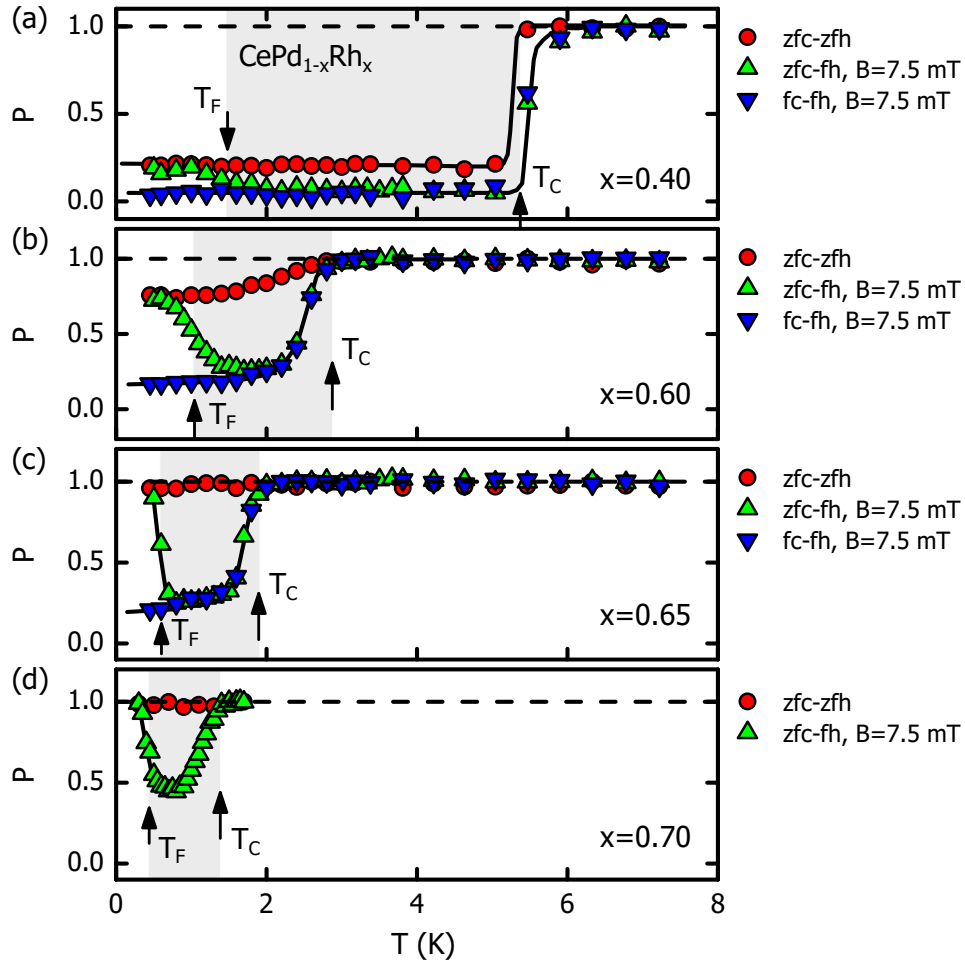


**Figure 5.5.:** Zfc-zfh and zfc-fh data from the measurements of  $\text{CePd}_{1-x}\text{Rh}_x$  samples with Rh concentrations  $x = 0.40$ ,  $x = 0.60$ ,  $x = 0.65$ , and  $x = 0.70$ , respectively. The zfc-fh scans were performed by cooling the samples in zero field, applying a field of 7.5 mT, and measuring during heating. Increasing the temperature leads to a decrease of the polarization until it reaches the fc-fh curve with the center of this drop in polarization being labeled as  $T_F$ . This transition can be interpreted as a freezing temperature of the FM clusters. Figure adapted from Ref. [84].

Fig. 5.6 shows the results obtained from zero-field measurements at POLI. The polarization was measured both above and below  $T_C$  and rotated (a) in the a-c plane of the sample described by the angle  $\Theta$  and (b) in the a-b plane described by  $\chi$ . The polarization shows sinusoidal behavior where the maxima and minima align with the crystallographic axes of the sample. Almost no depolarization is observed when the polarization vector is parallel to the c axis. This can be explained by an arrangement of domains where the domains primarily point parallel or antiparallel to the c axis. When the neutron spins are (anti)parallel to the fields  $B_0$  in the domains, no Larmor phase is acquired and, therefore, the neutron beam is not depolarized.

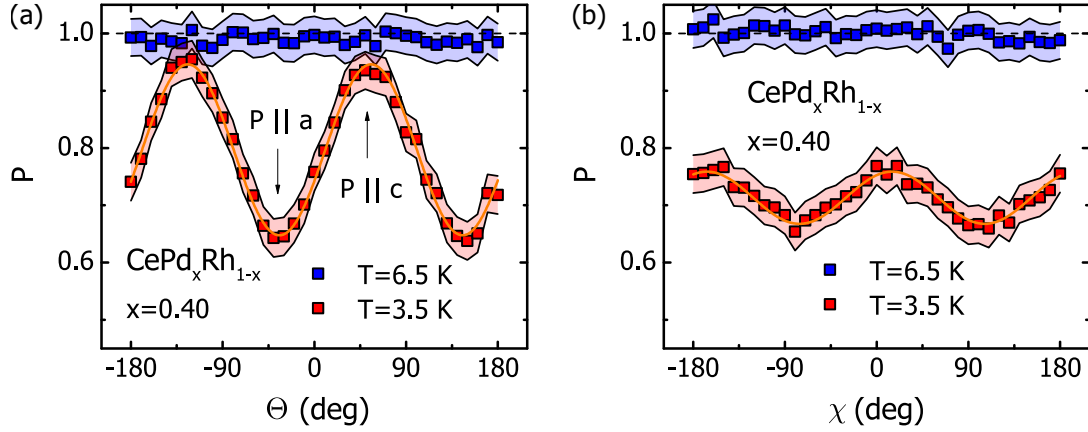


**Figure 5.6.:** Anisotropic behavior of the depolarization for a single crystal of  $\text{CePd}_{1-x}\text{Rh}_x$  with Rh concentration  $x = 0.40$ . For the measurements the polarization vector was rotated (a) in the a-c plane and (b) in the a-b plane of the sample with the rotation being described by the angles  $\Theta$  and  $\chi$ , respectively. The oscillation in the measurements below  $T_C$  is caused by the collinear orientation of the magnetic moments along the c-direction resulting in almost no depolarization for  $P \parallel c$ . Figure adapted from Ref. [84].

In the next step the effect of an applied field on this Ising-like FM was investigated using the 1d NDI setup and the same  $\text{CePd}_{1-x}\text{Rh}_x$  single crystal with  $x = 0.40$ . In zero field the sample tries to minimize its stray field which leads to an equal amount of domains pointing parallel (up) and antiparallel (down) to the c axis. An external field with a non-zero component along the c axis changes the ratio of domains pointing up or down resulting in an effective field  $B_{\text{int}}$  in the sample parallel to c. If the polarization is not aligned with the easy axis and a small field is applied, the polarization is affected by two effects simultaneously. On the one hand, the polarization is decreased due to the FM constellation of domains. On the other hand, the direction of the polarization changes as the polarization vector precesses around  $B_{\text{int}}$ . In general, both effects vary the polarization signal and cannot be measured separately with a 1d ND setup.

The magnitude of  $B_{\text{int}}$  is expected to increase when a stronger external field is applied. Thus, also the collected Larmor phase of the polarization increases. When continuously changing the external field, the rotation of the polarization caused by  $B_{\text{int}}$  results, therefore, in an oscillation of the polarization signal. Furthermore, the magnitude of  $B_{\text{int}}$  can also be affected by the temperature due to the temperature dependence of the magnetization, which can again result in an oscillation of the polarization signal. Summarized, when the easy axis of a FM single crystal is adjusted at an angle to the polarization vector in a 1d ND setup, the polarization signal can feature oscillations.

These oscillations were observed in NDI measurements of the  $\text{CePd}_{1-x}\text{Rh}_x$  single crystal with a Rh concentration of  $x = 0.40$  close to  $T_C$ . The crystal was oriented at an

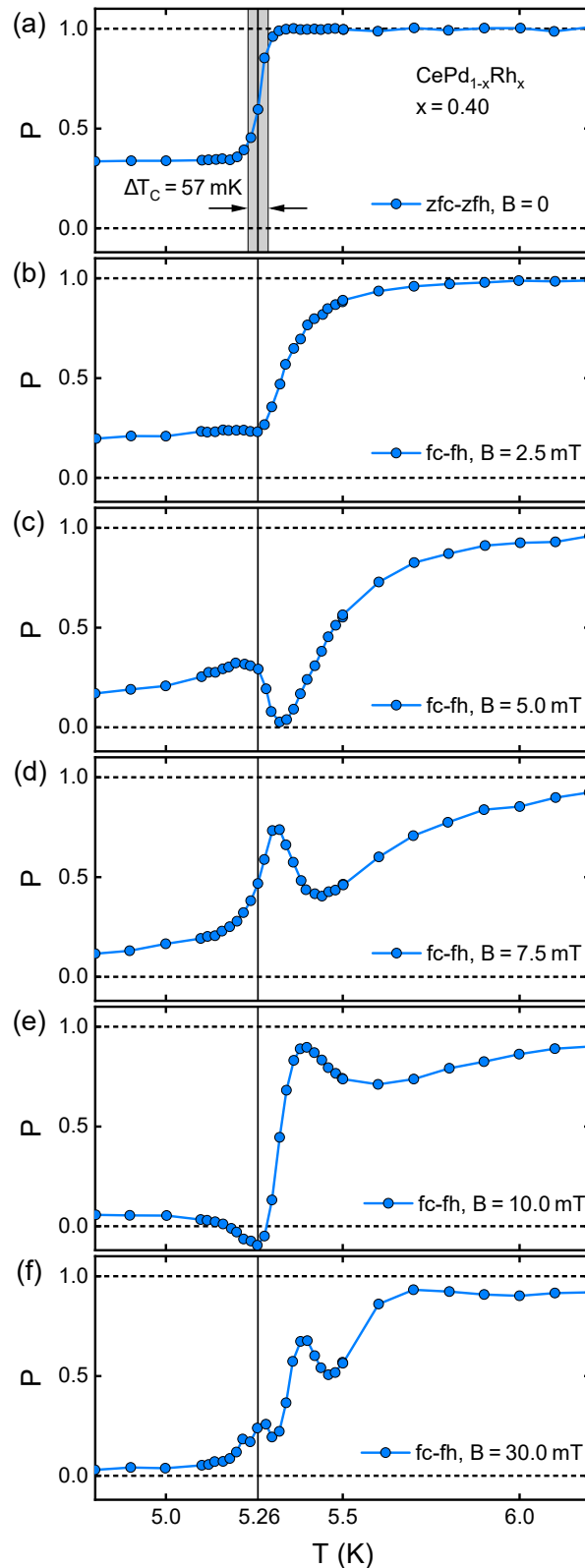


**Figure 5.7.:** Comparison of several fc-fh temperature scans for different magnetic fields of a  $\text{CePd}_{1-x}\text{Rh}_x$ ,  $x = 0.40$  single crystal. Applying small fields leads to a decrease of the polarization well above the ordering temperature  $T_C = 5.26$  K determined from the zfc-zfh scan. Additionally, oscillations close to  $T_C$  appear in the polarization signal if small fields are applied. The width of the transition as determined from a fit of Eq. 2.9 convoluted with a gaussian distribution to the zf data is  $\Delta T_C = 57$  mK. Figure adapted from Ref. [73].

angle of approximately  $\alpha = 45$  deg to the polarization vector. Fig. 5.7 shows temperature scans with different applied fields ranging from zero to 30 mT. The zero-field measurement shows a sharp drop at  $T_C = 5.26$  K and is in good agreement with the data shown in Figs. 5.4 and 5.5. Applying small fields shifts the onset of depolarization to higher temperatures and smears the phase transition. Additionally, oscillations in the polarization signal are observed in the temperature range around the phase transition. The negative polarization in the scan with a field of 10 mT is a clear indicator for a rotation of the polarization, excluding depolarization effects as a cause for the observed oscillations.

Similar oscillations also appear in field sweeps at temperatures above  $T_C$  as shown in Fig. 5.8. The frequency of the oscillations increases with decreasing temperature. Below  $T_C$  small fields of 20 mT are already sufficient to completely depolarize the neutron beam. The frequency and amplitude of the oscillations were extracted by fitting the ND data with a gaussian-damped cosine function.

### 5.2.3. Discussion of CePd<sub>1-x</sub>Rh<sub>x</sub>

The ND measurements confirm the magnetic phase diagram of CePd<sub>x-1</sub>Rh<sub>x</sub> up to a Rh concentration of  $x = 0.70$  and verify the FM nature of the ground state. The results shown in Figs. 5.4 and 5.5 can be explained in the framework of the Kondo cluster glass model [11] apart from a minor extension of this model, required to interpret the freezing transition at  $T_F$ .

Almost no depolarization is observed for  $x \geq 0.65$  while the application of small fields results in depolarization. This implies that the FM clusters are either too small or fluctuate too fast and, therefore, do not depolarize the neutron beam. Considering the time and length scale resolution of the NDI setup (c. Sec. 2.1.1.2), and previous results [100] on CePd<sub>1-x</sub>Rh<sub>x</sub>, an increase of the average domain size at  $T_F$  is the only explanation for the observed behavior. Therefore, the zfc state of samples in the tail region of the phase diagram are resembled by an ensemble of small FM clusters. Estimations of the cluster size from ND measurements are in the order of 5 nm which is in good agreement with estimations from Westerkamp *et al.* [100].

The decrease of depolarization towards larger  $x$  implies a decrease of the average cluster size. However, small magnetic fields enhance the depolarization significantly. This suggests that the Kondo-screened moments directly surrounding the FM clusters are reactivated (unscreened) by the magnetic field and, hence, increase the cluster size. Fig. 5.9 illustrates this behavior and shows the magnetic ground state of CePd<sub>1-x</sub>Rh<sub>x</sub> samples in the zero-field-cooled state (panels (a)-(c)) and in the field-cooled state (panels (d)-(f)). The Rh concentration  $x$  increases from top to bottom, i.e. the top panels (a) and (d) show

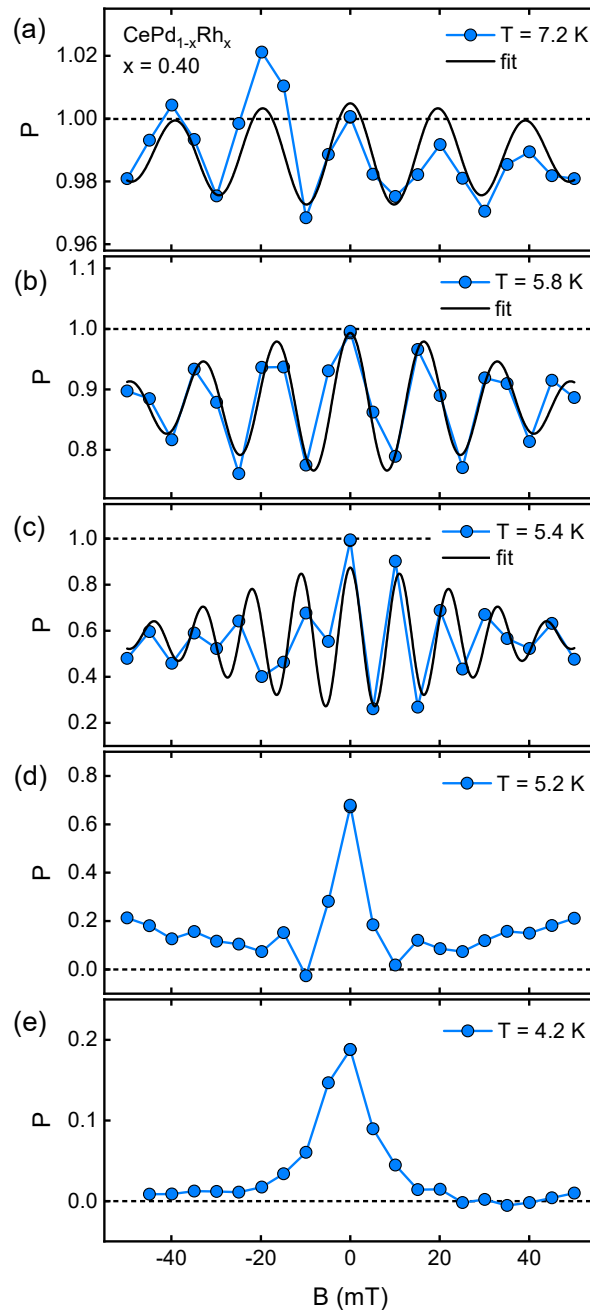


**Figure 5.8.:** Field scans of the  $\text{CePd}_{1-x}\text{Rh}_x$  sample with  $x = 0.40$  for different temperatures. An oscillation in the depolarization signal is visible for temperatures higher than  $T_C = 5.26$  K. The oscillations were fitted using a gaussian-damped cosine function. Figure adapted from Ref. [73].

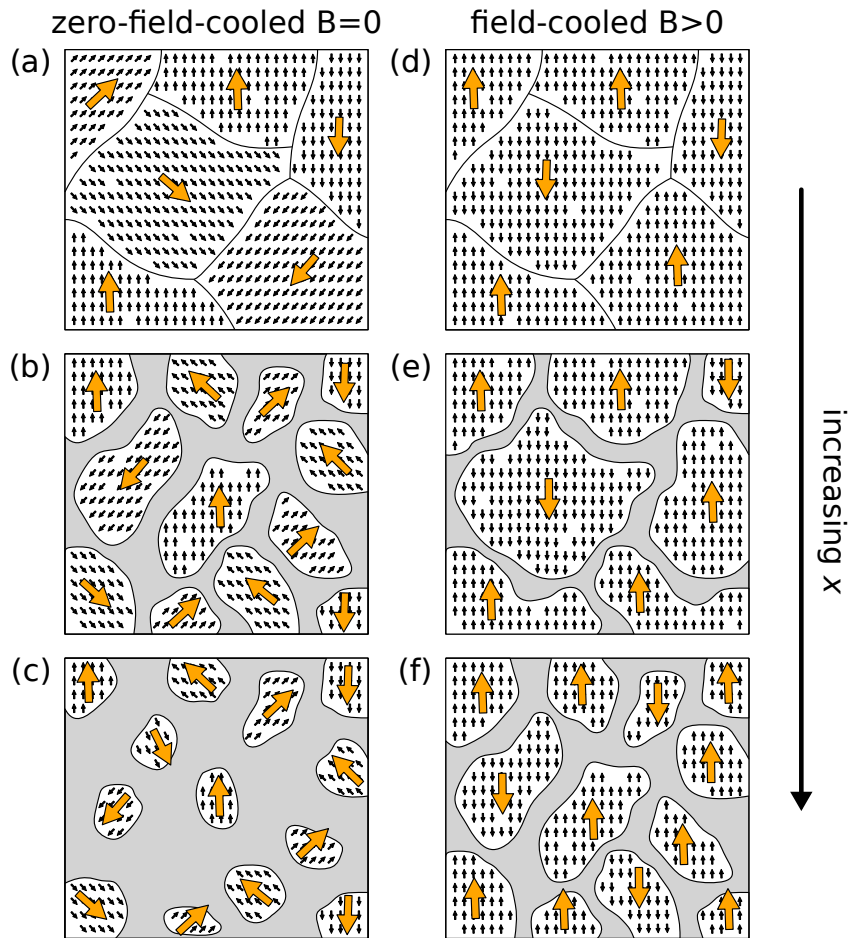


**Figure 5.9.:** Illustration of the transformation from a FM to a cluster glass in  $\text{CePd}_{1-x}\text{Rh}_x$  with increasing  $x$  for the zero-field-cooled (left column) and field-cooled case (right column), respectively. FM ordered domains are shown as white areas containing arrows (magnetic moments) while Kondo-screened parts are shown in gray. With increasing  $x$  the FM domains decrease in size and are surrounded by a sea of Kondo-screened moments. Applying a magnetic field during cooling increases the average cluster size. Figure adapted from Ref. [84].

a FM sample with low  $x$ , while the panels (c) and (f) show a sample in the tail region of the phase diagram.

Furthermore, the effects of a strong magnetic anisotropy on the polarization signal were investigated. The polarization data on a single-crystalline sample from the experiment at POLI suggests that the magnetic domains orient themselves mostly along the magnetic easy axis of the system, comparable to a 3d Ising FM, which is consistent with earlier magnetization measurements [99].

Modeling the FM order with domains pointing either parallel or antiparallel to the easy axis predicts oscillations in the polarization signal when magnetic fields are applied

to the single-crystalline sample as explained in the previous Sec. 5.2.2. These oscillations were observed close to  $T_C$  in temperature and field scans of a  $\text{CePd}_{1-x}\text{Rh}_x$  single crystal with  $x = 0.4$ .

As CePt crystallizes in the same CrB structure [228] as  $\text{CePd}_{1-x}\text{Rh}_x$  and also features an easy axis along the crystallographic  $c$  direction [68], a comparative ND study on CePt was performed. Despite the different control parameters – chemical pressure in the case of  $\text{CePd}_{1-x}\text{Rh}_x$  and hydrostatic pressure for CePt – the presented ND results on  $\text{CePd}_{1-x}\text{Rh}_x$  are a good foundation for the interpretation of the measurements on CePt.

## 5.3. Neutron Depolarization of CePt under Pressure

### 5.3.1. Introduction to CePt

At ambient pressure CePt orders ferromagnetically below  $T_C = 5.9\text{ K}$  [229, 230] with a magnetic moment of  $\mu = 1.39\ \mu_B$  [68, 231] per Ce ion. The magnetic moment is greatly reduced compared to the free ion value of Ce  $\mu_{\text{Ce}} = 2.54\ \mu_B$  which can be explained by crystal electric field effects and the Kondo effect [222]. Due to its orthorhombic structure CePt is highly anisotropic resulting in a collinear FM arrangement of the magnetic moments along the  $c$  axis [68, 232]. Next to the reduction of the magnetic moment, the Kondo effect is also observed as characteristic negative slopes in electrical resistivity measurements [231, 233, 234] and in specific heat measurements [235].

As CePt is one of the few FM Kondo lattices, it is of particular interest if the phase diagram predicted by Doniach is also observed in this compound. The parameter  $|Tn(E_F)|$  defining Doniach's phase diagram can be changed by hydrostatic or chemical pressure. Due to its simplicity compared to hydrostatic pressure, a large number of doping studies was performed [68, 222, 232, 236–248] mainly focusing on the alloying series  $\text{CeNi}_x\text{Pt}_{1-x}$  and related compounds. The enhanced Pauli PM CeNi is an intermediate-valence compound close to magnetism and crystallizes in the same CrB structure as CePt [249], suggesting a QPT at a finite Ni concentration  $x$ . The phase diagram of  $\text{CeNi}_x\text{Pt}_{1-x}$  features a dome-shaped FM phase which is suppressed at a critical concentration of  $x_C = 0.9$  [222]. This behavior is mainly caused by the volumetric effect of chemical doping since intermediate-valence states are only prominent for  $x \geq 0.95$  [240, 245, 246]. Further alloying studies [68, 232, 237, 238, 240–243, 247], partially also including the application of low hydrostatic pressures [236, 239], can all be well described in the picture of the Kondo lattice model.

The first high-pressure study on pure CePt was performed by Itoh *et al.* measuring the electrical resistivity up to a pressure of 3.2 GPa [233].  $T_C$  increases with increasing pressure and matches the phase diagram of  $\text{CeNi}_x\text{Pt}_{1-x}$  very well when  $p$  and  $x$  are converted to a

relative volume change. Due to the quantitative agreement the behavior of  $T_C$  is explained by the one-parameter Kondo lattice model: A pressure-induced band widening of the Ce 5d band results in a decrease of  $E_F$ , therefore, increasing  $\Gamma$  (c. Eq. 5.1) and  $T_C$  as well.

An in-depth study by Larrea *et al.* [37] measuring the electrical resistivity  $R$  and the susceptibility  $\chi$  of CePt extended the pressure range up to 14.6 GPa. Their obtained phase diagram of CePt is shown in Fig. 5.10. The Curie temperature  $T_C$  determined from features in  $R(T)$  and  $\chi(T)$  increases up to a pressure of  $\sim 9$  GPa and then drops rapidly to zero at  $p_C = 12.1$  GPa. The temperature dependence of  $R$  in the FM phase is interpreted by a model based on soft 2d spin wave modes [223]. At pressures above  $p_C$  the resistivity shows a  $\propto T^2$  dependence up to a coherence temperature  $T_{\text{coh}}$  suggesting FL behavior. Additionally, a linear temperature dependence over two decades of  $T$  was measured at pressures close to  $p_C$  indicating NFL behavior between the FM phase and the FL phase.

The phase diagram is in very good agreement with Doniach's Kondo lattice model and, therefore, strongly suggests a second order QPT. However, this is still under debate as recent theoretical studies generally predict a first order QPT for clean FMs [142] and the quick decrease of  $T_C$  for  $p > 10$  GPa – although consistent with Doniach's phase diagram – may look more like a first order QPT [2]. Furthermore, no direct measurements of the magnetization were performed at high pressures so far due to the experimental difficulties involved. As the magnetization is the order parameter of a FM QPT, its behavior could give new insights into the exact mechanism driving the QPT.

Recently, a series of studies on  $\text{Ce}_x\text{La}_{1-x}\text{Pt}$  and  $\text{Ce}_x\text{Y}_{1-x}\text{Pt}$  was published by Očko *et al.* investigating the origin of the FM order in CePt [250–253]. For the sake of completeness these studies are summarized and discussed in the following. However, the author of this thesis disagrees with several conclusions of Očko *et al.*, which will also be addressed.

In the first two publications [250, 251] resistivity, thermopower, magnetization, and susceptibility (ac and dc) measurements of  $\text{Ce}_x\text{La}_{1-x}\text{Pt}$  for Ce concentrations 0.25, 0.50, 0.75, and 1.0 are presented. La has a similar electron configuration as Ce and also a similar atomic radius, however, La is non-magnetic. Compounds where Ce is completely substituted by La are therefore often used as a reference for the determination of non-magnetic contributions, for example, to the resistivity. Due to the similar atomic radii almost no chemical pressure effects are expected in  $\text{Ce}_x\text{La}_{1-x}\text{Pt}$ .

The susceptibility measurements by Očko *et al.* yield PM Curie-Weiss moments of  $\sim 2.47 \mu_B$  close to the free ion value of Ce and low-temperature moments of  $\sim 1.5 \mu_B$ , both constant for all  $x$  [251]. This suggests a hybridization between 4f moments and conduction band independent of the Ce concentration  $x$ . As no pronounced Kondo effect (negative slopes) is observed in  $R(T)$  at low temperatures, but only at high temperatures, Očko *et*

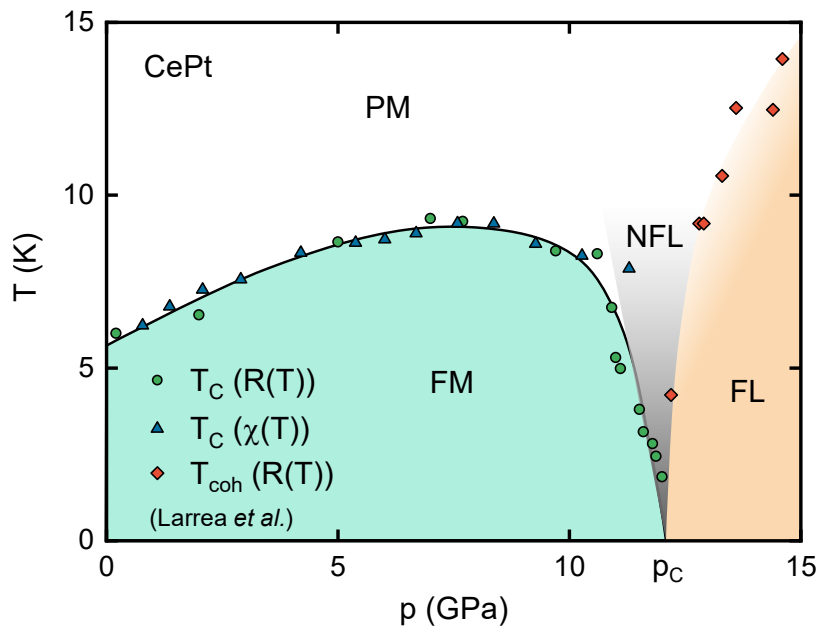


**Figure 5.10.:** Magnetic phase diagram of CePt under pressure determined by resistivity  $R$  and susceptibility  $\chi$  measurements. The dome-shaped FM phase ends at a critical pressure  $p_C = 12.1$  GPa where  $T_C$  is (presumably) suppressed to zero. Above  $p_C$  FL behavior is observed in the resistivity measurements up to a coherence temperature  $T_{\text{coh}}$ . Close to  $p_C$  the resistivity is linear over two decades of temperature suggesting NFL behavior. Data from Ref. [37].

*al.* ascribe the moment reduction completely to CEF effects. In contrast, Gignoux *et al.* estimated a moment reduction of approximately  $0.5 \mu_B$  caused by the CEF, whereas the remaining moment reduction is attributed to the Kondo effect [222].

The Curie temperature  $T_C(x)$  is extracted from resistivity and susceptibility measurements and shows a linear decrease with decreasing  $x$  [250, 251]. Očko *et al.* argue that the results cannot be explained in the Doniach picture as, on the one hand, the hybridization is constant, but on the other hand,  $T_C$  decreases. Furthermore, the linear decrease of  $T_C$  is also not predicted by Doniach's phase diagram. Therefore, Očko *et al.* conclude that the Kondo lattice model does not describe  $\text{Ce}_x\text{La}_{1-x}\text{Pt}$  properly and the RKKY interaction cannot be the main interaction driving CePt into a FM ground state. Alternatively, Očko *et al.* suggest the direct exchange as the main interaction between the Ce moments because a small overlap of the 4f orbitals seems possible when comparing the Ce-Ce distance in CePt (0.367 nm) and the metallic diameter of Ce (0.366 nm).

This interpretation of the measurements on  $\text{Ce}_x\text{La}_{1-x}\text{Pt}$  ignores that almost no chemical pressure is exerted with varying  $x$  due to the similar atomic radii of Ce and La. Therefore, the parameter  $\Gamma$  of the Kondo lattice model is not changed and a  $T_C$ -dependence as in Doniach's phase diagram is certainly not expected. The linear decrease of  $T_C$  is much

likelier explained by magnetic dilution as for example observed in  $\text{Ce}_x\text{La}_{1-x}\text{Ni}_{0.8}\text{Pt}_{0.2}$  [240]. Furthermore, a direct exchange interaction between the Ce atoms in CePt seems implausible as the 4f orbitals are situated much closer to the nucleus than the metallic radius of Ce.

In a second step resistivity, thermopower, magnetization, and susceptibility (ac and dc) measurements of  $\text{Ce}_x\text{Y}_{1-x}\text{Pt}$  for Ce concentrations 0.25, 0.50, 0.75, and 1.0 were performed by Očko *et al.* [252, 253] which are summarized in the following. The substitution of Ce by Y is expected to have a much larger chemical pressure effect compared to La due to the smaller atomic radius of Y [240].

The samples were characterized with X-ray diffraction confirming that all  $\text{Ce}_x\text{Y}_{1-x}\text{Pt}$  samples crystallize in the same CrB structure as CePt, although YPt crystallizes in the FeB structure. Additional Bragg peaks were observed in the diffraction patterns indicating small secondary phases. Furthermore, the Bragg peaks are comparatively wide suggesting disorder and/or internal stresses in the samples. The resistivity measurements show much larger room temperature values compared to  $\text{Ce}_x\text{La}_{1-x}\text{Pt}$ , presumably caused by sample imperfections. The temperature dependence of the resistivity also suggests a resistivity contribution from spin disorder which increases with decreasing  $x$ . More indicators for disorder in  $\text{Ce}_x\text{Y}_{1-x}\text{Pt}$  are the comparatively wide transitions at  $T_C$  observed in the resistivity and the small values of the measured thermopower.

The resistivity measurements show increasing Kondo characteristics with decreasing  $x$  which can be well described by a Kondo lattice featuring CEF effects [213, 252, 254]. The FM Curie temperatures of  $\text{Ce}_x\text{Y}_{1-x}\text{Pt}$  derived from resistivity and susceptibility measurements are in good agreement and decrease linearly with decreasing  $x$ . A comparison of  $\text{Ce}_x\text{La}_{1-x}\text{Pt}$  and  $\text{Ce}_x\text{Y}_{1-x}\text{Pt}$  shows that  $T_C(x)$  of both compounds coincides quantitatively. However, the magnetic moments of  $\text{Ce}_x\text{Y}_{1-x}\text{Pt}$  decrease with decreasing  $x$  while the moments of  $\text{Ce}_x\text{La}_{1-x}\text{Pt}$  are constant for all measured  $x$ . An exception from this behavior are both  $x = 0.75$  compounds with increased low temperature moments. Magnetization measurements of  $\text{Ce}_x\text{Y}_{1-x}\text{Pt}$  at 2 K yield magnetic moments of about  $1 \mu_B$  for all  $x$ . However, these measurements are not corrected by the necessary factor of 2 due to the uniaxial magnetic anisotropy as described in Ref. [222].

In a reinterpretation of their previous data on  $\text{Ce}_x\text{La}_{1-x}\text{Pt}$  from Refs. [250, 251] Očko *et al.* explain the linear decrease of  $T_C$  in Refs. [252, 253] now as a magnetic dilution effect. A combination of magnetic dilution and the Kondo lattice model is dismissed as an explanation for the  $\text{Ce}_x\text{Y}_{1-x}\text{Pt}$  results since it would yield different  $T_C(x)$  for both compounds. Instead, Očko *et al.* point to the roughly constant values of the magnetic moments from magnetization measurements and cite Ref. [255] which relates a magnetic

moment of  $\sim 1 \mu_B$  "to the stable state of the  $\text{Ce}^{3+}$  ion in [the] ferromagnetic state" [253]<sup>1</sup>. From this it is concluded that the Ce atoms are in the  $\text{Ce}^{3+}$  state below  $T_C$  and, therefore, the interaction between 4f moments and conduction electrons is zero excluding Kondo and RKKY interactions. The linear decrease of  $T_C(x)$  is explained by magnetic dilution similar to  $\text{Ce}_x\text{La}_{1-x}\text{Pt}$ . As the RKKY interaction is not possible in this framework, Očko *et al.* suggest again the direct exchange as the main Ce-Ce interaction with the same argumentation as in Refs. [250, 251].

Several points in the argumentation of Očko *et al.* are implausible: the (uncorrected) magnetization measurements of  $\text{Ce}_x\text{Y}_{1-x}\text{Pt}$  do not agree with previous literature values of CePt, making a quantitative model based on these arguable. Although clear evidence is presented for the Kondo effect in  $\text{Ce}_x\text{Y}_{1-x}\text{Pt}$  at temperatures above  $T_C$ , no explanation is given for the mechanism that abruptly destroys the hybridization at  $T_C$ . Furthermore, the  $\text{Ce}^{3+}$  state does not exclude Kondo interactions.

One important aspect in the interpretation of the  $\text{Ce}_x\text{Y}_{1-x}\text{Pt}$  measurements may have been neglected: disorder. Resistivity, thermopower, and x-ray diffraction measurements indicate considerable disorder in the  $\text{Ce}_x\text{Y}_{1-x}\text{Pt}$  samples which can drastically change the boundary of a FM phase as for example seen in  $\text{CePd}_{1-x}\text{Rh}_x$  (c. Sec. 5.2). In addition, the dilution effect tends to decrease  $T_C(x)$  with decreasing  $x$  while the chemical pressure effect is expected to increase  $T_C(x)$  [37, 236]. The interplay of these effects and disorder may as well result in the observed behavior of  $T_C(x)$ . The quantitative agreement of  $T_C(x)$  for  $\text{Ce}_x\text{La}_{1-x}\text{Pt}$  and  $\text{Ce}_x\text{Y}_{1-x}\text{Pt}$  is derived from the measurements at three Ce concentrations, where the samples with  $x = 0.75$  show anomalous behavior and the  $T_C(x = 0.25)$  is only determined by extrapolated susceptibility data as  $T_C(x = 0.25)$  is below the lowest measured temperature. The resulting low statistics do not exclude coincidence as an explanation for the agreement of  $T_C(x)$  of both compounds.

### 5.3.2. Experimental Results

As already stated in Sec. 2.3.3 a large CePt polycrystal (sample L) was prepared for the ND measurements. It was characterized by magnetization and ac susceptibility measurements using a standard PPMS from Quantum Design, as well as by NDI using the standard NDI setup at ANTARES (c. Sec. 2.1.2.3). The results of the PPMS characterization and the NDI measurements are given in Secs. 5.3.2.1 and 5.3.2.2, respectively. Furthermore, high-pressure ND measurements were performed on three pieces (samples A, B and C) of sample L where the results are shown in Sec. 2.1.2.4.

---

1 The author of this thesis was not able to find this statement in Ref. [255].

### 5.3.2.1. Magnetization and Susceptibility

The goal of the presented measurements in this section was merely the sample characterization of sample L, which is why rather coarse temperature and field scans were performed. Fig. 5.11 shows the inverse ac susceptibility  $\chi^{-1}$  as a function of temperature in a field of  $B = 100$  mT. For temperatures  $T > 80$  K the inverse susceptibility increases linearly indicating Curie-Weiss behavior except for small deviations between 215 and 250 K. These deviations are most likely caused by a faulty motor of the PPMS. The data was fitted with a Curie-Weiss law  $\chi = C/(T - \theta)$  where  $C$  is the material-specific Curie constant and  $\theta$  is the PM Curie-Weiss temperature. The parameters resulting from the fit shown as a black line in the figure are  $\theta = -40.7$  K and  $C = 0.372$  K. The Curie constant is given by  $C = N\mu_0\mu_{\text{eff}}^2/(3k_{\text{B}}V_{\text{uc}})$  with the number of magnetic atoms per unit cell  $N$ , the effective magnetic moment  $\mu_{\text{eff}}$ , the Boltzmann constant  $k_{\text{B}}$  and the volume of the unit cell  $V_{\text{uc}}$ . In the case of CePt,  $N = 4$  and  $V_{\text{uc}} = 190.2 \text{ \AA}^3$  [68] resulting in  $\mu_{\text{eff}} = 2.60 \mu_{\text{B}}$ . At  $T_{\text{C}} \approx 6$  K the FM transition is observed, however, the value of  $T_{\text{C}}$  is inaccurate due to the large temperature steps of the scan.

A magnetic field loop of sample L at 2 K is shown in Fig. 5.12 with the magnetization given in units of  $\mu_{\text{B}}$  per Ce atom. The fields were applied from 0 to 9 T (blue line), 9 to  $-9$  T (orange line), and  $-9$  to 9 T (green line). The data clearly shows FM behavior and a small coercivity of about 20 mT. A linear extrapolation of the high-field magnetic moment to  $B = 0$ , indicated in Fig. 5.12 by a dashed black line, yields a moment of  $0.64 \mu_{\text{B}}$ .

### 5.3.2.2. Neutron Depolarization Measurements at Zero Pressure

The sample characterization of the CePt poly-crystal (sample L) was continued using the NDI setup as described in Sec. 2.1.2.3 with a CC cryostat. This setup allows a precise determination of  $T_{\text{C}}$  and an investigation of the metallurgical homogeneity. Furthermore, the horizontal guide fields enable the ND measurements of complete field loops.

A field loop of sample L measured at 4 K is shown in Fig. 5.13 where the polarization is averaged over the whole sample. The sample was cooled in zero field, then the magnetic field was applied from 0 to 0.25 T (blue line), 0.25 T to  $-0.25$  T (green line), and  $-0.25$  T to 0.25 T (orange line). The polarization decreases rapidly from 0.4 to 0.18 when the field is turned up initially. For the remaining field loop the polarization stays nearly constant except for small polarization changes close to  $B = 0$ . The drop of the polarization at  $B = 0$  can be explained by a small misalignment of the horizontal guide fields. The small maxima at  $B \approx \pm 20$  mT are symmetric and consistent with the hysteresis observed in the previous magnetization measurements (c. Sec. 5.3.2.1).

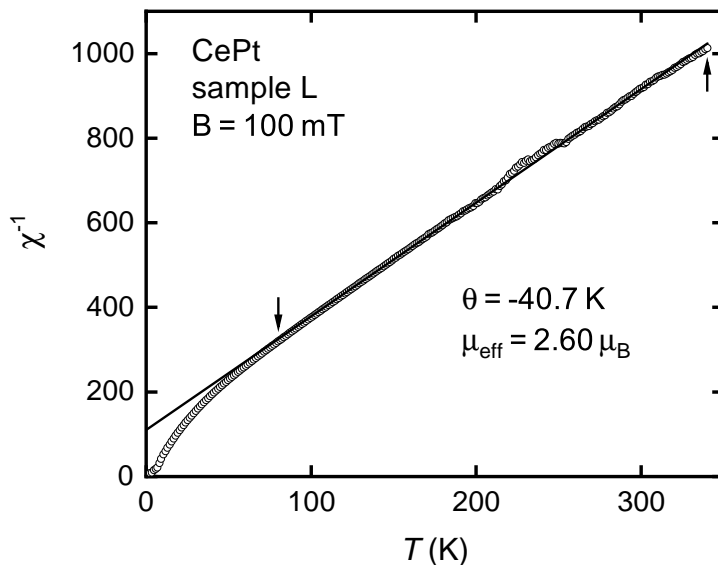


**Figure 5.11.:** Inverse ac susceptibility  $\chi^{-1}$  of the polycrystalline CePt sample L as a function of temperature. A constant magnetic field of  $B = 100$  mT was applied and the susceptibility was acquired at a frequency of 1000 Hz. Above 80 K the data follows a Curie-Weiss law  $\chi = C/(T - \theta)$  which is shown by the linear fit. The interval of the fit between 80 and 340 K is marked by arrows. From the fit a PM Curie-Weiss temperature of  $\theta = -40.7$  K and an effective magnetic moment of  $\mu_{\text{eff}} = 2.60 \mu_{\text{B}}$  were extracted.

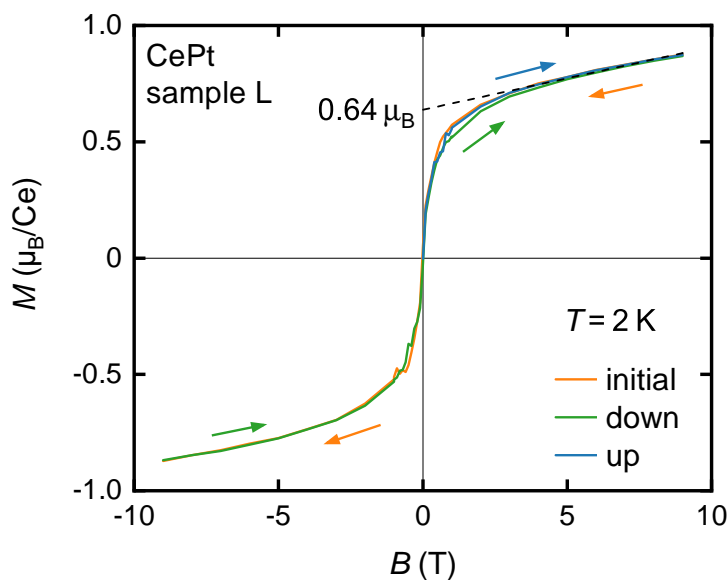


**Figure 5.12.:** Magnetization measurement of the polycrystalline CePt sample L at a temperature of 2 K. The magnetic field was scanned from 0 to 9 T (blue line), 9 to -9 T (orange line), and -9 to 9 T (green line). The magnetic moment extrapolated to  $B \rightarrow 0$  is  $0.64 \mu_{\text{B}}$ .

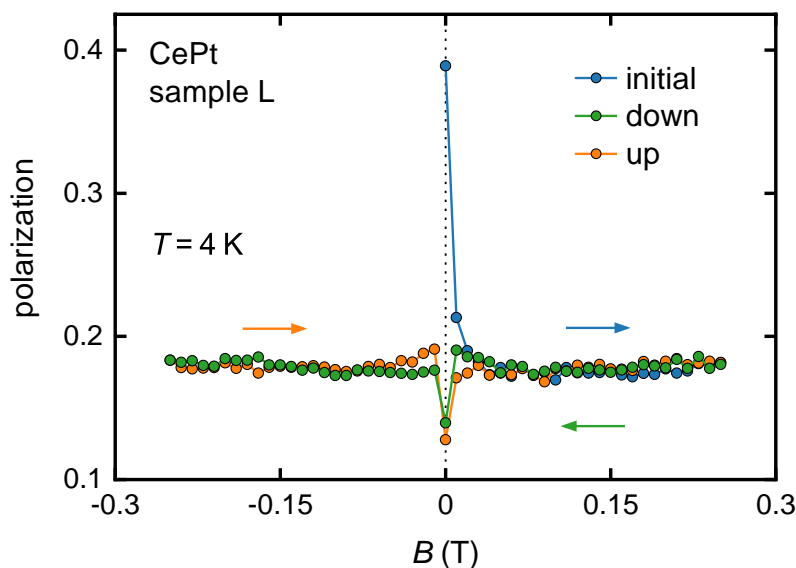


**Figure 5.13.:** ND field loop of the polycrystalline CePt sample L at a temperature of 4 K. The sample was cooled in zero field, then fields were applied from 0 to 0.25 T (blue line), 0.25 T to  $-0.25$  T (green line), and  $-0.25$  T to 0.25 T (orange line). A strong initial decrease of polarization is observed when small fields are applied. After that the polarization is almost constant except for fields close to  $B = 0$ .

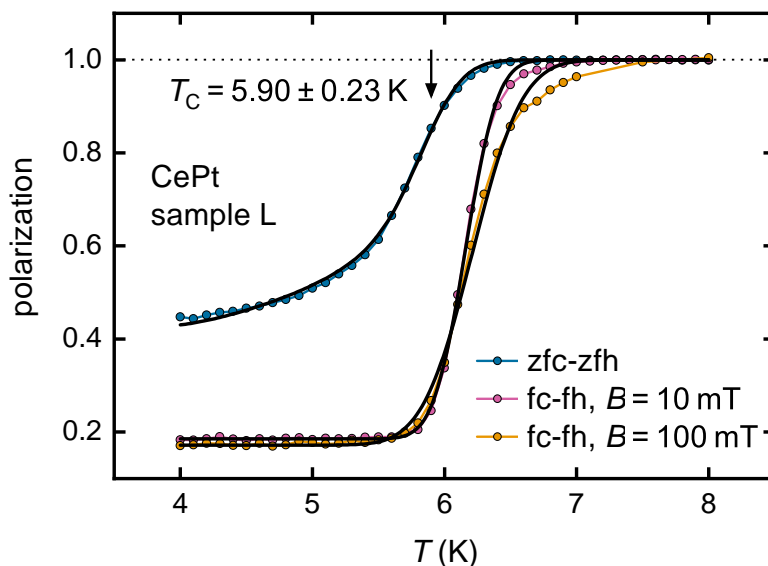


**Figure 5.14.:** ND temperature scans of the polycrystalline CePt sample L for different magnetic fields. The sample was cooled in the same field as measured during heating for each scan, respectively. Eq. 2.7 was fitted to the zero-field scan yielding a transition temperature of  $T_C = (5.90 \pm 0.23)$  K. The data sets at 10 and 100 mT were both fitted using Eq. 2.9. Applying a magnetic field increases the depolarization and shifts  $T_C$  to higher temperatures.

Temperature scans were performed in zero field, at 10 mT, and at 100 mT as can be seen in Fig. 5.14. For all scans the sample was cooled in the same field as measured during heating. The zero-field scan shows a decrease of the polarization setting in below 6.5 K indicating the onset of FM order. The data was fitted using Eq. 2.7 convoluted with a normalized gaussian distribution, yielding  $T_C = (5.90 \pm 0.23)$  K where the error is the standard deviation  $\Delta T_C$  of the gaussian.  $T_C$  is marked in Fig. 5.14 by a black arrow. Furthermore, the fit yields a value of  $B_0^2 \delta = 1.8 \cdot 10^{-8} \text{ T}^2 \text{ m}$ .

The application of finite fields shifts the onset of depolarization to larger temperatures and increases the overall depolarization, where both effects increase with increasing  $B$ . The scans at fields of 10 and 100 mT were fitted using Eq. 2.9 convoluted with a normalized gaussian distribution as both data sets reach a saturation value of the polarization at low temperatures. The resulting Curie temperatures for the scans at 10 and 100 mT are  $T_C = (6.16 \pm 0.27)$  K and  $T_C = (6.20 \pm 0.39)$  K, respectively. Both fits describe the polarization very well except for temperatures directly above  $T_C$ .

For the evaluation the polarization data of sample L at ambient pressure was averaged over the whole sample in the measurements presented above. Fig. 5.15 shows the NDI evaluation of the temperature scans from Fig. 5.14 where the fit functions were evaluated for every pixel. The three rows of figures are the three scans at (a-b)  $B = 0$ , (c-d)  $B = 10$  mT, and (e-f)  $B = 100$  mT with the  $T_C$ -maps on the left and the corresponding  $T_C$ -distributions on the right hand side. The color bars indicating the Curie temperatures in the  $T_C$ -maps are displayed with the same scale at the x-axis of the corresponding  $T_C$ -distribution. The arithmetic average and standard deviation of each distribution was calculated and is displayed as  $T_{\text{mean}}$  and  $T_{\text{std}}$ , respectively.

The  $T_C$ -map of the zero-field scan (Fig. 5.15(a)) reveals a central part of the sample with  $T_C \approx 5.9$  K, whereas the surrounding sample area shows a lower  $T_C \approx 5.8$  K. The  $T_C$ -distribution in panel (b) starts abruptly at 5.8 K and decreases with increasing  $T_C$  except for a delta-like peak at 5.9 K. As the values for  $T_C$  were automatically calculated by a fitting routine, it is important to note that the initial guess value for  $T_C$  was 6 K and the values of  $T_C$  summed up in the bin at 5.9 K are not identical. Furthermore, about 100 of the fits were plotted and manually reviewed in order to verify the convergence of the fits. The average Curie temperature of the distribution is  $T_{\text{mean}} = 5.85$  K and the standard deviation of the distribution is  $T_{\text{std}} = 0.04$  K. The latter value is contrary to the values of  $\Delta T_C$  which are in the order of 0.25 K and are not shown here. Furthermore, no correlation between  $T_C(x,y)$  and  $\Delta T_C(x,y)$  was found. The variation of  $T_C$  is therefore larger in z-direction than in the x-y-plane.

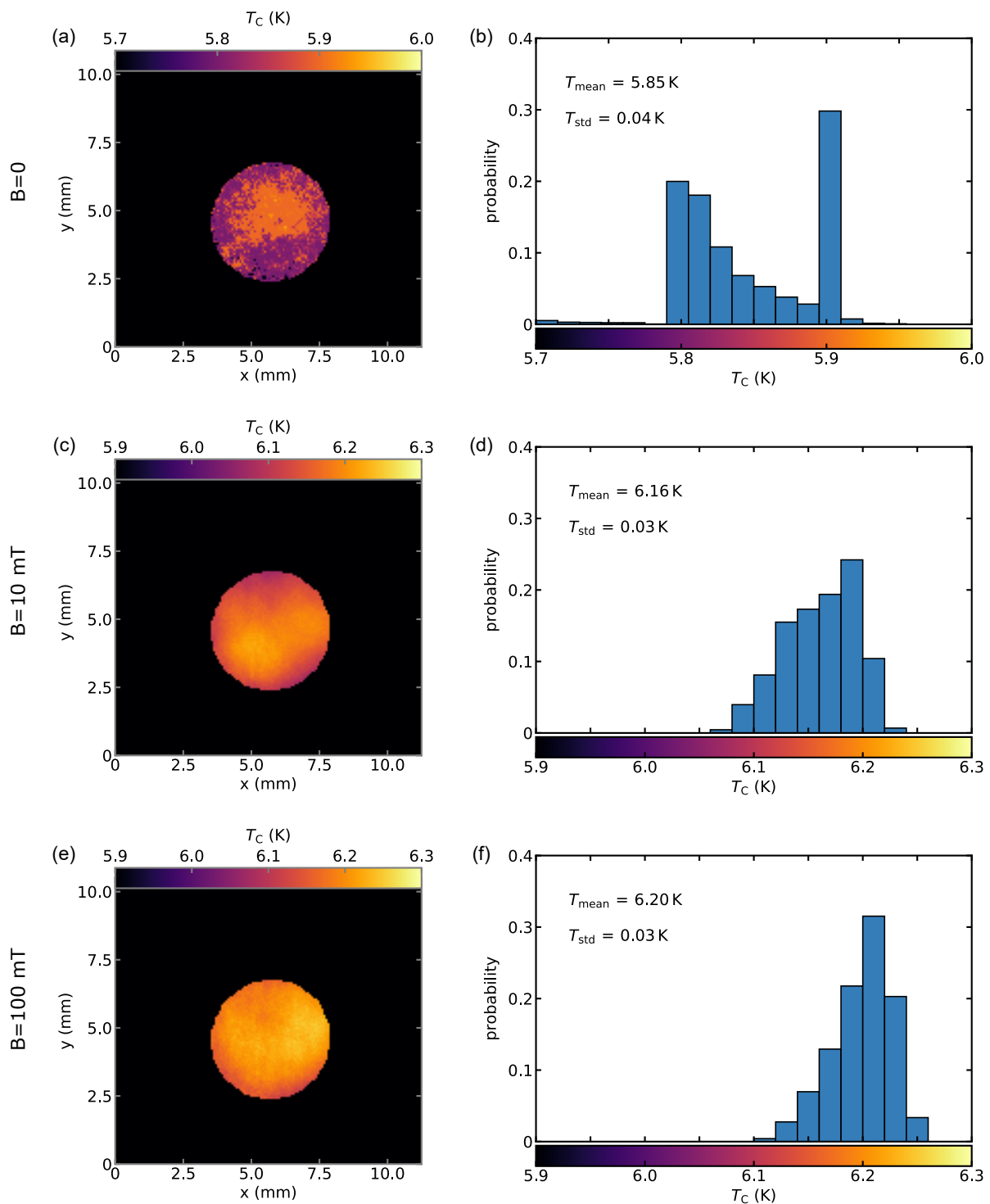


**Figure 5.15.:** NDI evaluation of the temperature scans shown in Fig. 5.14 for applied fields of (a-b)  $B = 0$ , (c-d)  $B = 10$  mT, and (e-f)  $B = 100$  mT. The figures on the left hand side show the obtained  $T_C$ -maps with the corresponding distribution of  $T_C$  on the right hand side. The values given in the  $T_C$ -distributions  $T_{\text{mean}}$  and  $T_{\text{std}}$  are the average and the standard deviation of each  $T_C$ -distribution.

The  $T_C$ -maps of the scans at (c)  $B = 10$  mT and (e)  $B = 100$  mT are much more homogeneous than the zero-field data. The corresponding  $T_C$ -distributions resemble a slightly asymmetric gaussian distribution with a well defined peak close to  $T_{\text{mean}}$ . Increasing the magnetic field shifts  $T_C$  to higher temperatures as already observed in Fig. 5.14 whereas the width of the distribution stays constant. The average values of  $\Delta T_C$  are 0.27 K and 0.39 K for  $B = 10$  mT and  $B = 100$  mT, respectively.

### 5.3.2.3. High Pressure Neutron Depolarization Measurements

In order to explore the phase diagram of CePt (c. Fig. 5.10) a series of ND measurements was performed at different pressures up to 12.2 GPa using the high-pressure ND setup as described in Sec. 2.1.2.4. The data shown in this section was acquired over three separate beam times using a new piece of sample L for each beam time (samples A, B, and C). Further details on samples A, B, and C are given in Sec. 2.3.3. In the following the presentation of the data is primarily ordered by pressure and not chronologically.

The high-pressure data mainly consists of temperature scans in order to determine  $T_C$  at different pressures. For all temperature scans the sample was cooled to 0.6 K and then measured during controlled heating up to temperatures between 14 and 16 K. Furthermore, the effects of different field histories were measured by performing similar temperature scans for zero-field cooling and field cooling. However, before covering the temperature scans, one field scan at low pressure is presented in order to show the effects of a magnetic field on the depolarization when investigating CePt.

Fig. 5.16 shows a ND field scan of CePt sample A at  $p = 1.1$  GPa and  $T = 0.6$  K. The polarization data was normalized using the same values as for the first zfc-fh scan (dark blue markers) shown further below in Fig. 5.20, since both data sets are from the same sample and at the same pressure. After cooling the sample in zero field to base temperature the magnetic field  $B$  was increased in steps up to 0.25 T (blue circles) while measuring the polarization. Thereafter, the field was decreased to zero in the same steps (orange circles) while also measuring the polarization. When increasing the field the polarization decreases linearly from 1 until the field reaches 130 mT. For larger fields a linear increase of the polarization is observed. When decreasing the field again, the polarization values at first match the increasing-field data set, down to a field of 130 mT. For smaller fields the polarization further decreases until at  $B = 50$  mT an increase is observed again. At  $B = 0$  the polarization values of both scan directions show small drops due to a slight misalignment of the guide fields. The initial value of  $P \approx 1$  at  $B = 0$  suggests that (almost) no depolarization is expected in zero-field temperature scans.

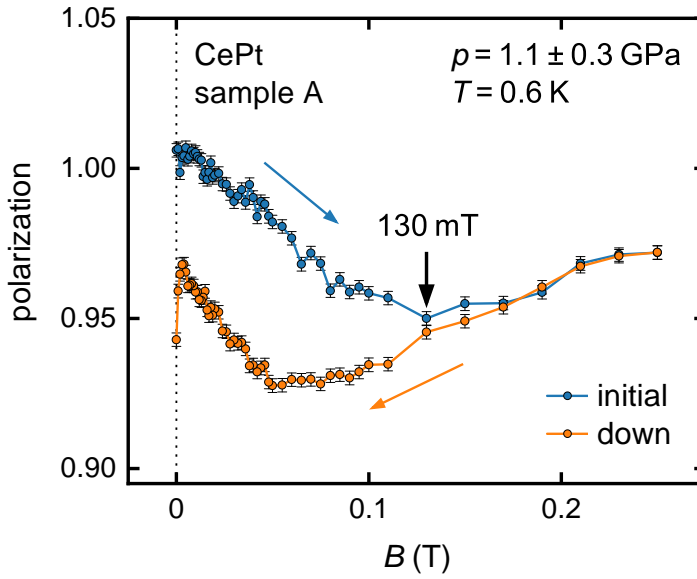


**Figure 5.16.:** Magnetic field scan at 0.6 K of CePt sample A at a pressure of 1.1 GPa. After cooling the sample in zero field, the field was first increased to 0.25 T (blue markers) and then again decreased to zero (orange markers). A splitting of the two curves is observed at 130 mT resulting in a large hysteresis.

The temperature scans at the lowest pressure were measured at  $p = 0.8$  GPa and are shown in Fig. 5.17. The ND of sample B was measured in a field of  $B = 50$  mT, once after zfc (blue circles) and once after fc (pink circles). The data is shown in Fig. 5.17(a) on the same scale and in Fig. 5.17(b) with a polarization offset of 0.01 for a better distinction of the single data points. In both scans the polarization starts to decrease at a temperature of  $T_C = 7.5$  K marking the FM transition temperature.

A prominent feature of the zfc-fh data set is an oscillatory behavior at temperatures above  $T_C$  with an amplitude much larger than the calculated error bars. This oscillation can be traced back to an oscillation of the temperature controller with strongly varying times  $\Delta t$  between the data points resulting in a pronounced afterglow effect. The onset of the oscillatory behavior at  $T_C$  is merely a coincidence. The algorithm introduced in Sec. 2.1.3.2 used to correct data sets affected by the afterglow effect could not be utilized in this case due to the large number of subsequently affected data points. In contrast, the fc-fh scan was treated using the afterglow algorithm which can be seen in Fig. 2.15 where this data set was shown as an example.

Below  $T_C$  both data sets reveal complex behavior deviating from the simple theory which would predict a step-like or exponential dependency. Therefore, in order to determine  $T_C$ , a line was fit to the polarization data in the region directly below  $T_C$  where the intersection

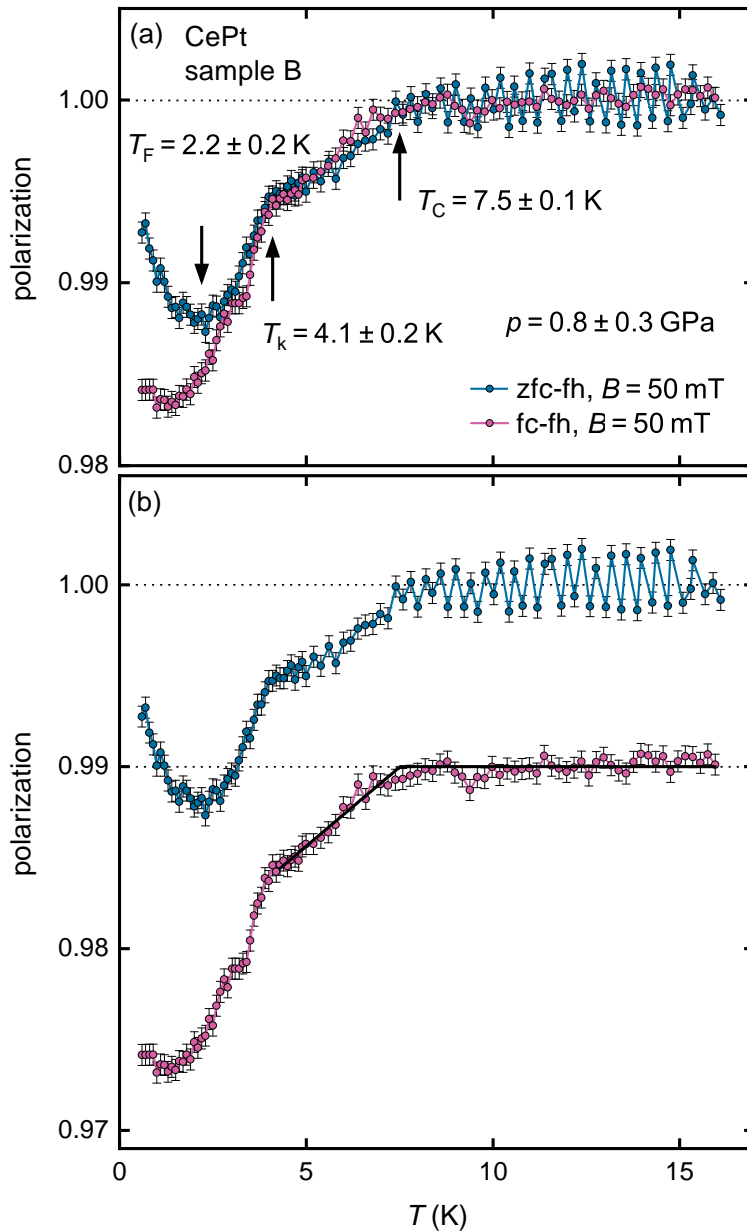


**Figure 5.17.:** ND temperature scans of CePt sample B at a pressure of 0.8 GPa. During both measurements a field of 50 mT was applied, however, in the first case the sample was cooled in zero field (blue circles) while in the second case the sample was cooled in a field of 50 mT (pink circles). The data in panel (b) is the same data as in (a) but with an artificial offset of 0.01. The polarization decreases below  $T_C = 7.5$  K indicating the onset of FM order. Further features in the data sets are marked with the temperatures  $T_k$  and  $T_F$  and are explained in the text.

of the fit with  $P = 1$  gives  $T_C$ . As the zfc-fh scan is strongly affected by the afterglow effect,  $T_C = 7.5$  K was determined only from the fit to the fc-fh scan which is shown as a black line in Fig. 5.17(b).

Going to lower temperatures a shoulder is observed in both data sets at  $T_k = 4.1$  K where the slope of the polarization changes significantly. Around 3 K a splitting of the zfc and the fc scans can be seen where the polarization of the fc data further decreases while the polarization of the zfc data levels out and increases for temperatures below  $T_F = 2.2$  K.

After increasing the pressure to 1.1 GPa two temperature scans were measured with the same field histories as at the previous pressure. The corresponding data is shown in Fig. 5.18 analogous to Fig. 5.17. The depolarization sets in at a slightly higher temperature with a subsequent linear decrease. As before a shoulder is observed at  $T_k = 4.2$  K in both data sets. Again, a splitting between the zfc and fc scans can be seen due to an increase of the polarization of the zfc data towards lowest temperatures. The slope of the zfc data changes sign at  $T_F = 2.1$  K.  $T_C$  was determined by linear fits shown as black lines in Fig. 5.18(b). The polarization at high temperatures of the zfc scan features a small increase of the polarization towards higher temperatures which we were not able to explain. Therefore, only the fit of the fc-fh scan was used to determine  $T_C = 7.8$  K.

Fig. 5.19 shows ND temperature scans of sample B measured at a pressure of 1.5 GPa. The intention was to perform scans with the same field histories as at the other two pressure points presented above. However, an incorrect measurement script prevented the control software from turning on the magnet in the case of the zfc-fh scan resulting in the measurement of a zfc-zfh scan (orange circles) instead. This data set shows very small depolarization on the order of  $1 \cdot 10^{-3}$  in the temperature range from 2.0 K to 7.5 K with a calculated polarization error of  $0.6 \cdot 10^{-3}$ .

Furthermore, a fc-fh temperature scan with an applied field of  $B = 50$  mT was measured showing similar behavior as the corresponding scans at 0.8 and 1.1 GPa. The FM ordering temperature  $T_C = 7.7$  K was determined from the fit of a line to the polarization values directly below  $T_C$ . A change of the slope can be seen at  $T_k = 4.7$  K.

Temperature scans at a pressure of 1.1 GPa were also performed in beam time A on a CePt sample A. Two zfc-fh scans and one fc-fh scan with applied fields of 50 mT were measured and are shown in Fig. 5.20. All three data sets show depolarization below 7.0 K but with much steeper slopes than the previously presented temperature scans from beam time B at similar pressures. The  $T_C$  of each scan was determined by fitting a line to the polarization data directly below  $T_C$  shown in Fig. 5.20(b) as black lines. As all measurements behave consistently around 7 K, the FM ordering temperature for this sample and pressure was calculated from the average of the three fits to  $T_C = 7.0$  K.

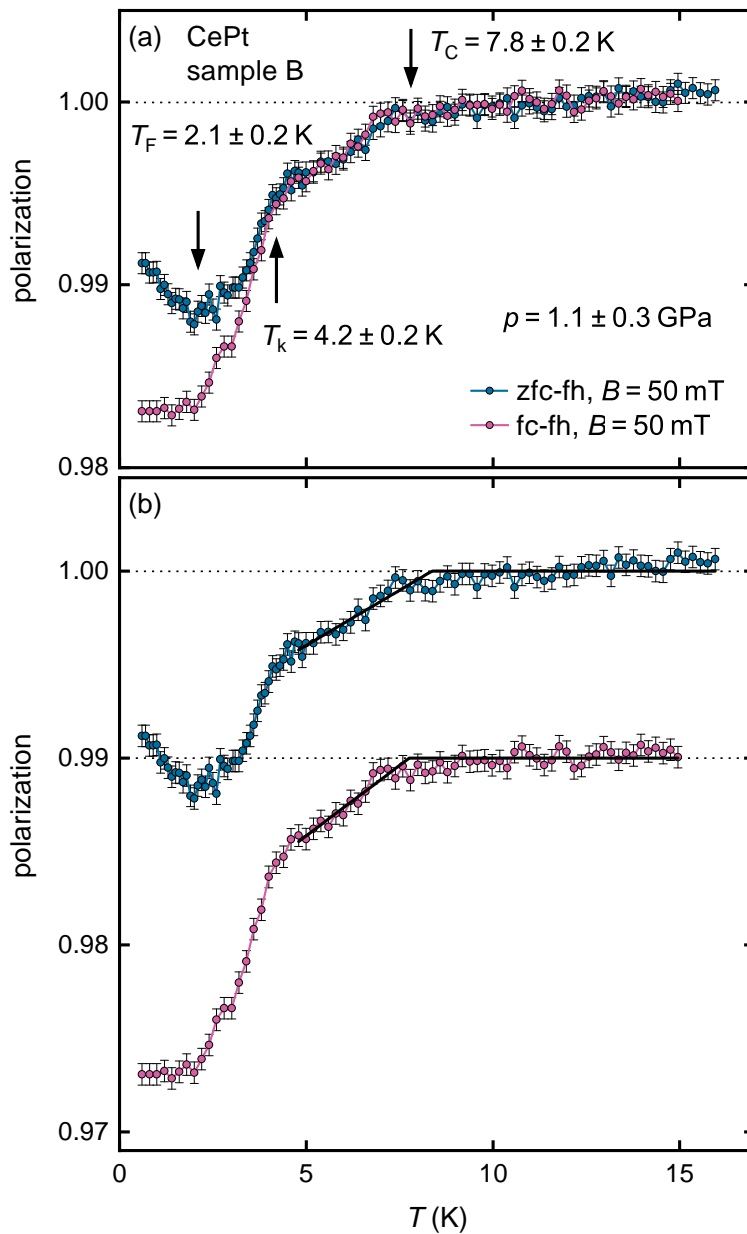


**Figure 5.18.:** ND temperature scans of CePt sample B at a pressure of 1.1 GPa using the same field histories as in the measurements at 0.8 GPa (c. Fig. 5.17). Again, the data is shown (a) on the same y-scale and (b) with a y-offset of 0.01.  $T_C = 7.8$  K was determined from a linear fit (black line in (b)) to the fc-fh scan. Below 3.5 K a splitting of the two polarization curves is observed.

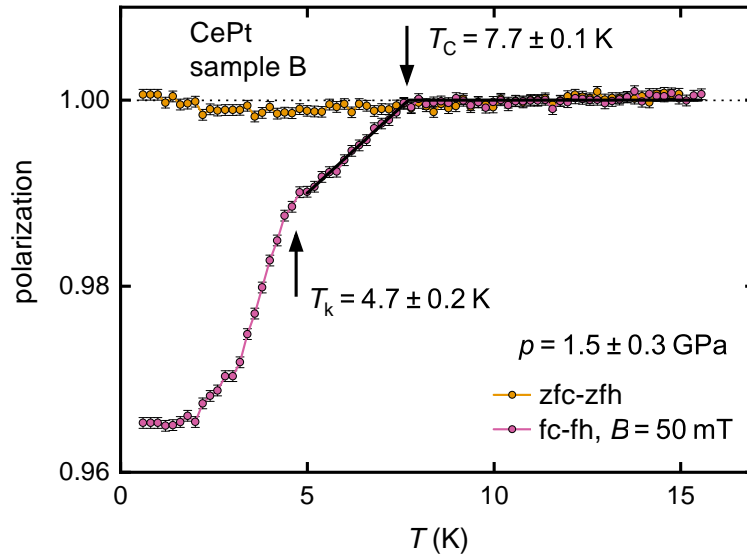


**Figure 5.19.:** ND temperature scans of CePt sample B at a pressure of 1.5 GPa. The fc-fh scan was performed in a field of  $B = 50$  mT while the zfc-zfh scan was performed in zero field. Similar to the previous fc-fh scans at slightly smaller pressures, the fc-fh data shows a linear decrease starting at  $T_C = 7.7$  K and a change of slope at  $T_k = 4.7$  K. In contrast, almost no depolarization can be seen in the zfc-zfh data set.

Similar to the measurements of sample B a splitting of the zfc and fc curves occurs at 3 K with an increase of the polarization towards lower temperatures starting at  $T_F = 2.0$  K in the case of the zfc measurements. However, no shoulder is observed in the data of sample A in the temperature region between 4 and 5 K, but at  $T_k = 3.0$  K and only in the fc-fh data. Furthermore, for  $T > 3$  K the ND curves resemble more an exponential dependency as described by Eq. 2.7. However, a quantitative evaluation using the equation is impossible here due to restrictions by the HP-ND setup as stated in Sec. 2.1.1.1.

Another difference to the measurements of sample B is the increased level of noise in the measurements of sample A. This observation is also consistent with further measurements of samples A and B shown below. As the calculation of the error bars using the algorithm discussed in Sec. 2.1.3.1 gives errors being too small to explain the observed noise, the error bars of all measurements of sample A were estimated from the standard deviation of the polarization above  $T_C$ . Evaluating the polarization of the six ROIs from the guide pattern separately shows strong correlation of the polarization curves on the level of noise. The source for the increased noise can therefore only be narrowed down to an effect that affects the overall measured intensity of the neutron beam, such as flux variations due to reactor control or the afterglow effect.

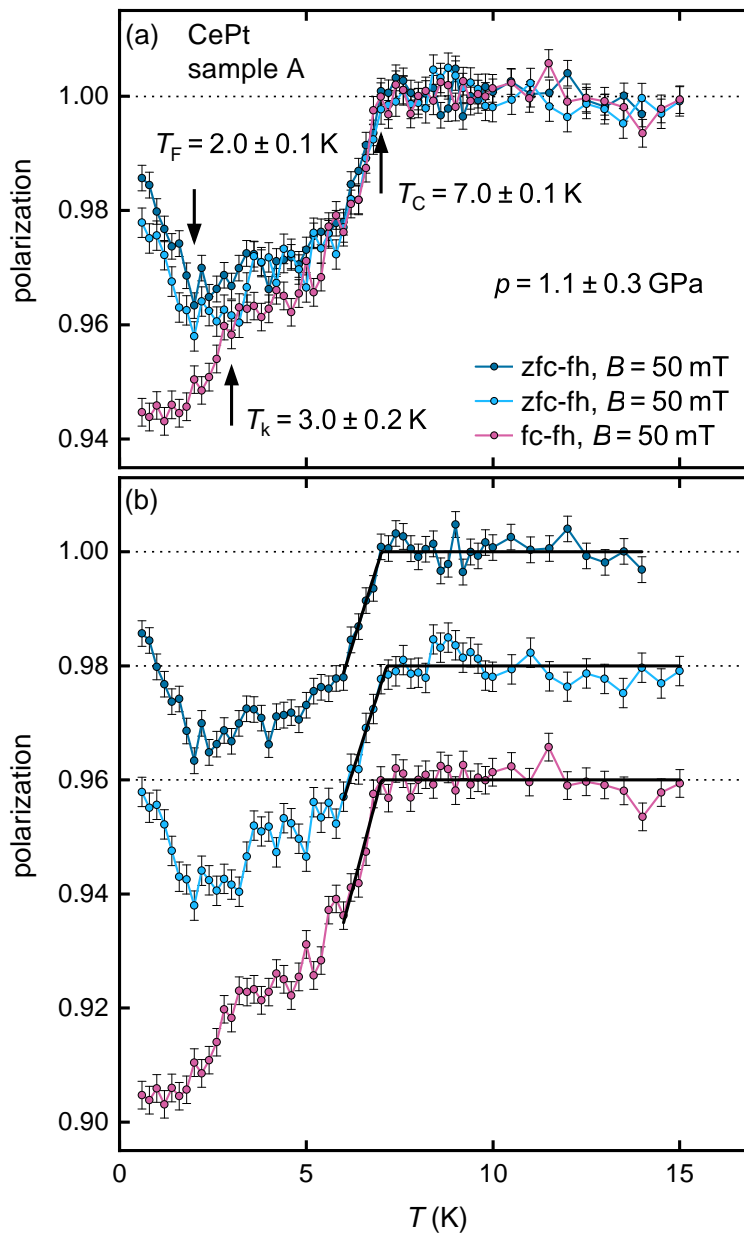


**Figure 5.20.:** ND temperature scans of CePt sample A at a pressure of 1.1 GPa. Two zfc-fh scans (light and dark blue circles) and one fc-fh scan (pink circles) were performed in a field of  $B = 50$  mT. The ND data is shown (a) on the same y-scale and (b) with a y-offset of 0.02 between the curves.  $T_C = 7.0$  K was determined from the average  $T_C$  of the three scans by fitting a linear function to each scan (black lines).

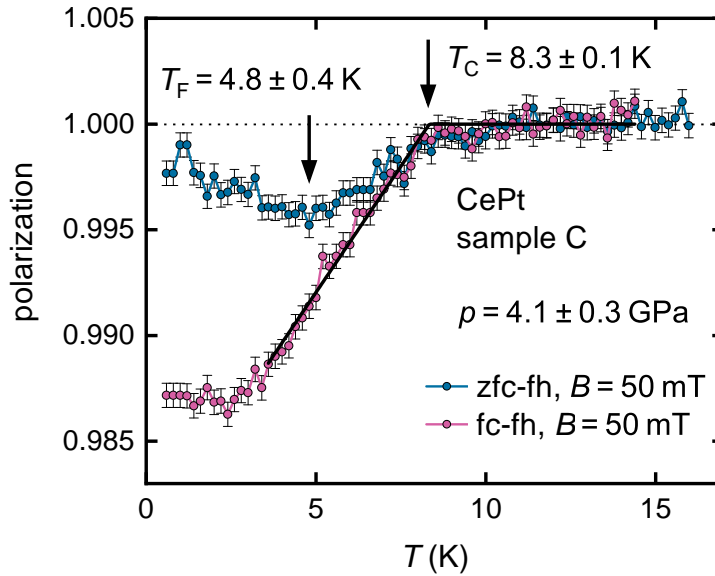


**Figure 5.21.:** ND temperature scans of CePt sample C at a pressure of 4.1 GPa. The polarization was measured with an applied field of 50 mT, once after zfc (blue circles) and once after fc (pink circles). The FM ordering temperature  $T_C = 8.3 \text{ K}$  was determined via a linear fit (black line) to the fc-fh data.

Fig. 5.21 shows temperature scans of sample C at a pressure of 4.1 GPa. No measurements of sample C at other pressures were performed as beam time C (p14766) was originally intended for measurements on  $\text{SrRuO}_3$ . Due to failures of the  $\text{SrRuO}_3$  pressure cells at the beginning of the beam time, CePt sample C was measured as a backup while a new pressure cell was loaded with  $\text{SrRuO}_3$ . Two temperature scans were measured in a field of  $B = 50 \text{ mT}$ , one after cooling in zero field (blue circles) and one after cooling in a field of 50 mT (pink circles). Both scans show depolarization below  $\sim 8 \text{ K}$  and a subsequent splitting at 7.5 K similar to the scans at lower pressures, however, shifted to higher temperatures. As the onset of depolarization is very gradual in the case of the zfc-fh data set, the much sharper fc-fh scan was used to determine  $T_C = 8.3 \text{ K}$  by fitting a line to the polarization data below  $T_C$ . Again, an increase of the polarization is observed in the zfc-fh scan towards lowest temperatures after passing a minimum at  $T_F = 4.8 \text{ K}$ .

Three temperature scans of sample A at 5.7 GPa were measured for different field histories and are shown in Fig. 5.22(a) on the same y-scale and in Fig. 5.22(b) with a y-offset of 0.02 between the data sets. The polarization was measured in a field of 50 mT after zfc (blue circles) and fc (pink circles), and in zero field after zfc (orange circles). In the case of the zfc-zfh scan the polarization stays constant and no depolarization can be seen. However, if a field is applied a depolarization of several percent is observed

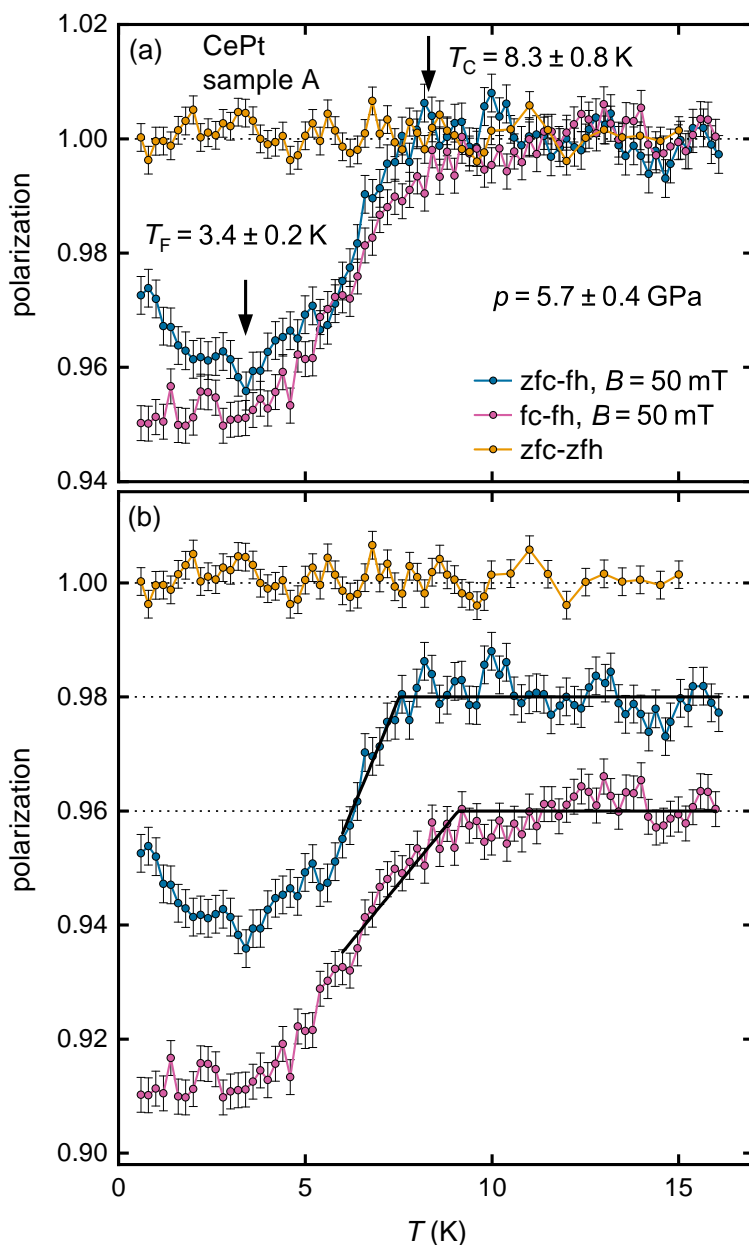


**Figure 5.22.:** ND temperature scans of CePt sample A at a pressure of 5.7 GPa. Temperature scans were measured in zero field and with a field of 50 mT for the field histories zfc-fh (blue circles), fc-fh (pink circles), and zfc-zfh (orange circles). The temperature scans are shown (a) on the same y-scale and (b) with a y-offset of 0.02 between the data sets. While no depolarization is observed in the zfc-zfh scan a decrease of polarization can be seen in the other scans below approximately 8 K. Below  $T_F = 3.4$  K the polarization of the zfc-fh scan increases again towards lower temperatures.

below  $\sim 8$  K. Extracting  $T_C$  using a linear fit as shown in Fig. 5.22(b) as black lines results in temperatures of  $(7.5 \pm 0.1)$  K and  $(9.1 \pm 0.2)$  K for the zfc-fh and the fc-fh scan, respectively. The Curie temperature  $T_C = 8.3$  K for this pressure was calculated using the average of the temperatures from the fits with a rather large error of 0.8 K calculated from the standard deviation. As in previous measurements a splitting of the zfc-fh and the fc-fh curves can be seen at low temperatures. The polarization of the zfc-fh measurement features a minimum at  $T_F = 3.4$  K.

Fig. 5.23 shows three temperature scans of sample A at a pressure of 9.3 GPa on the same y-scale in panel (a) and with a y-offset of 0.02 between the data sets in panel (b). As in previous measurements at lower pressures the polarization data was acquired in a field of 50 mT after zfc and fc. Additionally, a fc-fh scan in a field of 150 mT was measured. The polarization of the zfc-fh measurement is constant except for temperatures around 7.3 K and below 1.3 K. These deviations may be caused by the afterglow effect and are not interpreted as depolarization since no consistent trend towards a smaller polarization can be seen. In contrast, applying a field of 50 mT before cooling and heating results in a measurable depolarization starting at 9.4 K. Repeating the fc-fh scan with an increased field of 150 mT also increases the depolarization and shifts the onset of depolarization to slightly higher temperatures.  $T_C = 9.8$  K was determined by fitting a line to both fc-fh scans and taking the average of both values.

The same scans measured at 9.3 GPa were also performed at 10.5 GPa as shown in a similar way in Fig. 5.24. The polarization of the zfc-fh data set is constant up to 12 K where it starts to decrease. Also, an instability of the temperature controller was detected at 12 K resulting in a 20% shorter time between data points  $\Delta t$ . The decrease in the zfc-fh scan is, therefore, much likelier caused by a propagation of the afterglow effect after the anomaly at 12 K than by a depolarization effect. The fc scans both show a decrease of the polarization towards lower temperatures, however, at different temperatures. No  $\Delta t$  anomalies were found in the fc scans which coincide with polarization changes. Nevertheless, artifacts resulting from the afterglow effects cannot be excluded as the large deviation of polarization values in the 150 mT scan cannot be explained otherwise. Again, a linear fit was used for the determination of  $T_C$  yielding  $(10.3 \pm 0.5)$  K for  $B = 50$  mT and  $(6.8 \pm 0.6)$  K for  $B = 150$  mT. The average  $T_C = 8.6$  K of both values was taken for the Curie temperature at this pressure with an error of 1.8 K.

The highest pressure at which CePt was investigated in this study is 12.2 GPa; however, only one temperature scan could be measured due to time limitations. The fc-fh scan with an applied field of 50 mT of sample B is shown in Fig. 5.25. The polarization data shows very little deviation from  $P = 1$  with the deviations being smaller than the polarization

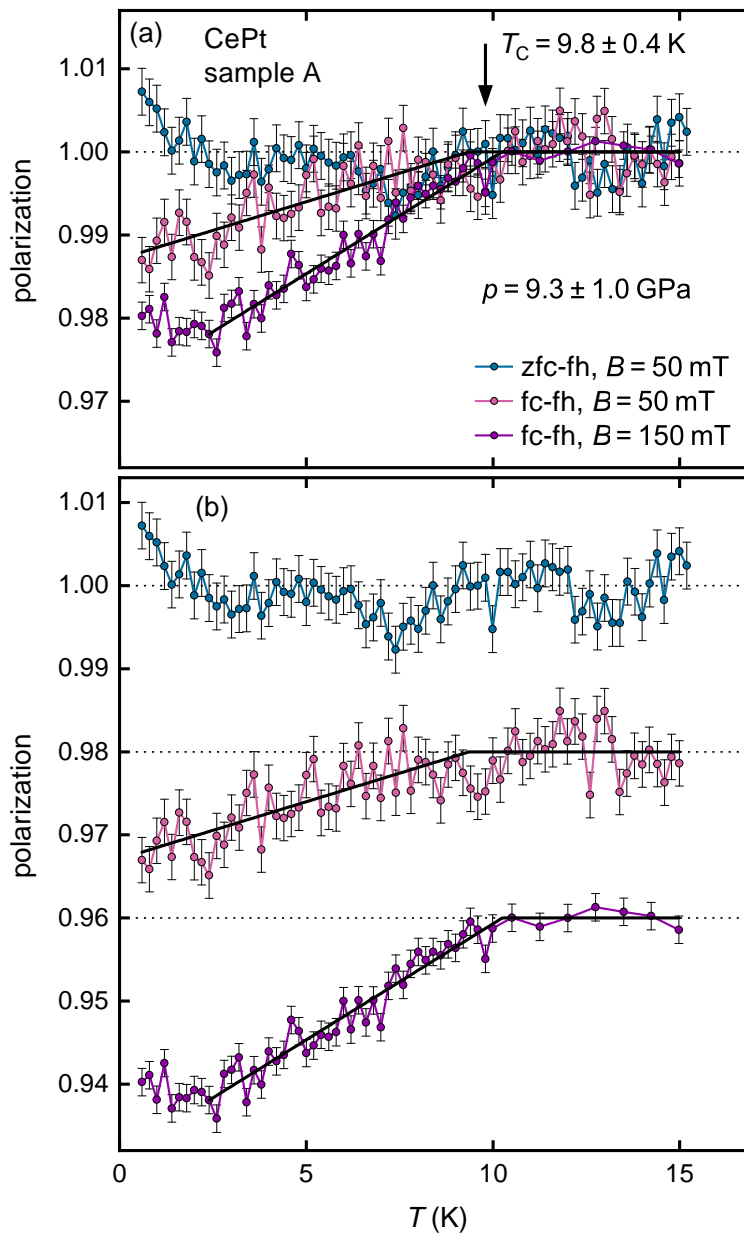


**Figure 5.23.:** ND temperature scans of CePt sample A at a pressure of 9.3 GPa. The polarization was measured in a field of 50 mT after zfc (blue circles) and fc (pink circles) as well as in a field of 150 mT after fc (purple circles). The temperature scans are shown (a) on the same y-scale and (b) with a y-offset of 0.02 between the data sets. While no consistent depolarization is observed in the zfc-fh scan, the fc scans show depolarization below  $T_C = 9.8$  K.

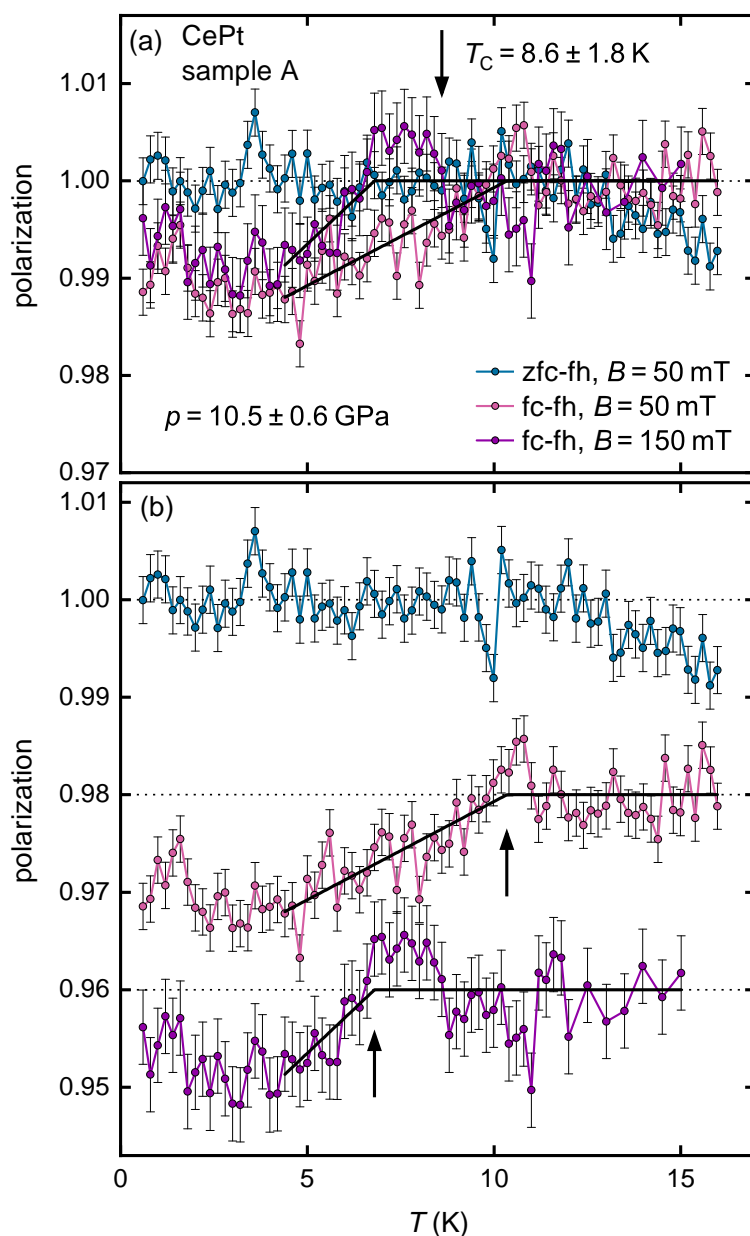


**Figure 5.24.:** ND temperature scans of CePt sample A at a pressure of 10.5 GPa. The scans were measured applying the same field histories as at the previous pressure of 9.3 GPa shown in Fig. 5.23. While the zfc-fh data features an unexpected decrease of polarization towards higher temperatures, depolarization can be seen in the fc-fh scans at lower temperatures.

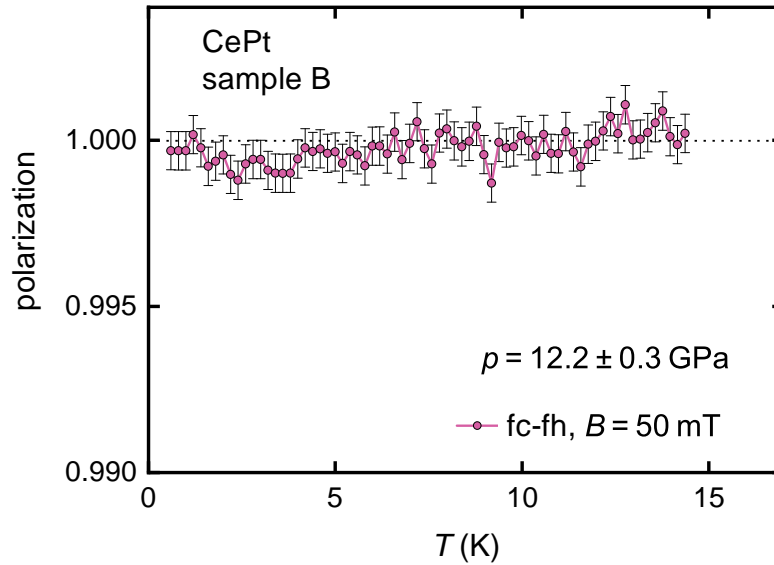


**Figure 5.25.:** ND temperature scan of CePt sample B at a pressure of 12.2 GPa. The polarization was measured in a field of 50 mT after cooling it in the same field. Within the error of  $5.8 \cdot 10^{-4}$  the polarization is constantly 1 except for a small region between 2 and 4 K.

error of  $5.8 \cdot 10^{-4}$  for all temperatures except for the interval between 2 and 4 K. It is questionable if the decrease of the polarization in this temperature interval is caused by depolarization, or if it is an artifact caused by statistical outliers or the afterglow effect. As no clear proof of FM order can be derived from this data set, the  $T_C$  for this pressure was set to zero.

### 5.3.3. Discussion of CePt

#### 5.3.3.1. Properties of CePt at Ambient Pressure

The PM Curie-Weiss moment of  $2.60 \mu_B$  extracted from the susceptibility measurements of sample L is close to the free ion value of Ce ( $2.54 \mu_B$ ) and in good agreement with the literature [222, 251]. The negative Curie-Weiss temperature is a strong indicator for Kondo interactions. Furthermore, the magnetization measurements shown in Fig. 5.13 resemble comparable data from the literature [222, 231, 238]. The magnetic moment of  $0.64 \mu_B$  in the FM phase has to be corrected by a factor of 2 due to the polycrystalline nature of the sample and the strong magnetic anisotropy along the crystallographic c-axis [222, 231, 232]. The resulting ordered moment of  $1.28 \mu_B$  is in good agreement with neutron scattering results [68].

The ND measurements of sample L presented in Sec. 5.3.2.2 resemble normal FM behavior. The Curie temperature  $T_C = 5.90$  K extracted from the zfc-zfh temperature scan is in good agreement with values from the literature [37, 222, 230, 231, 233, 234]. Using the value of  $B_0$  for CePt from Fig. 2.2 and  $B_0^2\delta = 1.8 \cdot 10^{-8} \text{ T}^2 \text{ m}$  from the fit of Eq. 2.7 to the zfc-zfh data, gives an average domain size  $\delta = 0.15 \mu\text{m}$  which is relatively small for a FM but may be expected from a strongly anisotropic material such as CePt. Furthermore, this value for  $\delta$  should only be taken as a coarse estimate as the calculation assumes a random orientation of domains and a constant thickness  $d$  which is not completely fulfilled in this case due to the strong anisotropy and the ellipsoid shape of the sample.

The low-temperature polarization of the scans in fields of 10 and 100 mT reaches a constant value indicating much larger domains than in the case of the zero-field measurement. Furthermore, the temperature scans at finite fields show deviations from the fit of Eq. 2.9 at temperatures above  $T_C$  in the form of an additional contribution to the depolarization. This can be explained by the fact that the ND technique is sensitive to fluctuating forms of FM order (c. Sec. 2.1.1.2). Directly above  $T_C$  the critical fluctuations are slowed down by the applied field to a frequency scale where the fluctuations cause depolarization. Thus, the polarization increases slower towards  $P = 1$  as seen in the fc-fh temperature scans.

Further information on the sample can be derived from the NDI evaluation of the temperature scans as shown in Fig. 5.3. The  $T_C$ -map of the zero-field scan features a central area with a slightly larger  $T_C$  than the edge of the sample. However, the spatial variation of  $T_C$  is on the order of the pixel size ( $75 \mu\text{m}$ ) which is much smaller than the actual resolution of the setup of about 0.7 mm. In contrast, the  $T_C$ -maps of the scans at 10 and 100 mT are smoother and more consistent with the resolution of the NDI setup. A comparison of the zero-field results with the results at finite fields excludes temperature gradients and strain within the sample as a cause for the distribution of  $T_C$ . As no physical effect explains the grainy distribution of  $T_C$  in the zf measurements, an artifact from the fitting algorithm is the likeliest explanation for the behavior of the zero-field results. For the fitting of the data at finite fields Eq. 2.9 was utilized which is simpler and has less free parameters than Eq. 2.7, which is used for the zero-field evaluation. The latter is therefore more susceptible to a false convergence of the fit. Although the fitting procedure was carefully checked by plotting about 4% of the total number of fits, a difference of 0.1 K in  $T_C$  may not be visible to the naked eye. As the exact origin of the artifact is unknown at this point, no better evaluation of the zero-field data can be given here.

The  $T_C$ -maps of the data at finite fields show only small variations of  $T_C$  with a standard deviation of 0.03 K across the sample indicating a homogeneous sample. Another value for  $\Delta T_C$  is derived for every pixel by convoluting the fitting function with a gaussian

distribution with a width of  $\Delta T_C$ . This value gives the distribution of  $T_C$  in the  $z$ -direction (along the flight path of the neutrons). In case of the CePt measurements the  $\Delta T_C$  in the  $z$ -direction is one order of magnitude larger than the  $\Delta T_C$  in the  $x$ - $y$ -plane. This discrepancy can be explained by the critical fluctuations of the magnetization close to the phase transition. As already seen in Fig. 5.14, the critical fluctuations cause an additional contribution to the depolarization resulting in a broadened phase transition. A large part of this broadening is captured in the width of the gaussian convolution, resulting therefore in an overestimated  $\Delta T_C$  in  $z$ -direction. The actual variation of  $T_C$  is thus better described by the value derived from the distribution of  $T_C$  in the  $x$ - $y$ -plane.

In conclusion, the results of the susceptibility, magnetization, and NDI measurements of CePt sample L are all in good agreement with values from the literature indicating a homogeneous CePt polycrystal with a good sample quality.

### 5.3.3.2. Properties of CePt at High Pressures

For the high-pressure ND measurements presented in Sec. 5.3.2.3 the much smaller samples A, B, and C were cut from the central part of sample L. The smaller number of grains in the cuboids in combination with the strong magnetic anisotropy enhances individual sample effects caused by textures, the sample shape or internal stresses. Therefore, deviations from the measurements of the bulk sample and features in the depolarization curves appearing only for a particular sample are expected in the high-pressure measurements. Furthermore, the overall amount of depolarization is expected to decrease with increasing pressure due to the progressing Kondo-shielding of the magnetic moments.

When comparing the temperature scans of sample B in the pressure range between 0.8 and 1.5 GPa to the temperature scan of sample A at 1.1 GPa, it is evident that the shoulders at  $T_k$  are at similar temperatures for sample B but not for sample A. In contrast, the drop of the polarization at  $T_C$  as well as the increase of polarization below  $T_F$  for the zfc-fh scans are consistent for both samples. This suggests that the features labeled with  $T_k$  result from individual sample properties such as textures and defects, while  $T_C$  and  $T_F$  show intrinsic magnetic behavior. At the intermediate pressure of 5.7 GPa a kink below  $T_C$  is not observed in the temperature scans of sample A implying a pressure dependence of the underlying effect. A possible explanation could be a preferred orientation of the grains (texture) in combination with the strong magnetic anisotropy. As the anisotropy of CePt decreases towards higher pressures [223], the kink gradually disappears at a sufficiently high pressure.

Fig. 5.26 shows an updated version of the magnetic phase diagram of CePt containing data from Ref. [37] and from this ND study.  $T_C$  and  $T_F$  derived from ND temperature

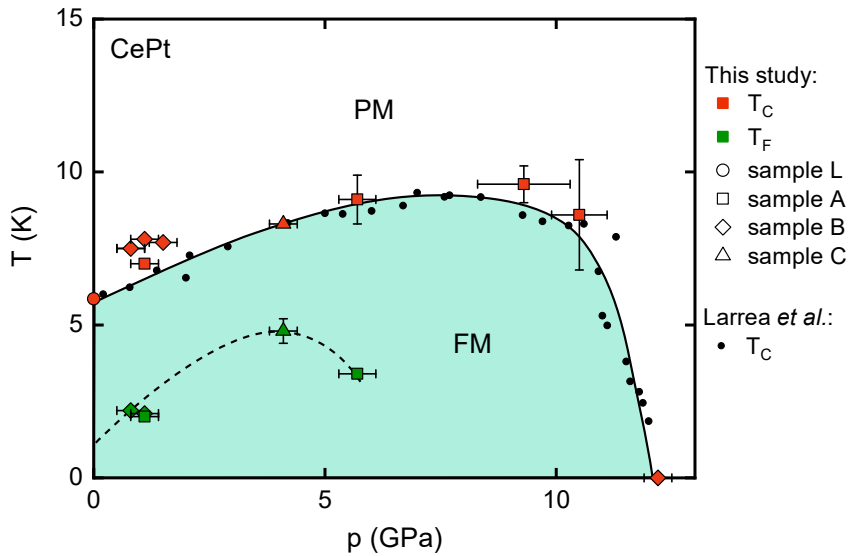


**Figure 5.26.:** High-pressure phase diagram of CePt including data from Larrea *et al.* [37] (black markers) and from this study (red and green markers). The color of the markers differentiates between  $T_C$  and  $T_F$ , and the shape of the markers indicates the measured sample.  $T_C$  derived from ND measurements follows the boundary of the FM phase, previously determined by resistivity and susceptibility measurements, but with a small offset to higher temperatures. In the low to intermediate pressure region an increase of the polarization towards lower temperatures is observed starting at  $T_F$  which is shown as green triangles. The dashed line is a guide to the eye.

scans are depicted by red and green markers, respectively, while  $T_k$  was omitted as the feature at  $T_k$  is not intrinsic to CePt. The different shapes of the markers refer to the investigated samples.  $T_C(p)$  is in good agreement with the measurements by Larrea *et al.* confirming a FM ground state up to a pressure of 10.5 GPa. At 12.2 GPa no depolarization could be detected as either  $T_C$  was suppressed to zero or the value of  $B_0^2\delta$  fell below the detection threshold.

The small positive offset of  $T_C$  in the phase diagram compared to the data from Larrea *et al.* – especially in the low-pressure region – can be explained by the critical fluctuations which start to depolarize the neutron beam slightly above  $T_C$ . Although a direct comparison of temperature scans at different pressures regarding the absolute depolarization is not possible, it is evident that the depolarizing effect weakens with increasing pressure. This behavior is consistent with the observation of a decreasing magnetic moment due to increasing Kondo interactions [37].

The low-temperature feature labeled as  $T_F$  in the zfc-fh temperature scans of CePt is reminiscent of the zfc-fh scans of  $\text{CePd}_{1-x}\text{Rh}_x$  (c. Fig. 5.5). Both systems are FM Kondo-lattices with an orthorhombic crystal structure and a strong magnetic anisotropy. However, the main difference between the systems is how the tuning parameter  $|\Gamma n(E_F)|$  is

adjusted. In the case of  $\text{CePd}_{1-x}\text{Rh}_x$  chemical pressure is exerted on the crystal structure by the substitution of Pd with smaller Rh, while in the case of CePt hydrostatic pressure is utilized. The substitution introduces disorder into  $\text{CePd}_{1-x}\text{Rh}_x$  with increasing Rh content  $x$ , resulting in a ground state described by the Kondo cluster glass model (c. Sec. 5.2.3). The low-temperature feature observed in the zfc-fh scans of  $\text{CePd}_{1-x}\text{Rh}_x$  is then explained by a thermal activation of Kondo-screened moments close to a FM cluster leading to a growth of the cluster. However, the Kondo cluster glass model cannot be used to describe CePt due to the much lower level of disorder compared to  $\text{CePd}_{1-x}\text{Rh}_x$ . The Kondo-screening of the magnetic moments in  $\text{CePd}_{1-x}\text{Rh}_x$  happens on a small spatial scale at very different temperatures resulting in FM clusters surrounded by screened moments. In contrast, previous studies on CePt are more consistent with a Kondo-screening as proposed in Doniach's phase diagram, i.e. the magnetic moments are gradually and equally screened, implying a homogeneous FM ground state up to high pressures.

Therefore, the initial decrease of the polarization up to  $T_F$  in the zfc-fh scans of CePt is better explained by a pinning of domain walls on lattice defects and grain boundaries at low temperatures. When cooling the sample in zero field only small domains form, which is in agreement with the ND field scans and the results of  $\text{CePd}_{1-x}\text{Rh}_x$ . Applying a finite field at base temperature results in a moderate increase of the average domain size, however, the domain walls are partially pinned at crystal defects or grain boundaries. With increasing temperature the domain walls are thermally activated and can overcome their pinning, leading to larger domains and, therefore, a decrease of polarization. The initial increase of  $T_F(p)$  towards intermediate pressures can be explained by the introduction of additional lattice defects caused by the increasing pressure. The difference in  $T_F$  at 4.1 and 5.7 GPa may result from varying pressure conditions of the two runs (sample A and C). This could introduce different amounts of lattice defects leading to different  $T_F$ .

## 5.4. Conclusions

The two FM Kondo lattices  $\text{CePd}_{1-x}\text{Rh}_x$  and CePt were investigated using the ND technique in order to trace the suppression of FM order caused by the Kondo effect. However, the effects of the different control parameters – chemical composition  $x$  and hydrostatic pressure  $p$ , respectively – lead to different manifestations of the Kondo-screening, affecting the FM domain structure and the FM itself. The ND technique is, therefore, an ideal tool to investigate these systems as it is sensitive to FM on the microscopic and the mesoscopic scale. Furthermore, NDI measurements were performed on the samples of both systems validating the magnetic homogeneity on the macroscopic scale.

The results of the ND measurements on  $\text{CePd}_{1-x}\text{Rh}_x$  are in good agreement with previous measurements of  $T_C(x)$  confirming the magnetic phase diagram. Furthermore, the observed behavior of the magnetic domains is well explained by the Kondo cluster glass model by Westerkamp *et al.*, highlighting the role of chemical disorder on the magnetic ground state. A small extension was added to the model in order to describe the freezing of the domains below a characteristic temperature  $T_F$ . Additionally, the effect of a strong magnetic anisotropy on ND experiments was investigated by measuring a  $\text{CePd}_{1-x}\text{Rh}_x$  single crystal. These measurements contribute to the interpretation of ND signals as they explain a secondary effect (next to the formation of FM domains) that can influence the neutron polarization.

In a second study, the pressure-driven phase diagram of CePt was investigated using the new high-pressure ND setup. FM behavior was confirmed up to 10.5 GPa and the boundary of the FM phase  $T_C(p)$  is in good agreement with values from the literature. Although sample-dependent behavior is observed in several temperature scans,  $T_C(p)$  shows clean and consistent behavior suggesting a possible QCP at  $\sim 12$  GPa. Additionally, an increase of the polarization in zfc-fh scans below  $T_F$  was observed, similar to equivalent scans of  $\text{CePd}_{1-x}\text{Rh}_x$ . While the reason for this is similar on the mesoscopic scale and can be described by a freezing of the domains, the reason on the microscopic scale is different. In  $\text{CePd}_{1-x}\text{Rh}_x$  the FM clusters are surrounded by Kondo-screened moments, which are re-activated above  $T_F$ , resulting in an increase of the domain size. However, in CePt the measurements suggest that the domain walls are pinned to lattice defects below  $T_F$ .



## 6. Conclusions

In the course of the present work the FM of magnetite,  $\text{SrRuO}_3$ ,  $\text{CePd}_{1-x}\text{Rh}_x$ , and  $\text{CePt}$  was investigated using the ND technique with the measurements on  $\text{SrRuO}_3$  and  $\text{CePt}$  being performed under high pressures. The results and main conclusions are summarized in the following.

Natural SD magnetite extracted from chiton teeth was investigated using ND and magnetization measurements. Magnetic field scans in both techniques above and below the Verwey transition showed an overall decrease of the coercivity with increasing temperature; however, the coercivities determined from the ND measurements featured consistently positive offset of 7 mT. The difference is ascribed to the change of the domain size with varying field since ND measurements are susceptible to the domain size while conventional magnetometry averages over the sample. An ND temperature scan across the Verwey transition revealed a feature at  $T_V = 118\text{ K}$  that is in very good agreement with magnetization measurements. This enables a systematic investigation of the pressure dependence of the Verwey transition using the HP-ND setup. The additional information about the domain sizes determined from ND measurements close to  $T_V$  could clarify the mechanism behind the feature at  $T_V$  in magnetic measurements that, in turn, could explain the pressure dependence of  $T_V$  after pressure-cycling. This would contribute to the efficacy of the usage of magnetite as a geobarometer.

The magnetic phase diagram of the itinerant FM  $\text{SrRuO}_3$  was investigated using the ND technique up to a hydrostatic pressure of 17.1 GPa. Values of the Curie temperature  $T_C$  could be determined up to 11.4 GPa and are in good agreement with the phase diagram by Hamlin *et al.* derived from susceptibility and resistivity measurements [33]. Although a measurement of  $T_C$  at 17.1 GPa failed due to a decreasing sample signal with increasing pressure, a ND magnetic field scan at this pressure featured hysteresis, indicating a FM ground state. Estimates show that ND magnetic field scans are able to extend the phase diagram of  $\text{SrRuO}_3$  to pressures above 17.1 GPa that could reveal if  $\text{SrRuO}_3$  features a tricritical point as seen in other quantum critical FMs.

ND studies of the FM Kondo-lattices  $\text{CePd}_{1-x}\text{Rh}_x$  and  $\text{CePt}$  were performed in order to compare their magnetic phase diagrams and their magnetic ground states as both systems crystallize in the same structure and the suppression of the FM relies

on the same mechanism. The ND measurements of  $\text{CePd}_{1-x}\text{Rh}_x$  at intermediate and high Rh concentrations confirm the phase diagram and are in good agreement with the Kondo cluster glass model by Westerkamp *et al.* [11]. Furthermore, ND measurements investigating the effect of a uniaxial anisotropy on the measured polarization were carried out utilizing the strong anisotropy of  $\text{CePd}_{1-x}\text{Rh}_x$ . The measurements feature oscillations in the polarization signal close to  $T_C$  that were explained by extending the ND theory developed by Halpern and Holstein [14].

The polycrystalline CePt sample was characterized using the NDI setup, indicating a homogeneous sample with a  $T_C$  in good agreement with values from the literature. Subsequently, ND measurements under high pressures up to 12.2 GPa were performed. The results are in good agreement with the phase diagram by Larrea *et al.* determined from susceptibility and resistivity measurements [37] and indicate a QCP at about 12 GPa. Furthermore, features in the polarization signal below  $T_C$  were observed which could be ascribed to a pinning of the domain walls at low temperatures.

Comparing the ND results of  $\text{CePd}_{1-x}\text{Rh}_x$  and CePt reveals the effect of disorder on the shape of the phase diagram and the magnetic ground state. CePt is driven by the clean control parameter  $p$  resulting in a phase diagram in good agreement with the Doniach model and a normal FM ground state. In contrast, the disorder introduced by doping in  $\text{CePd}_{1-x}\text{Rh}_x$  causes a smearing of the QPT and a complicated ground state consisting of FM clusters.

The appearance of complex types of FM order in quantum critical FMs emphasizes the need for ND measurements, as the ND technique can detect FM at high pressures and gives further information on the mesoscopic length scales of the FM order. Due to the high pressures involved in the present measurements and the consequently small sample sizes, the depolarization signals were in some cases close to the resolution limit of the utilized ND setups. In order to obtain robust polarization data, a strong emphasis was put on the data evaluation and the estimation of errors. Measurement protocols were implemented to reduce the effects of systematic errors and a guide for the interpretation of depolarization measurements was developed to distinguish between errors and actual depolarization. Furthermore, the resolution of the ND setups regarding the detectable length and time scales of FM order was calculated. Depending on the magnetic moment of the investigated system, FM domains on a length scale of nm and fluctuating forms of FM on a time scale of sub-ns can be detected.

For future measurements the potential of the ND technique can be used to investigate the phase diagrams of other quantum critical FMs such as  $\text{LaCrGe}_3$ . This system features a pressure-induced tricritical point at 1.5 GPa and a complete suppression of the FM

phase at  $p_C \sim 2.1$  GPa [256]. Additionally, an adjacent high-pressure phase was identified showing signs of a short-ranged FM order [257]. ND measurements are ideally suited to clarify the magnetic order observed in this phase.



# A. Appendix

## A.1. Neutron Depolarization Imaging of UGe<sub>2</sub>

UGe<sub>2</sub> shows FM with a Curie temperature of  $T_C = 53$  K at ambient pressure. Applying hydrostatic pressure weakens the FM order until  $T_C$  is suppressed to zero at a critical pressure of  $p_C = 1.58$  GPa [258]. Additionally, a low-temperature phase between 0.9 GPa and  $p_C$  featuring the simultaneous appearance of FM and superconductivity was found [5]. The nature of the unconventional superconductivity is still under debate. A study by Haslbeck *et al.* [259] using the novel neutron spectroscopy method MIEZE investigated the low-energy spin fluctuations of UGe<sub>2</sub> in order to find the driving mechanism for the unconventional superconductivity. As the sample quality and homogeneity plays an important role for the interpretation of the MIEZE results, the sample was characterized by susceptibility, neutron Laue, and NDI measurements. The results of the NDI measurements are presented here.

The annealed UGe<sub>2</sub> single crystal is a cylinder with a nearly constant diameter of 7 mm and a length of 15 mm. The sample was mounted in a CC cryostat with the c-axis in the horizontal plane and perpendicular to the beam direction (along the x-axis in the ANTARES coordinate system). An electro-magnet was not installed, however, a guide field of 0.5 mT was present at the sample position. The sample was cooled down to 10 K and measured during heating with a temperature step size of 1 K for  $T < 50$  K and  $T > 60$  K, and with temperature steps of 0.1 K in the region  $50 \text{ K} < T < 60 \text{ K}$ .

The sample length could not be fitted within one continuously polarized area of the analyzer. Therefore, in order to cover the whole sample, two polarization measurements with different x-positions of the sample were taken per temperature. Three up and down images were taken per polarization measurement. A spatial resolution of approximately 1 mm was achieved.

Due to the strong depolarization of the sample, Eq. 2.9 was chosen for the data evaluation. This equation convoluted with a gaussian distribution was then fit to every pixel-position (x,y) of the polarization data as a function of temperature. Therefore, the transition temperature  $T_C$  and the width of the gaussian distribution  $\Delta T_C$  can be

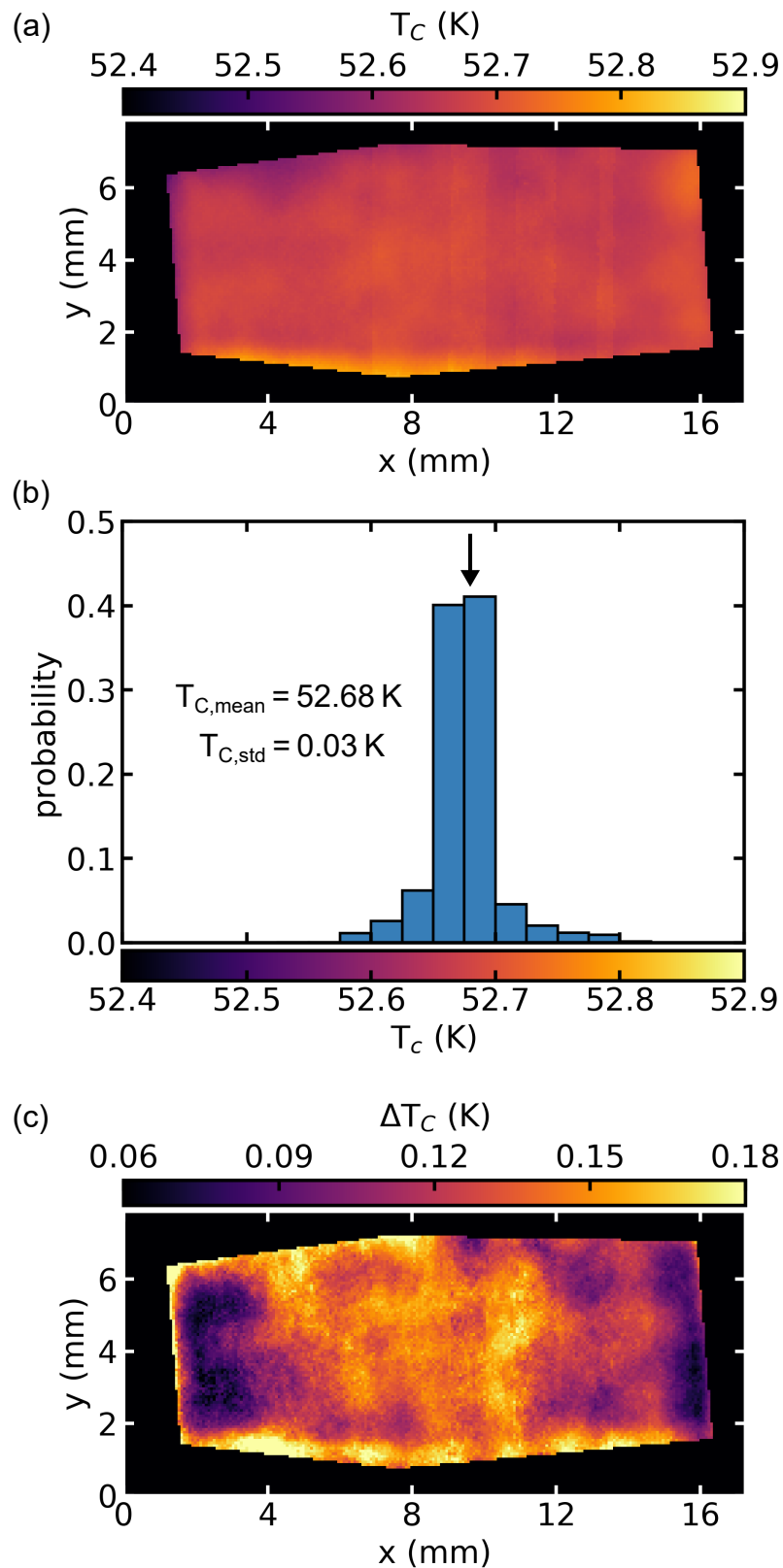


**Figure A.1.:** NDI results of a UGe<sub>2</sub> single crystal. (a)  $T_C$ -map of the UGe<sub>2</sub> sample where the Curie temperature  $T_C$  is shown as a function of position  $(x,y)$ . (b) Histogram representation of the data from the  $T_C$ -map. The average Curie temperature of the sample  $T_{C,\text{mean}} = 52.68$  K is marked with a black arrow. (c) 2d representation of the width  $\Delta T_C$  of the FM transition similar to a  $T_C$ -map.

determined for every pixel. Fig. A.1(a) shows the Curie temperature as a function of  $(x,y)$ , subsequently called a  $T_C$ -map.  $T_C$  is homogeneous across the whole sample except for small deviations at the top left and the bottom which may result from a small temperature gradient across the sample. The vertical lines on the right-hand side of the sample are artifacts from the data fusion of the polarization images at different x-positions. A histogram representation of the data from the  $T_C$ -map is given in Fig. A.1(b) where the x-axis displays the same temperature range as the color bar in (a). The  $T_C$ -distribution shows a sharp peak with an average of  $T_{C,\text{mean}} = 52.68$  K and a standard deviation of  $T_{C,\text{std}} = 0.03$  K. The average  $T_{C,\text{mean}}$  is in very good agreement with the susceptibility measurements and values from the literature [260]. Fig. A.1(c) shows the fit parameter  $\Delta T_C$  which is a measure for the distribution of  $T_C$  along the neutron flight path through the sample. Although the values vary widely from 0.06 to 0.18 K across the sample, a FM transition with a width of  $\Delta T_C < 0.2$  K at  $T_C = 52.68$  K is still very sharp. Furthermore, the values of  $\Delta T_C$  are in good agreement with  $T_{C,\text{std}} = 0.03$  K. To summarize, the narrow distribution of transition temperatures confirms that the sample homogeneity is adequate for the requirements of MIEZE measurements.

## A.2. Supplementary Magnetite Data

This section of the appendix contains additional magnetization data of two magnetite samples which were not shown in the main text. Magnetization measurements of VSM sample 2 at temperatures of 80, 140, and 300 K are shown in Fig. A.2. Additionally, magnetization measurements of the NDI sample temperatures of 80 and 300 K are shown in Fig. A.3. The coercivities determined from linear fits to the magnetization data close to  $M = 0$  are listed in the main text in Tabs. 3.1 and 3.2.

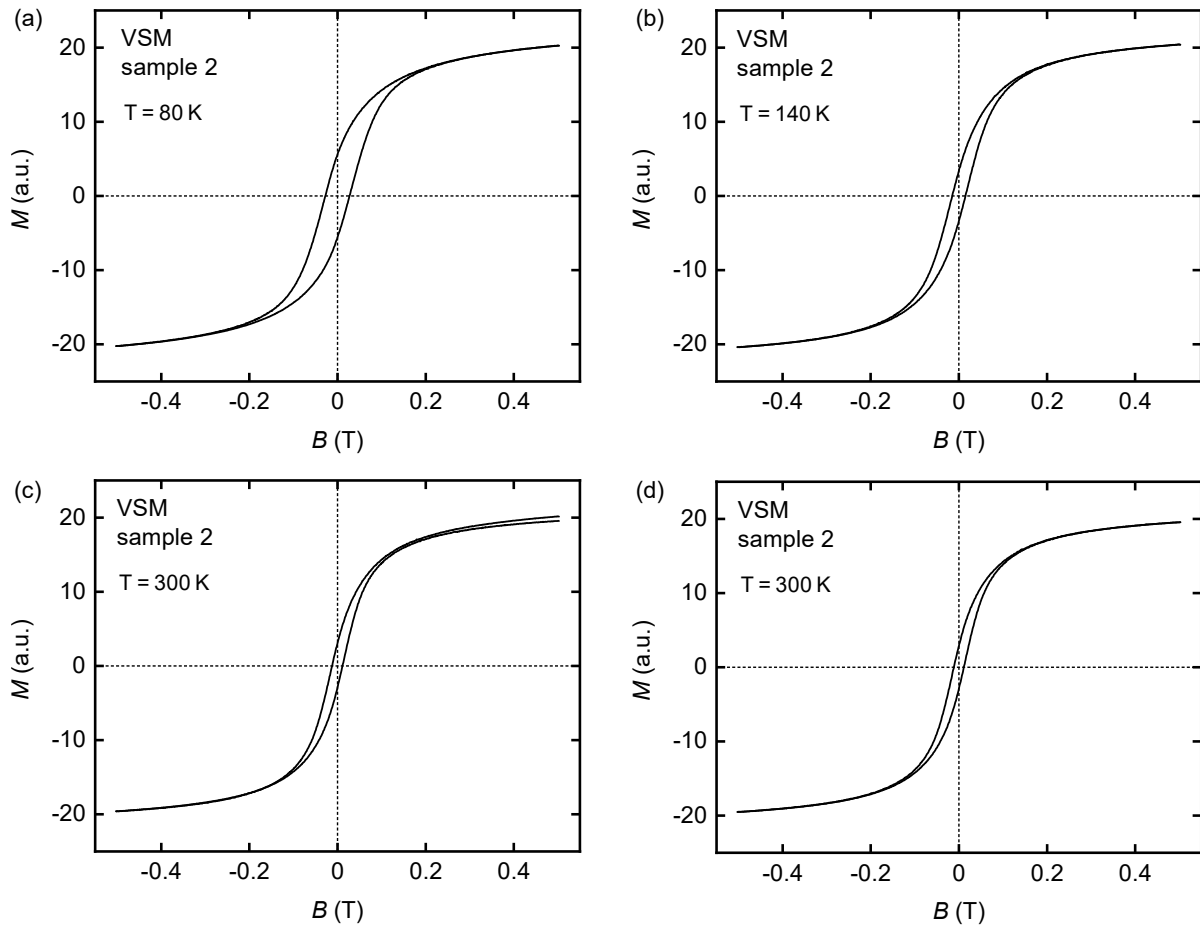


**Figure A.2.:** Magnetization measurements using a VSM of the magnetite sample identified as VSM sample 2 at temperatures of (a) 80 K, (b) 140 K, and (c-d) 300 K.

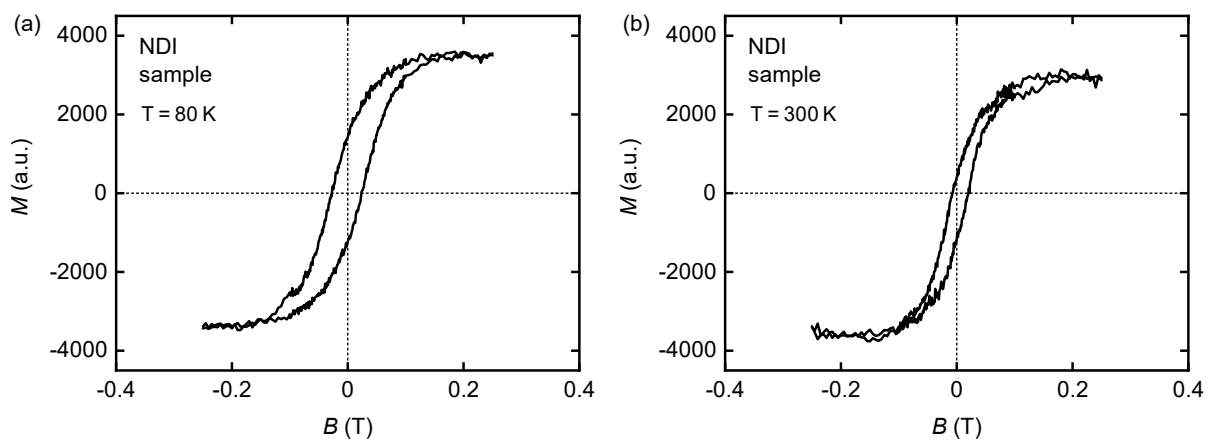
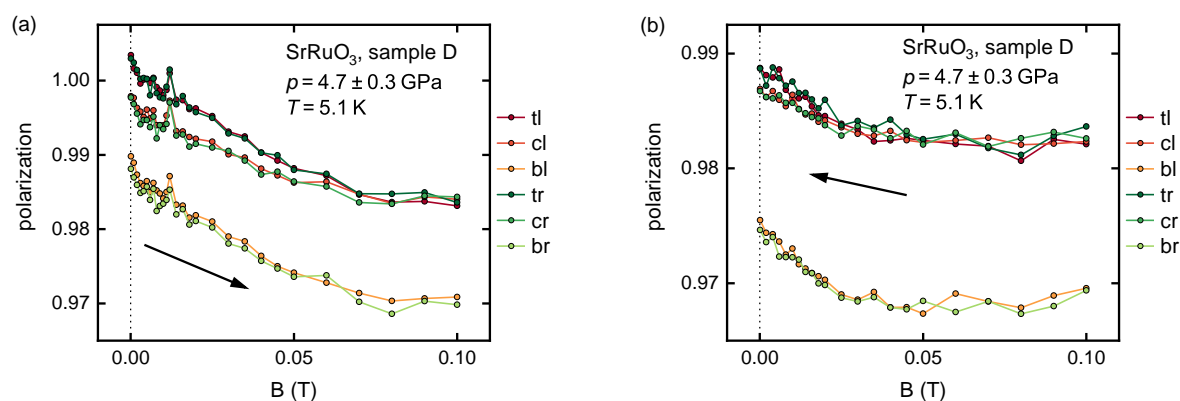


**Figure A.3.:** Magnetization measurements using a PPMS of the magnetite sample identified as NDI sample at temperatures of (a) 80 K and (b) 300 K.

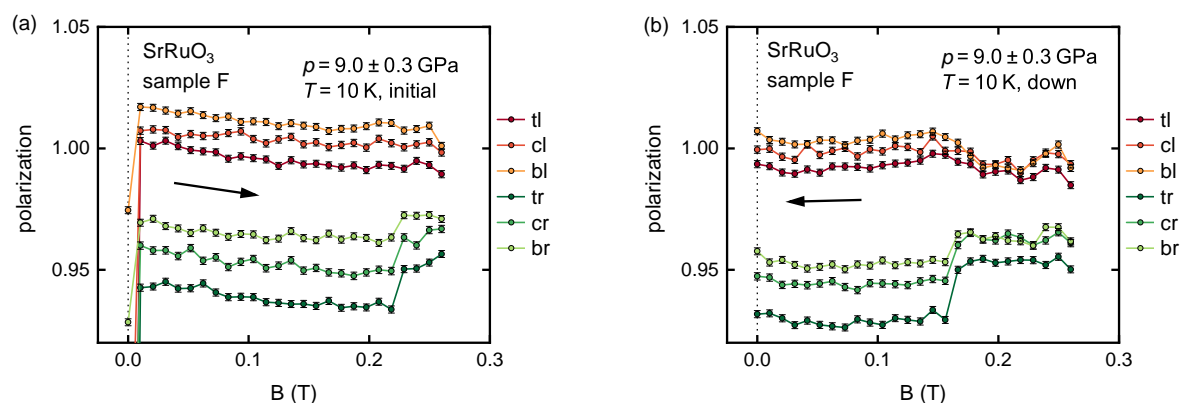
## A.3. Supplementary SrRuO<sub>3</sub> Data

As discussed in the main text several data sets of ND measurements on SrRuO<sub>3</sub> were moved to the appendix. Sec. A.3.1 contains the plots of  $3 \times 3$  guide pattern polarizations which correspond to the data shown in Sec. 4.2. Furthermore, ND measurements where no meaningful conclusion could be drawn are shown in Sec. A.3.2.

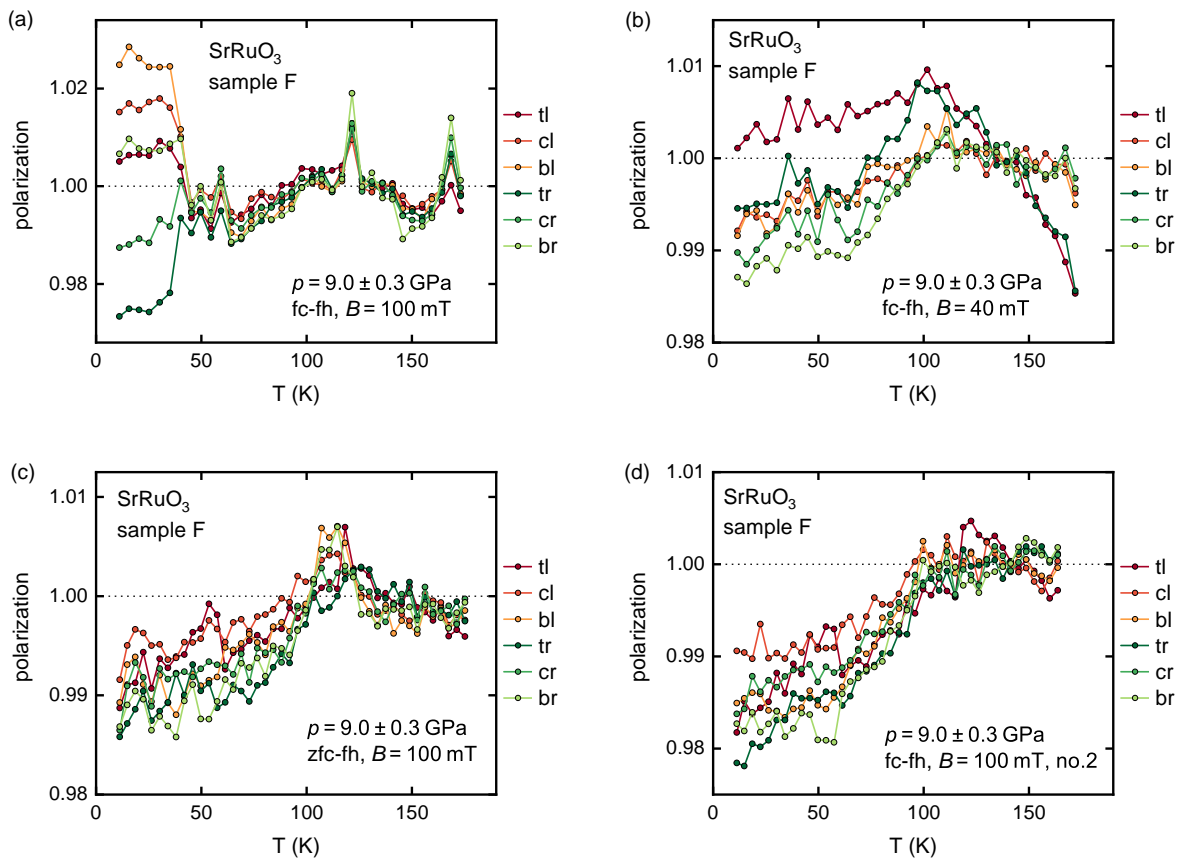
### A.3.1. $3 \times 3$ Guide Pattern Polarizations of Measurements Shown in Sec. 4.2



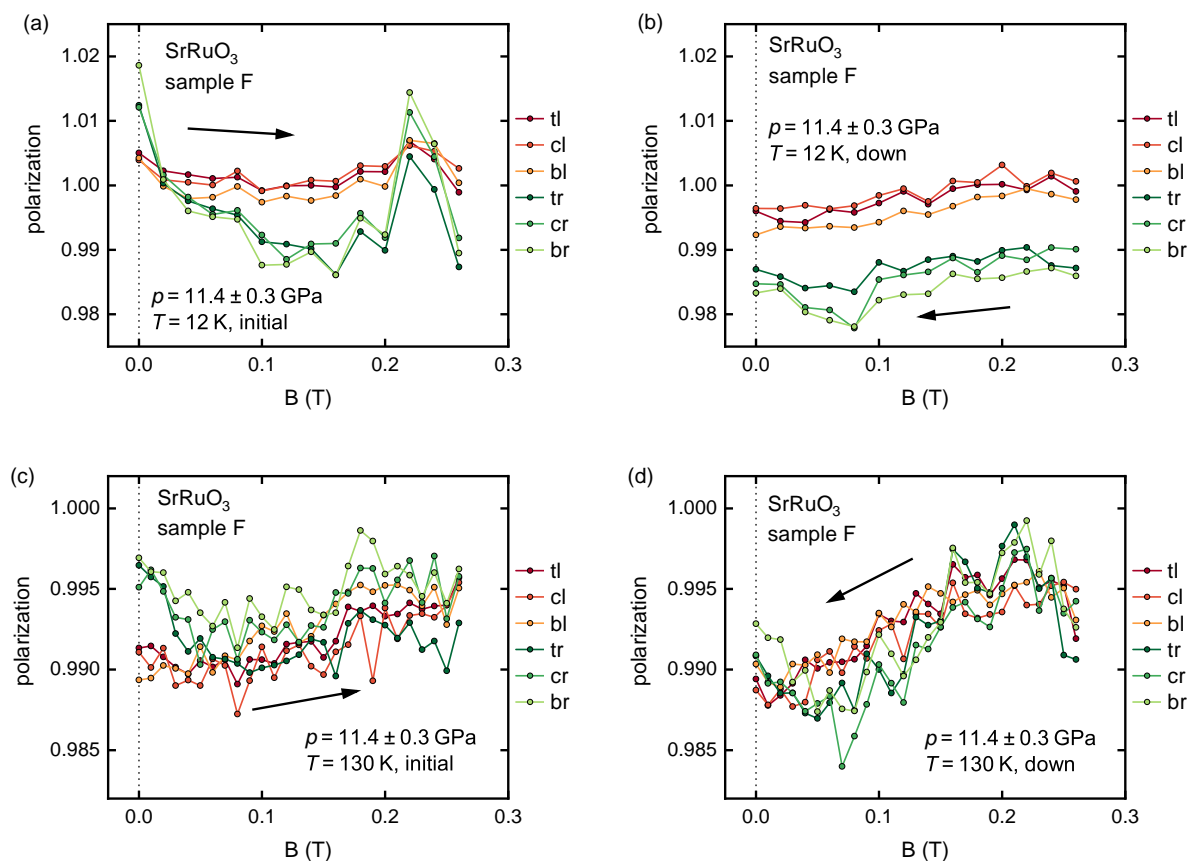
**Figure A.4.:** Raw polarizations of the magnetic field scan shown in Fig. 4.3. After cooling SrRuO<sub>3</sub> sample D in zero field to  $T = 5.1$  K the field was (a) increased to 100 mT and then (b) decreased to zero again.



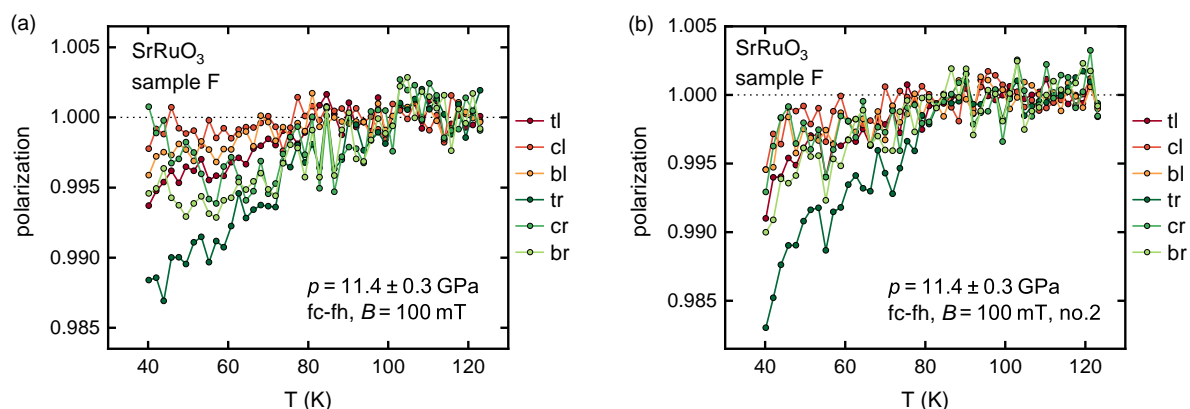
**Figure A.5.:** Raw polarizations of the magnetic field scan shown in Fig. 4.6. After cooling SrRuO<sub>3</sub> sample D in zero field to  $T = 10$  K the field was (a) increased to 100 mT and then (b) decreased to zero again. Jumps in the polarizations caused by a horizontal movement of the neutron guides are visible at (a) 225 mT and (b) 160 mT.



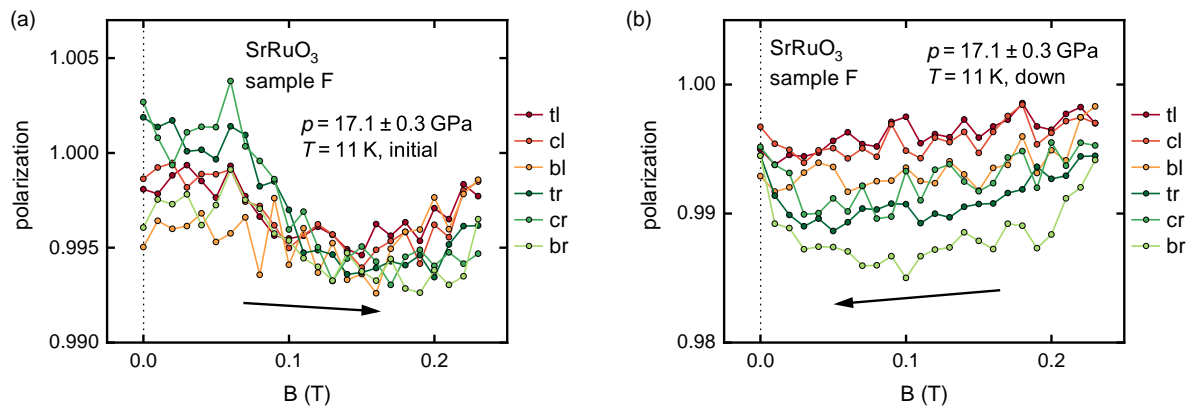
**Figure A.6.:** Raw polarizations of the temperature scans shown in Fig. 4.7. While the fc-fh scan in (a) features artifacts from the afterglow effect and the vertical movement of the pressure cell, an improving measurement protocol lead to a suppression of the artifacts in (d).



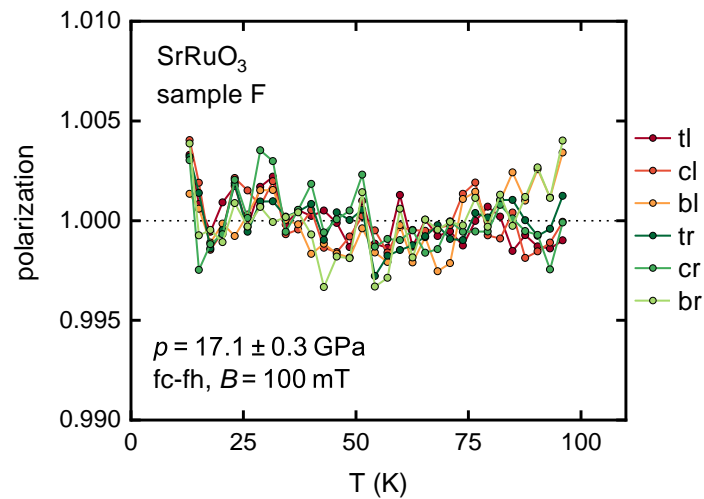
**Figure A.7.:** Raw polarizations of the magnetic field scans shown in Fig. 4.8. After cooling SrRuO<sub>3</sub> sample F in zero field to the intended temperature of (a)-(b) 12 K and (c)-(d) 130 K at a pressure of 11.4 GPa, the field was increased to 260 mT and then decreased to zero again.



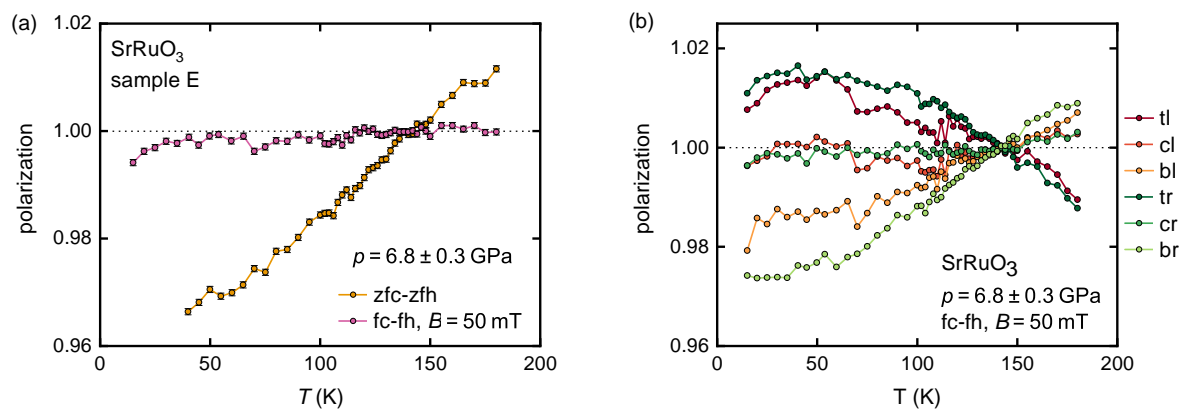
**Figure A.8.:** Raw polarizations of the temperature scans shown in Fig. 4.9. (a) Oscillations of the temperature controller cause a significant increase of noise at about 85 K due to the afterglow effect. (b) A repetition of the scan with identical parameters shows less artifacts.



**Figure A.9.:** Raw polarizations of the magnetic field scan shown in Fig. 4.10. After cooling SrRuO<sub>3</sub> sample F in zero field to  $T = 11$  K the field was (a) increased to 230 mT and then (b) decreased to zero again.



**Figure A.10.:** Raw polarizations of the temperature scan shown in Fig. 4.11.

A.3.2. Inconclusive SrRuO<sub>3</sub> Measurements

**Figure A.11.:** ND temperature scans of SrRuO<sub>3</sub> sample E at a pressure of 6.8 GPa. (a) Two temperature scans were performed, one in zero field (zfc-zfh) and one cooled in a field of 50 mT and measured in the same field. No signatures of the transition to the FM phase is visible due to artifacts resulting from a vertical movement of the pressure cell. (b) Raw polarizations of the fc-fh temperature scan at 50 mT. The raw polarizations of the zfc-zfh temperature scan were used as an example in the main text and are shown in Fig. 2.16.

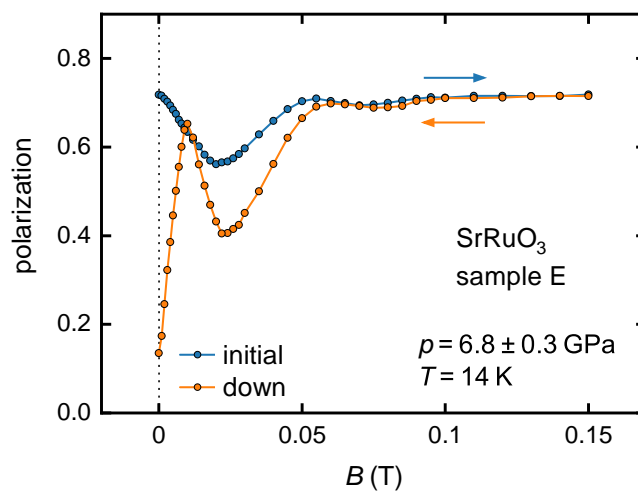


**Figure A.12.:** Magnetic field scan of SrRuO<sub>3</sub> sample E at 6.8 GPa and 14 K. Due to a misalignment of the fields along the neutron flight path the polarization rotates around the magnetic field created by the magnet. This manifests itself in the sine-like oscillations in the polarization with a large amplitude. Similar field scans were performed after a readjustment of the ND setup at 12 and 180 K also showing oscillations.

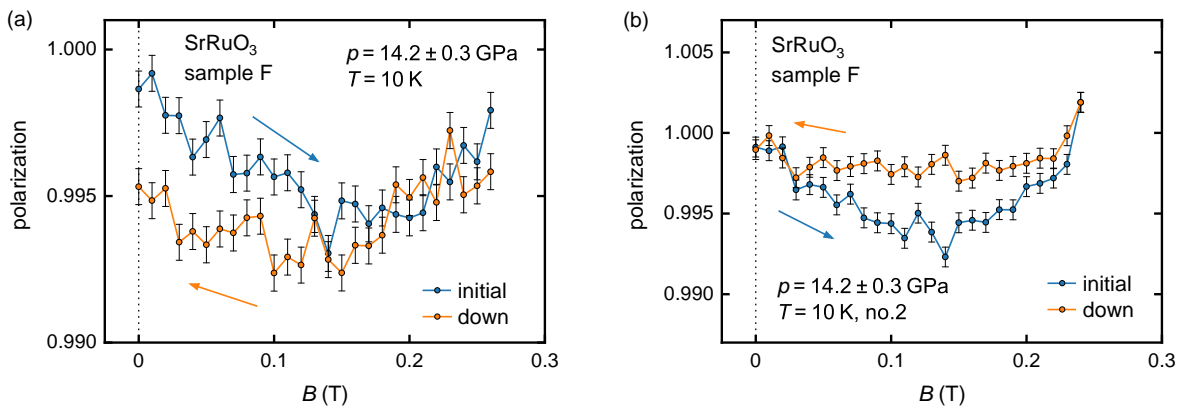


**Figure A.13.:** Magnetic field scans of SrRuO<sub>3</sub> sample F at 14.2 GPa and 10 K. (a) The field scan shows typical behavior for a FM, however, the hysteresis is comparatively small. (b) A repetition of the field scan shows strongly deviating behavior with the polarization of the field-increasing part being smaller than the polarization of the field-decreasing part. As both scans show opposite trends for the same external parameters, no meaningful conclusion can be drawn.

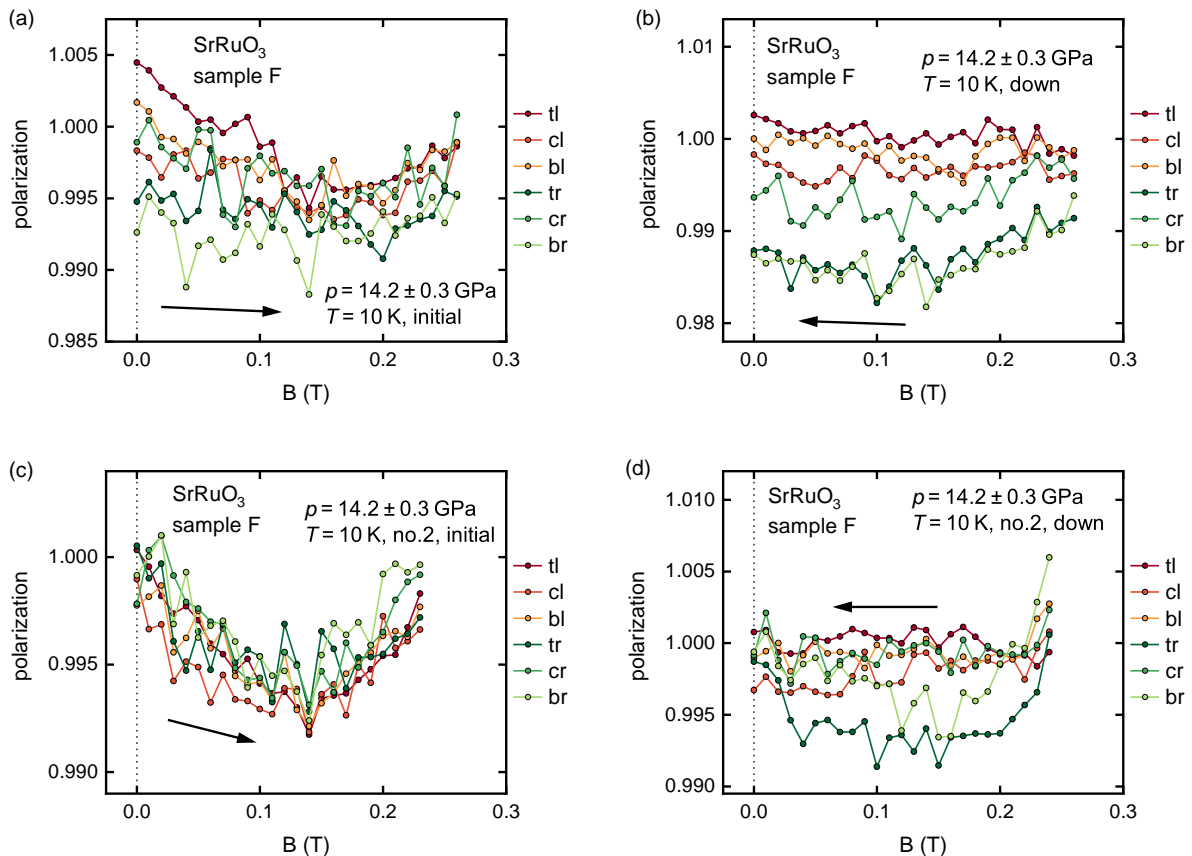


**Figure A.14.:** Raw polarizations of the magnetic field scans shown in Fig. A.13.

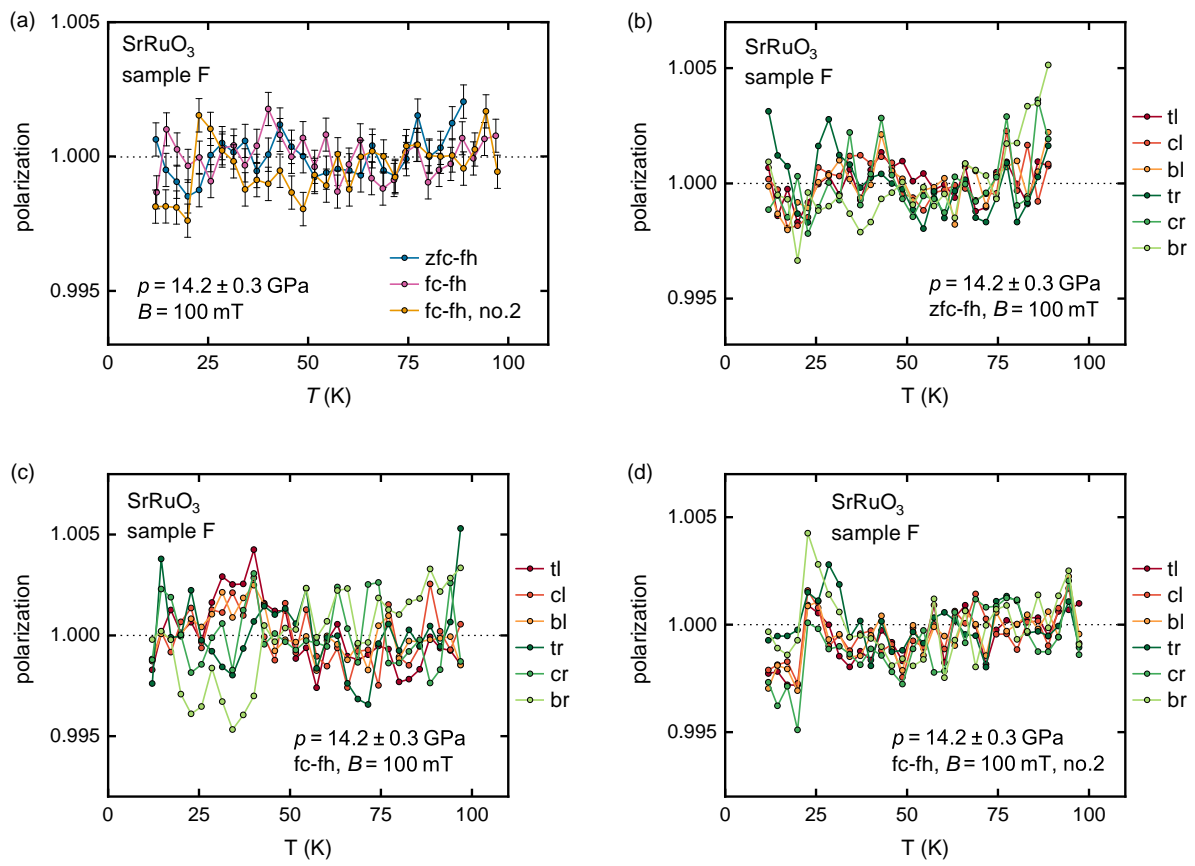


**Figure A.15.:** ND temperature scans of SrRuO<sub>3</sub> sample F at a pressure of 14.2 GPa. (a) Temperature scans were measured in a field of 100 mT once after zero-field cooling and twice after field cooling, however, no depolarization was observed. (b)-(d) Corresponding raw polarizations of the temperature scans shown in panel (a).

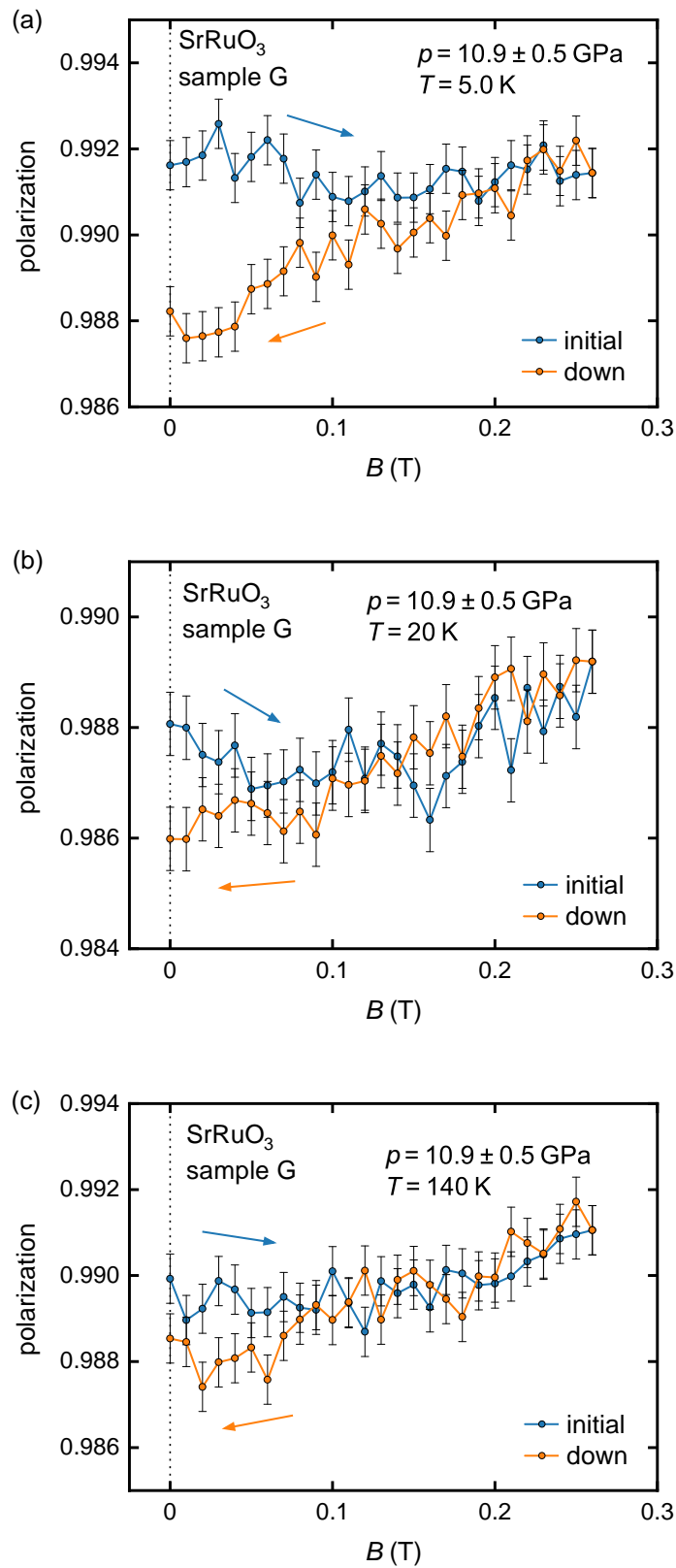


**Figure A.16.:** Magnetic field scans of SrRuO<sub>3</sub> sample G at 10.9 GPa and temperatures of (a) 5 K, (b) 20 K, and (c) 140 K. While hysteresis is observed at 5 K, no hysteresis can be seen at 20 and 140 K. Although this could imply a  $T_C$  below 20 K, this would disagree with the temperature scans at this pressure and with temperature scans of sample F at 11.4 GPa shown in Fig. 4.9.

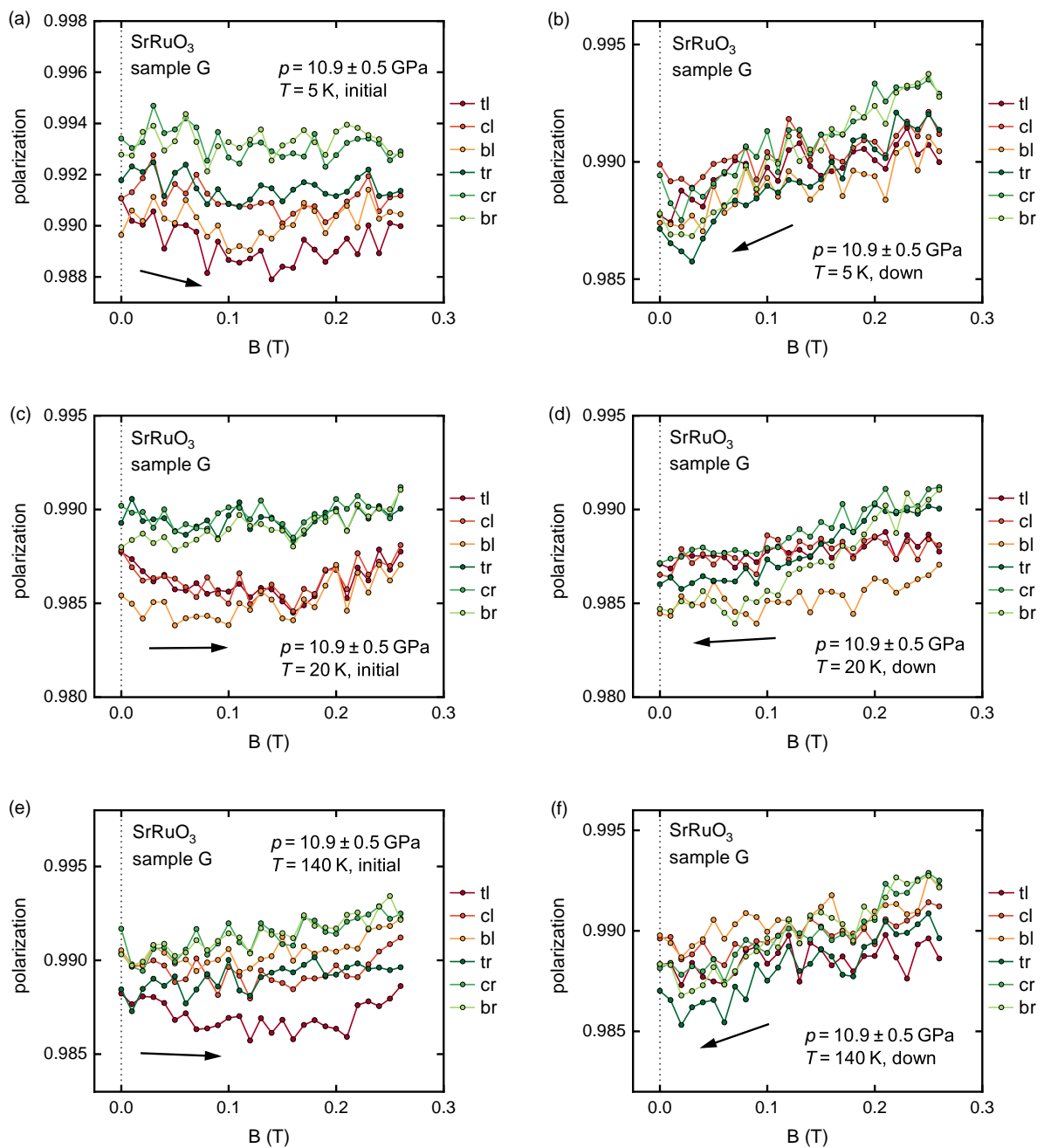
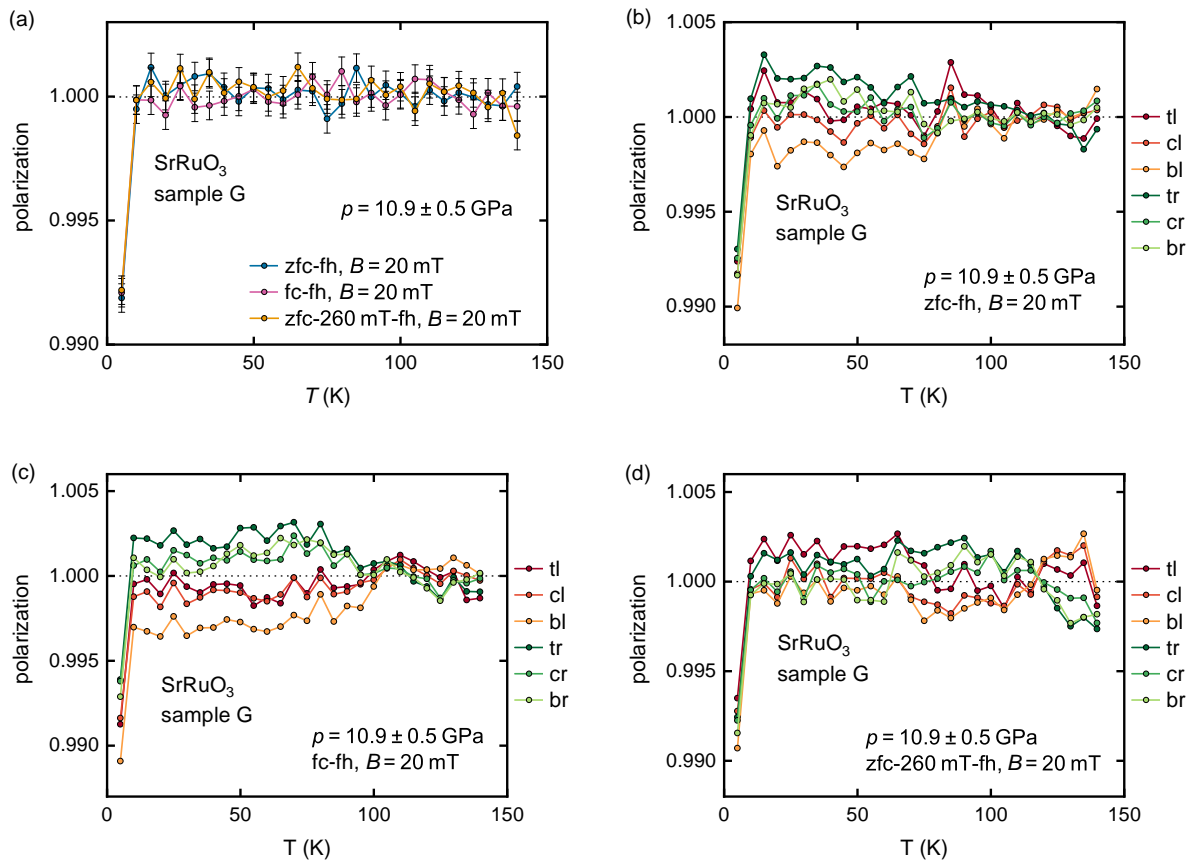
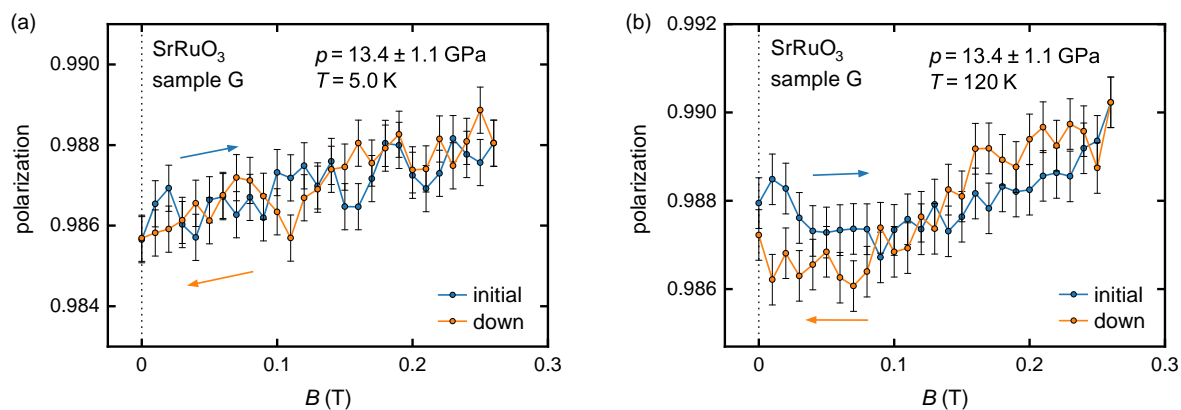


Figure A.17.: Raw polarizations of the magnetic field scans shown in Fig. A.16.



**Figure A.18.:** ND temperature scans of  $\text{SrRuO}_3$  sample G at a pressure of 10.9 GPa. (a) Temperature scans were measured in a field of 20 mT after zero-field cooling, after field cooling, and after cooling in zero field, then applying 260 mT for a few seconds and then measuring in a field of 20 mT. The latter scan was performed in order to reach a starting point of the temperature scan equivalent to a low-field value of a magnetic field "down" scan as shown in Fig. A.16. All temperature scans are affected by the afterglow effect at the lowest temperature and no depolarization is observed. (b)-(d) Corresponding raw polarizations of the temperature scans shown in panel (a). All temperature scans show a relative movement of the pressure cell to the neutron beam.



**Figure A.19.:** Magnetic field scans of SrRuO<sub>3</sub> sample G at 13.4 GPa and temperatures of (a) 5 K and (b) 120 K. While no hysteresis is observed at 5 K indications of hysteresis can be seen at 130 K. However, the latter is barely distinguishable from the theoretically calculated errors and may therefore lie within the actual error. Furthermore, the existence of hysteresis at 130 K would imply FM order at a temperature which is contradictory to the measurements shown in Sec. 4.2 and the non-existing hysteresis at 5 K.

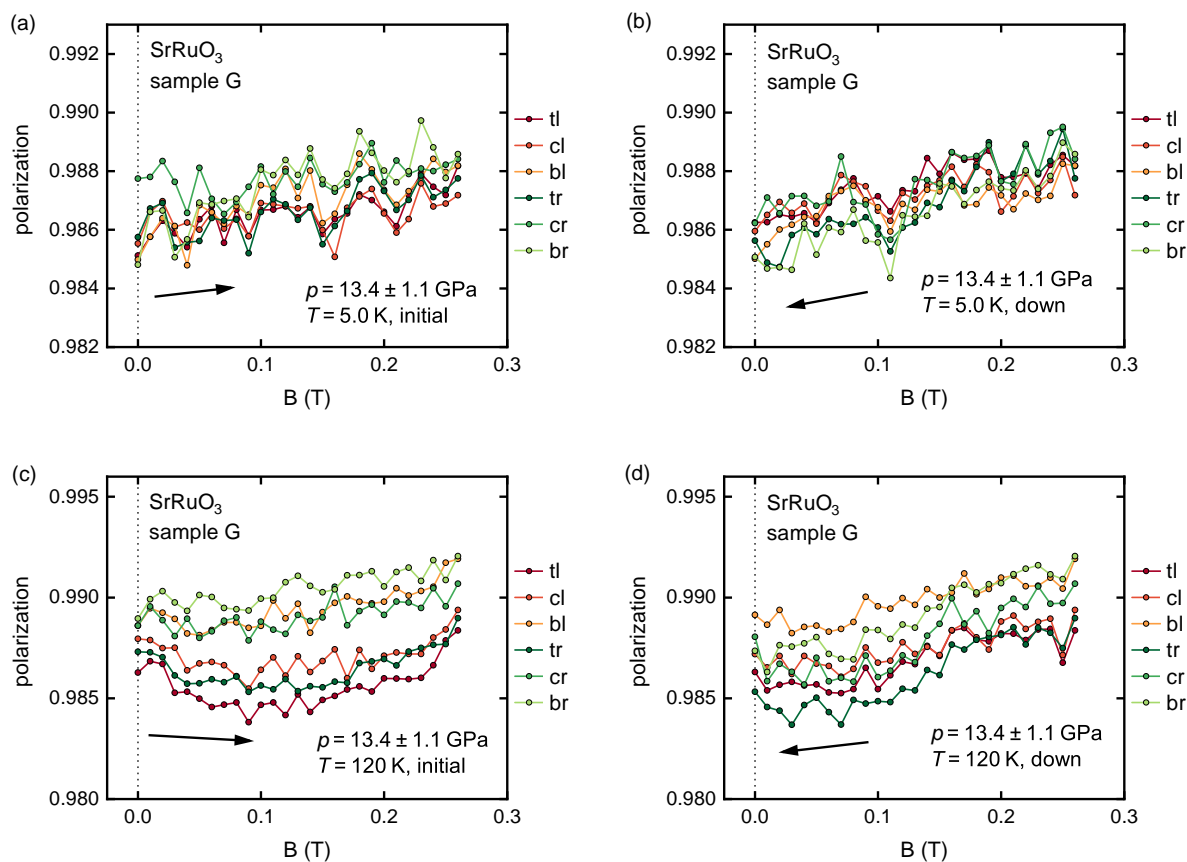


**Figure A.20.:** Raw polarizations of the magnetic field scans shown in Fig. A.19.

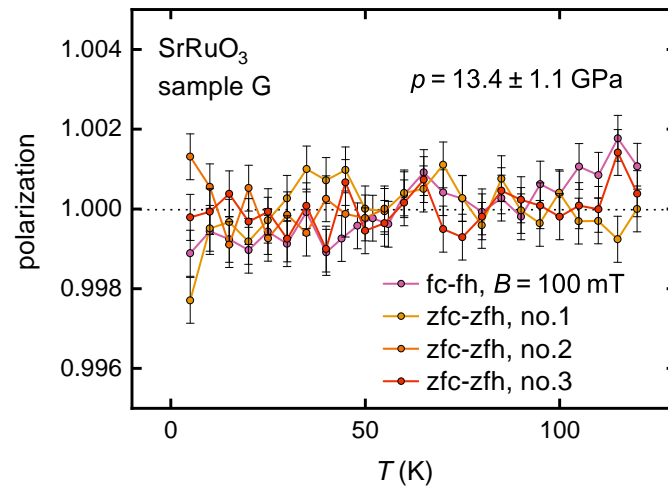


**Figure A.21.:** ND temperature scans of SrRuO<sub>3</sub> sample G at a pressure of 13.4 GPa for different applied fields. Three temperature scans were measured in zero field due to an error in the control software. After fixing the error, one temperature scan was measured after field-cooling in a field of 100 mT. However, no depolarization could be detected in any of the scans.

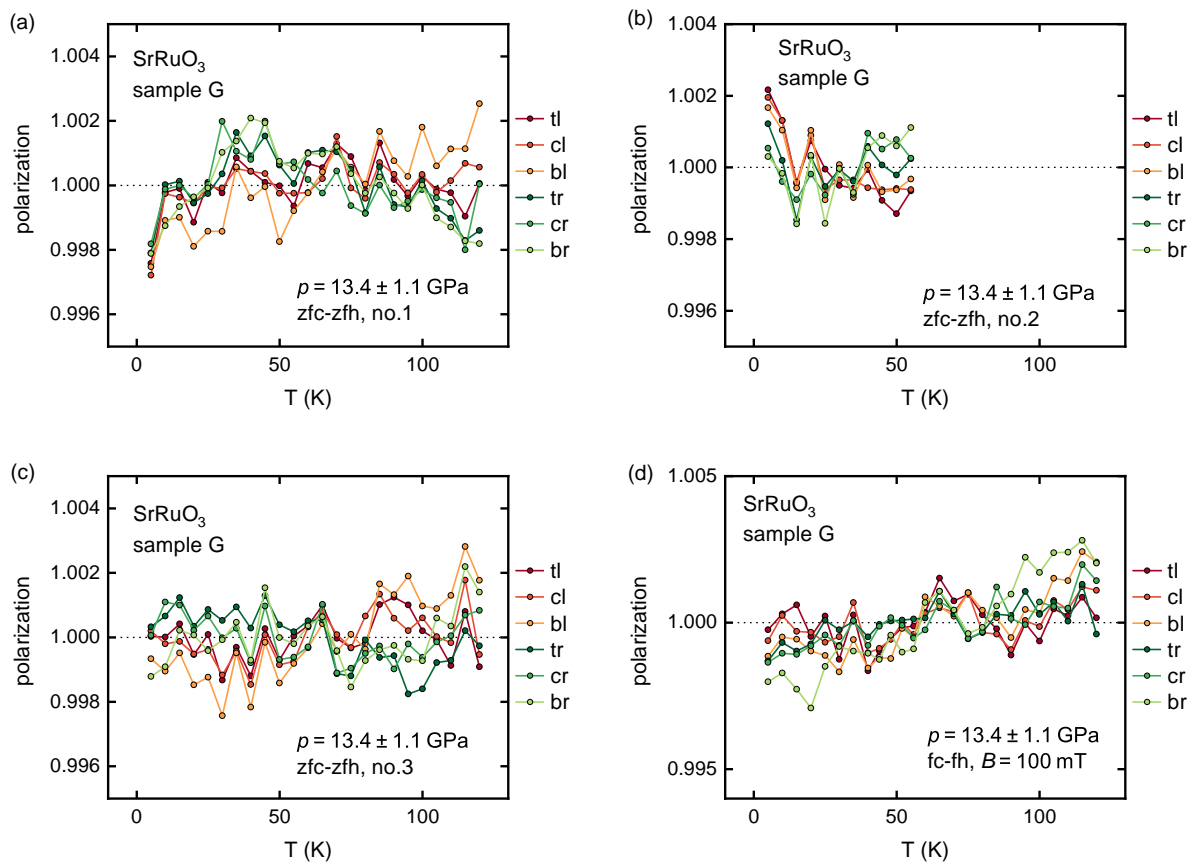


Figure A.22.: Raw polarizations of the temperature scans shown in Fig. A.21.



# Acknowledgments/Danksagungen

An dieser Stelle möchte ich all den wunderbaren Menschen danken, die zu dieser Arbeit beigetragen haben.

An erster Stelle möchte ich mich bei Christian Pfeiderer für die großartige Zeit am Lehrstuhl E51 bedanken und dafür, dass ich dort promovieren konnte. Vielen Dank für die Diskussionen, Ratschläge und Unterstützung, ohne die diese Arbeit nicht möglich gewesen wäre.

Ein riesiges Dankeschön auch an meinen Mentor Michael Schulz dafür, dass du dir immer Zeit nimmst für jegliche Diskussionen, für die Hilfe bei meinen Messzeiten, das Korrekturlesen meiner Arbeit und die argentinischen Grillfeste. Danke für die schöne Zeit am ANTARES, wo ich vor fast 10 Jahren als Werkstudent angefangen habe.

Bei Stuart Gilder möchte ich mich für die hervorragende Zusammenarbeit, die ergiebigen Diskussionen und die Einführung in die Welt des Paläomagnetismus bedanken.

Vielen Dank ebenso an Jim Schilling für die hilfreichen Diskussionen zum Thema Hochdruckphysik und für das Korrekturlesen meiner Arbeit. Es war mir eine Freude mit dir zusammenarbeiten zu dürfen.

Danke auch an Peter Böni für die unkomplizierte Hilfe bei sämtlichen Fragen zum Thema Neutronen. Im Nachhinein denke ich, dass deine Reden auf unseren Weihnachtsfeiern ausschlaggebend dafür waren, dass ich am Lehrstuhl E21/E51 geblieben bin.

Meinem Mitstreiter Pau Jorba: Ohne deine fantastische Vorarbeit, dem Design der Druckzellen und dem HP-ND Setup, wären meine Messungen definitiv nicht möglich gewesen. Herzlichsten Dank für deine Hilfe!

Meinen Mit-Doktoranden am FRM2: Tobi Neuwirth, Alex Backs, Lukas Beddrich und Simon Sebold. Vielen Dank für die wunderbare Zeit und die teils absurden Gespräche, die meist mit Physik beginnen, aber beliebig enden können. Vielen Dank für die technische Hilfe an Dominik Bausenwein, durch den ANTARES überhaupt erst funktioniert.

Letztendlich gebe ich Philipp Schmakat die Schuld an dieser Arbeit. Er hat mich irgendwann in dieses ND-Zeug mit reingezogen. Vielen Dank für den Schubs in diese Richtung und für die Einführung in die fabelhafte Welt der Neutronen-Depolarisation.

Danke auch an meine Kollegen vom FRM2, insbesondere der Imaging-Gruppe und der 12-Uhr-Mate-und-Kaffee-Runde für die Hilfe bei all den kleinen und großen Fragen

und für die schöne Zusammenarbeit. Zusätzlich auch ein großes Dankeschön an die FRM2-Probenumgebung, speziell Heiner Kolb, Peter Biber, Helga Ströhl und Jürgen Peters, für die Unterstützung mit den Kryostaten.

Den anderen beiden Mitgliedern des Vergnügungstriumvirats des E51, Franz Haslbeck und Steffen Säubert. Irgendwer muss ja für das Vergnügen am Lehrstuhl sorgen! Ohne euch wäre meine Zeit am E51 nur halb so witzig gewesen. Danke auch Georg Benka für die PPMS-Messungen, Jon Leiner für das Korrekturlesen dieser Arbeit und dem gesamten Lehrstuhl E51 für die schöne Zeit und die bodenlosen Gespräche in der Kaffeerunde.

Zum Schluss möchte ich mich noch ganz herzlich bei meinen Freunden und meiner Familie bedanken, insbesondere bei meinen Eltern für ihre Unterstützung. Nessi, vielen Dank für alles!

# Bibliography

- [1] C. Pfleiderer, S. R. Julian, and G. G. Lonzarich, Non-Fermi-Liquid Nature of the Normal State of Itinerant-Electron Ferromagnets, [Nature](#) **414**, 427 (2001).
- [2] M. Brando, D. Belitz, F. M. Grosche, and T. R. Kirkpatrick, Metallic Quantum Ferromagnets, [Reviews of Modern Physics](#) **88**, 025006 (2016).
- [3] E. P. Wohlfarth, *Physics of Solids under High Pressure* (North-Holland, Amsterdam, 1981).
- [4] C. Pfleiderer, D. Reznik, L. Pintschovius, H. v. Löhneysen, M. Garst, and A. Rosch, Partial Order in the Non-Fermi-Liquid Phase of MnSi, [Nature](#) **427**, 227 (2004).
- [5] S. S. Saxena, P. Agarwal, K. Ahilan, F. M. Grosche, R. K. W. Haselwimmer, M. J. Steiner, E. Pugh, I. R. Walker, S. R. Julian, P. Monthoux, G. G. Lonzarich, A. Huxley, I. Sheikin, D. Braithwaite, and J. Flouquet, Superconductivity on the Border of Itinerant-Electron Ferromagnetism in UGe<sub>2</sub>, [Nature](#) **406**, 587 (2000).
- [6] J. A. Hertz, Quantum Critical Phenomena, [Physical Review B](#) **14**, 1165 (1976).
- [7] C. Pfleiderer, G. J. McMullan, S. R. Julian, and G. G. Lonzarich, Magnetic Quantum Phase Transition in MnSi under Hydrostatic Pressure, [Physical Review B](#) **55**, 8330 (1997).
- [8] M. Uhlarz, C. Pfleiderer, and S. M. Hayden, Quantum Phase Transitions in the Itinerant Ferromagnet ZrZn<sub>2</sub>, [Physical Review Letters](#) **93**, 256404 (2004).
- [9] D. Belitz, T. R. Kirkpatrick, and T. Vojta, First Order Transitions and Multicritical Points in Weak Itinerant Ferromagnets, [Physical Review Letters](#) **82**, 4 (1999).
- [10] S. Raymond, D. Raoelison, S. Kambe, L. P. Regnault, B. Fåk, R. Calemczuk, J. Flouquet, P. Haen, and P. Lejay, Magnetic Instabilities in CeRu<sub>2</sub>Si<sub>2</sub> Compounds, [Physica B: Condensed Matter](#) **259-261**, 48 (1999).

- [11] T. Westerkamp, M. Deppe, R. KÜchler, M. Brando, C. Geibel, P. Gegenwart, A. P. Pikul, and F. Steglich, Kondo-Cluster-Glass State near a Ferromagnetic Quantum Phase Transition, *Physical Review Letters* **102**, 206404 (2009).
- [12] S. Drotziger, C. Pfeiderer, M. Uhlarz, H. v. Löhneysen, D. Souptel, W. Löser, and G. Behr, Suppression of Ferromagnetism in CeSi<sub>1.81</sub> under Temperature and Pressure, *Physical Review B* **73**, 214413 (2006).
- [13] S. Drotziger, *Korrelierte Elektronensysteme unter hohem Druck: Itineranter Ferromagnetismus in CoS<sub>2</sub> und Supraleitung in BaFe<sub>2</sub>As<sub>2</sub>*, PhD thesis, Universität Karlsruhe, Karlsruhe (2009).
- [14] O. Halpern and T. Holstein, On the Passage of Neutrons Through Ferromagnets, *Physical Review* **59**, 960 (1941).
- [15] G. M. Drabkin, E. I. Zabidarov, Y. A. Kasman, and A. I. Okorokov, Critical Scattering of Polarized Neutrons in Nickel, *Soviet Journal of Experimental and Theoretical Physics Letters* **2**, 541 (1965).
- [16] M. T. Rekveldt, Study of Ferromagnetic Bulk Domains by Neutron Depolarization in Three Dimensions, *Zeitschrift fuer Physik* **259**, 391 (1973).
- [17] W. H. Kraan and M. T. Rekveldt, Calculation of Neutron Depolarization in a Uniaxial Ferromagnet, *Journal of Magnetism and Magnetic Materials* **8**, 168 (1978).
- [18] M. T. Rekveldt, Transmission of Polarised Neutrons in Magnetic Materials, *Physica B: Condensed Matter* **267-268**, 60 (1999).
- [19] M. Schulz, A. Neubauer, S. Masalovich, M. Mühlbauer, E. Calzada, B. Schillinger, C. Pfeiderer, and P. Böni, Towards a Tomographic Reconstruction of Neutron Depolarization Data, *Journal of Physics: Conference Series* **211**, 012025 (2010).
- [20] P. Schmakat, M. Wagner, R. Ritz, A. Bauer, M. Brando, M. Deppe, W. Duncan, C. Duvinage, C. Franz, C. Geibel, F. M. Grosche, M. Hirschberger, K. Hradil, M. Meven, A. Neubauer, M. Schulz, A. Senyshyn, S. Süllow, B. Pedersen, P. Böni, and C. Pfeiderer, Spin Dynamics and Spin Freezing at Ferromagnetic Quantum Phase Transitions, *The European Physical Journal Special Topics* **224**, 1041 (2015).
- [21] D. A. Kishkinev and N. S. Chernetsov, Magnetoreception Systems in Birds: A Review of Current Research, *Biology Bulletin Reviews* **5**, 46 (2015).

- [22] J. L. Kirschvink, A. Kobayashi-Kirschvink, and B. J. Woodford, Magnetite Biomineralization in the Human Brain, [Proceedings of the National Academy of Sciences](#) **89**, 7683 (1992).
- [23] S. Khan and D. Cohen, Using the Magnetoencephalogram to Noninvasively Measure Magnetite in the Living Human Brain, [Human Brain Mapping](#) **40**, 1654 (2019).
- [24] S. A. Gilder, M. Wack, L. Kaub, S. C. Roud, N. Petersen, H. Heinsen, P. Hillenbrand, S. Milz, and C. Schmitz, Distribution of Magnetic Remanence Carriers in the Human Brain, [Scientific Reports](#) **8**, 11363 (2018).
- [25] R. Arras, L. Calmels, and B. Warot-Fonrose, Half-Metallicity, Magnetic Moments, and Gap States in Oxygen-Deficient Magnetite for Spintronic Applications, [Applied Physics Letters](#) **100**, 032403 (2012).
- [26] D. T. Vaniman, D. L. Bish, D. W. Ming, T. F. Bristow, R. V. Morris, D. F. Blake, S. J. Chipera, S. M. Morrison, A. H. Treiman, E. B. Rampe, M. Rice, C. N. Achilles, J. P. Grotzinger, S. M. McLennan, J. Williams, J. F. Bell, H. E. Newsom, R. T. Downs, S. Maurice, P. Sarrazin, A. S. Yen, J. M. Morookian, *et al.*, Mineralogy of a Mudstone at Yellowknife Bay, Gale Crater, Mars, [Science](#) **343**, 1243480 (2014).
- [27] J. P. Grotzinger, D. Y. Sumner, L. C. Kah, K. Stack, S. Gupta, L. Edgar, D. Rubin, K. Lewis, J. Schieber, N. Mangold, R. Milliken, P. G. Conrad, D. DesMarais, J. Farmer, K. Siebach, F. Calef, J. Hurowitz, S. M. McLennan, D. Ming, D. Vaniman, J. Crisp, A. Vasavada, *et al.*, A Habitable Fluvio-Lacustrine Environment at Yellowknife Bay, Gale Crater, Mars, [Science](#) **343**, 1242777 (2014).
- [28] N. J. Tosca, I. A. M. Ahmed, B. M. Tutolo, A. Ashpitel, and J. A. Hurowitz, Magnetite Authigenesis and the Warming of Early Mars, [Nature Geoscience](#) **11**, 635 (2018).
- [29] D. J. Dunlop and Ö. Özdemir, *Rock Magnetism: Fundamentals and Frontiers* (Cambridge University Press, New York, 1997).
- [30] G. Kletetschka, P. J. Wasilewski, and P. T. Taylor, Hematite vs. Magnetite as the Signature for Planetary Magnetic Anomalies? [Physics of the Earth and Planetary Interiors](#) **119**, 259 (2000).
- [31] G. Hervé, S. A. Gilder, C. L. Marion, G. R. Osinski, J. Pohl, N. Petersen, and P. J. Sylvester, Paleomagnetic and Rock Magnetic Study of the Mistastin Lake

- Impact Structure (Labrador, Canada): Implications for Geomagnetic Perturbation and Shock Effects, *Earth and Planetary Science Letters* **417**, 151 (2015).
- [32] I. Biało, A. Kozłowski, M. Wack, A. Włodek, Ł. Gondek, Z. Kakol, R. Hochleitner, A. Zywczak, V. Chlan, and S. A. Gilder, The Influence of Strain on the Verwey Transition as a Function of Dopant Concentration: Towards a Geobarometer for Magnetite-Bearing Rocks, *Geophysical Journal International* **219**, 148 (2019).
- [33] J. J. Hamlin, S. Deemyad, J. S. Schilling, M. K. Jacobsen, R. S. Kumar, A. L. Cornelius, G. Cao, and J. J. Neumeier, Ac Susceptibility Studies of the Weak Itinerant Ferromagnet SrRuO<sub>3</sub> under High Pressure to 34 GPa, *Physical Review B* **76**, 014432 (2007).
- [34] S. Kim, R. I. Dass, and J. B. Goodenough, Interatomic versus Intraatomic Ru Interactions in Perovskites, *Journal of Solid State Chemistry* **181**, 2989 (2008).
- [35] C.-Q. Jin, J. S. Zhou, J. B. Goodenough, Q. Q. Liu, J. G. Zhao, L. X. Yang, Y. Yu, R. C. Yu, T. Katsura, A. Shatskiy, and E. Ito, High-Pressure Synthesis of the Cubic Perovskite BaRuO<sub>3</sub> and Evolution of Ferromagnetism in ARuO<sub>3</sub> (A = Ca, Sr, Ba) Ruthenates, *Proceedings of the National Academy of Sciences* **105**, 7115 (2008).
- [36] S. Doniach, The Kondo Lattice and Weak Antiferromagnetism, *Physica B+C* **91**, 231 (1977).
- [37] J. Larrea, M. B. Fontes, A. D. Alvarenga, E. M. Baggio-Saitovitch, T. Burghardt, A. Eichler, and M. A. Continentino, Quantum Critical Behavior in a CePt Ferromagnetic Kondo Lattice, *Physical Review B* **72**, 035129 (2005).
- [38] M. Burgy, D. J. Hughes, J. R. Wallace, R. B. Heller, and W. E. Woolf, Double Transmission and Depolarization of Neutrons, *Physical Review* **80**, 953 (1950).
- [39] S. V. Maleev, Scattering of Polarized Neutrons in Magnets near the Phase-Transition Point, *Soviet Journal of Experimental and Theoretical Physics Letters* **2**, 338 (1965).
- [40] H. K. Bakker, M. T. Rekveldt, and J. J. Van Loef, Neutron Depolarization Measurements in Nickel near the Curie Point, *Physics Letters A* **27**, 69 (1968).
- [41] G. M. Drabkin, A. I. Okorokov, E. I. Zabidarov, and Y. A. Kasman, Influence of the Magnetic Field on the Phase Transition in Nickel, *Soviet Journal of Experimental and Theoretical Physics Letters* **8**, 335 (1968).

- [42] H. Rauch and E. Löffler, Untersuchung der Neutronendepolarisation von Dy in der Umgebung von magnetischen Umwandlungspunkten, *Zeitschrift für Physik A Hadrons and nuclei* **210**, 265 (1968).
- [43] G. M. Drabkin, E. I. Zabidarov, Y. A. Kasman, and A. I. Okorokov, Investigation of a Phase Transition in Nickel with Polarized Neutrons, *Soviet Journal of Experimental and Theoretical Physics* **29**, 261 (1969).
- [44] F. Söffge, Neutronen-Depolarisation an Nickel in der Nähe des Curiepunktes, *Journal of Magnetism and Magnetic Materials* **6**, 265 (1977).
- [45] S. Mitsuda and Y. Endoh, Neutron Depolarization Studies on Magnetization Process Using Pulsed Polarized Neutrons, *Journal of the Physical Society of Japan* **54**, 1570 (1985).
- [46] Y. Endoh and Y. Ishikawa, Pulsed Polarized Neutron Studies at KENS, *Physica B: Condensed Matter* **136**, 64 (1986).
- [47] I. Mirebeau, S. Itoh, S. Mitsuda, T. Watanabe, Y. Endoh, M. Hennion, and R. Pappoular, Neutron Depolarization in a Reentrant Spin-Glass System: Amorphous Fe-Mn, *Physical Review B* **41**, 11405 (1990).
- [48] I. Mirebeau, S. Itoh, S. Mitsuda, F. Watanabe, Y. Endoh, M. Hennion, and P. Calmettes, Neutron Depolarization in Reentrant Spin Glasses Ni(1-x)Mn(x), *Journal of Applied Physics* **67**, 5232 (1990).
- [49] Y. Endoh, S. Itoh, T. Watanabe, and S. Mitsuda, Neutron Depolarization Studies on Mesoscopic Magnetism, *Physica B: Condensed Matter* **180-181**, 34 (1992).
- [50] S. Mitsuda, H. Yoshizawa, and Y. Endoh, Neutron-Depolarization Studies on Re-Entrant Spin Glass, *Physical Review B* **45**, 9788 (1992).
- [51] S. Itoh, Y. Endoh, and S. W. Charles, Polarized Neutron Studies of Ferrofluids, *Journal of Magnetism and Magnetic Materials* **111**, 56 (1992).
- [52] I. Mirebeau, C. Bellouard, M. Hennion, J. L. Dormann, C. Djega-Mariadassou, and M. Tessier, Small Angle Neutron Scattering in a Superparamagnet, *Journal of Magnetism and Magnetic Materials* **104-107**, 1560 (1992).
- [53] P. A. Miles, S. J. Kennedy, K. N. R. Taylor, and G. D. Gu, Neutron Depolarisation Studies in Bi<sub>2</sub>Sr<sub>2</sub>CaCu<sub>2</sub>O(8+x) Superconductors, *Journal of Magnetism and Magnetic Materials* **140**, 1317 (1995).

- [54] S. Sakarya, N. H. van Dijk, and E. Brück, Determination of the Magnetic Domain Size in the Ferromagnetic Superconductor UGe<sub>2</sub> by Three-Dimensional Neutron Depolarization, *Physical Review B* **71**, 174417 (2005).
- [55] N. Kardjilov, I. Manke, M. Strobl, A. Hilger, W. Treimer, M. Meissner, T. Krist, and J. Banhart, Three-Dimensional Imaging of Magnetic Fields with Polarized Neutrons, *Nature Physics* **4**, 399 (2008).
- [56] M. Schlenker and J. Baruchel, Neutron Techniques for the Observation of Ferro- and Antiferromagnetic Domains, *Journal of Applied Physics* **49**, 1996 (1978).
- [57] R. Rosman and M. T. Rekveldt, Neutron Depolarization in Particulate Media: A Review of Theory and Experimental Results, *Journal of Magnetism and Magnetic Materials* **95**, 319 (1991).
- [58] S. V. Maleev and V. A. Ruban, Depolarization of Neutrons Passing through a Ferromagnet, *Soviet Journal of Experimental and Theoretical Physics* **31**, 111 (1970).
- [59] B. P. Toperverg and J. Weniger, On Neutron Depolarization in Magnetized Media, *Zeitschrift für Physik B - Condensed Matter* **74**, 105 (1989).
- [60] H. J. L. van der Valk and M. T. Rekveldt, Neutron Depolarization in Ferromagnets in Terms of Correlation Functions, *Journal of Magnetism and Magnetic Materials* **28**, 88 (1982).
- [61] R. Rosman and M. T. Rekveldt, Neutron Depolarization Theory in the Larmor and the Scattering Approach, *Zeitschrift für Physik B - Condensed Matter* **79**, 61 (1990).
- [62] R. Rosman, *Magnetic Particles Studied with Neutron Depolarization and Small-Angle Neutron Scattering*, PhD thesis, Delft University of Technology, Delft (1991).
- [63] R. R. Newton and C. Kittel, On a Proposal for Determining the Thickness of the Transition Layer between Ferromagnetic Domains by a Neutron Polarization Experiment, *Physical Review* **74**, 1604 (1948).
- [64] P. Jorba, M. Schulz, M. Seifert, V. Tsurkan, P. Böni, and C. Pfleiderer, Meissner Flux Repulsion and Trapped Flux in Sub-Millimeter Superconductors Observed with Enhanced Neutron Depolarization, (in preparation).
- [65] J. Felber, R. Gähler, R. Golub, and K. Prechtel, Coherence Volumes and Neutron Scattering, *Physica B: Condensed Matter* **252**, 34 (1998).

- [66] M. E. Fleet, The Structure of Magnetite, *Acta Crystallographica Section B Structural Crystallography and Crystal Chemistry* **37**, 917 (1981).
- [67] P. Morrall, F. Schedin, S. Langridge, J. Bland, M. F. Thomas, and G. Thornton, Magnetic Moment in an Ultrathin Magnetite Film, *Journal of Applied Physics* **93**, 7960 (2003).
- [68] J. C. Gómez Sal, J. I. Espeso, J. Rodríguez Fernández, J. A. Blanco, and J. Rodríguez Carvajal, Crystallographic Study and Magnetic Structures of CeNi(x)Pt(1-x) and Diluted Related Compounds, *Solid State Communications* **87**, 863 (1993).
- [69] C. W. Jones, P. D. Battle, P. Lightfoot, and W. T. A. Harrison, The Structure of SrRuO<sub>3</sub> by Time-of-Flight Neutron Powder Diffraction, *Acta Crystallographica Section C: Crystal Structure Communications* **45**, 365 (1989).
- [70] T. Kiyama, K. Yoshimura, K. Kosuge, H. Mitamura, and T. Goto, High-Field Magnetization of Sr(1-x)Ca(x)RuO<sub>3</sub>, *Journal of the Physical Society of Japan* **68**, 3372 (1999).
- [71] T. Sato, T. Shinohara, T. Ogawa, and M. Takeda, Spin Freezing Process in a Reentrant Ferromagnet Studied by Neutron Depolarization Analysis, *Physical Review B* **70**, 134410 (2004).
- [72] M. T. Rekveldt, N. H. van Dijk, S. V. Grigoriev, W. H. Kraan, and W. G. Bouwman, Three-Dimensional Magnetic Spin-Echo Small-Angle Neutron Scattering and Neutron Depolarization: A Comparison, *Review of Scientific Instruments* **77**, 073902 (2006).
- [73] M. Seifert, P. Schmakat, M. Schulz, P. Jorba, V. Hutanu, C. Geibel, M. Deppe, and C. Pfleiderer, Neutron Depolarization Imaging of the Kondo-Cluster-Glass CePd(1-x)Rh(x), (in preparation).
- [74] M. T. Rekveldt and F. J. van Schaik, Static and Dynamic Neutron Depolarization Studies of Ferromagnetic Domain Structures, *Journal of Applied Physics* **50**, 2122 (1979).
- [75] I. Mirebeau, G. Jehanno, I. A. Campbell, F. Hippert, B. Hennion, and M. Hennion, Magnetic Order and Canting in a Reentrant Alloy Studied by Magnetization, Mössbauer and Neutron Scattering, *Journal of Magnetism and Magnetic Materials* **54**, 99 (1986).
- [76] M. Schulz and B. Schillinger, ANTARES: Cold Neutron Radiography and Tomography Facility, *Journal of Large-Scale Research Facilities* **1**, 17 (2015).

- [77] Andor, iKon-L 936, <https://andor.oxinst.com/products/ikon-xl-and-ikon-large-ccd-series/ikon-l-936> (2020).
- [78] T. Neuwirth, B. Walfort, S. Sebold, and M. Schulz, Light Yield Response of Neutron Scintillation Screens to Sudden Flux Changes, [Journal of Imaging](#) **6**, 134 (2020).
- [79] RC-TRITEC-AG, Scintillators for Neutron Imaging, <https://www.rcritec.com/en/scintillators/products.html> (2020).
- [80] F. M. Piegsa and M. Schneider, A Short-Length Neutron Transmission Polariser for Large Beam Cross-Sections, [Nuclear Instruments and Methods in Physics Research Section A: Accelerators, Spectrometers, Detectors and Associated Equipment](#) **594**, 74 (2008).
- [81] P. Böni, Polarizing Supermirrors, [Journal of Neutron Research](#) **5**, 63 (1996).
- [82] F. Mezei, Neutron Spin Echo: A New Concept in Polarized Thermal Neutron Techniques, [Zeitschrift für Physik A Hadrons and nuclei](#) **255**, 146 (1972).
- [83] T. Reimann, *Vortex Matter beyond SANS*, PhD thesis, Technische Universität München, München (2017).
- [84] P. Schmakat, *Neutron Depolarisation Measurements of Ferromagnetic Quantum Phase Transitions & Wavelength-Frame Multiplication Chopper System for the Imaging Instrument ODIN at the ESS*, PhD thesis, Technische Universität München, München (2015).
- [85] P. Jorba, M. Schulz, D. S. Hussey, M. Abir, M. Seifert, V. Tsurkan, A. Loidl, C. Pfleiderer, and B. Khaykovich, High-Resolution Neutron Depolarization Microscopy of the Ferromagnetic Transitions in Ni<sub>3</sub>Al and HgCr<sub>2</sub>Se<sub>4</sub> under Pressure, [Journal of Magnetism and Magnetic Materials](#) **475**, 176 (2019).
- [86] P. Jorba, *New Magnetic Phases under Extreme Conditions in Transition Metal Compounds*, PhD thesis, Technische Universität München, München (2021).
- [87] A. Gustschin, Alternativer Gamma Filter, personal communication, (2019).
- [88] G. Van Rossum and F. L. Drake Jr, *Python Reference Manual* (Centrum voor Wiskunde en Informatica Amsterdam, 1995).
- [89] V. F. Sears, Neutron Scattering Lengths and Cross Sections, [Neutron News](#) **3**, 26 (1992).

- [90] A. Jayaraman, Ultrahigh Pressures, [Review of Scientific Instruments](#) **57**, 1013 (1986).
- [91] I. L. Spain and D. J. Dunstan, The Technology of Diamond Anvil High-Pressure Cells: II. Operation and Use, [Journal of Physics E: Scientific Instruments](#) **22**, 923 (1989).
- [92] D. J. Dunstan and I. L. Spain, Technology of Diamond Anvil High-Pressure Cells: I. Principles, Design and Construction, [Journal of Physics E: Scientific Instruments](#) **22**, 913 (1989).
- [93] K. Syassen, Ruby under Pressure, [High Pressure Research](#) **28**, 75 (2008).
- [94] G. J. Piermarini, S. Block, J. D. Barnett, and R. A. Forman, Calibration of the Pressure Dependence of the R1 Ruby Fluorescence Line to 195 Kbar, [Journal of Applied Physics](#) **46**, 2774 (1975).
- [95] A. Regnat, *Low-Temperature Properties and Magnetic Structure of CrB<sub>2</sub>, MnB<sub>2</sub>, and CuMnSb*, PhD thesis, Technische Universität München, München (2019).
- [96] J. L. Kirschvink and H. A. Lowenstam, Mineralization and Magnetization of Chiton Teeth: Paleomagnetic, Sedimentologic, and Biologic Implications of Organic Magnetite, [Earth and Planetary Science Letters](#) **44**, 193 (1979).
- [97] J. C. Weaver, Q. Wang, A. Miserez, A. Tantuuccio, R. Stromberg, K. N. Bozhilov, P. Maxwell, R. Nay, S. T. Heier, E. DiMasi, and D. Kisailus, Analysis of an Ultra Hard Magnetic Biomineral in Chiton Radular Teeth, [Materials Today](#) **13**, 42 (2010).
- [98] M. Seifert, M. Schulz, G. Benka, C. Pfeiderer, and S. Gilder, Neutron Depolarization Measurements of Magnetite in Chiton Teeth, [Journal of Physics: Conference Series](#) **862**, 012024 (2017).
- [99] M. Deppe, P. Pedrazzini, N. Caroca-Canales, C. Geibel, and J. G. Sereni, Investigations of CePd(1-x)Rh(x) Single Crystals Located near a Ferromagnetic Quantum Critical Point, [Physica B: Condensed Matter](#) **378-380**, 96 (2006).
- [100] T. Westerkamp, *Quantenphasenübergänge in den Schwere-Fermionen-Systemen Yb(Rh(1-x)M(x))<sub>2</sub>Si<sub>2</sub> und CePd(1-x)Rh(x)*, PhD thesis, Technische Universität Dresden, Dresden (2008).
- [101] J. G. Sereni, T. Westerkamp, R. Küchler, N. Caroca-Canales, P. Gegenwart, and C. Geibel, Ferromagnetic Quantum Criticality in the Alloy CePd(1-x)Rh(x), [Physical Review B](#) **75**, 024432 (2007).

- [102] S. Kunkemöller, F. Sauer, A. A. Nugroho, and M. Braden, Magnetic Anisotropy of Large Floating-Zone-Grown Single-Crystals of SrRuO<sub>3</sub>, [Crystal Research and Technology](#) **51**, 299 (2016).
- [103] T. P. A. Tong, *Transport Studies of SrRuO<sub>3</sub> under Pressure*, Master's thesis, Technische Universität München, München (2020).
- [104] J. A. Tarduno, R. D. Cottrell, R. K. Bono, H. Oda, W. J. Davis, M. Fayek, O. v. Erve, F. Nimmo, W. Huang, E. R. Thern, S. Fearn, G. Mitra, A. V. Smirnov, and E. G. Blackman, Paleomagnetism Indicates That Primary Magnetite in Zircon Records a Strong Hadean Geodynamo, [Proceedings of the National Academy of Sciences](#) **117**, 2309 (2020).
- [105] N. R. Nowaczyk, H. W. Arz, U. Frank, J. Kind, and B. Plessen, Dynamics of the Laschamp Geomagnetic Excursion from Black Sea Sediments, [Earth and Planetary Science Letters](#) **351-352**, 54 (2012).
- [106] E. J. W. Verwey, Electronic Conduction of Magnetite (Fe<sub>3</sub>O<sub>4</sub>) and Its Transition Point at Low Temperatures, [Nature](#) **144**, 327 (1939).
- [107] H. J. Williams, R. M. Bozorth, and M. Goertz, Mechanism of Transition in Magnetite at Low Temperatures, [Physical Review](#) **91**, 1107 (1953).
- [108] F. Walz, The Verwey Transition - a Topical Review, [Journal of Physics: Condensed Matter](#) **14**, R285 (2002).
- [109] S. Grenier, A. Bailly, A. Y. Ramos, M. De Santis, Y. Joly, J. E. Lorenzo, S. Garaudée, M. Frericks, S. Arnaud, N. Blanc, and N. Boudet, Verwey Transition in a Magnetite Ultrathin Film by Resonant X-Ray Scattering, [Physical Review B](#) **97**, 104403 (2018).
- [110] P. Novák, H. Štěpánková, J. Englich, J. Kohout, and V. A. M. Brabers, NMR in Magnetite below and around the Verwey Transition, [Physical Review B](#) **61**, 1256 (2000).
- [111] T. G. Pokhil and B. M. Moskowitz, Magnetic Force Microscope Study of Domain Wall Structures in Magnetite, [Journal of Applied Physics](#) **79**, 6064 (1996).
- [112] A. R. Muxworthy and W. Williams, Critical Single-Domain/Multidomain Grain Sizes in Noninteracting and Interacting Elongated Magnetite Particles: Implications for Magnetosomes, [Journal of Geophysical Research: Solid Earth](#) **111** (2006).

- [113] J. F. J. Bryson, T. Kasama, R. E. Dunin-Borkowski, and R. J. Harrison, Ferrimagnetic/Ferroelastic Domain Interactions in Magnetite below the Verwey Transition: Part II. Micromagnetic and Image Simulations, *Phase Transitions* **86**, 88 (2013).
- [114] Y. Kakudate, N. Mori, and Y. Kino, Pressure Effect on the Anomalous Electrical Conductivity of Magnetite, *Journal of Magnetism and Magnetic Materials* **12**, 22 (1979).
- [115] N. Mōri, S. Todo, N. Takeshita, T. Mori, and Y. Akishige, Metallization of Magnetite at High Pressures, *Physica B: Condensed Matter* **312-313**, 686 (2002).
- [116] S. K. Ramasesha, M. Mohan, A. K. Singh, J. M. Honig, and C. N. R. Rao, High-Pressure Study of Fe<sub>3</sub>O<sub>4</sub> through the Verwey Transition, *Physical Review B* **50**, 13789 (1994).
- [117] G. K. Rozenberg, G. R. Hearne, M. P. Pasternak, P. A. Metcalf, and J. M. Honig, Nature of the Verwey Transition in Magnetite (Fe<sub>3</sub>O<sub>4</sub>) to Pressures of 16 GPa, *Physical Review B* **53**, 6482 (1996).
- [118] G. A. Samara, Effect of Pressure on the Metal-Nonmetal Transition and Conductivity of Fe<sub>3</sub>O<sub>4</sub>, *Physical Review Letters* **21**, 3 (1968).
- [119] S. Todo, N. Takeshita, T. Kanehara, T. Mori, and N. Mōri, Metallization of Magnetite (Fe<sub>3</sub>O<sub>4</sub>) under High Pressure, *Journal of Applied Physics* **89**, 7347 (2001).
- [120] L. Carporzen and S. A. Gilder, Strain Memory of the Verwey Transition, *Journal of Geophysical Research: Solid Earth* **115** (2010).
- [121] R. Aragón, R. J. Rasmussen, J. P. Shepherd, J. W. Koenitzer, and J. M. Honig, Effect of Stoichiometry Changes on Electrical Properties of Magnetite, *Journal of Magnetism and Magnetic Materials* **54-57**, 1335 (1986).
- [122] P. Wang, Z. Kąkol, M. Wittenauer, and J. M. Honig, Electrical Properties of Zinc Ferrites Fe(3-x)Zn(x)O<sub>4</sub> with 0 ≤ x < 0.3, *Physical Review B* **42**, 4553 (1990).
- [123] Z. Kąkol, J. Sabol, J. Stickler, and J. M. Honig, Effect of Low-Level Titanium(IV) Doping on the Resistivity of Magnetite near the Verwey Transition, *Physical Review B* **46**, 1975 (1992).
- [124] J. P. Hodych, Single-Domain Theory for the Reversible Effect of Small Uniaxial Stress upon the Initial Magnetic Susceptibility of Rock, *Canadian Journal of Earth Sciences* **13**, 1186 (1976).

- [125] A. Kosterov, Magnetic Hysteresis of Pseudo-Single-Domain and Multidomain Magnetite below the Verwey Transition, *Earth and Planetary Science Letters* **186**, 245 (2001).
- [126] J. G. King and W. Williams, Low-Temperature Magnetic Properties of Magnetite, *Journal of Geophysical Research: Solid Earth* **105**, 16427 (2000).
- [127] J. M. Honig, Analysis of the Verwey Transition in Magnetite, *Journal of Alloys and Compounds* **229**, 24 (1995).
- [128] J. P. Shepherd, J. W. Koenitzer, R. Aragón, J. Spalek, and J. M. Honig, Heat Capacity and Entropy of Nonstoichiometric Magnetite  $\text{Fe}_3(1-\delta)\text{O}_4$ : The Thermodynamic Nature of the Verwey Transition, *Physical Review B* **43**, 8461 (1991).
- [129] R. F. Butler and S. K. Banerjee, Theoretical Single-Domain Grain Size Range in Magnetite and Titanomagnetite, *Journal of Geophysical Research* **80**, 4049 (1975).
- [130] S. Blundell, *Magnetism in Condensed Matter* (Oxford University Press, Oxford, 2001).
- [131] M. Pénicaud, B. Siberchicot, C. B. Sommers, and J. Kübler, Calculated Electronic Band Structure and Magnetic Moments of Ferrites, *Journal of Magnetism and Magnetic Materials* **103**, 212 (1992).
- [132] M. S. Senn, J. P. Wright, and J. P. Attfield, Charge Order and Three-Site Distortions in the Verwey Structure of Magnetite, *Nature* **481**, 173 (2012).
- [133] X. Liu, W. Mi, Q. Zhang, and X. Zhang, Anisotropic Magnetoresistance across Verwey Transition in Charge Ordered  $\text{Fe}_3\text{O}_4$  Epitaxial Films, *Physical Review B* **96**, 214434 (2017).
- [134] R. S. Coe, R. Egli, S. A. Gilder, and J. P. Wright, The Thermodynamic Effect of Nonhydrostatic Stress on the Verwey Transition, *Earth and Planetary Science Letters* **319-320**, 207 (2012).
- [135] A. Wiecheć, R. Zach, Z. Kakol, Z. Tarnawski, A. Kozłowski, and J. M. Honig, Magnetic Susceptibility Studies of Single-Crystalline Zinc Ferrites under Pressure, *Physica B: Condensed Matter* **359-361**, 1342 (2005).
- [136] J. Spalek, A. Kozłowski, Z. Tarnawski, Z. Kąkol, Y. Fukami, F. Ono, R. Zach, L. J. Spalek, and J. M. Honig, Verwey Transition in  $\text{Fe}_3\text{O}_4$  at High Pressure: Quantum Critical Point at the Onset of Metallization, *Physical Review B* **78**, 100401 (2008).

- [137] M. Matsui, S. Todo, and S. Chikazumi, Specific Heat and Electrical Conductivity of Low Temperature Phase of Magnetite, [Journal of the Physical Society of Japan](#) **42**, 1517 (1977).
- [138] Y. Nagasawa, M. Kosaka, S. Katano, N. Môri, S. Todo, and Y. Uwatoko, Effect of Uniaxial Strain on Verwey Transition in Magnetite, [Journal of the Physical Society of Japan](#) **76**, 110 (2007).
- [139] Ö. Özdemir, D. J. Dunlop, and B. M. Moskowitz, Changes in Remanence, Coercivity and Domain State at Low Temperature in Magnetite, [Earth and Planetary Science Letters](#) **194**, 343 (2002).
- [140] E. C. Stoner, Collective Electron Ferronmagnetism, [Proceedings of the Royal Society of London. Series A. Mathematical and Physical Sciences](#) **165**, 372 (1938).
- [141] D. Belitz, T. R. Kirkpatrick, and J. Rollbühler, Tricritical Behavior in Itinerant Quantum Ferromagnets, [Physical Review Letters](#) **94**, 247205 (2005).
- [142] T. R. Kirkpatrick and D. Belitz, Universal Low-Temperature Tricritical Point in Metallic Ferromagnets and Ferrimagnets, [Physical Review B](#) **85**, 134451 (2012).
- [143] C. Pfleiderer, G. J. McMullan, and G. G. Lonzarich, Critical Behaviour at the Transition from a Magnetic to a Nonmagnetic Metallic State in MnSi as a Function of Hydrostatic Pressure, [Physica B: Condensed Matter](#) **199-200**, 634 (1994).
- [144] F. Le Marrec, A. Demuer, D. Jaccard, J.-M. Triscone, M. K. Lee, and C. B. Eom, Magnetic Behavior of Epitaxial SrRuO<sub>3</sub> Thin Films under Pressure up to 23 GPa, [Applied Physics Letters](#) **80**, 2338 (2002).
- [145] A. Demuer, D. Jaccard, J. W. Reiner, C. H. Ahn, and J.-M. Triscone, Magnetism of SrRuO<sub>3</sub> Thin Films under High Hydrostatic Pressure, [Annalen der Physik](#) **13**, 72 (2004).
- [146] A. Callaghan, C. W. Moeller, and R. Ward, Magnetic Interactions in Ternary Ruthenium Oxides, [Inorganic Chemistry](#) **5**, 1572 (1966).
- [147] J. M. Rondinelli, N. M. Caffrey, S. Sanvito, and N. A. Spaldin, Electronic Properties of Bulk and Thin Film SrRuO<sub>3</sub>: Search for the Metal-Insulator Transition, [Physical Review B](#) **78**, 155107 (2008).
- [148] J. J. Randall and R. Ward, The Preparation of Some Ternary Oxides of the Platinum Metals, [Journal of the American Chemical Society](#) **81**, 2629 (1959).

- [149] J. M. Longo, P. M. Raccach, and J. B. Goodenough, Magnetic Properties of SrRuO<sub>3</sub> and CaRuO<sub>3</sub>, *Journal of Applied Physics* **39**, 1327 (1968).
- [150] G. L. Catchen, T. M. Rearick, and D. G. Schlom, High-Temperature Phase Transitions and Low-Temperature Magnetic Ordering in SrRuO<sub>3</sub> and CaRuO<sub>3</sub> Ceramics Studied Using Perturbed-Angular-Correlation Spectroscopy, *Physical Review B* **49**, 318 (1994).
- [151] S. L. Cuffini, J. A. Guevara, and Y. P. Mascarenhas, Structural Analysis of Polycrystalline CaRuO<sub>3</sub> and SrRuO<sub>3</sub> Ceramics from Room Temperature Up to 1273 K, *Materials Science Forum* **228-231**, 789 (1996).
- [152] B. C. Chakoumakos, S. E. Nagler, S. T. Misture, and H. M. Christen, High-Temperature Structural Behavior of SrRuO<sub>3</sub>, *Physica B: Condensed Matter* **241**, 358 (1998).
- [153] A. Kanbayasi, Magnetic Properties of SrRuO<sub>3</sub> Single Crystal, *Journal of the Physical Society of Japan* **41**, 1876 (1976).
- [154] A. Kanbayasi, Magnetocrystalline Anisotropy of SrRuO<sub>3</sub>, *Journal of the Physical Society of Japan* **41**, 1879 (1976).
- [155] G. Cao, F. Freibert, and J. E. Crow, Itinerant-to-Localized Electron Transition in Perovskite CaRu(1-x)Rh(x)O<sub>3</sub>, *Journal of Applied Physics* **81**, 3884 (1997).
- [156] S. N. Bushmeleva, V. Y. Pomjakushin, E. V. Pomjakushina, D. V. Sheptyakov, and A. M. Balagurov, Evidence for the Band Ferromagnetism in SrRuO<sub>3</sub> from Neutron Diffraction, *Journal of Magnetism and Magnetic Materials* **305**, 491 (2006).
- [157] J. G. Cheng, J. S. Zhou, and J. B. Goodenough, Lattice Effects on Ferromagnetism in Perovskite Ruthenates, *Proceedings of the National Academy of Sciences* **110**, 13312 (2013).
- [158] K. Jenni, S. Kunkemöller, D. Brüning, T. Lorenz, Y. Sidis, A. Schneidewind, A. A. Nugroho, A. Rosch, D. I. Khomskii, and M. Braden, Interplay of Electronic and Spin Degrees in Ferromagnetic SrRuO<sub>3</sub>: Anomalous Softening of the Magnon Gap and Stiffness, *Physical Review Letters* **123**, 017202 (2019).
- [159] S. Kunkemöller, K. Jenni, D. Gorkov, A. Stunault, S. Streltsov, and M. Braden, Magnetization Density Distribution in the Metallic Ferromagnet SrRuO<sub>3</sub> Determined by Polarized Neutron Diffraction, *Physical Review B* **100**, 054413 (2019).

- [160] D. J. Singh, Electronic and Magnetic Properties of the 4d Itinerant Ferromagnet SrRuO<sub>3</sub>, *Journal of Applied Physics* **79**, 4818 (1996).
- [161] I. I. Mazin and D. J. Singh, Electronic Structure and Magnetism in Ru-Based Perovskites, *Physical Review B* **56**, 2556 (1997).
- [162] G. Santi and T. Jarlborg, Calculation of the Electronic Structure and the Magnetic Properties of SrRuO<sub>3</sub> and CaRuO<sub>3</sub>, *Journal of Physics: Condensed Matter* **9**, 9563 (1997).
- [163] T. Kiyama, K. Yoshimura, K. Kosuge, H. Michor, and G. Hilscher, Specific Heat of (Sr-Ca)RuO<sub>3</sub>, *Journal of the Physical Society of Japan* **67**, 307 (1998).
- [164] G. Cao, S. McCall, M. Shepard, J. E. Crow, and R. P. Guertin, Thermal, Magnetic, and Transport Properties of Single-Crystal Sr(1-x)Ca(x)RuO<sub>3</sub> (0, *Physical Review B* **56**, 321 (1997).
- [165] F. Fukunaga and N. Tsuda, On the Magnetism and Electronic Conduction of Itinerant Magnetic System Ca(1-x)Sr(x)RuO<sub>3</sub>, *Journal of the Physical Society of Japan* **63**, 3798 (1994).
- [166] L. Klein, J. S. Dodge, C. H. Ahn, J. W. Reiner, L. Mievilte, T. H. Geballe, M. R. Beasley, and A. Kapitulnik, Transport and Magnetization in the Badly Metallic Itinerant Ferromagnet SrRuO<sub>3</sub>, *Journal of Physics: Condensed Matter* **8**, 10111 (1996).
- [167] P. T. Barton, R. Seshadri, and M. J. Rosseinsky, Electrical and Magnetic Properties of the Complete Solid Solution Series between SrRuO<sub>3</sub> and LaRhO<sub>3</sub>: Filling T<sub>2g</sub> versus Tilting, *Physical Review B* **83**, 064417 (2011).
- [168] R. Ranjan, A. Senyshyn, R. Garg, and H. Boysen, Magnetic Structure and Magneto-Elastic-Structural Coupling in Cr-Modified SrRuO<sub>3</sub>: A Neutron Powder Diffraction Study, *Journal of Applied Physics* **109**, 073908 (2011).
- [169] S. Kunkemöller, D. Brüning, A. Stunault, A. A. Nugroho, T. Lorenz, and M. Braden, Magnetic Shape-Memory Effect in SrRuO<sub>3</sub>, *Physical Review B* **96**, 220406 (2017).
- [170] A. F. Marshall, L. Klein, J. S. Dodge, C. H. Ahn, J. W. Reiner, L. Mievilte, L. Antagonazza, A. Kapitulnik, T. H. Geballe, and M. R. Beasley, Lorentz Transmission Electron Microscope Study of Ferromagnetic Domain Walls in SrRuO<sub>3</sub>: Statics, Dynamics, and Crystal Structure Correlation, *Journal of Applied Physics* **85**, 4131 (1999).

- [171] P. B. Allen, H. Berger, O. Chauvet, L. Forro, T. Jarlborg, A. Junod, B. Revaz, and G. Santi, Transport Properties, Thermodynamic Properties, and Electronic Structure of SrRuO<sub>3</sub>, [Physical Review B](#) **53**, 4393 (1996).
- [172] S. Middey, P. Mahadevan, and D. D. Sarma, Dependence of Magnetism on GdFeO<sub>3</sub> Distortion in the T<sub>2g</sub> System ARuO<sub>3</sub> (A = Sr, Ca), [Physical Review B](#) **83**, 014416 (2011).
- [173] H. Kobayashi, M. Nagata, R. Kanno, and Y. Kawamoto, Structural Characterization of the Orthorhombic Perovskites: [ARuO<sub>3</sub> (A = Ca, Sr, La, Pr)], [Materials Research Bulletin](#) **29**, 1271 (1994).
- [174] G. Cao, S. McCall, J. Bolivar, M. Shepard, F. Freibert, P. Henning, J. E. Crow, and T. Yuen, Itinerant-to-Localized Electron Transition in CaRu(1-x)Sn(x)O<sub>3</sub> and SrRu(1-x)Pb(x)O<sub>3</sub>, [Physical Review B](#) **54**, 15144 (1996).
- [175] D. Fuchs, C. L. Huang, J. Schmalian, M. Wissinger, S. Schuppler, and K. Grube, Competing Ground States in Transition Metal Oxides: Behavior of Itinerant Sr(1-x)Ca(x)RuO<sub>3</sub> Close to the Classical and Quantum Critical Ferromagnetic Phase Transition, [The European Physical Journal Special Topics](#) **224**, 1105 (2015).
- [176] T. He and R. J. Cava, Disorder-Induced Ferromagnetism in CaRuO<sub>3</sub>, [Physical Review B](#) **63**, 172403 (2001).
- [177] L. Klein, L. Antognazza, T. H. Geballe, M. R. Beasley, and A. Kapitulnik, Possible Non-Fermi-Liquid Behavior of CaRuO<sub>3</sub>, [Physical Review B](#) **60**, 1448 (1999).
- [178] H. Mukuda, K. Ishida, Y. Kitaoka, K. Asayama, R. Kanno, and M. Takano, Spin Fluctuations in the Ruthenium Oxides RuO<sub>2</sub>, SrRuO<sub>3</sub>, CaRuO<sub>3</sub>, and Sr<sub>2</sub>RuO<sub>4</sub> Probed by Ru NMR, [Physical Review B](#) **60**, 12279 (1999).
- [179] L. T. Nguyen, M. Abeykoon, J. Tao, S. Lapidus, and R. J. Cava, Long-Range and Local Crystal Structures of the Sr(1-x)Ca(x)RuO<sub>3</sub> Perovskites, [Physical Review Materials](#) **4**, 034407 (2020).
- [180] L. Demko, S. Bordacs, T. Vojta, D. Nozadze, F. Hrahsheh, C. Svoboda, B. Dora, H. Yamada, M. Kawasaki, Y. Tokura, and I. Kezsmarki, Disorder Promotes Ferromagnetism: Rounding of the Quantum Phase Transition in Sr(1-x)Ca(x)RuO<sub>3</sub>, [Physical Review Letters](#) **108**, 185701 (2012).

- [181] Y. J. Uemura, T. Goko, I. M. Gat-Malureanu, J. P. Carlo, P. L. Russo, A. T. Savici, A. Aczel, G. J. MacDougall, J. A. Rodriguez, G. M. Luke, S. R. Dunsiger, A. McCollam, J. Arai, C. Pfleiderer, P. Böni, K. Yoshimura, E. Baggio-Saitovitch, M. B. Fontes, J. Larrea, Y. V. Sushko, and J. Sereni, Phase Separation and Suppression of Critical Dynamics at Quantum Phase Transitions of MnSi and Sr(1-x)Ca(x)RuO<sub>3</sub>, [Nature Physics](#) **3**, 29 (2007).
- [182] I. M. Gat-Malureanu, J. P. Carlo, T. Goko, A. Fukaya, T. Ito, P. P. Kyriakou, M. I. Larkin, G. M. Luke, P. L. Russo, A. T. Savici, C. R. Wiebe, K. Yoshimura, and Y. J. Uemura, Muon Spin Relaxation and Susceptibility Measurements of an Itinerant-Electron System Sr(1-x)Ca(x)RuO<sub>3</sub>: Quantum Evolution from Ferromagnet to Paramagnet, [Physical Review B](#) **84**, 224415 (2011).
- [183] J. S. Zhou, K. Matsubayashi, Y. Uwatoko, C.-Q. Jin, J. G. Cheng, J. B. Goodenough, Q. Q. Liu, T. Katsura, A. Shatskiy, and E. Ito, Critical Behavior of the Ferromagnetic Perovskite BaRuO<sub>3</sub>, [Physical Review Letters](#) **101**, 077206 (2008).
- [184] N. Menyuk, J. A. Kafalas, K. Dwight, and J. B. Goodenough, Pressure-Effect Measurements Using a Vibrating-Coil Magnetometer, [Journal of Applied Physics](#) **40**, 1324 (1969).
- [185] J. J. Neumeier, A. L. Cornelius, and J. S. Schilling, Influence of Pressure on the Ferromagnetic Transition Temperature of SrRuO<sub>3</sub>, [Physica B: Condensed Matter](#) **198**, 324 (1994).
- [186] M. Shikano, T.-K. Huang, Y. Inaguma, M. Itoh, and T. Nakamura, Pressure Dependence of the Magnetic Transition Temperature for Ferromagnetic SrRuO<sub>3</sub>, [Solid State Communications](#) **90**, 115 (1994).
- [187] M. K. Jacobsen, R. S. Kumar, G. Cao, J. J. Neumeier, and A. L. Cornelius, High Pressure Structural Studies on SrRuO<sub>3</sub>, [Journal of Physics and Chemistry of Solids](#) **69**, 2237 (2008).
- [188] J. Pietosa, B. Dabrowski, A. Wisniewski, R. Puzniak, R. Kiyonagi, T. Maxwell, and J. D. Jorgensen, Pressure Effects on Magnetic and Structural Properties of Pure and Substituted SrRuO<sub>3</sub>, [Physical Review B](#) **77**, 104410 (2008).
- [189] Y. Cai, Y. Wei, X. Ming, F. Du, X. Meng, C. Wang, and G. Chen, Prediction of the Phase Transition from Ferromagnetic Perovskite to Non-Magnetic Post-Perovskite in SrRuO<sub>3</sub>: A First-Principles Study, [Solid State Communications](#) **151**, 798 (2011).

- [190] G. H. Zhong, J. L. Wang, Y. L. Li, Z. Liu, and H. Q. Lin, High-Pressure and Substitution Induced Effects in SrRuO<sub>3</sub>: First-Principles Insights, *Journal of Applied Physics* **109**, 07E163 (2011).
- [191] M. Zhernenkov, G. Fabbris, O. Chmaissem, J. F. Mitchell, H. Zheng, and D. Haskel, Pressure-Induced Volume Collapse and Structural Phase Transitions in SrRuO<sub>3</sub>, *Journal of Solid State Chemistry* **205**, 177 (2013).
- [192] C. H. Kronbo, L. R. Jensen, F. Menescardi, D. Ceresoli, and M. Bremholm, High-Pressure, Low-Temperature Studies of Phase Transitions in SrRuO<sub>3</sub> – Absence of Volume Collapse, *Journal of Solid State Chemistry* **287**, 121360 (2020).
- [193] Y. Maeno, H. Hashimoto, K. Yoshida, S. Nishizaki, T. Fujita, J. G. Bednorz, and F. Lichtenberg, Superconductivity in a Layered Perovskite without Copper, *Nature* **372**, 532 (1994).
- [194] T. M. Rice and M. Sigrist, Sr<sub>2</sub>RuO<sub>4</sub>: An Electronic Analogue of 3He? *Journal of Physics: Condensed Matter* **7**, L643 (1995).
- [195] S. A. Grigera, R. S. Perry, A. J. Schofield, M. Chiao, S. R. Julian, G. G. Lonzarich, S. I. Ikeda, Y. Maeno, A. J. Millis, and A. P. Mackenzie, Magnetic Field-Tuned Quantum Criticality in the Metallic Ruthenate Sr<sub>3</sub>Ru<sub>2</sub>O<sub>7</sub>, *Science* **294**, 329 (2001).
- [196] G. Cao, S. Chikara, J. W. Brill, and P. Schlottmann, Anomalous Itinerant Magnetism in Single-Crystal Sr<sub>4</sub>Ru<sub>3</sub>O<sub>10</sub>: A Thermodynamic and Transport Investigation, *Physical Review B* **75**, 024429 (2007).
- [197] G. Cao, O. Korneta, S. Chikara, and L. E. DeLong, Decisive Influence of Cation Size on the Magnetic Groundstate and Non-Fermi Liquid Behavior of ARuO<sub>3</sub> (A = Ca, Sr), arXiv:0805.0741 (2008), [arXiv:0805.0741](https://arxiv.org/abs/0805.0741) .
- [198] W. Bensch, H. W. Schmalke, and A. Reller, Structure and Thermochemical Reactivity of CaRuO<sub>3</sub> and SrRuO<sub>3</sub>, *Solid State Ionics* **43**, 171 (1990).
- [199] C. B. Eom, R. J. Cava, R. M. Fleming, J. M. Phillips, R. B. van Dover, J. H. Marshall, J. W. P. Hsu, J. J. Krajewski, and W. F. Peck, Single-Crystal Epitaxial Thin Films of the Isotropic Metallic Oxides Sr(1-x)Ca(x)RuO<sub>3</sub> (0 ≤ x ≤ 1), *Science* **258**, 1766 (1992).
- [200] X. D. Wu, S. R. Foltyn, R. C. Dye, Y. Coulter, and R. E. Muenchausen, Properties of Epitaxial SrRuO<sub>3</sub> Thin Films, *Applied Physics Letters* **62**, 2434 (1993).

- [201] P. Mahadevan, F. Aryasetiawan, A. Janotti, and T. Sasaki, Evolution of the Electronic Structure of a Ferromagnetic Metal: Case of SrRuO<sub>3</sub>, [Physical Review B](#) **80**, 035106 (2009).
- [202] G. Koster, L. Klein, W. Siemons, G. Rijnders, J. S. Dodge, C. B. Eom, D. H. A. Blank, and M. R. Beasley, Structure, Physical Properties, and Applications of SrRuO<sub>3</sub> Thin Films, [Reviews of Modern Physics](#) **84**, 253 (2012).
- [203] Z. Fang, N. Nagaosa, K. S. Takahashi, A. Asamitsu, R. Mathieu, T. Ogasawara, H. Yamada, M. Kawasaki, Y. Tokura, and K. Terakura, The Anomalous Hall Effect and Magnetic Monopoles in Momentum Space, [Science](#) **302**, 92 (2003).
- [204] Y. Chen, D. L. Bergman, and A. A. Burkov, Weyl Fermions and the Anomalous Hall Effect in Metallic Ferromagnets, [Physical Review B](#) **88**, 125110 (2013).
- [205] S. Itoh, Y. Endoh, T. Yokoo, S. Ibuka, J.-G. Park, Y. Kaneko, K. S. Takahashi, Y. Tokura, and N. Nagaosa, Weyl Fermions and Spin Dynamics of Metallic Ferromagnet SrRuO<sub>3</sub>, [Nature Communications](#) **7**, 1 (2016).
- [206] K. Takiguchi, Y. K. Wakabayashi, H. Irie, Y. Krockenberger, T. Otsuka, H. Sawada, S. A. Nikolaev, H. Das, M. Tanaka, Y. Taniyasu, and H. Yamamoto, Quantum Transport Evidence of Weyl Fermions in an Epitaxial Ferromagnetic Oxide, [Nature Communications](#) **11**, 1 (2020).
- [207] A. Zarzycki, M. Rams, E. A. Goerlich, and K. Tomala, Investigation of Anomalous Thermodynamic and Transport Properties of Sr(1-x)Ca(x)RuO<sub>3</sub> (X>0.8), arXiv:1806.03923 [cond-mat] (2018), [arXiv:1806.03923 \[cond-mat\]](#) .
- [208] J. Kondo, Resistance Minimum in Dilute Magnetic Alloys, [Progress of Theoretical Physics](#) **32**, 37 (1964).
- [209] N. Greve and F. Steglich, Heavy Fermions, in *Handbook on the Physics and Chemistry of Rare Earths*, Vol. 14 (Elsevier, 1991) pp. 343–474.
- [210] Q. Si and F. Steglich, Heavy Fermions and Quantum Phase Transitions, [Science](#) **329**, 1161 (2010).
- [211] B. D. White, J. D. Thompson, and M. B. Maple, Unconventional Superconductivity in Heavy-Fermion Compounds, [Physica C: Superconductivity and its Applications](#) **514**, 246 (2015).

- [212] F. Steglich and S. Wirth, Foundations of Heavy-Fermion Superconductivity: Lattice Kondo Effect and Mott Physics, [Reports on Progress in Physics](#) **79**, 084502 (2016).
- [213] B. Coqblin and J. R. Schrieffer, Exchange Interaction in Alloys with Cerium Impurities, [Physical Review](#) **185**, 847 (1969).
- [214] J. R. Schrieffer and P. A. Wolff, Relation between the Anderson and Kondo Hamiltonians, [Physical Review](#) **149**, 491 (1966).
- [215] M. Lavagna, C. Lacroix, and M. Cyrot, Volume Collapse in the Kondo Lattice, [Physics Letters A](#) **90**, 210 (1982).
- [216] M. A. Continentino, G. M. Japiassu, and A. Troper, Critical Approach to the Coherence Transition in Kondo Lattices, [Physical Review B](#) **39**, 9734 (1989).
- [217] L. P. Gor'kov and J. H. Kim, Interplay between the Kondo Effect and the Ruderman-Kittel-Kasuga-Yosida Interaction in the Two-Impurity Model, [Philosophical Magazine B](#) **74**, 447 (1996).
- [218] G. R. Stewart, Non-Fermi-Liquid Behavior in d- and f-Electron Metals, [Reviews of Modern Physics](#) **73**, 797 (2001).
- [219] M. E. Macovei, M. Nicklas, C. Krellner, C. Geibel, and F. Steglich, Pressure-Temperature Phase Diagram of the Ferromagnetic Kondo Lattice Compound CeRuPO, [Physica B: Condensed Matter](#) **404**, 2934 (2009).
- [220] H. Wilhelm and D. Jaccard, Transport Properties of CeRu<sub>2</sub>Ge<sub>2</sub> at High Pressure, [Solid State Communications](#) **106**, 239 (1998).
- [221] V. A. Sidorov, E. D. Bauer, N. A. Frederick, J. R. Jeffries, S. Nakatsuji, N. O. Moreno, J. D. Thompson, M. B. Maple, and Z. Fisk, Magnetic Phase Diagram of the Ferromagnetic Kondo-Lattice Compound CeAgSb<sub>2</sub> up to 80 Kbar, [Physical Review B](#) **67**, 224419 (2003).
- [222] D. Gignoux and J. C. Gomez-Sal, Competition between the Kondo Effect and Exchange Interactions in the CeNi(x)Pt(1-x) Compounds, [Physical Review B](#) **30**, 3967 (1984).
- [223] J. Larrea, M. Fontes, E. Baggio-Saitovitch, A. Eichler, M. M. Abd-Elmeguid, C. Geibel, and M. Continentino, Quantum Criticality of CePt and YbFe<sub>2</sub>Ge<sub>2</sub> Heavy Fermions under Pressure, [J. Phys. Soc. Jpn.](#) **76**, 156 (2007).

- [224] J. P. Kappler, Crossover between Intermediate Valence and Magnetic Order in  $\text{CeRh}(1-x)\text{Pd}(x)$ , *Physica B: Condensed Matter* **171**, 346 (1991).
- [225] J. G. Sereni, Systematics on the Cerium Magnetic Transformations Induced by Alloying, *Journal of Alloys and Compounds* **207**, 229 (1994).
- [226] J. G. Sereni, Thermodynamic Analysis of the Quantum Critical Behavior of Ce-Lattice Compounds, *Philosophical Magazine* **93**, 409 (2013).
- [227] V. Hutanu, W. Lubertetter, E. Bourgeat-Lami, M. Meven, A. Sazonov, A. Steffen, G. Heger, G. Roth, and E. Lelièvre-Berna, Implementation of a New Cryopad on the Diffractometer POLI at MLZ, *Review of Scientific Instruments* **87**, 105108 (2016).
- [228] A. E. Dwight, R. A. Connor, and J. Downey, Equiatomic Compounds of the Transition and Lanthanide Elements with Rh, Ir, Ni and Pt, *Acta Crystallographica* **18**, 835 (1965).
- [229] J. G. Huber, Paramagnetic Susceptibility of UPt and CePt, *Le Journal de Physique Colloques* **39**, 781 (1978).
- [230] B. J. Holt, J. D. Ramsden, H. H. Sample, and J. G. Huber, Low Temperature Specific Heat of Ferromagnetic CePt and Isostructural LaPt, *Physica B+C* **107**, 255 (1981).
- [231] D. Gignoux and J. C. Gomez-Sal, Resistivity and Magnetic Measurements on the CePt Ferromagnet, *Solid State Communications* **45**, 779 (1983).
- [232] G. Fillion, M. A. Frémy, D. Gignoux, J. C. Gomez-Sal, and B. Gorges, Magnetic Properties of the  $\text{CeNi}_{0.8}\text{Pt}_{0.2}$  Dense Kondo Ferromagnet Studied on a Single Crystal, *Journal of Magnetism and Magnetic Materials* **63**, 117 (1987).
- [233] Y. Itoh, H. Kadomatsu, M. Kuriso, and H. Fujiwara, Electrical Resistivity of Dense Kondo System CePt under Pressure, *Journal of the Physical Society of Japan* **56**, 1159 (1987).
- [234] J. D. Ramsden and J. G. Huber, Resistivity of Ferromagnetic CePt, *Journal of the Less Common Metals* **161**, 223 (1990).
- [235] R. Burriel, M. Castro, J. A. Blanco, J. I. Espeso, J. Rodríguez Fernández, J. C. Gomez-Sal, C. Lester, M. de Podesta, and K. A. McEwen, Specific Heat and Thermal Expansion of CePt in the 0.7–300 K Temperature Range, *Physica B: Condensed Matter* **206**, 264 (1995).

- [236] D. Gignoux and J. Voiron, Pressure Effects in  $\text{CeNi}(x)\text{Pt}(1-x)$  Dense Kondo Ferromagnets, *Physics Letters A* **108**, 473 (1985).
- [237] Y. Isikawa, K. Mori, A. Fuji, and K. Sato, Formation of Kondo Lattice in  $\text{La}(1-x)\text{Ce}(x)\text{Ni}$ , *Journal of the Physical Society of Japan* **55**, 3165 (1986).
- [238] D. Gignoux, J. C. Gomez-Sal, and J. Rodríguez Fernandez, Effect of Substitution of Ce by La in the  $\text{CeNi}(x)\text{Pt}(1-x)$  Dense Kondo Ferromagnets, *Journal of Magnetism and Magnetic Materials* **66**, 101 (1987).
- [239] J. M. Barandiarán, J. A. Blanco, D. Gignoux, J. C. Gómez Sal, J. Rodríguez Fernández, and J. Voiron, Overview of the Magnetic Properties of the Ferromagnetic Kondo System  $\text{CeNi}(x)\text{Pt}(1-x)$ , and Its Related Diluted Alloys, *Journal of Magnetism and Magnetic Materials* **90-91**, 145 (1990).
- [240] J. A. Blanco, D. Gignoux, J. C. Gomez-Sal, J. Rodríguez Fernandez, J. Voiron, and J. M. Barandiaran, Evolution from Kondo Ferromagnet to Intermediate Valence in the  $\text{Ce}(x)\text{Y}(1-x)\text{Ni}_{0.8}\text{Pt}_{0.2}$  System, *Journal of Physics: Condensed Matter* **2**, 677 (1990).
- [241] J. A. Blanco, M. de Podesta, J. I. Espeso, J. C. Gómez Sal, C. Lester, K. A. McEwen, N. Patrikios, and J. Rodríguez Fernández, Specific Heat of  $\text{CeNi}(x)\text{Pt}(1-x)$  Pseudobinary Compounds and Related Dilute Alloys, *Physical Review B* **49**, 15126 (1994).
- [242] J. C. Gomez-Sal, J. A. Blanco, J. I. Espeso, J. Rodriguez Fernández, and D. Gignoux, Enhancement of the Localized Behavior in  $\text{CeNi}_{0.8}\text{Pt}_{0.2}$  Kondo Compound Replacing Ce by Magnetic Ions (Pr,Nd), *Journal of Applied Physics* **76**, 6118 (1994).
- [243] J. Sakurai, J. C. Gomez-Sal, and J. Rodríguez Fernández, Thermopower and Electric Resistivity of  $\text{Ce}(1-x)(\text{La or Y})(x)\text{Ni}_{0.8}\text{Pt}_{0.2}$  Kondo System, *Journal of Magnetism and Magnetic Materials* **140**, 1223 (1995).
- [244] J. I. Espeso, J. A. Blanco, M. Reiffers, J. Rodríguez Fernández, and J. C. Gomez-Sal, New Aspects of the Magnetic Evolution of the  $\text{CeNi}(1-x)\text{Pt}(x)$  System, *Journal of Magnetism and Magnetic Materials* **157**, 685 (1996).
- [245] J. I. Espeso, J. C. Gomez-Sal, and J. Chaboy, Role of the Electronic State of Cerium in the Magnetic Properties of  $\text{CeNi}(x)\text{Pt}(1-x)$  Compounds, *Physical Review B* **63**, 014416 (2000).

- [246] J. Sakurai, A. Iwasaki, Q. Lu, D. Huo, Y. Isikawa, J. Rodríguez Fernández, and J. C. Gomez-Sal, Thermoelectric Power of CePt(1-x)Ni(x), *Journal of the Physical Society of Japan* **71**, 2829 (2002).
- [247] I. Kawasaki, K. Tenya, M. Yokoyama, and H. Amitsuka, Quantum Critical Phenomena of Ferromagnetic CePt(1-x)Rh(x), *Physica B: Condensed Matter* **403**, 1284 (2008).
- [248] N. Bagrets, V. Fritsch, K. Grube, and H. von Löhneysen, Quantum Criticality in CePt(1-x)Ni(x) Due to Hydrostatic and Chemical Pressure, *physica status solidi (b)* **247**, 703 (2010).
- [249] D. Gignoux, F. Givord, and R. Lemaire, Intermediate Valence State of Ce in CeNi, *Journal of the Less Common Metals* **94**, 165 (1983).
- [250] M. Očko, Transport Properties of the Ce(x)La(1-x)Pt Alloy System, *Journal of Alloys and Compounds* **482**, 43 (2009).
- [251] M. Očko, K. Zadro, D. Drobac, I. Aviani, K. Salamon, D. Mixson, E. D. Bauer, and J. L. Sarrao, Study of the Magnetic Properties of the Ce(x)La(1-x)Pt Alloy System: Which Interaction Establishes Ferromagnetism in Kondo Systems? *Journal of Magnetism and Magnetic Materials* **417**, 359 (2016).
- [252] M. Očko, K. Zadro, D. Drobac, I. Aviani, K. Salamon, E. D. Bauer, and J. L. Sarrao, Transport Properties of the Ce(x)Y(1-x)Pt Alloy System: Unusual Concentration Dependence of the Curie Temperature, *Journal of Magnetism and Magnetic Materials* **426**, 40 (2017).
- [253] M. Očko, K. Zadro, D. Drobac, I. Aviani, K. Salamon, D. Mixson, E. D. Bauer, and J. L. Sarrao, Magnetic Properties of Ce(x)Y(1-x)Pt Compared to Ce(x)La(1-x)Pt Ones, *Journal of Magnetism and Magnetic Materials* **451**, 727 (2018).
- [254] B. Cornut and B. Coqblin, Influence of the Crystalline Field on the Kondo Effect of Alloys and Compounds with Cerium Impurities, *Physical Review B* **5**, 4541 (1972).
- [255] J. G. Sereni, Low-Temperature Behaviour of Cerium Compounds: Specific Heat of Binary and Related Intermetallics, in *Handbook on the Physics and Chemistry of Rare Earths*, Vol. 15 (Elsevier, 1991) pp. 1–59.
- [256] U. S. Kaluarachchi, S. L. Bud'ko, P. C. Canfield, and V. Taufour, Tricritical Wings and Modulated Magnetic Phases in LaCrGe<sub>3</sub> under Pressure, *Nature Communications* **8**, 546 (2017).

- [257] E. Gati, J. M. Wilde, R. Khasanov, L. Xiang, S. Dissanayake, R. Gupta, M. Matsuda, F. Ye, B. Haberl, U. Kaluarachchi, R. J. McQueeney, A. Kreyssig, S. L. Bud'ko, and P. C. Canfield, Formation of Short-Range Magnetic Order and Avoided Ferromagnetic Quantum Criticality in Pressurized LaCrGe<sub>3</sub>, [Physical Review B](#) **103**, 075111 (2021).
- [258] C. Pfleiderer and A. D. Huxley, Pressure Dependence of the Magnetization in the Ferromagnetic Superconductor UGe<sub>2</sub>, [Physical Review Letters](#) **89**, 147005 (2002).
- [259] F. Haslbeck, S. Säubert, M. Seifert, C. Franz, M. Schulz, A. Heinemann, T. Keller, P. Das, J. D. Thompson, E. D. Bauer, C. Pfleiderer, and M. Janoschek, Ultra-High Resolution Neutron Spectroscopy of Low-Energy Spin Dynamics in UGe<sub>2</sub>, [Physical Review B](#) **99**, 014429 (2019), [arXiv:1801.10278](#) .
- [260] Y. Onuki, I. Ukon, S. W. Yun, I. Umehara, K. Satoh, T. Fukuhara, H. Sato, S. Takayanagi, M. Shikama, and A. Ochiai, Magnetic and Electrical Properties of U-Ge Intermetallic Compounds, [Journal of the Physical Society of Japan](#) **61**, 293 (1992).